Electronic spin precession in all solid state magnetic tunnel transistor

Christopher Vautrin

To cite this version:

Christopher Vautrin. Electronic spin precession in all solid state magnetic tunnel transistor. Physics [physics]. Université de Lorraine, 2017. English. NNT : 2017LORR0075 . tel-01584065

HAL Id: tel-01584065
https://theses.hal.science/tel-01584065
Submitted on 8 Sep 2017

Université de Lorraine, Collegium Sciences et Technologies
Ecole Doctorale EMMA " Energie, Mécanique et Matériaux "

THÈSE

Pour l'obtention du titre de :

DOCTEUR DE L'UNIVERSITÉ DE LORRAINE

Spécialité : Physique

Présentée par :

VAUTRIN Christopher

Electronic spin precession in all solid state magnetic tunnel transistor

---

Thèse soutenue publiquement le 12 juillet 2017 à Nancy devant le jury composé de :

Mme. Claire BARADUC	Ingénieur CEA, Laboratoire SPINTEC	Rapporteur
M. Wolfgang WEBER	Professeur, Université deStrasbourg	Rapporteur
M. Bertrand KIERREN	Professeur, Université de Lorraine	Examinateur
M. Coriolan TIUSAN	Professeur, Technical University of Cluj-Napoca	Examinateur
M. Michel HEHN	Professeur, Université de Lorraine	Directeur de thèse
M. Daniel LACOUR	Chargé de recherche, CNRS	Co-directeur de thèse

Institut Jean Lamour - UMR 7198 - Département P2M - Equipe 101
Faculté des Sciences et Technologies - Campus Victor Grignard
BP 70239 - 54506 Vandœuvre-lès-Nancy Cedex
Université de Lorraine - Pôle M4 : matière, matériaux, métallurgie, mécanique

Contents

PART I

INTRODUCTION

Chapter 1

State of the art review of the electronic spin precession - Goal of this thesis

---

In this first chapter, we will review some previous works and their related results on the electronic spin precession in a magnetic field. In a first step, based on the Landau-Lifshitz-Gilbert (LLG) equation, we will show how a magnetic field disturbs a magnetic moment by reorientating it towards the magnetic field direction with a complex trajectory, including a precession motion. In a second step, we will report experimental results of the electronic spin precession in thin films, either around an external applied field or around the molecular field of a ferromagnetic layer. While sections 2 and 3 report the results of the electronic spin precession around an external applied field in solid state devices including a non-magnetic metal (with electrons at the Fermi level) or a semiconductor (with hot electrons) respectively, section 4 shows the results about the spin precession around the molecular field of a ferromagnetic thin film with an energy higher than $E_F + 5eV$. Finally, we will expose the goal of this thesis in the light of the existing state of the art and show how this work is complementary to previous published studies.

I. Effect of a magnetic field on a magnetic moment

I.A. Theoretical description

Even before our understanding of the matter, the fact that a metal can be attracted by a magnet was already well known from ancient times. The first magnetic compass was used around the year 1000, when Chinese scientists understood that a magnetic needle could show a fixed direction that is the Earth magnetic north. In fact, when a magnetic field is applied to a magnetic moment (and by extension to a magnetic needle), the latter tends to align with the direction of the magnetic field in order to minimise the energy. This reorientation is driven by the torque that is exerted by a magnetic field $\overrightarrow{B}$ on a magnetic moment $\overrightarrow{m}$, which equals:

$$\overrightarrow{\Gamma} = \overrightarrow{m} \times \overrightarrow{B} \tag{1.1}$$

The motion of a magnetic moment around a magnetic field is much more complex than a continuous rotation towards the field direction. Indeed, the trajectory is computed by using the kinetic moment theory:

$$\frac{d\overrightarrow{J}}{dt} = \overrightarrow{\Gamma} \tag{1.2}$$

with $\overrightarrow{J}$ the angular momentum. In a magnetic material, the magnetic moment is given by:

$$\overrightarrow{m} = \gamma \overrightarrow{J} \tag{1.3}$$

where $\gamma = -eg/2m_0$ is the gyromagnetic factor, g the Landé factor, e the electronic charge and m_0 the mass of a free electron. Using equation 1.3, equation 1.2 can be rewritten:

$$\frac{d\overrightarrow{m}}{dt} = \gamma \overrightarrow{m} \times \overrightarrow{B} \tag{1.4}$$

From this equation, a precession of the magnetic moment around the magnetic field axis is predicted with a frequency equal to $w_L = \gamma \mid \overrightarrow{B} \mid$, called the Larmor frequency. Considering a free electron, a typical value of $w_L = 1.7 \cdot 10^{11}\ rad.s^{-1}.T^{-1}$ can be calculated.

The previous equation of magnetisation dynamics considers only conservative interactions. According to this, the magnetic moment has to precess indefinitely around the direction of the applied field. Nevertheless, the magnetic moment always dissipates energy and eventually reaches its stable and static equilibrium position parallel to the applied field. This phenomenon has been taken into account in the magnetisation dynamics by adding a dissipation term in the previous equation 1.4. The resulting equation is called the Landau–Lifshitz–Gilbert (*LLG*) equation. The origin of the dissipation term is for example the emission of phonons or magnons. The reader can find additional information in [1] on the damping processes.

Considering that in our macroscopic magnetic sample the magnetic moments of all the atoms are parallel, the total magnetic moment of the magnetic material equals the sum of all the atomic magnetic moment that also equals $\vec{M} = M_s V \vec{u}$ (with M_s the saturation magnetisation, V the volume and $\vec{u}$ a unit vector in the direction of the macroscopic magnetic moment). The LLG equation of magnetisation motion under the influence of a magnetic field $\vec{B}$ and including the damping term re-writes:

$$\frac{d\vec{u}}{dt} = \gamma\vec{u}\times\vec{B} - \gamma\alpha\vec{u}\times(\vec{u}\times\vec{B}) \tag{1.5}$$

in which α is the damping parameter. The LLG equation can be solved numerically in order to find the direction of the magnetisation as a function of time. An example of trajectory is given in figure I.1.

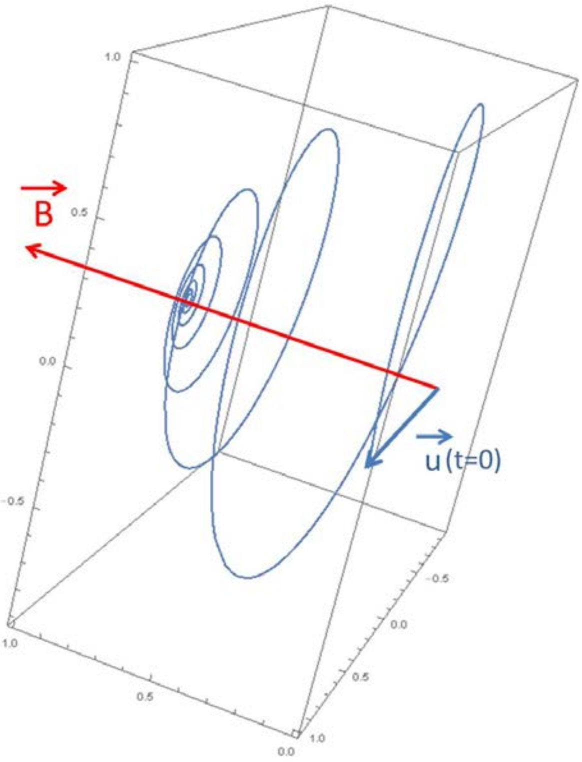

Fig. I.1: *Resolution with Mathematica of the LLG equation 1.5 for $\vec{u}$, with an initial magnetic moment perpendicular to the magnetic field. The applied field has an intensity of $5400T$ and the value of the damping parameter is 0.1.*

As can be seen in the simulation, and depending on the value of α, the magnetic moment rotates several times around $\overrightarrow{B}$ before aligning with it. This enables the control of the electronic spin direction, which is of prime importance in a spintronic device. Using a typical value of $10^6 m.s^{-1}$ for the velocity of electrons and the value of w_L given before, a rotation of $0,17 rad.T^{-1}$ can be obtained for a travel distance of $1\mu m$. As a result, if a control of the spin angle, and so the precession around the field, over 2π is targeted, either the device has to be long or the applied field has to be high.

I.B. Control of the spin of electrons in matter using an applied field

Two strategies have been used to study the spin precession of injected electrons in matter.

The first one consists in measuring devices for which the travel distance is long. A demonstration has been done by Jedema *et al.* who have studied the electronic spin precession in an aluminium layer under the influence of an external magnetic field [2]. The electrons are spin-polarised in a first ferromagnetic layer and injected in an Al strip. The lateral transport of electrons over a μm distance occurs in the diffusive regime. A second ferromagnetic layer measures the spin accumulation that enables the quantification of the electronic spin precession angle. Another demonstration has been given by Appelbaum *et al.* who have studied the electronic spin precession in a silicon layer under the influence of an external magnetic field [3]. In this case, the spin precession of hot electrons is considered, with energies up to 2eV above the Fermi level, and the perpendicular transport over a 10 μm distance with an analysis in energy is studied.

The second strategy consists in increasing the value of the applied field above hundreds of Tesla. This can be done in a magnetic thin film. Indeed, the exchange field (or molecular field) that exists in a magnetic material can reach several hundreds of Tesla, which is much larger than any magnetic field that can be obtained in a laboratory. As a result, even in thin layers with typical thickness of several nanometers, high precession angles can be observed. This strategy has been followed by Weber *et al.* [4, 5, 6] using hot electrons injected from an external spin-polarised beam, with energies of 5eV and more above the Fermi level.

In the following, we will detail those research works and show how our study is complementary and innovative.

II. Electronic spin precession in a metallic layer at the Fermi level

In order to study the spin precession in a metallic layer, Jedema *et al.* used a device based on a lateral spin valve [2]. The active layer for the spin precession is an aluminium nano-wire, which is surrounded by two aluminium tunnel barriers (Al_2O_3). On top of the Al_2O_3 layer, two ferromagnetic electrodes of Co have been deposited in order to enable the injection of a spin-polarised current in the *Al* wire ($Co1$) but also a spin-dependent detection (Co2). The final device $Co/Al_2O_3/Al/\ Al_2O_3/Co$ is shown in figure I.2. The two ferromagnetic electrodes have different widths leading to different coercive fields. As a result, parallel and anti-parallel configurations of the magnetisations can be obtained easily.

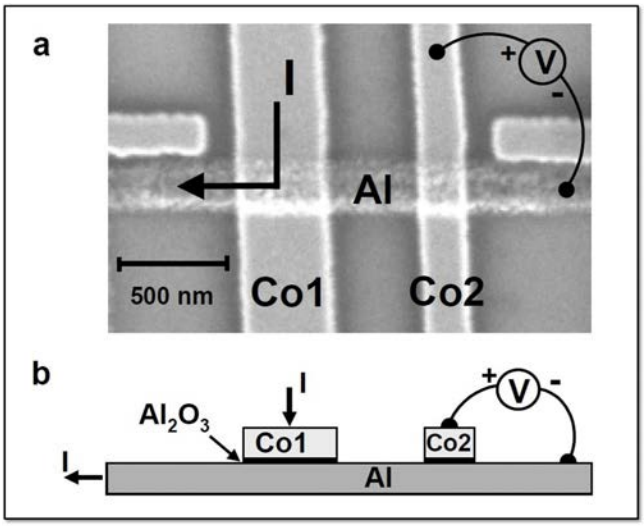

Fig. I.2: *(a) Scanning electron microscope image of the device. The cobalt electrodes spacing is $L = 650nm$. The current is injected from $Co1$ into the left side of the Al strip. The voltage is measured between $Co2$ and the right side of the Al strip. (b) Schematic of the cross-section of the device. Figures excerpted from [2].*

The electrons injected from Co1 to the Al strip are spin-polarised and create a spin accumulation under the Co1 contact. The second ferromagnetic electrode (Co2) is used to detect the spin accumulation at a distance L from the injector. During the diffusion from Co1 to Co2, the direction of the spin can be modified either by spin-flip scattering processes or, if an external magnetic field is applied, by the precession around the applied field. Both phenomena have been measured. The first experiment consists in measuring the amplitude of the voltage on the $Co2/Al_2O_3/Al$ tunnel junction as a function of the distance L between the Co electrodes. The magnitude of the output signal as a function of L can be calculated by solving the spin-coupled diffusion equations for the spin-up and spin-down electrons in the Al strip [2]. If the tunnel barrier resistances are considered much larger than the resistance of the Al strip over the spin relaxation length, the expression can be written as:

$$\frac{V}{I} = \pm P^2 \frac{\lambda_{sf}}{2A\sigma_{Al}} exp\left(-\frac{L}{\lambda_{sf}}\right) \tag{1.6}$$

where P is the spin polarisation of the injected current, λ_{sf} the spin relaxation length in the Al strip, A the cross sectional area and σ_{Al} the Al conductivity. A positive sign corresponds to a parallel magnetic configuration of the spin valve (a negative sign to an anti-parallel configuration). The spin relaxation length can be deduced from the curve $\Delta R = \Delta V/I$ as a function of the Co electrode spacing L (figure I.3).

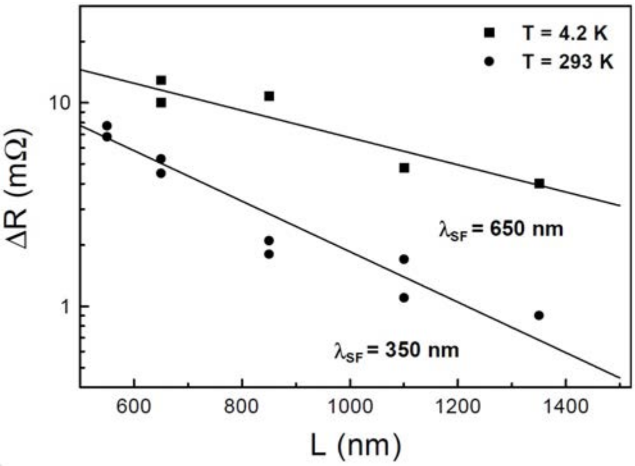

Fig. I.3: *spin-dependent resistance ΔR (in logarithmic scale) as a function of the Co electrodes spacing. The solid squares are the measurements taken at low temperature (4.2K). The solid circles represents the measurements at room temperature. The solid lines are the best fits based on equation 1.6. Excerpted from [2].*

By using equation 1.6 to fit the curves, the spin relaxation length λ_{sf} is found to be equal to $\lambda_{sf} = (650 \pm 100)\ nm$ at low temperature ($4.2K$) and $\lambda_{sf} = (350 \pm 50)\ nm$ at room temperature.

By using this important parameter, a second experiment can be made to measure the electronic spin precession. The experiment consists in measuring the amplitude of the spin signal on the Co2/Al_2O_3/Al tunnel junction as a function of an applied magnetic field. The device is first prepared in a given magnetic configuration by applying a field in the sample plane. Then, a magnetic field $H_\perp$ is applied perpendicular to the sample plane. The electronic spins precess around the field axis, and the output voltage signal will be modified according the equation:

$$\frac{V(H_\perp)}{I} = \pm\frac{P^2}{e^2N(E_F)}\int_0^\infty D(t)cos(w_lt)e^{-t/\tau_{sf}} \tag{1.7}$$

in which $D(t)$ is the probability per unit of volume for an injected electron to cross the Al strip without spin flip. Since the magnetic field is perpendicular to the film plane, the magnetisations of Co electrodes will also slightly rotate by an angle θ towards the field direction. This rotation can be taken into account and equation 1.7 can be rewritten as:

$$\frac{V(H_\perp,\theta)}{I} = V(H_\perp)cos^2(\theta) + V(H_\perp = 0)sin^2(\theta) \tag{1.8}$$

Experimental curves of the output voltage as a function of the applied field for different values of the Co electrodes spacing L are shown in the figure I.4.

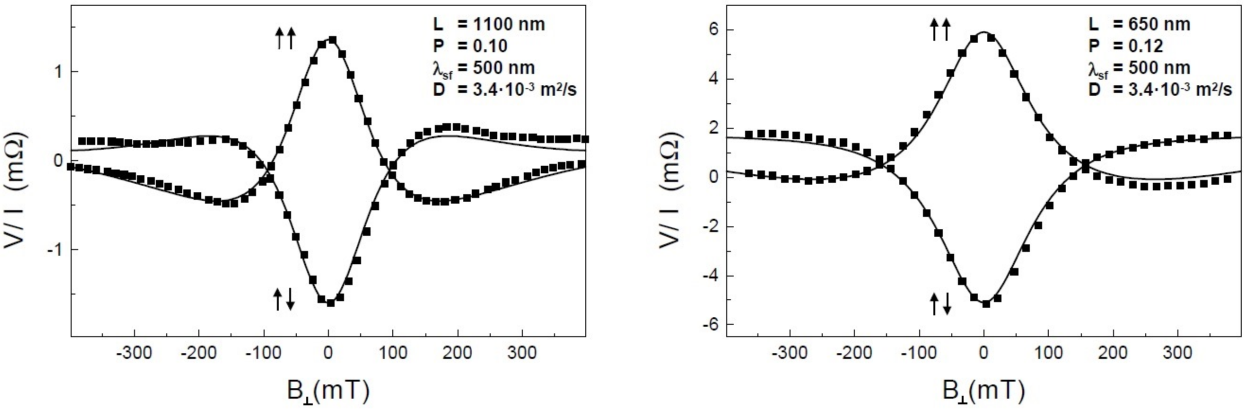

Fig. I.4: *Output signal (V/I) as a function of the perpendicular magnetic field $H_\perp$, for $L = 650nm$ and $L = 1100nm$. Data were taken at RT. The solid lines represent the best fits based on equations 1.7 and 1.8. Excerpted from [7].*

In the parallel configuration of the spin valve, the signal is positive without magnetic field. When $\mid H_\perp \mid$ increases, the magnitude of the output voltage decreases. The precession angle is around 90^o when the two curves cross. In fact, when the electronic spins have precessed by an angle of 90^o, they have their orientations perpendicular to the direction of the Co2 magnetisation, regardless the magnetic configuration of the spin valve. When the precession angle reaches 180^o, the output voltage will change its sign: the spin-up population has been converted into a spin-down population.

This first demonstration of spin precession in a metallic layer integrated in a device for temperature ranging from room temperature to 4K highlights limitations of the strategy for which the travel distance is long. First of all, since our metal is diffusive, the travel or diffusion time t between injector and detector is not unique. Indeed, many different paths exist for spins to go from Co1 to Co2. Therefore a spread in the diffusion times t occurs and hence a spread in precession angles $\epsilon = w_L t$. Second, spin diffusion lengths are short, which limits the length of the device. By the use of ballistic hot electrons injected in semiconductors, those limitations are lifted.

III. Electronic spin precession of hot electrons in a semiconductor

In a semiconductor (SC), the spin lifetime and the diffusion length are much higher than in a metal. Thus, SC could be suitable for spintronic devices to study the electronic spin precession.

In order to study the spin precession in a $10\mu m$ thick Si layer, Appelbaum *et al.* have used a 4 terminal device derived from a Magnetic Tunnel Transistor (MTT). A sketch of the experiment is represented in the figure I.5. An Al/Al_2O_3/Al tunnel junction injects hot electrons in a thin CoFe layer. Since the mean free path of hot electrons is strongly spin-dependent (see chap II, section II), electrons with spin oriented antiparallel to the CoFe magnetisation are strongly scattered and thermalised. Their propagation is blocked at the CoFe/Si Schottky interface. Electrons with spin oriented parallel to the CoFe magnetisation are injected in Si. As a result, the flow of electrons injected in the Si is highly spin-polarised. During propagation in Si, the spins are subjected to an applied field and precess. After propagation, the spin direction is analysed in the NiFe through spin-dependent scattering and energy analysis of the Cu/Si Schottky barrier.

The electronic spin precession in the SC results in an oscillation of the collected current I_{c2} with the magnitude of the applied field. Because of the action of random diffusion, spin dephasing occurs with higher precession angles, and results in higher-order damped oscillations. Therefore, just two multiples of π precession angle are seen without accelerating voltage bias. When the electric drift field is increased with an applied voltage bias V_{c1}, the transit time is reduced, and the precession angle at any fixed magnetic field is consequently also reduced. This pushes the extrema to higher values of perpendicular magnetic fields, clearly shown in figure I.5b and c at respectively 0.5 V and 1.0 V accelerating voltages. Under these conditions of higher accelerating electric field, drift is even more dominant than in figure I.5a, and precession angles up to 4π can be seen.

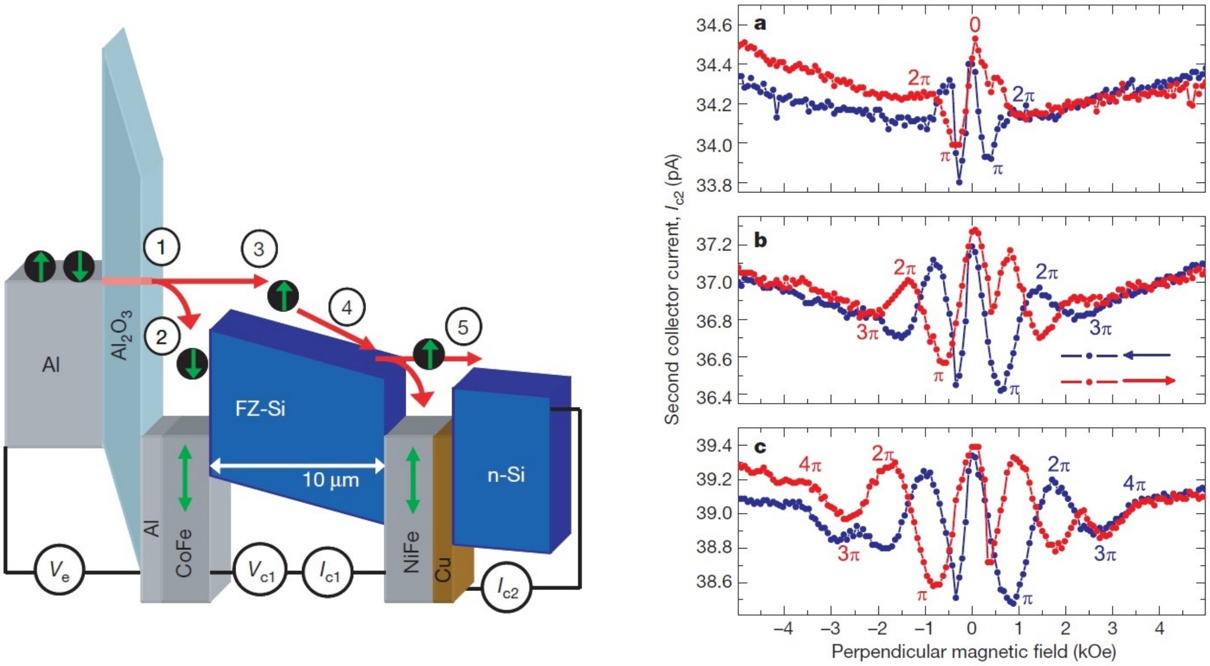

Fig. I.5: Left: schematic band diagram of the experiment. The emitter voltage (V_e) defines the hot electrons energy. The "first collector current" (I_{c1}) at the NiFe contact and the "second collector current" (I_{c2}) at the n-Si substrate contact are measured, under optional voltage bias (V_{c1}) across the single-crystal undoped float-zone Si (FZ-Si) drift region. Right: Spin precession and dephasing in a perpendicular magnetic field at constant emitter voltage $V_e = -1.8V$ and $85K$. The accelerating voltage bias V_{c1} is equal to 0V (a), 0.5V (b) or 1V (c). Excerpted from [3].

This second demonstration of spin precession validates the strategy for which the travel distance is long. However, the fabrication of such kind of devices is very complex with a step of waferbounding in order to get the Si/NiFe/Cu/Si structure with high quality Si layers. This limits the number of devices and material combinations that can be studied.

IV. Electronic spin precession in a ferromagnetic layer at high energy

Let us now have a look at the second strategy that consists in increasing the value of the applied field above hundreds of Tesla. In these experiments, hot spin-polarised electrons are injected from the vacuum into a freestanding Au/Co/Au trilayer. The spin-polarised current is emitted by a GaAs photo-cathode. The analysis of the reflected or transmitted current is made by Mott polarimeters, which are spin and energy selective. A scheme of the experiment is represented in the figure I.6.

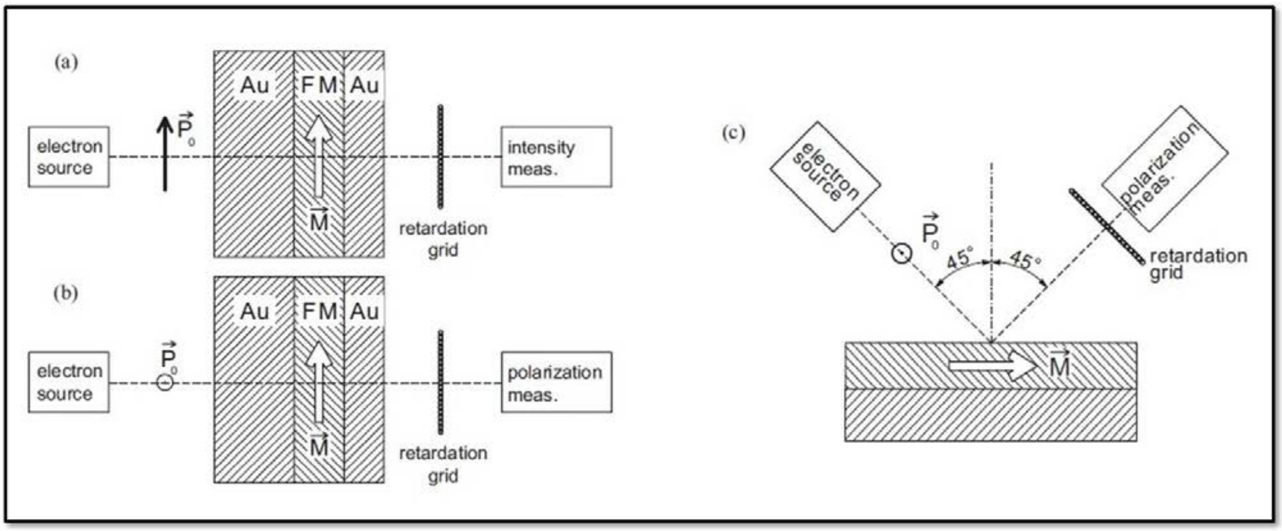

Fig. I.6: *Schematics of the experiment. The intensity and the degree of spin polarisation is measured for the electrons transmitted in a trilayer (left-hand side) or reflected on the surface of a magnetic layer (right-hand side). The spin polarisation of the incoming electrons can be oriented parallel (a) or perpendicular to the magnetisation (b) and (c) . Excerpted from [4].*

The spin polarisation vector of the emitted electrons is noted $\overrightarrow{P_0}$. We consider the magnetisation of the ferromagnetic layer $\overrightarrow{M}$ uniform. When electrons propagate through the magnetic layer, the spin polarisation vector will be modified by the spin precession and the spin filtering. The spin filtering tends to align the spin polarisation with the direction of the magnetisation (angle θ in the figure I.7). The second effect is the electronic spin precession under the influence of the molecular field in the ferromagnet (angle ϵ in the figure I.7).

The incoming flux of electrons has a spin polarisation vector $\overrightarrow{P_0}$ (along the x-axis for instance) perpendicular to $\overrightarrow{M}$ (along the z-axis). The wave function describing that state is expressed as:

$$\Psi_{incident} = \frac{1}{\sqrt{2}}\left(\begin{pmatrix}1\\0\end{pmatrix} + \begin{pmatrix}0\\1\end{pmatrix}\right)e^{i\zeta} \tag{1.9}$$

In a ferromagnetic material, the diffusion depends on the spin of the electron. Thus, the part of the wave function associated to the minority spins will be more attenuated than the one associated to the majority spins: it is the consequence of the spin filtering. The wave function of the transmitted electrons can be written:

$$\Psi_{transmitted} = \frac{1}{\sqrt{2}}\left(\sqrt{1+A}\begin{pmatrix}1\\0\end{pmatrix}e^{-i\frac{E_{\uparrow}}{\hbar}t} + \sqrt{1-A}\begin{pmatrix}0\\1\end{pmatrix}e^{-i\frac{E_{\downarrow}}{\hbar}t}\right)e^{i\zeta} \tag{1.10}$$

in which A is defined as the spin asymmetry $A = (I^{\uparrow} - I^{\downarrow})/(I^{\uparrow} + I^{\downarrow})$ for a pure spin state ($P_0 = 1$), $E_{\uparrow}$ ($E_{\downarrow}$) the energy eigenvalue for the majority (minority) spin wave function, and t the time spent by the electrons within the ferromagnet. The transmitted wave function can be re-written as follows:

$$\Psi_{transmitted} = \frac{1}{\sqrt{2}}\left(\sqrt{1+A}\begin{pmatrix}1\\0\end{pmatrix} + \sqrt{1-A}\begin{pmatrix}0\\1\end{pmatrix}e^{-i\frac{E_{\downarrow}-E_{\uparrow}}{\hbar}t}\right)e^{i\zeta}e^{-i\frac{E_{\uparrow}}{\hbar}t} \tag{1.11}$$

The precession appears then as a phase-shift. The precession angle equals $\epsilon = \frac{\Delta E_{exch}}{\hbar}t$, with $\Delta E_{exch} = E_{\uparrow} - E_{\downarrow}$ is the exchange splitting that occurs in a ferromagnetic material. By defining the group velocity v of the electronic flux, which is expressed in a free electron model as $v = \sqrt{2E/m_e}$, and d the distance crossed by the electrons in the ferromagnetic layer, which equals the film thickness in the hypothesis of a ballistic trajectory, the precession angle becomes:

$$\epsilon = \sqrt{\frac{m_e}{2\hbar^2}}\,\frac{\Delta E_{exch}}{\sqrt{E}}\,d \tag{1.12}$$

In the case of a magnetisation along the z axis, the spin polarisation vector of the transmitted electrons is expressed as:

$$\overrightarrow{P} = \begin{pmatrix} P_0\,\sqrt{1-A^2}\,cos(\epsilon) \\ P_0\,\sqrt{1-A^2}\,sin(\epsilon) \\ P_0\,A \end{pmatrix} \tag{1.13}$$

As a consequence, the rotation angle θ towards the direction of the magnetisation is given by:

$$\theta = arctan\left(\frac{A}{\sqrt{1-A^2}}\right) \tag{1.14}$$

Therefore, if the spin polarisation of the incoming electrons P_0 is known, the measurement of the spin polarisation after the ferromagnetic layer gives access to ϵ, the precession angle, and θ, the angle of rotation towards $\overrightarrow{M}$.

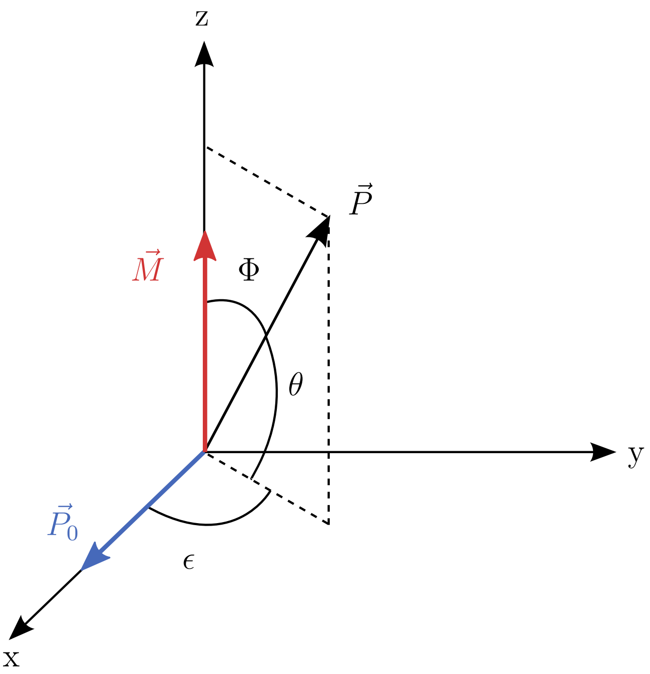

Fig. I.7: *Schematic drawing of the precession angle (ϵ) and rotation angle linked to the spin filtering (θ) of the electronic spin polarisation vector* $\vec{P}$ *around the magnetisation* $\vec{M}$ *of a ferromagnetic layer oriented along the z-axis. The initial spin polarisation vector* $\vec{P}_0$ *is along the x-axis.*

The first set of experiments consists in measuring both angles as a function of the ferromagnetic material thickness. On the left-hand side, ϵ is measured for a Co layer at 8eV above the Fermi level. On the right-hand side, $\Phi = \pi/2 - \theta$ is measured for Fe or Co layers at $E - E_F$=5eV and for a Ni layer at 7eV above E_F (figure I.8).

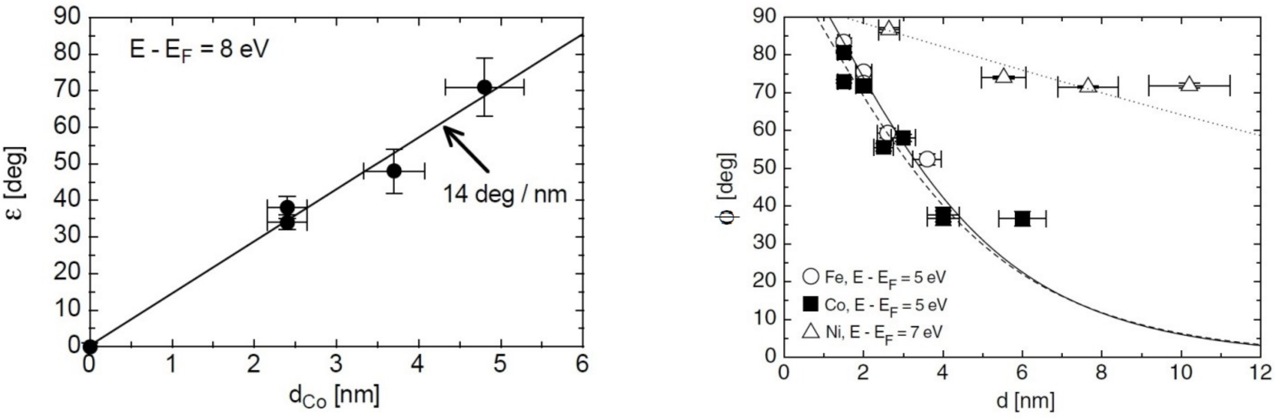

Fig. I.8: *Left: precession angle* ϵ *as a function of the Co thickness. The energy of the incoming electrons is* $E - E_F = 8eV$*. Right: rotation of the electronic spin* Φ *as a function of the thickness for different ferromagnetic materials (Co, Ni and Fe). Excerpted from [6].*

If the goal is to control the spin direction using the spin precession, the spin filtering should be removed or limited. On the right-hand side of figure I.8, it is shown that the spin filtering is strongly dependent on the nature of the ferromagnetic material. It appears that spin filtering in Ni is much smaller than in Co or Fe. Indeed, when the electronic spin is injected in a direction perpendicular to the ferromagnetic magnetisation, it is almost completely filtered in Co or Fe for layer thicknesses above 10nm. Even if spin filtering occurs, the precession angle can be measured and is reported on the left-hand side of figure I.8 for a Co layer at 8eV above the Fermi level. As expected from equation 1.12, a linear dependence of the precession angle with the ferromagnetic layer thickness is observed. At 8eV above the Fermi level in a Co layer, a precession of $\tilde{\epsilon} = 14^o/nm$ is measured. This is equivalent to a Larmor precession with a molecular field equals to 4000T!

In the second set of experiments, the precession angle is measured as a function of the energy of the incoming electrons. However, all the energies are not available for the electrons in this experiment. Indeed, the electrons are injected from the vacuum, and they need an energy higher than the work function of the metal, which is around 4eV, to enter in the metal. Moreover, the transmitted current is small at intermediate energies, which increases the difficulty of the experiment. Indeed, the inelastic mean free path is minimum in the energy range [10eV-100eV]. The figure I.9 presents the precession angle as a function of the energy for a large range of energy on the right-hand side, and a focus for low energy on the left-hand side.

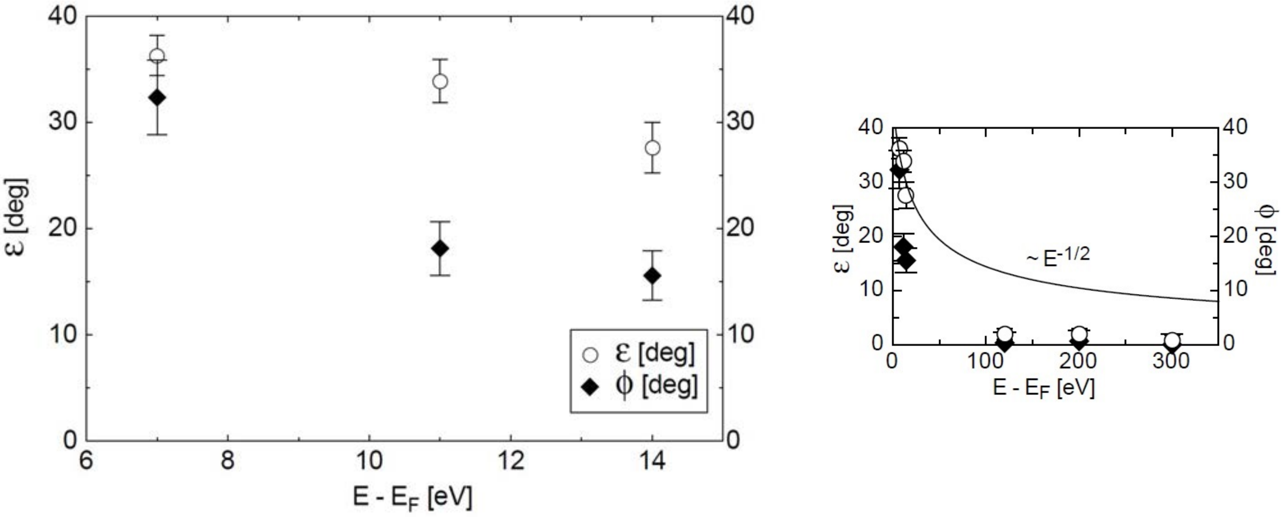

Fig. I.9: Left: precession and rotation angles as a function of the energy of the electrons $E - E_F$ for a 2.4nm thick Co layer. Right: precession angle ϵ as a function of the electrons energy in a large range of energy for the same Co layer. Excerpted from [6].

According equation 1.12, the precession angle must be proportional to the inverse of $\sqrt{E}$. The curve $\epsilon = f(E - E_F)$ fits the function $E^{-1/2}$ only at low energies. The vanishing of the precession angle cannot be explained only by the strong increase of the group velocity with the energy (multiplied by a factor of 3 from the low-energy to the high-energy regime). The exchange energy ΔE_{exch} also strongly decreases with increasing energy.

V. Goal of this thesis works

The goal of my PhD work consists in measuring the electronic spin precession in a ferromagnet for hot electrons with an energy smaller than $E_F + 4eV$ in order to extend the pioneer work of Weber. This range of energy can only be accessed using all solid state devices. Therefore, in our work, the injection strategy will be similar than the one developed by Appelbaum using a magnetic tunnel junction. This all solid state device, with an injection geometry perpendicular to the film plane will also be useful in the future for spintronics devices in which the direction of the spin polarisation of a current can be controlled using external parameters like an applied voltage. From the fundamental point of view, we will be able to check if, as predicted in a simple model (equation 1.12), the precession angle varies as $\Delta E_{exch}/\sqrt{E}$. The trend seems to be followed for energies above $E_F + 5eV$ as shown by Weber *et al.* In our solid state device, experiments as a function of the applied voltage on the tunnel barrier will allow us to change the electron energy between 0.7eV and 1.5eV. The upper limit is given by the breakdown voltage of the tunnel barrier, while the lower limit is imposed by the Schottky barrier. In our study, we have chosen the use of an MgO tunnel barrier to get high TMR ratios and injected currents of the order of magnitude of several mA. The barrier is drawn in blue in the energy landscape of our device (figure VII.1).

In the experiment, we want to analyse the spin precession of ballistic electrons into the structure. This will limit the spread in the diffusion times and the spread in precession angles encountered in the Jedema's experiments. Therefore, a Schottky barrier is inserted in our structure on the right (interface between Cu(dark green) and Si(green)). This Schottky barrier lets only electrons with an energy larger than the Schottky threshold ($\sim 0.7eV$) enter in the SC. Furthermore, thanks to its acceptance cone (see Chap II), only electrons that have their propagation vector nearly perpendicular to the multilayer interfaces will be collected in the SC and participate to the signal depending on the spin precession. So, a study of the spin precession of electrons is possible in an energy range [E_F+0.7eV < E < E_F+1.5eV].

Then, three magnetic layers have to be used: a first one to polarise the spin of the electrons, a second one that hosts the spin precession with, if possible, limitation of the spin filtering, and a last one that enables the analysis of the spin direction changes. A non-collinear configuration of the three magnetisations is needed with an optimal situation for which the magnetisations point in the three directions of space as shown in figure I.11.

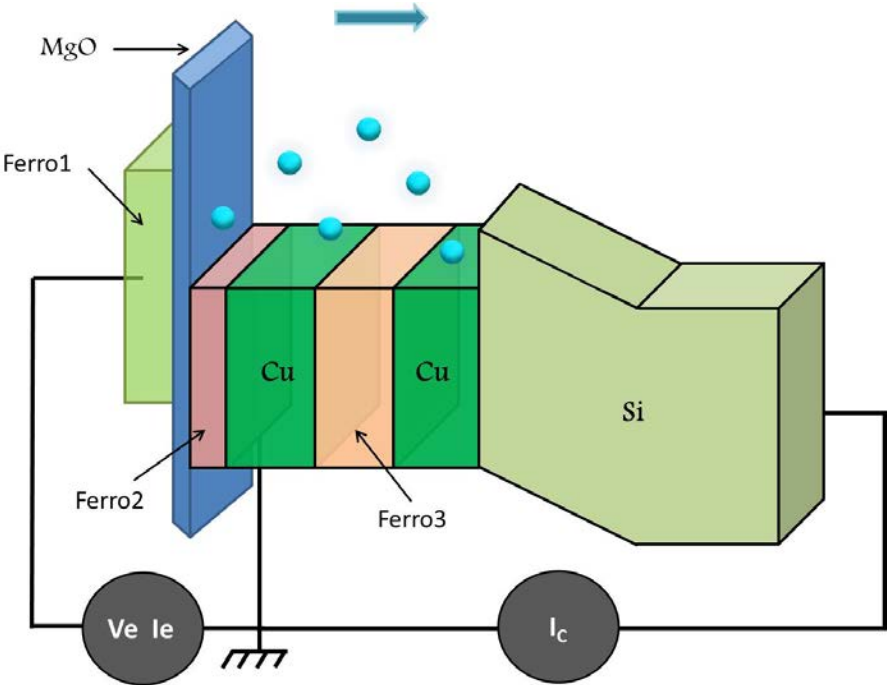

Fig. I.10: *Energy diagram of our device. The electrons injected through the MgO tunnel barrier are spin-polarised thanks to a first ferromagnetic layer (Ferro1). A phenomenon of precession takes place in the second ferromagnet (Ferro2). The spin polarisation changes are measured via a third ferromagnetic thin film (Ferro3). A Schottky barrier collects only electrons with an energy higher than* $\sim E_F + 0.7eV$.

The 3-dimensional magnetic configuration is particularly difficult to stabilise especially in zero applied field with the constraint to have a current of hot electrons in the SC with values above 100 pA (the limit of detection of our set up). Therefore, in contrast to the Appelbaum's configuration, the current in our structure is not polarised after the tunnel barrier but a spin-polarised current is injected through the tunnel barrier. In this case, the direction of the spin of the electrons is given by the magnetisation of $Ferro1$ and its direction will be locked using a ferromagnetic/anti-ferromagnetic bilayer.

In order to be able to change easily the nature of the magnetic layer that hosts the spin precession ($Ferro2$), we have optimised the magnetic properties of Ferro3, the layer with perpendicular magnetisation that will be common to all the samples studied in my PhD work ($Ferro3$). As will be shown in Chap IV, a [Co/Ni] multilayer has been chosen especially because of its predicted high spin polarisation. The precession angle will then be measured via a Giant Magneto-Resistance (*GMR*) effect between the precession layer and the [Co/Ni] multilayer. If the precession angle is equal to $\pi/2$, the spin will be aligned with the magnetisation of the third ferromagnetic layer. The mean free path of the electrons is long and electrons do not lose their energy: they are collected in the Si and the current is high. If the precession angle is equal to π, the spin is in an opposite direction than the magnetisation of the third layer. The mean free path of the electrons is short and electrons lose their energy: they are not collected in the Si and the current is low. Thus, the collected current is a direct picture of the precession angle between the two extreme cases described just above.

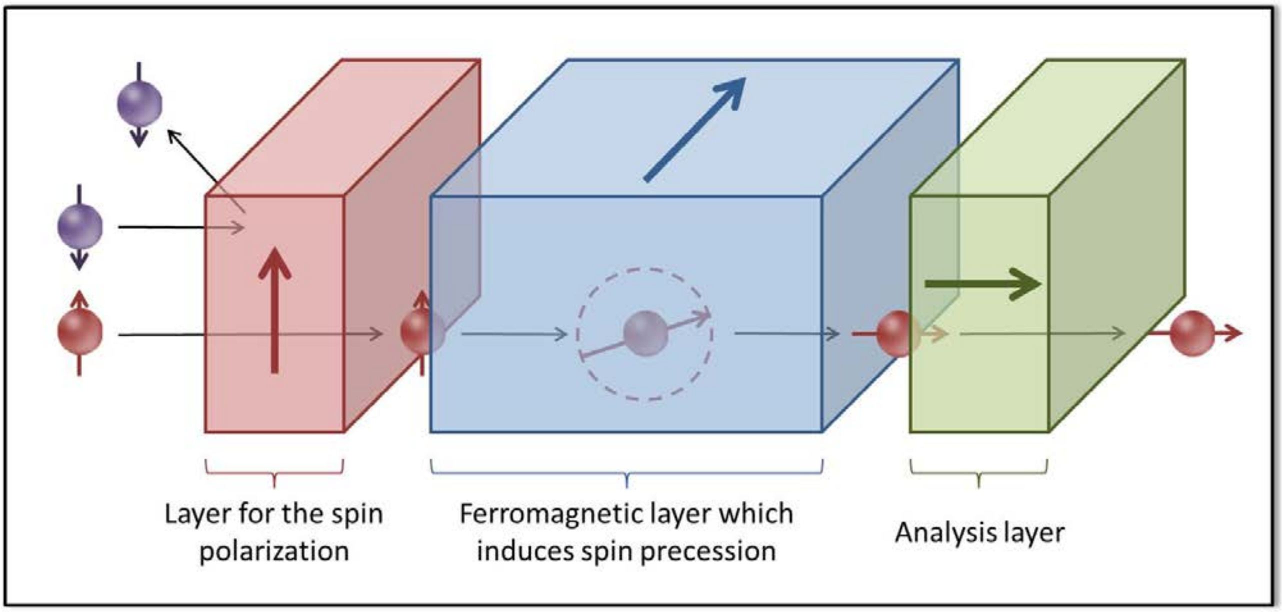

Fig. I.11: *Schematics of our experiment. The incoming electrons are spin-polarised thanks to a first ferromagnetic layer (Ferro1). A phenomenon of precession takes place in the second ferromagnet (Ferro2). The spin polarisation changes are measured via a third ferromagnetic thin film (Ferro3).*

As precession layers, Co, CoFeB and CoAl materials have been tested. The value of the spin precession angle (and so the expected signal) will depend on the molecular field (the stronger the field is, the faster the precession is), on the energy of the hot electrons and on the time spent in the ferromagnetic layer (and so the thickness of the layer).

VI. PhD manuscript organisation

Due to the complexity of the devices required to achieve my PhD goal, we have proceeded with a step by step approach. To obtain a magnetic layer that exhibits a perpendicular magnetic anisotropy and high spin polarisation, the structural and magnetic properties of [Co/Ni] multilayers grown on a Schottky diode have been studied. Then, the magneto-current of the magnetic tunnel transistor with crossed magnetisation has to be optimised. Therefore, we have used a MTT without magnetic spin polariser electrode. The hot electron current has been associated to the magnetic measurements in order to fully understand the response of the device. Especially, the variation of the MC as a function of the field (magnitude and angle) could be reproduced. Once the magneto-current was optimised, the third ferromagnetic layer has been added in order to spin polarise the injected electrons. At this stage, we have tried to measure the electronic spin precession in Co or CoFeB thin films. In order to show that the results are undoubtedly linked to precession, we have used a CoAl alloy in which a strong change of the molecular field with the temperature is expected. Because of the almost total absence of experimental studies on such alloys, we had to study first the magnetic properties for different compositions as a function of the temperature and then the response of the magnetic tunnel junctions.

The PhD manuscript is divided in three main parts that detail the step by step process followed along the PhD work.

- The first part gives a general introduction to the subject.

Chapter I: State of the art review of the electronic spin precession - Goal of this thesis

In this chapter, we review some previous studies devoted to the electronic spin precession. This part discusses the effect of a magnetic field on a magnetic moment. In particular, the Landau-Lifshitz-Gilbert (LLG) equation will be described. Then examples of recent studies on electronic spin precession in matter are reviewed in order to show how our project positions itself in the literature. The end of the chapter is devoted to highlight the thesis goals.

Chapter II: From a tunnel barrier to a magnetic tunnel transistor: overview

This chapter gives the key ingredients to understand the basics of the magnetic tunnel transistor, and presents the geometry of the device that will be used to study the spin precession.

In a first step, the physics of magnetic tunnel junctions is described. Then the transport of the hot electrons in ferromagnetic layers is evoked. The different scattering mechanisms will be discussed. Finally, the concept of MTT is developed.

- The second part of this PhD manuscript details the experimental work that led to the growth of a MTT with three ferromagnetic layers having magnetisations oriented in the three directions of space.

Chapter III: Overview of the magnetic anisotropy in Co/Ni multilayers

In this chapter, the theoretical bases to understand the magnetic behaviour of a thin magnetic film are given. The state of the art review of the perpendicualr magnetic anisotropy (*PMA*) on [Co/Ni] multilayers is also done.

Chapter IV: Magnetic and structural properties of [Co/Ni] multilayers

In this chapter, we show how we got [Co/Ni] multilayer with PMA on top of a Schottky diode. The insertion of a Ta nanolayer into the multilayer is shown to be a good solution to get the [111] texture, the only crystallographic configuration that exhibits a PMA. The magnetic behaviour is also studied as a function of the temperature, the number of [Co/Ni] repetitions, and the nature of the interfaces.

Chapter V: Magnetic properties of a CoAl alloy

In order to show that the experimental results on Co and CoFeB are linked to spin precession, we decided to measure the electronic spin precession in a ferromagnetic layer having a Curie temperature in the working range of our MTT. Therefore, we studied the magnetic properties of CoAl thin films, the CoAl layer that will be inserted in the MTT as a precession layer.

- The third part of this thesis is devoted to the electronic transport measurements.

Chapter VI: MC optimisation in the spin valve

In this chapter, the magneto-current in the spin valve is studied as a function of the number of repetitions of the [Co/Ni] multilayer. We show that the MC increases with the number of [Co/Ni] repetitions and that a MC about 85% can be obtained (close to the theoretical maximum of 100%). The angular dependence of the MC in a rotating field is also shown.

Chapter VII: Electronic spin precession

This chapter shows the growth of the top layer that spin-polarises the hot electrons injected. Then, the principle of the electronic spin precession measurements is given, especially by developing the theoretical expression of the transfer ratio as a function of the magnetic configuration of the device.

Chapter VIII: Electronic spin precession in a Co layer

In this chapter, the electronic transport measurements done in a MTT including a Co precession layer are shown. The tunnel junction characterisation and the measurement of the transfer ratio for different MTT configurations are realised. A precession velocity is finally extracted.

Chapter IX: Electronic spin precession in a CoFeB layer

In this chapter, the electronic transport measurements realised in a MTT including a CoFeB precession layer are shown. The tunnel junction characterisation and the measurement of the transfer ratio for different MTT configurations are done. A precession velocity is finally extracted.

Chapter X: Electronic spin precession in a CoAl alloy

In this chapter, the electronic transport measurements realised in a MTT including a CoAl precession layer are shown. The effect of the temperature on the behaviour of the MTT is especially demonstrated.

Résumé du chapitre :

L'objectif de ce chapitre est de de décrire ce qu'est la précession du spin de l'électron et de passer en revue les travaux qui ont été réalisés sur ce phénomène. Dans un premier temps, nous avons montré quels sont les effets d'un champ magnétique sur un moment magnétique. Deux types de mouvements peuvent être distingués : tout d'abord, le moment magnétique va précesser autour du champ magnétique ; ensuite il va s'aligner avec la direction du champ pour minimiser son énergie. Ce mouvement est régi par l'équation de Landau-Lifshitz-Gilbert (LLG) :

$$\frac{d\overrightarrow{u}}{dt} = \gamma\overrightarrow{u} \times \overrightarrow{B} - \gamma\alpha\overrightarrow{u} \times (\overrightarrow{u} \times \overrightarrow{B})$$

La résolution numérique de cette équation montre qu'un contrôle de l'angle de précession entre 0 et 2π est possible soit si l'électron parcourt une grande distance (de l'ordre du μm) sous un champ appliqué de faible intensité (de l'ordre du Tesla), soit si l'électron parcourt des distances nanométriques mais sous un champ très intense de plusieurs milliers de Tesla.

Dans un deuxième temps, nous avons reporté les résultats expérimentaux concernant la précession du spin électronique dans des films minces, soit autour d'un champ externe sur des distances micrométriques, soit en utilisant le champ moléculaire d'un ferromagnétique de taille nanométriques. Les sections 2 et 3 de ce chapitre relèvent du premier cas. Jedema étudie tout d'abord la précession du spin de l'électron dans une bande d'aluminium de plusieurs μm de long, en appliquant un champ externe de quelques Tesla. Applebaum ensuite met en évidence ce phénomène dans une couche de Si dont l'épaisseur est de l'ordre de $10\mu m$, avec un champ externe appliqué également de quelques Tesla. La quatrième section montre quant à elle les travaux de Weber sur la précession du spin électronique dans des matériaux ferromagnétiques. Il a mesuré en particulier une précession de $14\deg/nm$ dans du Co pour des électrons possédant une énergie de 8eV au-dessus du niveau de Fermi. Il a également montré que l'angle de précession varie en $1/\sqrt{E}$ pour de hautes énergies.

Dans un troisième temps, l'objectif de cette thèse est mis en lumière par rapport aux travaux antérieurs, en particulier ceux de Weber. Notre but est de mesurer la précession du spin de l'électron dans des matériaux ferromagnétiques, pour des électrons possédant une faible énergie au-dessus du niveau de Fermi ($E_F < E < E_F + 2eV$). Cela permettrait notamment de vérifier la loi en $1/\sqrt{E}$ donnée par Weber et de construire un dispositif tout solide dans lequel l'orientation du spin d'un faisceau d'électrons est donnée par l'application d'une tension électrique ou par l'épaisseur d'une couche ferromagnétique.

Chapter 2

From a tunnel barrier to a magnetic tunnel transistor: overview

As shown in the previous chapter, we propose to measure the electronic spin precession in a ferromagnet at low energy with a Magnetic Tunnel Transistor (MTT). This chapter introduces the basics of such a device. In a first step, the concept of tunnel barrier is described, especially the properties of a magnetic tunnel junction. In the second part, the transport of the electrons with energies above the Fermi level is evoked and an overview of the scattering mechanisms is given. Finally, the third part is devoted to the magnetic tunnel transistor.

I. Tunnel Magneto-Resistance

I.A. What is a magnetic tunnel junction?

Basically, a magnetic tunnel junction (*MTJ*) is a trilayer composed of two ferromagnetic layers spaced by a thin insulator, typically few nanometers thick. When a voltage is applied between the two ferromagnetic layers, a net current flows through the insulator: the electrons cross the insulator by the so-called tunnel effect. When electrodes are made of magnetic materials, the level of the current depends on the magnetic configuration (figure II.1). This phenomenon arises as a consequence of the fact that tunnelling preserves the spin and that the band structure of the electrodes is spin-dependent. The normalised resistance variation is called tunnel magneto-resistance (*TMR*).

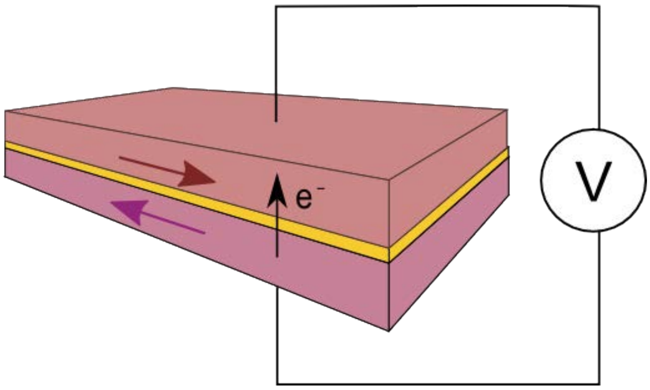

Fig. II.1: *Sketch of a tunnel junction. The insulator is represented in yellow. The two ferromagnetic layers (in red and purple) are in an anti-parallel magnetic configuration. A net electron flow exists across the insulator when a voltage V is applied between the two electrodes.*

The first experimental evidence of a TMR signal was established in 1975 by Jullière in a Fe/Ge/Co junction [8]. A resistance variation of 14% was measured at 4.2K. Since 1995, this field of research has found a new impetus by the discovery of TMR at room temperature by Moodera *et al.* in an Al_2O_3 based MTJ [9]. Indeed, with high TMR and high resistance, those devices were forecasted to industrial applications, like low-consumption sensors or MRAM memories.

I.B. Tunnel transport and equivalent tunnel resistance

I.B.1 Conventional quantum mechanics calculations

One main prediction of quantum mechanics is the fact that a particle has a non zero probability to cross an energy barrier even if its energy is lower than the barrier height. This situation, called *"tunnel effect"*, is completely forbidden in classical mechanics. The analytical resolution of the problem can be found in every book of quantum physics. The energy barrier is modelled by a rectangular potential of height U_0 and width d along the x-direction. An electron of mass m moves from $x < 0$ towards the barrier with an energy $E < U_0$ (figure II.2).

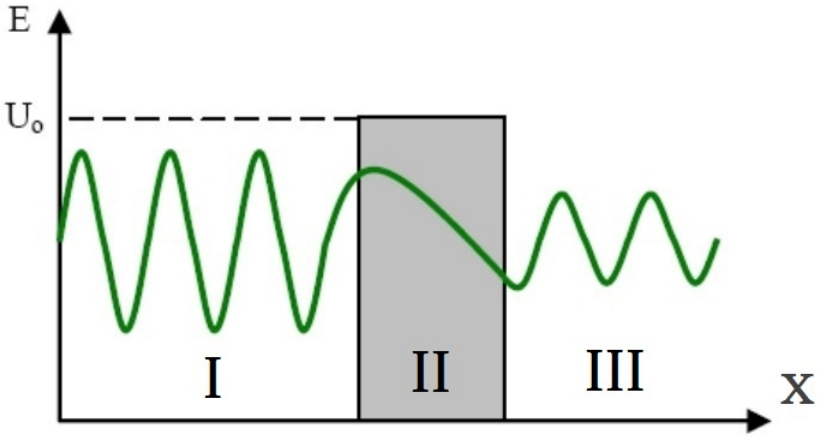

Fig. II.2: *Sketch of the tunnel effect. An electron moves towards a barrier with an energy lower than the barrier height. The wave function of the electron is represented in green.*

By considering that the electron is free in both y and z-directions, the wave function of the electron can be written as: $\psi(x,y,z) = e^{i(k_y y + k_z z)}\Phi(x)$. Thus, a 1-dimensional energy barrier can be considered and a 1-dimensional Schrödinger equation has to be solved:

$$-\frac{\hbar^2}{2m_0}\frac{\partial^2\Phi(x)}{\partial x^2} + V(x)\Phi(x) = E\Phi(x) \tag{2.1}$$

Then, the problem is separated in three regions:

- In the first and the third regions, the potential $V(x)$ is equal to zero: the Schrödinger equation is reduced to $-\frac{\hbar^2}{2m_0}\frac{\partial^2\Phi(x)}{\partial x^2} = E\Phi(x)$. The solution is $\Phi(x) = Ae^{ikx} + A'e^{-ikx}$, with $k = \sqrt{2mE}/\hbar$.

- Within the energy barrier (region II), the potential is different from zero and we have $E < V(x) = U_0$. A solution $\Phi(x) = Be^{\rho x} + B'e^{-\rho x}$ is found with $\rho = \sqrt{2m(U_0 - E)}/\hbar$.

By considering finally that the wave function and its derivative are continuous at the interface between the three regions, and by assuming that $\rho d \gg 1$, the transmission through the barrier is found as:

$$T \simeq 16 \, \frac{E(U_0 - E)}{U_0^2} \, exp\left(-2d \, \frac{\sqrt{2m(U_0 - E)}}{\hbar}\right) \tag{2.2}$$

Nevertheless, our problem cannot be treated with a simple model of rectangular potential. Indeed, when a voltage is applied to the tunnel junction, the barrier is distorted, leading to a potential that depends on the position inside the barrier (see figure II.3). The WKB approximation can be used to deal with this complication.

I.B.2 Brinkman's model of a tunnel junction

In the WKB approximation, the behaviour of the studied system is treated with classical physics at first, and then quantum fluctuations around the classical trajectory are treated as small corrections. In 1961, Harrison used the WKB approximation to calculate the electron tunnelling probability from a conducting region I to a conducting region III, through the forbidden energy gap of an insulator [10] (region II). By using this pioneer work, Brinkman calculated in 1962 the dynamical conductance of a tunnel junction [11]. He considered a trapezoidal barrier, of mean height $\bar{\Phi} = \frac{\Phi_1 + \Phi_2}{2}$ with an asymmetry $\Delta\Phi$ at zero bias (figure II.3). For an applied voltage lower than $\bar{\Phi}/10$, the dynamical conductance $G_d(V) = dI/dV$ is expressed as a function of the voltage as:

$$\frac{G_d(V)}{G_d(0)} \; = \; 1 \; - \; \left(\frac{A_0 \Delta\Phi}{16 \bar{\Phi}^{3/2}}\right) eV \; + \; \left(\frac{9 A_0^2}{128 \bar{\Phi}}\right) (eV)^2 \tag{2.3}$$

in which $\Delta\Phi$ is the barrier asymmetry and $\bar{\Phi}$ its average height. e is the electronic charge and $A_0 = 4d\sqrt{2m}/3\hbar$ with m the mass of an electron and d the barrier thickness. The dynamical conductance at zero bias $G_d(0)$ is given by:

$$G_d(0) \; = \; 3.16 \cdot 10^{10} \, \frac{\bar{\Phi}^{1/2}}{d} \, exp(-1.25 d \bar{\Phi}) \tag{2.4}$$

where d is in angstroms and $\bar{\Phi}$ is in volts.

The last equation shows a strong dependence of $G_d(0)$ with the thickness and the height of the barrier; it underlines the importance of monitoring these parameters to have a good control on the barrier electrical resistance.

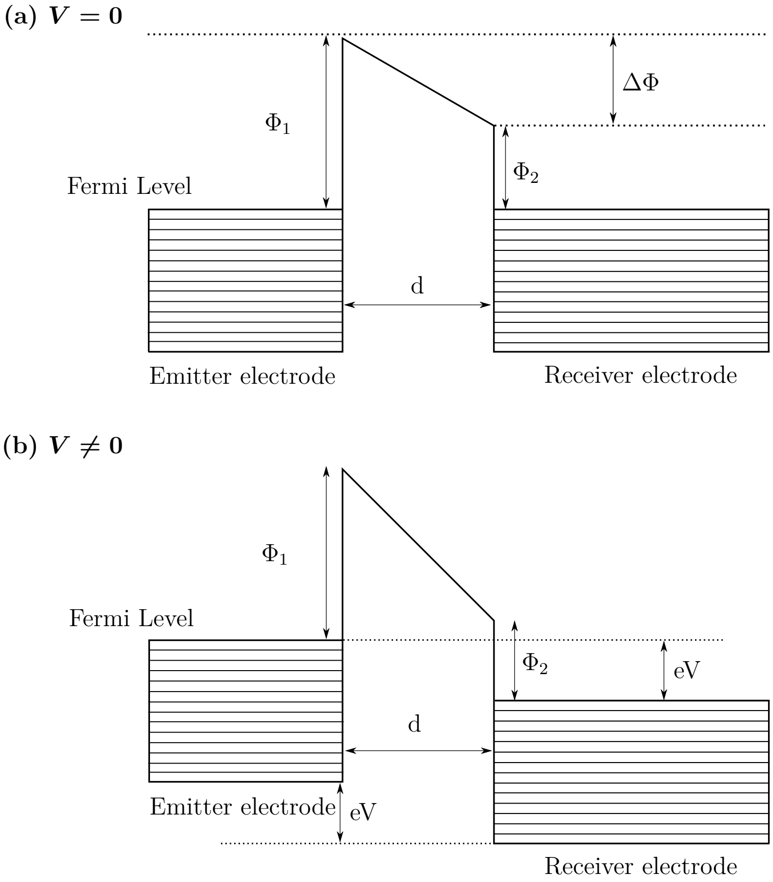

Fig. II.3: *Energy diagram of a magnetic tunnel junction with an asymmetry $\Delta\Phi$ and a thickness d. The first diagram (a) represents the case without polarisation ($V = 0$) whereas in the second one (b), a positive voltage is applied, resulting in a shift of the Fermi levels.*

This model is often used to extract the parameters of the barrier by fitting the current/voltage characteristic. In fact, by integrating equation 2.3 over the junction surface and over the applied voltage, the relation between the current I and the voltage V can be obtained. Nevertheless, the model can be used to determine the characteristics of the junction only for low applied voltages. Moreover, it does not anticipate a potential anomaly of conduction that can occur at low voltage. A second limitation is that it only takes into account the barrier: the density of states of the ferromagnetic electrodes are neglected. As a consequence, this model cannot explain the phenomenon of magneto-resistance.

I.B.3 Temperature dependence of the tunnel resistance

One way to study the tunnelling process across an insulating layer consists in studying the electrical conductance versus temperature. In 1962, Stratton studied this dependence theoretically in defects free structures, and also experimentally [12]. He considered that, in the free electron model, the temperature affects the population of the electronic states close to the Fermi level. When the temperature increases, an enlargement of the Fermi-Dirac distribution was considered. The resistance R versus temperature T is found to vary as:

$$\frac{R(T)}{R(0)} = \frac{sin(CT)}{CT} \tag{2.5}$$

with $C = 2d\sqrt{2m}/\hbar\sqrt{\bar{\Phi}}$, where m is the mass of an electron. In the case where $CT \ll 1$, equation 2.5 can be rewritten as:

$$R(T) = R(0)\left(1 - \frac{(CT)^2}{6}\right) = R(0)\left(1 - \frac{d^2(C'T)^2}{6\bar{\Phi}}\right) \tag{2.6}$$

In which C' is a numerical constant, d the barrier thickness and $\bar{\Phi}$ the average height. This equation predicts a decrease of the tunnel resistance when the temperature increases. This variation depends on the applied voltage, via $\bar{\Phi}$. In fact, the effective average height of the barrier can be written $\bar{\Phi} - |e|V/2$. Thus, when the applied voltage increases, the effective average height of the barrier decreases.

This behaviour is typical of a tunnel conductance in a perfect MTJ. Nevertheless, the resistance versus temperature characteristic can change dramatically when defects are present in the barrier, as metallic bridges (*pinholes*) or localized states [13]. For example, the presence of pinholes in the barrier induces a metallic behaviour of the junction and the resistance of the junction increases with the temperature. If localized states exist in the barrier, a hopping process of the electrons can occur and the resistance of the barrier increases exponentially with a decrease of temperature.

I.C. Tunnel Magneto-Resistance

I.C.1 Jullière's model

The description of the tunnel effect made before cannot explain why the conductance depends on the spin of the electron. The first experiment showing a spin-dependent tunnel effect was made by Tedrow and Meservey in the seventies [14]. They have studied a ferromagnetic/insulator/superconductor junction. The ferromagnetic layer emits electrons, which cross the insulator towards the superconductor. Here, the superconductor allows to probe the density of states (*DOS*) of the ferromagnet. In the case where no external magnetic field is applied, the DOS of the superconductor is not spin-splitted, and the conductance dI/dV is symmetric according to the voltage (solid line in figure II.4). Nevertheless, because of the Zeeman effect, the DOS becomes spin-splitted when a magnetic field is applied (shift $+\mu H$ for spin-up and $-\mu H$ for spin-down, dashed line in figure II.4).

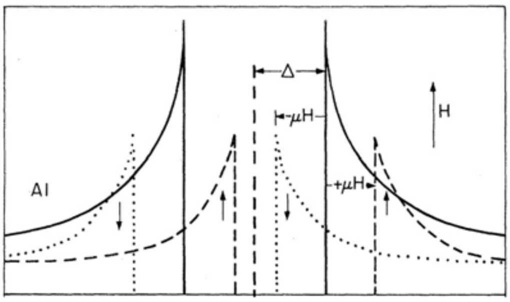

Fig. II.4: *Tunnelling density-of-states diagram of the superconductor (Al at 0.4K). The DOS splits into spin-up (increased in energy by μH) and spin-down (decreased in energy by $-\mu H$) parts. Excepted from [14].*

If at the Fermi energy the DOS of the ferromagnetic electrode in the majority spin $D^{\uparrow}$ is larger than that in the minority spin direction $D^{\downarrow}$ as shown in figure II.5(b), the measured conductance appears asymmetric (figure II.5(c)).

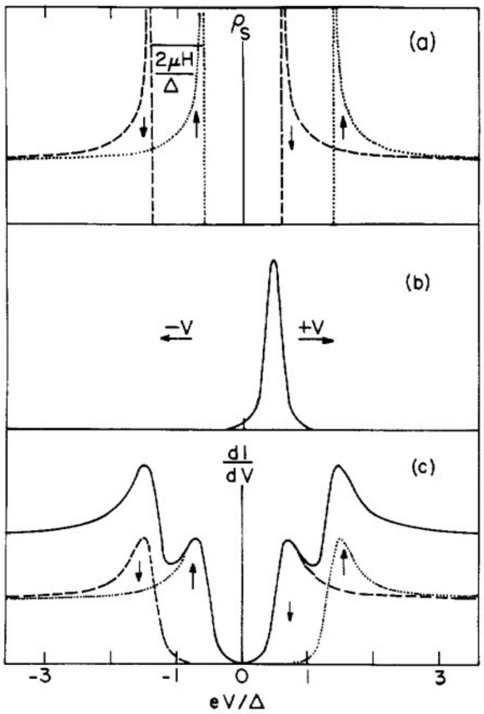

Fig. II.5: *(a) Spin-splitted DOS of the superconducting in presence of a magnetic field H. (b) DOS of majority and minority spin of a ferromagnet. (c) Asymetric conductance obtained because of the applied field. Excerpted from [15].*

These measurements enable the quantification of the ferromagnetic metal spin polarisation, which is defined as:

$$P = \frac{D^{\uparrow}(E_f) - D^{\downarrow}(E_f)}{D^{\uparrow}(E_f) + D^{\downarrow}(E_f)} \tag{2.7}$$

with $D^{\uparrow,\downarrow}$ the density of states at the Fermi level for the ferromagnetic electrode and for a spin direction ↑ or ↓. It also proved that the spin-flips are limited during the tunnelling process, which is very important to get a spin-dependent MTJ behaviour.

The first observation of a spin-dependent conduction across a tunnel barrier was achieved by Jullière in 1975 during his PhD work [8]. He measured a resistance that depended on the magnetic configuration across the insulator. A relative variation of the tunnel resistance between the parallel and the anti-parallel magnetic configurations, defined as "tunnel magneto-resistance" (TMR), of 14% was measured at a temperature of 4K.

$$TMR = \frac{R_{AP} - R_P}{R_P} \tag{2.8}$$

In order to explain the resistance variation in the MTJ, he developed a model to describe his experiment, by assuming that:

- The electronic spin is conserved during the tunnel effect: spin-up and spin-down channels can be considered as independent.
- For each magnetic configuration, the conductance depends on the density of states of the ferromagnetic electrodes.

Thus, the fact that an electron belongs to an energy band with a density of states that depends on the spin has to be taken into account. It is really different from the approach described above, where free electrons in the electrodes are considered. In a ferromagnetic layer, because of the exchange interaction, there is an asymmetry in the band structure (see figure II.6), resulting in a spin polarisation P.

Thanks to the first hypothesis, the total conductance can be re-written as:

$$G = G_{\uparrow} + G_{\downarrow} \tag{2.9}$$

An electron coming from the emitter electrode with a certain spin can be accepted only by free states with the same spin direction in the receiver electrode. According to the Fermi golden rule, the conductance is proportional to the product of the densities of states occupied or unoccupied at the Fermi level of each side of the barrier. In an anti-parallel magnetic configuration, a high density of states on one side corresponds to low density of states on the other side of the tunnel barrier. In this case, the conductance is expressed as:

$$G_{AP} \;=\; D_1^{\uparrow} D_2^{\downarrow} + D_1^{\downarrow} D_2^{\uparrow} \tag{2.10}$$

The current is then limited by the lowest density of states. In the parallel configuration, a high density of states is available on each side of the barrier for one direction of spin, resulting in a high current. The conductance is given by:

$$G_P \;=\; D_1^{\uparrow} D_2^{\uparrow} + D_1^{\downarrow} D_2^{\downarrow} \tag{2.11}$$

As a consequence, the magneto-resistance can be written as:

$$\begin{aligned} TMR &= \frac{R_{AP} - R_P}{R_P} \qquad (2.12)\\ &= \frac{G_P - G_{AP}}{G_{AP}} \qquad (2.13)\\ &= \frac{(D_1^{\uparrow} D_2^{\uparrow} + D_1^{\downarrow} D_2^{\downarrow}) - (D_1^{\uparrow} D_2^{\downarrow} + D_1^{\downarrow} D_2^{\uparrow})}{D_1^{\uparrow} D_2^{\downarrow} + D_1^{\downarrow} D_2^{\uparrow}} \qquad (2.14) \end{aligned}$$

with an index P (AP) for the parallel (anti-parallel) magnetic configuration respectively. By using equation 2.7, the TMR can also be expressed as a function of the polarisation of both ferromagnetic electrodes:

$$TMR \;=\; \frac{2P_1P_2}{1 - P_1P_2} \tag{2.15}$$

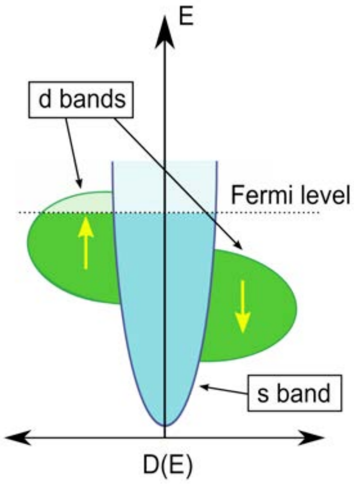

Fig. II.6: *Simplified density of states of a strong ferromagnet. The sub-band d is completely full for spin-down electrons.*

The Jullière's model has predicted correct values of TMR for some basic experiments, but it does not take into account the probability of transmission through the tunnel barrier: the TMR appears here only as an effect of both electrodes polarisation. Indeed, it neglects the influence of the material, the height and the thickness of the barrier. It also neglects the impact of the defects inside the tunnel barrier and the inelastic transport.

I.C.2 Slonczewski's model

A more accurate description of the junction has been made 15 years after the pioneer work of Jullière. Slonczewski considered the entire tunnel junction as a single entity to model especially the impact of the tunnel barrier properties [16]. In this model, only electrons close to the Fermi level and with a wave vector normal to the interface ($k_{//} = 0$) contribute to the tunnel process. By resolving the Schrödinger equation, the transmission through the barrier is expressed as:

$$T_{\uparrow(\downarrow)} \;=\; 16\,\frac{\kappa^2 k_1^{\uparrow(\downarrow)} k_2^{\uparrow(\downarrow)}}{\kappa^2(k_1^{\uparrow(\downarrow)} + k_2^{\uparrow(\downarrow)})^2 + \kappa^2(k_1^{\uparrow(\downarrow)} - k_2^{\uparrow(\downarrow)})^2}\, e^{-2d\kappa} \tag{2.16}$$

in which $k_i^{\uparrow}$ ($k_i^{\downarrow}$) is the wave vector of the spin-up (spin-down) electrons in the electrode i, and κ the imaginary part of the wave vector in the barrier. By adding the transmissions of the two spin channels, the conductance of the MTJ in both magnetic configurations is:

$$G_P \;\propto\; \frac{\kappa}{d}\,(T_{\uparrow\uparrow} + T_{\downarrow\downarrow}) \tag{2.17}$$

$$G_{AP} \;\propto\; \frac{\kappa}{d}\,(T_{\uparrow\downarrow} + T_{\downarrow\uparrow}) \tag{2.18}$$

The tunnel magneto-resistance (TMR) is then given by:

$$TMR = \frac{G_P - G_{AP}}{G_{AP}} = \frac{2P_1^{eff}P_2^{eff}}{1 - P_1^{eff}P_2^{eff}} \tag{2.19}$$

in which P_i^{eff} is the effective polarisation of the couple ferromagnetic electrode i / barrier. Its expression is given by:

$$P_i^{eff} \;=\; \frac{k_i^{\uparrow} - k_i^{\downarrow}}{k_i^{\uparrow} + k_i^{\downarrow}}\,\frac{\kappa^2 - k_i^{\uparrow}k_i^{\downarrow}}{\kappa^2 + k_i^{\uparrow}k_i^{\downarrow}} \tag{2.20}$$

In the case where there is an angle θ between the electrodes magnetisations, the tunnel resistance can be written as:

$$R(\theta) \;=\; R_{\perp}\,\frac{1}{1+\frac{MR}{2}cos(\theta)} \tag{2.21}$$

with $R_{\perp} = (R_{AP} + R_P)/2$ and $MR = 2(R_{AP} - R_P)/(R_{AP} + R_P)$. Equation 2.21 can be simplified in the case of a small MR:

$$R(\theta) \;=\; \frac{1}{2}\left[R_{AP} + R_P - (R_{AP} - R_P)cos(\theta)\right] \tag{2.22}$$

One can notice that equation 2.19 is really close to the one proposed by Jullière (eq. 2.15), excepted that the polarisation is replaced by an effective polarisation. This latter depends not only on the spin polarisation of the ferromagnet but also on the nature of the barrier (through the dependence with κ). Moreover, in the particular case of a high barrier (κ much larger than $k^{\uparrow}$ and $k^{\downarrow}$), the result of Jullière is retrieved. Even if some physical parameters are still ignored (as the barrier thickness), this model is innovative in the way that it underlines the importance of the metal-barrier couple for the TMR. The impact of the metal-barrier couple has been for example highlighted by the experiments performed by Moodera *et al.* [9] (the first one who observed TMR at room temperature) or De Teresa [17].

I.D. Injection of spin-polarised hot electrons

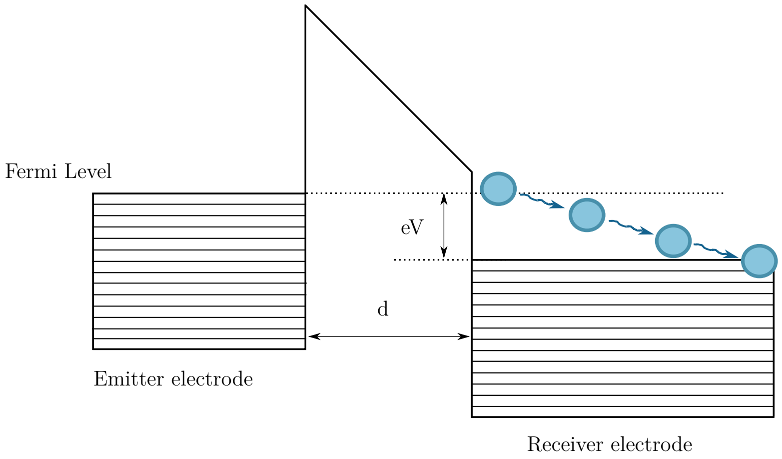

Fig. II.7: *Energy diagram of a magnetic tunnel junction in the case of a shift of the Fermi levels due to an applied voltage V. Electrons are injected in the receiver electrode with an energy eV via an elastic tunnel emission. Scattering events during the transport in the electrode bring back the electrons at the the Fermi level.*

As evoked before in the PhD manuscript, MTJs are devices that can easily be used to inject spin-polarised hot electrons in thin layers. This is straightforward when the energy diagram of a magnetic tunnel junction is observed (figure II.7). Due to elastic tunnel emission, electrons enter the receiver electrode with an energy eV above the Fermi level. These are called hot electrons. During their propagation towards the right-hand side of the device, they gradually lose some energy in the receiver electrode until they reach the Fermi level. As it will be discussed in the following, different sources of scattering exist and scattering can be spin-dependent.

II. Spin dependence of the hot electrons mean free path in a ferromagnet

II.A. Hot electrons in a ferromagnetic layer

When an electron scatters, it interacts with another particle or quasi-particle. These particles can be other electrons, impurity atoms, atoms at crystal dislocations or atoms at interfaces. Electrons can scatter also on quasi-particles, like phonons (quasi-particles of the lattice vibrations) and spin-waves (quasi-particles of the vibrations of the magnetisation). From quantum mechanical perturbation theory, the transition time constant (τ) from one initial quantum state (i) to another final quantum state (f) is known as Fermi's golden rule, and is expressed as:

$$\frac{1}{\tau_{i\rightarrow f}} = W_{i\rightarrow f} = \frac{2\pi}{\hbar} H_{fi}^2 \delta(E_f - E_i) \tag{2.23}$$

$H_{fi} = \langle \Psi_f | H' | \Psi_i \rangle$ represents the overlap between initial and final states of the quantum system, H' is the Hamiltonian of the interaction. This equation shows that a transition can happen only if the total amount of energy is conserved (term $\delta(E_f - E_i)$ in equation 2.23). By assuming that all individual scattering probabilities are independent, the Matthiesen's rule [18] can be used to obtain the overall electron relaxation $\chi = \hbar/\tau$ from all microscopic relaxation channels χ_j:

$$\chi = \frac{\hbar}{\tau} = \Sigma \chi_j \tag{2.24}$$

$$\frac{1}{\tau} = \Sigma \frac{1}{\tau_j} \tag{2.25}$$

where j represents the different kind of scattering. The scattering rate is dependent on the density of states (DOS). Moreover, the DOS are exchange-splitted in magnetic materials.

Thus, the scattering for spin-up and spin-down electrons is different. This results in two different resistivities, $\rho_\uparrow$ for electrons in the majority band (those with the moment aligned with the net magnetisation) and $\rho_\downarrow$ for minority electrons (those with their moments in the opposite direction to the magnetisation).

In the following, the different sources of scattering that an electron can meet are described, by focussing on the case of hot electrons. Mechanisms of scattering on other particles (other electrons, impurity atoms, atoms at crystal dislocation or at interfaces) and on quasi-particles (phonons and magnons) will be developed.

II.B. Scattering mechanisms

II.B.1 Electron-electron scattering

Some experiments [18, 19, 20] have shown recently that the most effective mechanism of inelastic scattering (*i.e.* the total amount of energy is not conserved for the electron) for hot electrons in a metal is given by collisions with the bath of thermalized electrons. This inelastic scattering is done through a Coulomb interaction. The mechanism, called a Stoner excitation (figure II.8), transfers energy and momentum of a hot electron to a cold electron, bringing this one from below the Fermi level to above it and leaving hot holes in the conduction band below E_F. In other words, secondary electron-hole pairs are created during relaxation of primary hot electrons.

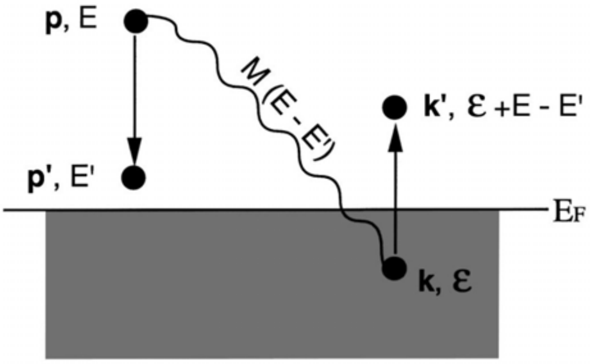

Fig. II.8: *Sketch of a Stoner excitation [21]. On the left, the hot-electron scatters to a lower energy above the Fermi-level. On the right a secondary electron, which comes from below the Fermi-level, scatters into an empty state above it.*

To calculate the scattering probabilities, the Pauli's exclusion principle is considered: we can have scattering only if both hot and secondary electrons are transmitted into previously unoccupied electronic states. The Fermi golden's rule can be written as an integral over all the energies available for a hot electron to scatter into [21]:

$$\frac{1}{\tau(E)} = \frac{2\pi}{\hbar}\int_{E_F}^{E}[1-f(E')]\rho(E')dE'\int_{0}^{E_F} f(\epsilon)\rho(\epsilon)[1-f(\epsilon+E-E')]\rho(\epsilon+E-E') \mid M(E-E') \mid^2 d\epsilon \tag{2.26}$$

with $f(E)\rho(E)$ the number of electrons that can be excited at an energy E and $[1-f(E)]\rho(E)$ the number of empty states for the interacting electron to scatter into. By assuming that the matrix element M is constant and the density of states is as shown on the left-hand side of figure II.9, we obtain in the case of a metal at an energy where only s-electrons are involved:

$$\frac{1}{\tau(E)} = \frac{\pi}{\hbar}\rho_s^3 \mid M_{ss}^{ss} \mid^2 (E-E_F)^2 = a_0(E-E_F)^2 \tag{2.27}$$

in which $\mid M_{l_f s_f}^{l_i s_i} \mid^2$ is the diffusion matrix element when a primary electron goes from band l_i to l_f and a secondary electron goes from band s_i to s_f. In the case of Cu, experimental results give $a_0 \approx 2.3 \cdot 10^{-2} fs^{-1} eV^{-2}$ [21].

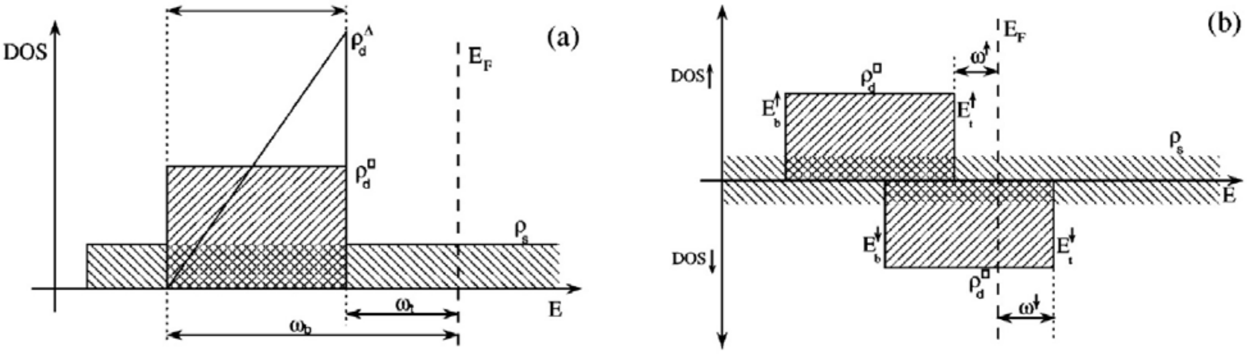

Fig. II.9: *Left: schematic density of states for noble metals (like Cu, Ag and Au). Right: schematic density of states for Co, as used in the calculations. Excerpted from [21].*

In the case of ferromagnetic material as Co (see DOS on the right-hand side of figure II.9), electrons can be excited from both s and d-bands. Moreover, these d-bands are exchange splitted and about 5 times as high as the s-states. For spin-up, there are two distinct cases: if the energy is lower than $\omega^\uparrow$ and if the energy is higher than $\omega^\uparrow$. If $E < \omega^\uparrow$, a hot spin-up electron can excite only spin-down electrons from a d-state below the Fermi level to an other d-state above it. If $E > \omega^\uparrow$, there are additional scattering possibilities with a spin-up electron excited from spin-up d-band into an empty s-state. In both cases, the primary spin-up electron relaxes in s-state above the Fermi level. The resulting inelastic lifetime for $E > \omega^{\uparrow}$ due to these two contributions is given by:

$$\frac{1}{\tau^{\uparrow}(E)} = a_0^{\uparrow}(E - E_F)^2 + a_1^{\uparrow}(E - E_F - \omega^{\uparrow})^2 \tag{2.28}$$

Spin-down hot electrons can directly scatter into the more abundant d-state, while exciting an other d-state electron from below to above E_F. Also here, we can excite above $\omega^{\uparrow}$ electrons from the spin-up (and down of course) d-band. The lifetime can be written as:

$$\frac{1}{\tau^{\downarrow}(E)} = a_0^{\downarrow}(E - E_F)^2 + a_1^{\downarrow}(E - E_F - \omega^{\uparrow})^2 \tag{2.29}$$

Aeschlimann *et al.* [22] have measured the spin-dependent inelastic lifetime in Co by 2PPE (Two-photon photoelectron spectroscopy), and the energy dependence was fitted by Zarate *et al.* [21] (figure II.10). The fit gives $a_0^{\uparrow} = 0.14\ fs^{-1}eV^{-2}$, $a_1^{\uparrow} = 0.04\ fs^{-1}eV^{-2}$ for spin-up electrons and $a_0^{\downarrow} = 0.17\ fs^{-1}eV^{-2}$, $a_1^{\downarrow} = 0.65\ fs^{-1}eV^{-2}$ for spin-down electrons.

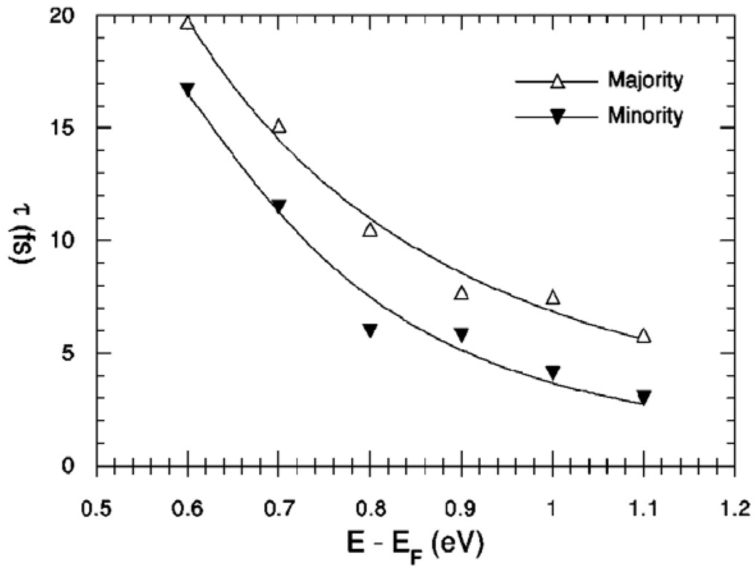

Fig. II.10: The inelastic lifetimes for Co measured by spin-dependent 2PPE (dots are experimental results; the line is the best fit from equation 2.29).

II.B.2 Electron-defect scattering

In a spintronics device, electrons can meet a finite number of defects that depends on the quality of the material, *i.e.* the purity (impurities, vacancies ...), the crystallographic quality (texture, epitaxy, dislocation, grain boundaries), the quality of the interfaces ... which are not negligible in a real sample. These defects will act as scattering centers leading to elastic processes which randomise the propagation direction of the electron and favour an isotropic distribution. For example, in epitaxial multilayers, the mismatch between the materials can reach several percent at each interface, so that stacking faults and vacancies are regularly built into the epitaxial lattice at the interfaces. However, lattice strain relaxes within the bulk of the layers. The spatial defect distribution will contribute to the standard deviation of electron attenuation by averaging characteristics obtained on different probing locations on the sample.

II.B.3 Electron-phonon scattering

In a lattice, electrons can scatter with phonons, which are quasi-particles associated to the lattice vibrations. In fact, electrons couple to phonon as well since they experience the ion Coulomb potential of each atom. Phonons can be emitted either spontaneously when the temperature is different from zero or by excited electrons even at T=0K. The latter process creates phonons with a maximum energy $\hbar w_{max}$, which gives an energy transfer equivalent to $\Delta E \approx 10meV$ per scattering event. The impact on momentum relaxation is larger, and electron backscattering is even facilitated. Since the electron-phonon relaxation is weakly elastic (quasi-elastic), just a fraction of the spin-dependent free phase space in ferromagnetic materials is sampled when compared to electron-electron scattering.

Recently, several approaches (theoretical, time-resolved Kerr experiments or resolved photoemission spectroscopy) [23, 24, 25, 26] have determined hot electron lifetime τ_{e-ph} due to this relaxation channel. These are found to be of the order of 10fs at room temperature and larger at low temperature. In fact, this phenomenon increases when the temperature decreases. As a consequence, a direct fingerprint of electron-phonon relaxation could be the decrease of the magneto-current of a spin valve with the temperature.

The assessment of $\tau_{e-e} < \tau_{e-ph}$ and the fact that electron-electron scattering samples a much larger phase space strongly suggests that phonon scattering processes do not contribute so much to relaxation of hot electrons compared to electron-electron scattering.

II.B.4 Electron-magnon scattering

In a recent experiment of spin-polarised electron energy loss spectroscopy (SPEELS) [27] it has been shown that hot-electrons can also interact with spin-waves, also known as magnons. Magnons are the quasi-particles associated to the vibration of the magnetisation. At 0K, all the individual magnetic moments of the atoms in the lattice are aligned within domains. When the temperature is increased, the individual moment can slightly move around the equilibrium position. Thus, they will begin to precess around the net magnetisation of the material, in a collective mode called *spin-waves* [28]. In figure II.11, this collective precession is depicted, and when viewed from above, it is clear why we talk about a spin-wave.

The behaviour of a magnon can be described by its dispersion relation linking its energy and its momentum: $E \approx Dq^2$, with D the spin-stiffness constant ($D \approx 400meV\text{Å}^2$ for Co and $D \approx 555meV\text{Å}^2$ for Ni [29]). Furthermore, a spin-wave owns a spin $S = -\hbar$ and permits interaction only by flipping the electronic spin. As a consequence, a spin-up electron $S = +1/2\hbar$ can only absorb a spin-wave and becomes a spin-down $S = -1/2\hbar$. This is only possible with thermal spin-waves, emitted only for $T \neq 0K$. On the contrary, a spin-down electron can emit a spin-wave, even at $T = 0K$, thus becoming a spin-up electron.

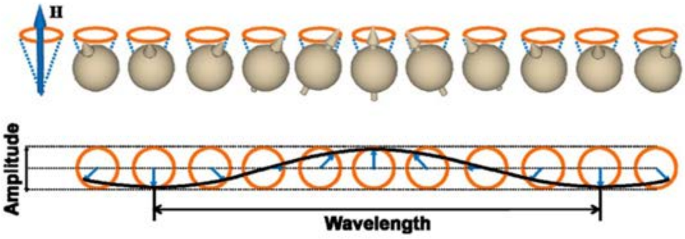

Fig. II.11: *Collective dynamic behaviour of individual spins coupled with each other, representing a wave form. Excerpted from [30]*

The latter process is not limited to small energies ($\sim kT$) as for a thermal magnon, but larger energy losses are possible for hot electrons. In a spin valve, these high energy losses contribute to the inelastic scattering length. Calculation by Hong and Mils has been done about spin-waves emissions by spin-down hot electrons [31, 32]. In figure II.12, a result of their calculation for Fe shows that spin-wave scattering can be about as strong as electron-electron scattering for spin-down (minority) electrons around 1eV.

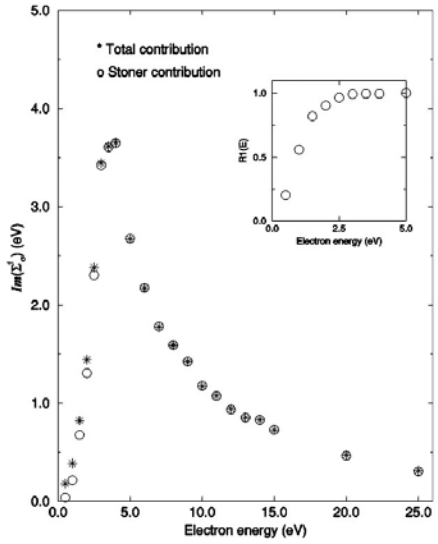

Fig. II.12: *The imaginary part of the self-energy* $Im(\Sigma_\downarrow) = -\hbar/2\tau_\downarrow$ *due to spin-wave emission and Stoner excitations as a function of the hot-electron energy for spin-down electrons in Fe. The inset shows the partial contribution of the Stoner excitations compared to the total self energy. For further details, see [32].*

The thermal excitation of spin-waves reduces the magnetisation of a material with one unit of spin $(-\hbar)$. Therefore, at low temperatures ($T \leq 0.4T_c$) the reduction of the magnetisation with temperature is mainly due to spin-waves.

III. Magnetic tunnel transistor

III.A. What is a Magnetic Tunnel Transistor?

A magnetic tunnel transistor (MTT) is a three terminals device. A current of hot electrons (which are, for reminder, electrons with energies above the Fermi level) is injected in a metallic base made either of a ferromagnetic layer or a spin valve composed by two ferromagnetic layers spaced by a non-magnetic metal. In a MTT, the injection is made through a tunnel barrier, composed generally by Al_2O_3 or MgO. To contribute to the current collected out of the transistor, hot electrons have to overcome an energy barrier: usually, the interface between a semiconductor and a metal, which defines a Schottky diode, is used to filter according to the electrons energy. Thus, only ballistic electrons (those which did not lose energy during the crossing of the base) have enough energy to be collected. Furthermore, as will be shown in the following, an acceptance angle also exists at the Schottky interface that ensures also a filtering by wave vector: it will be shown that mainly electrons with a wave vector perpendicular to the interface can overcome the Schottky diode.

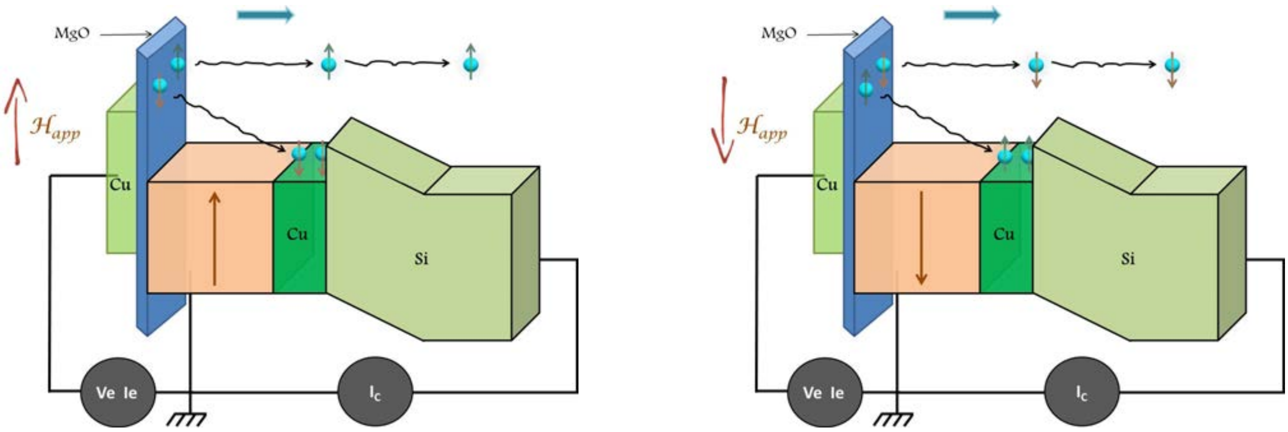

Fig. II.13: *Energy diagram of a MTT with a base composed by a single ferromagnetic layer, with a magnetisation up (left-hand side) or down (right-hand side).*

To understand the mechanism of energy loss in the metallic base, the electronic spin must be considered. If the spin of the electron is aligned with the magnetisation of the ferromagnetic layer, the scattering (elastic or inelastic) will be less important than in the case where the spin is in the opposite direction: as a consequence, the thermalisation length is larger for spin-up than for spin-down electrons $\lambda_\uparrow > \lambda_\downarrow$ (see section II of this chapter). In the case where the base is a single ferromagnetic layer, a current of spin-up electrons is collected if the magnetisation of the ferromagnetic is up, and a spin-down current is collected in the opposite case (figure II.13). This appears to be a very good strategy to inject electrons with high polarisation in a semiconductor.

In the following, the theory of the Schottky diode is developed in order to understand its key role in the MTT.

III.B. Schottky diode

III.B.1 Energy landscape of a Schottky diode

A Schottky diode is made by contacting a metal and a semiconductor (SC). When a n-type SC is brought in intimate contact with a metal, the Fermi level of the two materials will align, without any external voltage applied. Since the conduction bands of the semiconductor are above the Fermi level, whereas the metal ones are below the Fermi level, electrons from the semiconductor can fall in the lowest conduction bands of the metal. This results in a depletion of charge in the SC, bending the conduction band upwards (resulting in a bandbending of qV_{bi}) and creating a Schottky barrier, as shown in figure II.14. This barrier will increase up to a dynamical equilibrium value, where the number of electrons moving from the SC to the metal is exactly equal to the number of electrons taking the inverse path. The value $q\Phi_B$ of the barrier height is dependent on the SC and the metal.

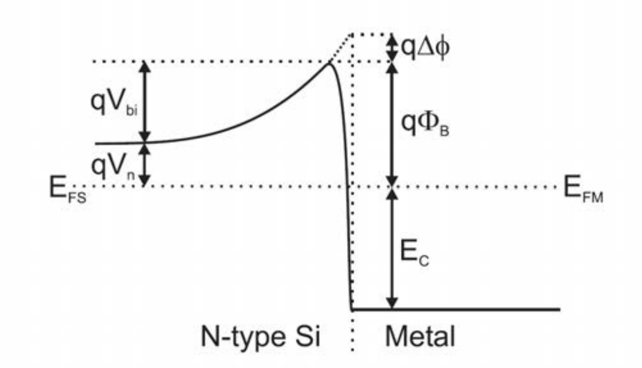

Fig. II.14: Schematic energy diagram of the conduction band minimum (solid line) in a Schottky barrier (with the image force lowering $q\Delta\Phi$).

One can also notice that the maximum of the Schottky barrier is inside the semiconductor, at a distance $x_m \simeq 10$Å. A huge electrical field $E_{image} \simeq 109V/m$ exists between the maximum of the Schottky barrier and the physical metal/silicon interface. In his book, S. M. Sze explains this phenomenon via an image-force effect [33]. He also calculates the resulting current density from the silicon into the metal ($J_{s\longrightarrow m}$), by applying the thermionic-emission theory:

$$J_{Schottky} = A^{**}T^2 exp\left(-\frac{q\Phi_B}{kT}\right)\left[exp(\frac{qV}{kT}) - 1\right] \tag{2.30}$$

with the effective Richardson constant for Si of:

$$A^{**}_{Si} = 110A/cm^2/K^2 \tag{2.31}$$

III.B.2 Schottky collector

To be collected in the semiconductor and contribute to the current, electrons have to overcome the Schottky diode. Only electrons with enough energy and the right momentum can do that. It is important to notice that the total energy ($E = E_K + E_P$) of an electron coming from the metal to the semiconductor is conserved. Thus, the total energy of the electron when it is in the base equals the energy at the top of the Schottky barrier. By taking for reference the Fermi level, this can be expressed as:

$$\frac{1}{2}m^*_m(v^2_{mx} + v^2_{my} + v^2_{mz}) - E_C = \frac{1}{2}m^*_{Si}(v^2_{sx} + v^2_{sy} + v^2_{sz}) + q\Phi_B \tag{2.32}$$

Two additional equations come from the conservation of the parallel momentum (the SC/metal interface is defined as normal to the x direction):

$$m_m^* v_{my} = m_{Si}^* v_{sy} \tag{2.33}$$

$$m_m^* v_{mz} = m_{Si}^* v_{sz} \tag{2.34}$$

By combining these equations, the velocity v_{sx} of an electron can be calculated at the maximum of the Schottky barrier:

$$v_{sx} = \sqrt{\frac{m_m^*}{m_{Si}^*}\left[v_{mx}^2 - \left(\frac{m_m^*}{m_{Si}^*}\right)(v_{my}^2 + v_{mz}^2)\right] - \frac{2}{m_{Si}^*}[E_C + q\Phi_B]} \tag{2.35}$$

So as to overcome the energy barrier and contribute to the current, the electron has to keep a positive velocity in the x-direction (otherwise, it will be reflected back into the base). This results in a maximum incidence angle up to which an electron with energy E can be collected. This acceptance cone angle is:

$$\sin\theta_c^2 = \frac{v_{my}^2 + v_{mz}^2}{v_{mx}^2 + v_{my}^2 + v_{mz}^2} = \frac{m_{Si}^*}{m_m^*}\left(\frac{E - q\Phi_B}{E + E_C}\right) \tag{2.36}$$

In order to estimate the magnitude of θ_c, let us consider the case of copper grown onto Si[100]. For $m_{Si}^*/m_m^* = 0.2$, $q\Phi_B = 0.75eV$ and $E_C = 7.1eV$, the acceptance cone angle is $\theta_c = 4.5^o$ for E=1eV. Thus, only electrons with an almost normal incidence may enter the semiconductor collector.

As a conclusion, only electrons with an energy $E > E_F + q\Phi_B$ and an angle of incidence below the critical value θ_c can be collected. So, the Schottky barrier will be used to measure only electrons that have kept their initial energy and their wave vector perpendicular to the multilayer interfaces.

III.C. Spin valve

As explained above, the base of a magnetic tunnel transistor can be composed either by a single ferromagnetic layer or by a spin valve. A spin valve is a trilayer made of a thin non-magnetic metal sandwiched between two ferromagnetic layers.

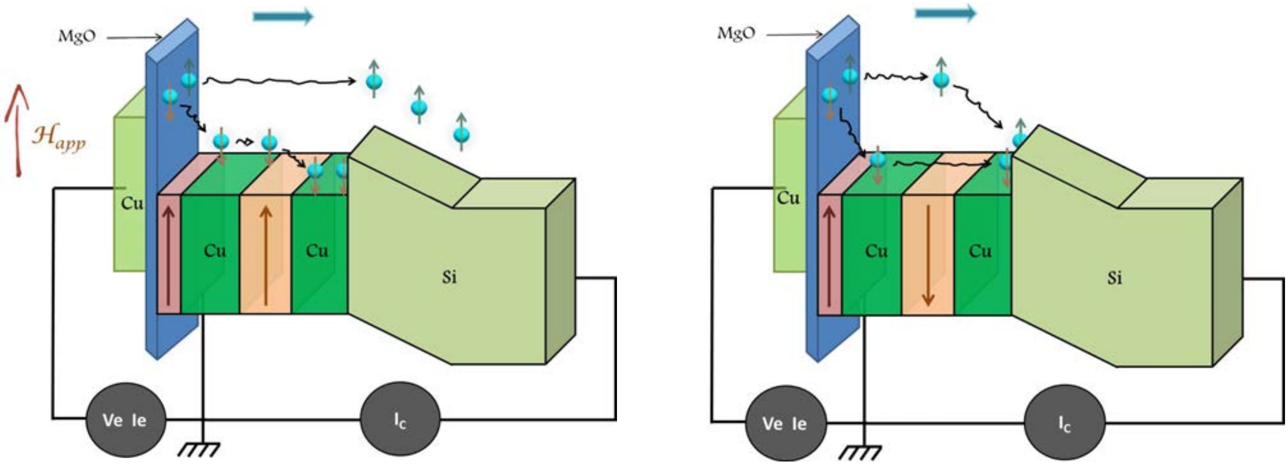

Fig. II.15: **Energy diagram of a magnetic tunnel transistor with a spin valve. On the left-hand side, a current of spin-polarised electrons can be collected for the parallel configuration. On the right-hand side, only a weak current can be collected for the anti-parallel configuration.**

This kind of base is very interesting because it can give to the transistor a strong dependence on the hot electron current with the magnetic configuration of the spin valve:

- In a parallel configuration (both ferromagnetic layers have the magnetisation in the same direction, up for instance), spin-up electrons experience few scattering events, and most have enough energy to be collected after the Schottky diode. Nevertheless, spin-down electrons suffer strong scattering events in both ferromagnetic layers. At the end, they have not enough energy to be collected. Thus, a current of spin-up electrons I_P is collected.
- In an anti-parallel configuration, spin-up electrons undergo strong scattering in only one ferromagnetic layer, as do spin-down electrons, resulting in a very low current I_{AP} because both kind of electrons have not enough energy to overcome the energy barrier.

Thus, the magneto current (MC) can be defined as:

$$MC = \frac{I_P - I_{AP}}{I_{AP}}$$

Considering that the current I_{AP} of the anti-parallel configuration is very low, a huge MC can be measured. In a previous study, Lu *et al.* have shown that a MC of 2700% can be measured on samples made in the sputtering used in this PhD work [34].

III.D. Specificity of the spin valve with crossed geometry

Up to now, only magnetic tunnel transistors with collinear magnetisations have been developed [34, 35]. Nevertheless, according to their high MC, it can be very interesting to develop a MTT in which one ferromagnetic layer of the spin valve has a perpendicular magnetic anisotropy. Indeed, such a geometry could be used for highly sensitive magnetic field sensors [36] or to study the spin precession of hot electrons in a ferromagnetic layer [37]. In the following, the specific MC obtained with this geometry will be calculated.

To calculate the MC of a crossed spin valve, the Valet-Fert model [38] is used. The semi-classical Boltzmann equation is solved to simulate the Current Perpendicular to the Plane (CPP) transport through a magnetic multilayer. This full model includes spin-dependent resistivities in the bulk and across the interfaces, and can take spin-mixing into account. Here, the spin-mixing has been neglected. In this case, the total current is constituted of the spin-up and spin-down electrons that carry the current independently.

By introducing factors $\Gamma_{i(o)}$ reflecting the spin-dependent input (index i) and output (index o) transmission for hot electrons at the interfaces of the considered base layer, we account for the possibility of a spin-dependent bandstructure mismatch. Therefore, the current of the parallel or anti-parallel configurations of the magnetisation can be written as:

$$I_C^P \sim T_M^{FM1} T_M^{FM2} + T_m^{FM1} T_m^{FM2} \tag{2.37}$$

$$I_C^{AP} \sim T_M^{FM1} T_m^{FM2} + T_m^{FM1} T_M^{FM2} \tag{2.38}$$

in which M (m) refers to Majority (minority) spins. If the mean free path of Majority (minority) spins is noted $\lambda_{M(m)}$, the overall spin-dependent hot electron transmission of the considered base layer $T_{M(m)}$ is given by [39]:

$$T_{M(m)} = \Gamma_{M(m),i} \; exp\left(-\frac{d}{\lambda_{M(m)}}\right) \Gamma_{M(m),o} \tag{2.39}$$

with d the thickness of the ferromagnetic layer crossed.

In our case, the magnetic anisotropy of one layer of the spin valve is perpendicular to the sample plane and the anti-parallel configuration will not be accessible experimentally. Thus, we have to define not the current of the anti-parallel configuration I_C^{AP} as usual but the current when the magnetisations are crossed:

$$I_C^{\perp} \sim T_M^{FM1}\left(\frac{1}{2}T_M^{FM2}+\frac{1}{2}T_m^{FM2}\right) + T_m^{FM1}\left(\frac{1}{2}T_M^{FM2}+\frac{1}{2}T_m^{FM2}\right) \tag{2.40}$$

The magneto-current between the crossed and the parallel configuration is expressed as:

$$MC^{\perp} = \frac{I_C^P - I_C^{\perp}}{I_C^{\perp}} \tag{2.41}$$

From equations 2.37, 2.38 and 2.40, we can deduce that $I_C^{\perp} = \frac{1}{2}I_C^P + \frac{1}{2}I_C^{AP}$. An expression of $MC^{\perp}$ can be written as:

$$\begin{aligned} MC^{\perp} &= \frac{I_C^P - \frac{1}{2}I_C^P - \frac{1}{2}I_C^{AP}}{\frac{1}{2}I_C^P + \frac{1}{2}I_C^{AP}} && (2.42)\\ &= \frac{I_C^P - I_C^{AP}}{I_C^P + I_C^{AP}} && (2.43)\\ &= \frac{I_C^P - I_C^{AP}}{I_C^{AP}}\left(\frac{I_C^{AP}}{I_C^{AP}+I_C^P}\right) && (2.44)\\ &= MC^{max}\left(\frac{I_C^{AP}}{I_C^{AP}+I_C^P}\right) && (2.45)\end{aligned}$$

With this formula, one can see that the larger the difference between I_C^{AP} and I_C^P is, the smaller the $MC^{\perp}$ will be compared to MC^{max} (figure II.16).

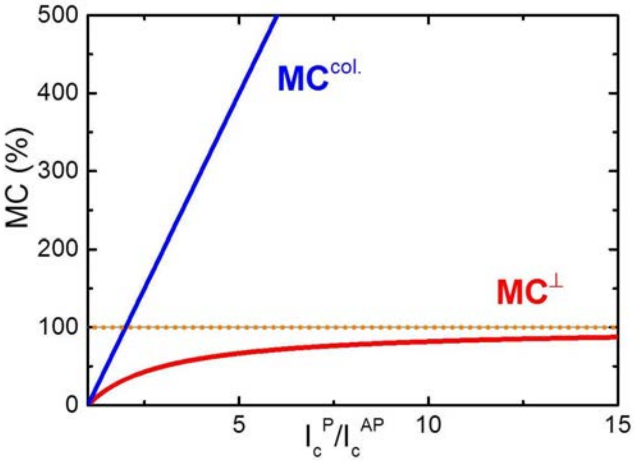

Fig. II.16: *Simulation of the magneto-current as a function of* $x = \frac{I_C^P}{I_C^{AP}}$. *The blue curve represents the* MC^{max} *for a collinear spin valve whereas the orange one represents the* $MC^{\perp}$ *of a crossed spin valve.*

One main point to notice here is that the MC of such a crossed configuration can not be larger than 100%.

IV. Conclusion

In this chapter, we have defined the building block of a magnetic tunnel transistor: injection of spin-polarised hot electrons, base made of a spin valve, and energy and wave vector analysis using a Schottky barrier.

The first part was dedicated to the tunnel magneto-resistance, which is the relative variation of the resistance of a trilayer FM/I/FM (ferromagnetic/insulator/ferromagnetic). By applying a voltage through the tunnel barrier, spin-polarised hot electrons are injected into the second ferromagnetic layer.

The second part explains what happens to these hot electrons once injected into the ferromagnet. We have seen that they relax towards the Fermi sea, by suffering different scattering mechanisms. The key point here is that the mean free path in the ferromagnetic layer depends strongly on the spin of the electron.

This important effect is used in a magnetic tunnel transistor, which is presented in the third section of this chapter. After the ferromagnet, there is an energy filter which collects only ballistic electrons. The interface between a metal and a semiconductor plays that role. Finally, only electrons that do not lose energy in the ferromagnet can overcome the Schottky barrier to be collected in the SC. An other kind of MTT was discussed in this chapter: after the tunnel barrier, a spin valve (which is composed by two ferromagnets and a metallic layer) can give a passing or a blocking state to the transistor, according to the magnetic configuration of the ferromagnetic layers.

Résumé du chapitre :

Dans ce deuxième chapitre, nous avons introduit les concepts de base permettant de comprendre le fonctionnement d'un transistor tunnel magnétique (TTM). Ces notions permettent de comprendre comment il est possible d'étudier la précession du spin de l'électron dans un TTM pour lequel les trois couches ferromagnétiques ont des aimantations qui pointent dans les trois directions de l'espace.

Dans un premier temps, le concept de barrière tunnel est décrit, en soulignant en particulier les propriétés d'une jonction tunnel magnétique. Après une brève introduction de l'effet tunnel, nous avons développé les principaux modèles théoriques les plus simples permettant de décrire une jonction tunnel, notamment celui de Brinkman, le premier qui prenait en compte la distorsion de la barrière sous l'effet d'une tension. Le premier à avoir décrit le comportement d'une jonction tunnel magnétique, composée de deux ferromagnétiques et d'un isolant, est Jullière en 1975. Il développe notamment le concept de magnétorésistance tunnel (MRT), qui est la différence relative des courants obtenus pour des configurations où les aimantations des électrodes ferromagnétiques sont parallèles ou antiparallèles. Il a également introduit le concept de polarisation en spin de l'électrode ferromagnétique P. La MRT peut alors s'écrire :

$$MRT = \frac{2P_1P_2}{1 - P_1P_2}$$

Nous nous sommes interrogés dans un deuxième temps sur le devenir de l'électron une fois injecté à une certaine énergie dans une électrode ferromagnétique. Les différentes sources de collisions qui diffusent les électrons lors du transport dans une couche ferromagnétique sont alors décrites. Nous montrons notamment que le libre parcours moyen dépend du spin de l'électron. S'il est orienté dans la même direction que l'aimantation de la couche ferromagnétique, le libre parcours moyen sera plus grand que s'il est orienté en sens inverse.

Le concept de TTM est alors introduit dans un troisième temps. Après l'injection via une jonction tunnel, les électrons perdent une certaine quantité d'énergie en fonction de la direction de leur spin lors de leur propagation. Ainsi, en mettant un filtre en énergie à l'issue de la couche ferromagnétique, il est possible de ne collecter que les électrons dont le spin était orienté dans la direction de l'aimantation. L'interface entre un semi-conducteur et un métal, couramment appelée diode Schottky, joue le rôle de filtre en énergie. Des TTM plus complexes peuvent être construits en remplaçant la couche ferromagnétique par une vanne de spin, composée de deux couches ferromagnétiques espacées par un métal non magnétique. Le courant collecté après la diode Schottky va alors dépendre de la configuration magnétique de la vanne de spin. Cela permet de définir le magnéto-courant, qui est la différence relative des courants des configurations magnétiques parallèle et antiparallèle de la vanne de spin.

Dans un quatrième temps, la spécificité du TTM envisagé dans cette thèse est développée. Pour étudier la précession du spin électronique, une couche de la vanne de spin doit posséder une anisotropie magnétique perpendiculaire. Nous avons montré en particulier que le magnéto-courant ne peut pas excéder 100% dans un tel système.

PART II

MAGNETISM

Chapter 3

Magnetism of [Co/Ni] multilayers: Overview

In order to study the electronic spin precession in an active magnetic layer, a non-collinear configuration between the three ferromagnetic layers of the magnetic tunnel transistor is needed. In particular, one magnetic layer must exhibit an out-of-plane anisotropy. This chapter, divided in two parts, explains how a perpendicular magnetic anisotropy (PMA) can be obtained in [Co/Ni] multilayers. The first section defines and identifies the different contributions to the magnetic anisotropy in magnetic nano-structures. The second section describes the state of the art concerning PMA in [Co/Ni] multilayers.

I. Introduction to magnetism in thin films

I.A. Magnetic energy

Many effects in magnetism can be understood as a competition between different interactions. This part defines the main interactions that a magnetic moment can experience.

I.A.1 Zeeman energy

When a magnetic field is applied to a magnetic moment, the interaction between them is described by the Zeeman energy E_Z:

$$E_Z \;=\; -\mu_0 \; \overrightarrow{m} \cdot \overrightarrow{B_{ext}}$$

with $\mu_0 = 4\pi.10^{-7} kg.m.A^{-2}.s^{-2}$ the vacuum permeability. If the local magnetisation $\overrightarrow{M}(\vec{r})$ of a magnetic sample is considered, this equation can be re-written as:

$$E_Z \;=\; -\mu_0 \int_V \overrightarrow{M}(\vec{r}) \cdot \overrightarrow{B_{ext}} \; dV$$

where V is the sample volume. By using the principle of the energy minimisation, this expression implies that the local magnetisation tends to align with the magnetic field.

In the simple case where the sample is represented by an ellipsoid, and if the magnetic moment of the sample follows the macrospin approximation (which means that all the magnetic moments are oriented in the same direction, giving a net magnetisation), the Zeeman energy is written as:

$$E_Z \;=\; -\mu_0 M_s B_{ext} \; cos(\alpha - \theta) \; V$$

with $\alpha - \theta$ the angle between the external magnetic field and the magnetisation (see figure III.1).

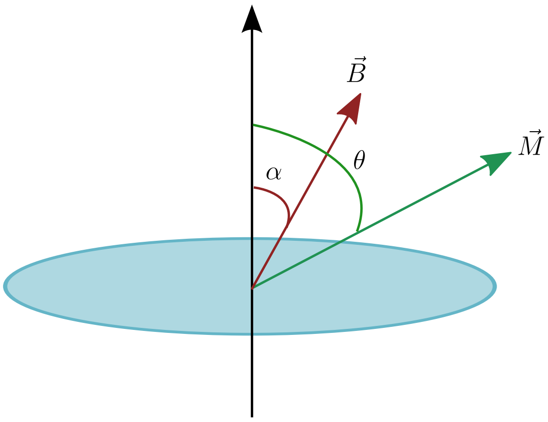

Fig. III.1: *Sketch of a sample approximated by an ellipsoid, with an applied field $\vec{B}$.*

I.A.2 Exchange interaction

In a magnetic material, the exchange interaction between spins leads to a long range magnetic order. This interaction is due to a Coulomb interaction, associated with the Pauli principle that prevents two electrons from being in the same state. If two spins $\overrightarrow{S_i}$ and $\overrightarrow{S_j}$ at the position $\overrightarrow{r_i}$ and $\overrightarrow{r_j}$ are considered, the exchange energy is given by:

$$E_{exch} = -J \, \overrightarrow{S_i} \cdot \overrightarrow{S_j}$$

J is called the exchange constant, which only depends on the distance between the two spins $J(\overrightarrow{r_i} - \overrightarrow{r_j})$.

Fig. III.2: *Sketches of a ferromagnetic order if $J > 0$ (on the left-hand side) or an anti-ferromagnetic order with $J < 0$ (on the right-hand side).*

This interaction is a short range interaction, thus limited to the first neighbours. The sign of J has a huge impact on the magnetic configuration of the system:

- If $J > 0$, the exchange energy is minimised when the spins are parallel: a ferromagnetic order is induced.
- If $J < 0$, an anti-parallel arrangement minimises the energy: an anti-ferromagnetic order is induced.

At a finite temperature T, a magnetic moment is excited at an average energy $k_B T$ with k_B the Boltzmann constant. If this energy exceeds the exchange energy, the long range magnetic order is lost. This happens above a critical temperature, called Curie temperature (T_C) for a ferromagnetic order and Néel temperature (T_N) for an anti-ferromagnetic order.

I.A.3 Demagnetising field

A magnetic moment creates a magnetic field: the dipolar field. In the sample, it is in the opposite direction of the magnetisation $\overrightarrow{M}$ and it is called the demagnetising field $\overrightarrow{H_d}$. This field is in fact the result of surface magnetisation currents generated by the projection of the magnetisation at magnetic matter surfaces. The interaction between the magnetic moment and its demagnetising field leads to an energy:

$$E_d = -\frac{1}{2}\mu_0 \int_V \overrightarrow{M}(\vec{r}) \cdot \overrightarrow{H_d}(\vec{r})\ dV$$

The fact that this energy is always positive ($\overrightarrow{M}$ and $\overrightarrow{H_d}$ are in opposite directions) indicates that the magnetic moment tends to be in a direction where the value of the projection of $\overrightarrow{H_d}$ is minimum. In general, the exact calculation of the demagnetising field is extremely complicated, except for second order geometries like ellipsoidal one and in the case of an uniform magnetisation, where the demagnetising field can be re-written by introducing a demagnetising tensor $\overline{\overline{N}}$ that depends only on the geometry of the system:

$$\overrightarrow{H_d} = -\overline{\overline{N}}\overrightarrow{M}$$

In the case of a thin film (which can be considered as an ellipsoid with an aspect ratio between the semi-major and the semi-minor axis $c/a \ll 1$), only one diagonal element of the demagnetising tensor is different from zero. Therefore, an in-plane direction for the magnetic moment of a thin film is favoured, and the demagnetising energy is expressed as:

$$E_d = -\frac{1}{2}\mu_0 M_s^2 sin^2(\theta)\ V$$

V being the sample volume, M_s the saturation magnetisation, and θ the angle between the magnetisation $\overrightarrow{M}$ and an axis perpendicular to the sample surface.

I.A.4 Magnetic anisotropy of thin films

Magneto-crystalline anisotropy (*MCA*)

A spin-orbit interaction between the orbital moment of the electrons and the crystal electric field occurs in a magnetic material. This induces a magnetisation direction oriented preferentially along specific axes of the material, called easy axes. On the contrary, a hard axis is a direction in which it costs a maximum of energy to orientate the magnetisation.

In the case of cubic crystals (as Ni or Fe crystals), the magneto-crystalline energy is:

$$E_K \; = \; [\; K_1(\alpha_1^2\alpha_2^2 + \alpha_1^2\alpha_3^2 + \alpha_2^2\alpha_3^2) + K_2(\alpha_1^2\alpha_2^2\alpha_3^2) + ... \;]\; V$$

where K_1 (respectively K_2) is the first (respectively second) order anisotropy constant, and α_1, α_2, α_3 are the cosines of the angles between the magnetisation and the crystal axis.

In the case of an uni-axial symmetry, the magneto-crystalline energy becomes:

$$E_K \; = \; (\; K_1 sin^2\theta + K_2 sin^4\theta \;)\; V$$

with θ the angle between the magnetisation and the easy axis of the crystal, which is defined perpendicular to the sample plane in this chapter.

Surface or interface anisotropy

As seen before, the magnetic moment in a thin film tends to be oriented in the sample plane because of the existence of the demagnetising field $\overrightarrow{H_d}$, with the demagnetising energy $E_d = K_{shape} sin^2(\theta) V$ ($K_{shape} = -1/2\mu_0 M_s^2$ is the shape anisotropy constant and M_s is the saturation magnetisation). The negative sign of K_{shape} indicates that this anisotropy favours an in-plane orientation of the magnetisation. Nevertheless, experimental results have shown that a perpendicular magnetic anisotropy (*PMA*) can be obtained in thin heterostructures. As a consequence, there must be some sources of anisotropy that overcome the shape anisotropy to favour a PMA. This section aims to define two possible contributions to the anisotropy that could switch the magnetic anisotropy out of the sample plane in the case of a thin film.

L. Néel has predicted in 1954 [40] a contribution of the surface or the interfaces of the thin film to the magneto-crystalline anisotropy, by considering the broken symmetry that occurs at the thin layers interfaces when the thickness reaches the nanometer range. It distinguishes the axis perpendicular to the sample plane, which becomes an easy axis of magnetisation. This phenomenon was observed either for interfaces between a magnetic layer and a non-magnetic one (*e.g.* [*Co/Pd*] multilayers [41]) or for interfaces between magnetic layers (*e.g.* [*Co/Ni*] multilayers [42]). The surface or interface anisotropy can be expressed as:

$$E_{Ks} \;=\; \left(\frac{K_s^1}{t} + \frac{K_s^2}{t}\right) sin^2(\theta)\; V$$

where K_s^1 and K_s^2 are the anisotropy constants of both interfaces, t the thickness of the magnetic layer and θ the angle between the magnetisation and the easy axis perpendicular to the sample plane.

Magneto-elastic anisotropy

In the same way as the surface anisotropy, the magneto-elastic anisotropy appears in multilayers when the layers thicknesses reach the atomic size. In fact, strains can appear and alter the direction of magnetisation before relaxation. These strains are a consequence of the lattice mismatch that can exist between the different layers of the heterostructure. The magneto-elastic anisotropy can be either a volume or a surface effect. We define a critical thickness t_c to distinguish the two regimes:

- If $t < t_c$, each layer has the same lattice parameter equal to an intermediary value of the lattice parameter that enables the minimisation of the system energy. Thus, the strains are constant in the volume and we call that the coherent regime. The magneto-elastic anisotropy energy is expressed as:

  $$E_{me} \;=\; K_{V,me} sin^2(\theta)\; V$$

  where $K_{V,me}$ is the volume magneto-elastic constant.

- If $t > t_c$, the magneto-elastic anisotropy becomes a surface effect. In this case, it is more favourable to have misfit dislocations at the interface, and both layers keep their own lattice parameters. In this regime, called incoherent regime, the strain is proportional to $1/t$ and the energy is given by:

  $$E_{me} \;=\; \frac{1}{t}\;\left[K_{S,me} sin^2(\theta)\right]\; V$$

  where $K_{V,me}$ is the surface magneto-elastic constant.

I.B. Macrospin model

In the macrospin model, all the magnetic moments rotate coherently like a giant spin at $T = 0K$. As a consequence, the exchange interaction between individual spins, which is responsible for the long range magnetic order, is not considered. This model can simply determine the global magnetic behaviour of the sample.

I.B.1 Total energy

By taking into account the surface or interface anisotropy and the magneto-elastic anisotropy specific to a thin film in addition to the shape anisotropy and the magneto-crystalline anisotropy, the magnetic anisotropy E_A can be expressed as:

$$\begin{aligned} E_A = & \left[\left(K_1 + K_{V,me} - \frac{\mu_0 M_s^2}{2}\right) + \left(\frac{K_s^1 + K_s^2 + K_{S,me}}{t}\right)\right] sin^2(\theta)\ V \ + K_2\ sin^4(\theta)\ V \\ = & \left(K_{eff}\ sin^2(\theta) + K_2\ sin^4(\theta)\right) V \end{aligned}$$

with K_{eff} the effective anisotropy constant which is composed of a volume contribution K_V and a surface contribution K_S:

$$\begin{aligned} K_{eff} &= K_V + K_S/t \\ K_V &= K_1 + K_{V,me} - \mu_0 M_s^2/2 \\ K_S &= K_s^1 + K_s^2 + K_{S,me} \end{aligned}$$

When an external magnetic field is applied to the sample, the Zeeman energy, which tends to align the magnetisation with the magnetic field direction, competes with the anisotropy energy, which aligns preferentially the magnetic moments along the easy axis of magnetisation. The total energy of the system is expressed as:

$$E = \left(K_{eff}\ sin^2(\theta) + K_2\ sin^4(\theta) - \mu_0 M_s H_{ext}\ cos(\alpha - \theta)\right) V$$

The magnetic configuration of the system is obtained when the energy is minimised with respect to θ for given values of α and H_{ext}, that is to say by solving:

$$\frac{\partial E}{\partial \theta} = 0 \text{ and } \frac{\partial^2 E}{\partial \theta^2} > 0$$

.

In a first approximation, only the second order in the magnetic anisotropy (term in $sin^2(\theta)$) can be considered: it is the Stoner-Wolhfart model.

I.B.2 Stoner-Wolhfart

In a first approximation, the magnetic anisotropy can be written as $E_A = K_{eff} sin^2(\theta)\ V$ and the total energy of the system with a magnetic field H_{ext} applied is expressed as:

$$E = \left(K_{eff}\ sin^2(\theta) - \mu_0 M_s H_{ext}\ cos(\alpha - \theta)\right) V$$

Analytical solutions can only be found in two extreme cases in which the energy minimisation can be easily solved: when the magnetic field is applied parallel to the easy axis of magnetisation ($\alpha = 0^o$) or when the magnetic field is applied perpendicular to the easy axis of magnetisation($\alpha = 90^o$) (figure III.3).

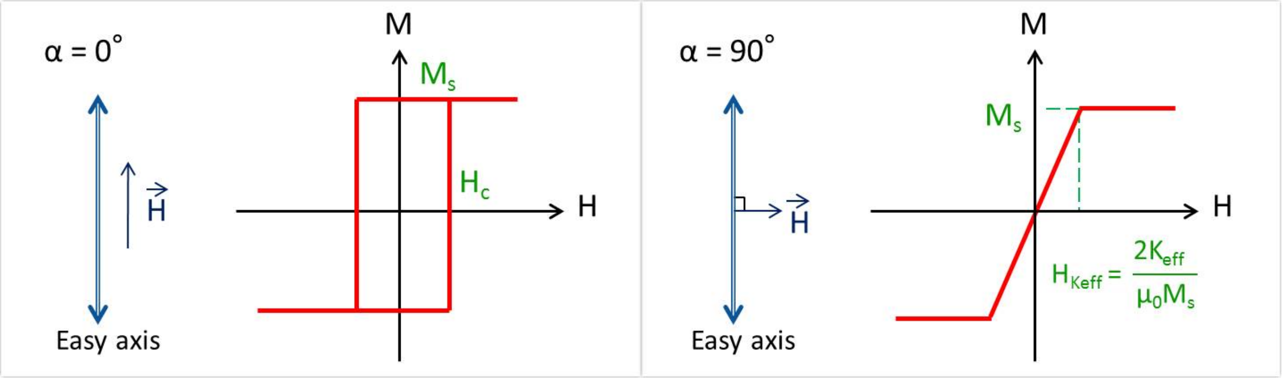

Fig. III.3: *M(H) loops for the particular cases when the magnetic field is applied along the easy axis ($\alpha = 0^o$) or perpendicular to it ($\alpha = 90^o$).*

When the magnetic field is applied along the easy axis of magnetisation ($\alpha = 0^o$), an hysteresis loop is obtained. Then, the coercive field H_c is defined as the field necessary to obtain a zero magnetisation. M_s is the remaining magnetisation at zero field and it is called the saturation magnetisation. When the field is applied along a hard axis ($\alpha = 90^o$), the magnetisation has a linear response, with zero magnetisation in that direction when the magnetic field goes back to zero. The field needed to saturate the magnetisation is called the anisotropy field H_{Keff} and is equal to:

$$H_{Keff} = \frac{2K_{eff}}{\mu_0 M_s}$$

This model determines also the magnetic response and the coercive field as a function of the angle α between the magnetic field and the easy axis of magnetisation. This is the well-known Stoner-Wohlfarth asteroid:

$$H_c = \frac{2K_{eff}}{\mu_0 M_s} \frac{1}{(sin^{2/3}(\alpha) + cos^{2/3}(\alpha))}$$

In this simple model, one finds that $H_c = H_{Keff}$ when the field is applied along an easy axis of magnetisation. Nevertheless, this is true only for small nano-structures. Usually, the coercive field H_c is smaller than the anisotropy field H_{Keff}. Indeed, the magnetisation switching is usually induced by the propagation of domains which nucleate where the sample presents defects. However, it is possible to estimate properly the anisotropy constant via the anisotropy field, which is obtained in the case of an external field applied along the hard axis of magnetisation.

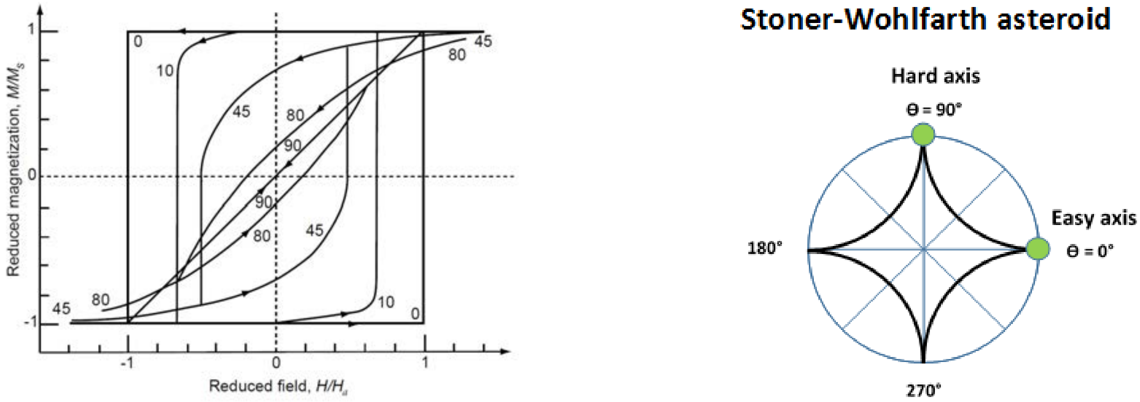

Fig. III.4: *Left: M(H) loops for different angles of the applied field α. Right: Stoner Wolhfart asteroid. Excerpted from [43].*

I.B.3 Modelisation

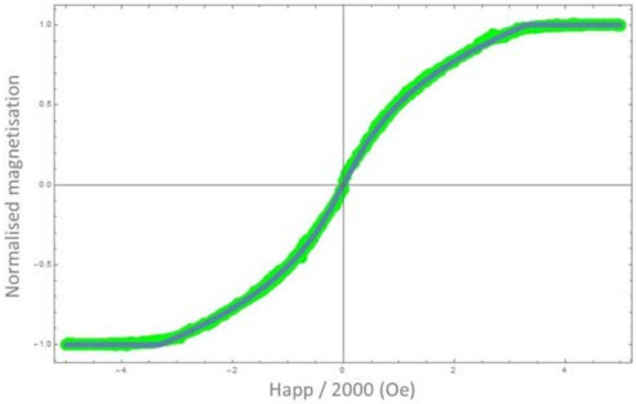

Fig. III.5: *Magnetisation normalized by the magnetisation at saturation as a function of the magnetic field (divided by a factor 2000). The green curve corresponds to the experiment. The blue curve is the simulation on Mathematica. We can deduce from it the values of K_{eff} and K_2.*

In this thesis, magnetometry and electronic transport measurements have been associated with calculations using the Wolfram language named *Mathematica*, in which the magnetic behaviour is simulated by minimising the energy with respect to the angle θ between the magnetisation and the easy axis. An example is given in the figure III.5 in which the M(H) loop is simulated by minimising the total energy (with the fourth order in the anisotropy energy), when the magnetic field is applied perpendicular to the easy axis.

II. PMA state of the art in [Co/Ni] multilayers

In order to study the electronic spin precession in a magnetic tunnel transistor, it is mandatory to have a thin magnetic layer that exhibits a perpendicular magnetic anisotropy. This layer must be integrated in the transistor, and this can induce some experimental problems. The goal of this part is to understand the important parameters that enable the obtaining of a PMA.

According to the previous section about the magnetic anisotropy, a magnetic layer can exhibit a PMA only if the total anisotropy contribution overcomes the shape anisotropy. In thin films, the surface or interface anisotropy, induced by a broken symmetry at the interface, and the magneto-elastic anisotropy, due to a misfit between the lattice parameters of the layers, are the main contributions to anisotropy. In both cases, it is clear that the surface morphology and the crystallographic orientation of the heterostructure are important. Consequently, the PMA strongly depends on the growth conditions (nature of the substrate, quality of its surface, deposition technique, deposition parameters like pressure ...). In my PhD work, we have decided to focus the experimental study on [Co/Ni] multilayers since it is well known that this kind of multilayer exhibits a PMA. Moreover, [Co/Ni] mulilayers have a strong spin polarisation, which is an important parameter for our study of the electronic spin precession in a magnetic tunnel transistor. As a consequence, the following bibliographic study is centered on [Co/Ni] multilayers only.

The first prediction of a PMA in a [Co/Ni] multilayer was made by G.H.O. Daalderop *et al.* in 1992 [42]. They have shown from ab initio calculations that multilayers with a thickness ratio $t_{Ni}/t_{Co} = 2$ and oriented $[111]_{fcc}$ can exhibit PMA. Co and Ni elements differ by only one valence electron. Thus, the lattice mismatch is small (0.8%). However, the presence of an interface between ultrathin close-packed layers of Co and Ni is sufficient to have a large interface magnetic anisotropy. Moreover, the total number of valence electrons with Co_1Ni_2 multilayers places the Fermi level close to $x^2 - y^2$ and xy bands, in which the spin-orbit coupling favours a PMA.

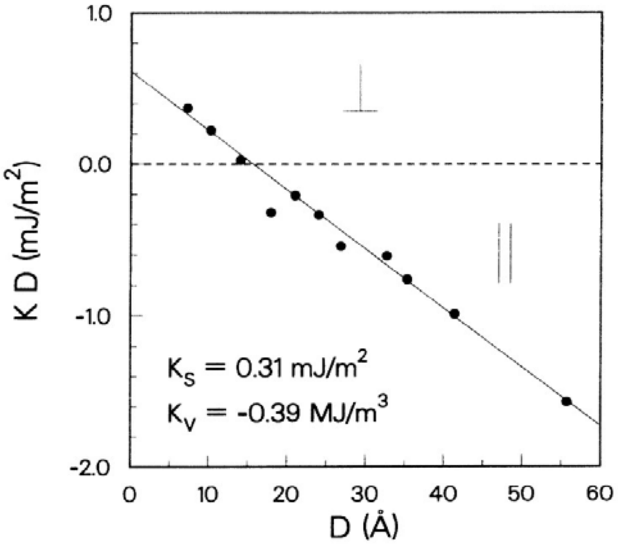

Fig. III.6: *Magnetic anisotropy constant multiplied by the bilayer thickness* (KD) *VS bilayer thickness* (D) *for Co/Ni multilayers with a constant thickness ratio* $t_{Ni}/t_{Co} = 2.2$*. The number of repetitions was* $N = 20$ *for thicknesses up to* $D = 24$Å *and decreased to reach* $N = 10$ *for* $D = 60$Å*. Excerpted from [42].*

In this figure, it is shown that $Co_1Ni_{2.2}$ multilayers can exhibit a PMA with a total thickness up to 12Å. The volume anisotropy constant equals to $K_V = 0.39MJ/m^3$, and the surface anisotropy constant is $K_S = 0.31mJ/m^2$.

In the same year, F.J.A. Den Broeder *et al.* [44] have made an experimental study of several [Co/Ni] multilayers grown by vapor deposition in high vaccum. With 2Å of Co, it displays a PMA for Ni thicknesses from 2Å to 30Å, whereas the anisotropy goes back to the sample plane when there is 4Å of Co and more than 8Å of Ni (figure III.7).

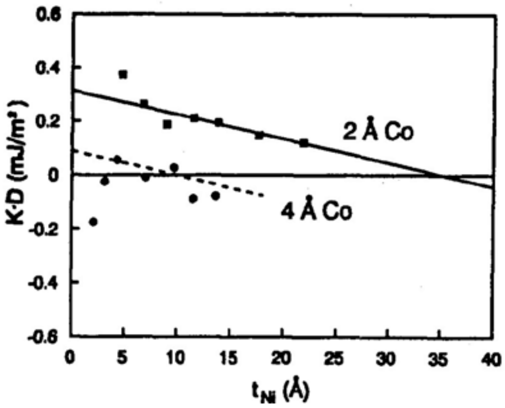

Fig. III.7: *Magnetic anisotropy constant of a Co/Ni bilayer VS Ni thickness, for* 2Å *and* 4Å *of Co. Excerpted from [44].*

They have also shown that the surface anisotropy constant is favoured by the magneto-elastic contribution, due to internal stresses. Nevertheless, the lattice mismatch between Co and Ni layers is low (0.8%). So, this is rather a volume contribution to the anisotropy, even for small thicknesses. The coherent strain in the volume is caused by the lattice misfit between the multilayer and the underlayer, which is more favourable to a PMA with a [111] orientation.

Because of the influence of the crystallographic quality and surface morphology, which are directly related to the magnetic anisotropy constant, the deposition parameters are important. The following figure (figure III.8) shows the variation of the anisotropy with the deposition rate of Co and with the substrate temperature.

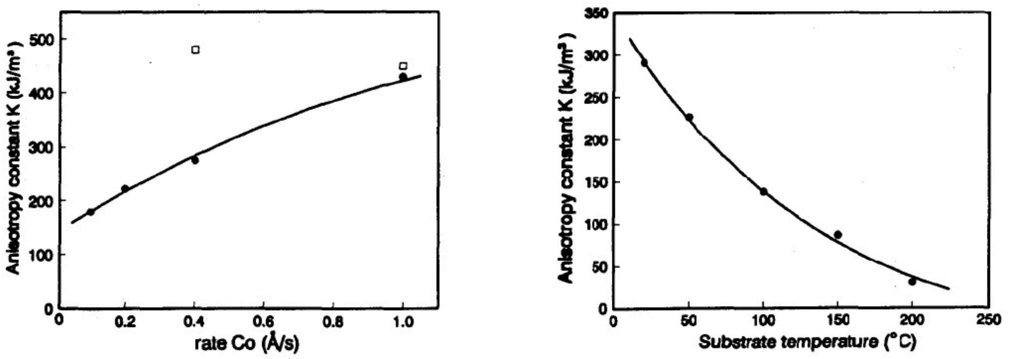

Fig. III.8: *Anisotropy constant of* $[Co(2\text{Å})/Ni(4\text{Å})]_{20}$ *as a function of the Co deposition rate on the left-hand side, and as a function of the substrate temperature on the right-hand side. Excerpted from [44].*

To prove experimentally the influence of the crystallographic orientation of the multilayer, M.T. Johnson *et al.* [45] have deposited a Ni/Co/Ni sandwich on different substrates in order to orientate the multilayers along the [100], [110] or [111] directions (figureIII.9).

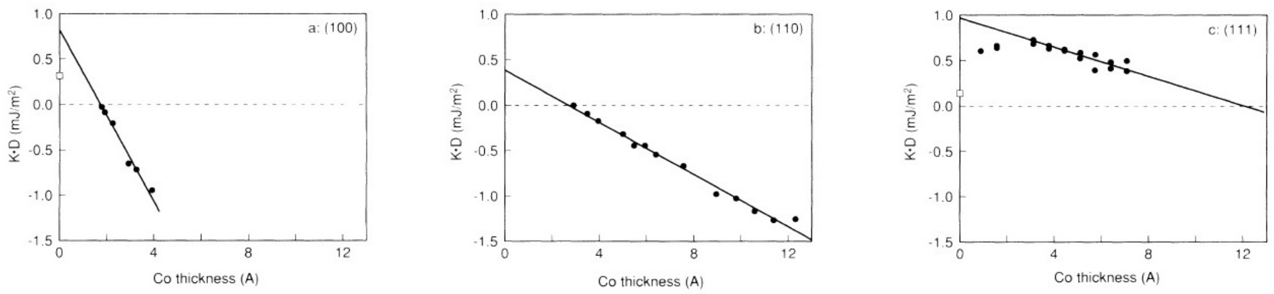

Fig. III.9: *Magnetic anisotropy constant multiplied by the bilayer thickness* KD *VS bilayer thickness* D *for* $Ni(8\text{Å})Co(t)Ni(8\text{Å})$ *multilayers, for crystallographic orientations along the [100], [110] and [111] directions. Excerpted from [45].*

A remarkable property displayed on the graphs above is that a [111] orientation of the multilayer favours a PMA ($KD > 0$) compared to a [100] or a [110] orientation.

III. Conclusion

The first part of this chapter gives an overview of the different contributions to the magnetic anisotropy. In order to obtain a PMA, the surface contribution must be larger than the demagnetisation one. Surface or interface anisotropy and magneto-elastic anisotropies, that both appear for thin heterostructures, contribute widely to the surface anisotropy and allow a thin magnetic film to exhibit PMA. When a magnetic field is applied, the Zeeman energy competes with the anisotropy energy. The magnetic behaviour of the magnetic layer can be deduced by the minimisation of the total energy.

The second part relates to the state of the art of [Co/Ni] multilayers. The literature on that subject shows that a multilayer oriented [111] and with a thickness ratio $t_{Ni}/t_{Co} > 2$ can exhibit a PMA. These results will be the starting point of the construction of a magnetic tunnel transistor which contains three ferromagnetic layers with the magnetisations in the three space directions. The next chapter treats the experimental work done to grow a [Co/Ni] multilayer which exhibits a PMA on top of a Schottky diode.

Résumé du chapitre :

Afin d'étudier la précession du spin de l'électron dans un ferromagnétique à l'aide d'un transistor tunnel magnétique, il faut nécessairement qu'une couche de la vanne de spin ait son anisotropie magnétique perpendiculaire au plan de l'échantillon. L'objectif de ce chapitre est de décrire comment une couche à anisotropie perpendiculaire peut être obtenue sur une barrière Schottky de bonne qualité, et qui permettra d'avoir un courant d'électrons chauds mesurable ainsi qu'un fort magnéto-courant.

La première partie a permis de décrire les différentes contributions à l'anisotropie magnétique dans une nanostructure magnétique. Nous avons montré notamment que l'anisotropie d'interface ainsi que l'anisotropie magnéto-élastique favorise une anisotropie hors du plan et contrebalance le champ démagnétisant qui favorise quant à lui une anisotropie dans le plan. La direction de l'aimantation est obtenue par la minimisation de l'énergie du système, composée d'une part de l'énergie d'anisotropie et d'autre part de l'énergie Zeeman. Le modèle de Stoner Wohlfarth, qui ne prend en compte que l'ordre 2 dans l'énergie d'anisotropie, permet de déterminer la valeur de l'aimantation en fonction du champ appliqué.

La deuxième partie nous a permis d'examiner l'état de l'art concernant l'obtention d'une anisotropie magnétique perpendiculaire dans des nanostructures. Nous avons choisi d'utiliser dans cette thèse une multicouche composée de Co et Ni, la littérature montrant qu'un tel type de multicouche exhibe une anisotropie magnétique perpendiculaire. Les différents travaux sur ce sujet ont notamment permis de montrer que la multicouche possède bien une anisotropie magnétique perpendiculaire si le rapport des épaisseurs entre le Co et le Ni est supérieur à 2 $t_{Ni}/t_{Co} > 2$.

Chapter 4

Magnetic and structural properties of [Co/Ni] multilayers

The key point for the development of a crossed Magnetic Tunnel Transistor (*MTT*) to measure the electronic spin precession is the growth of a magnetic layer with Perpendicular Magnetic Anisotropy (*PMA*) and with a high spin polarisation. As it was introduced in the previous chapter, several parameters influence PMA in a magnetic multilayer and have to be optimised. In this chapter, we focus our study on a [Co/Ni] multilayer, which has been chosen since predicted to have high spin polarisation and PMA. But the magnetic properties of such a multilayer have been shown to be strongly dependent on the texture. Thus, the substrate, the technique used to clean the substrate, the buffer layer or the number of repetitions of the multilayer will strongly influence the magnetic properties, and especially the anisotropy.

The results are presented in two steps. First of all, we will point out that the cleaning of the substrate, of prime importance to grow a Schottky diode with electrical characteristics compatible with our study, has an impact on the magnetic anisotropy of the multilayer. We have found a close accordance between literature and results on our samples by confronting vibrating sample magnetometer and X-ray diffraction experiments. The second part is devoted to the influence of different parameters of the multilayer, like the number of repetitions of the multilayer or the nature of interfaces.

I. [Co/Ni] multilayers with PMA on a Schottky barrier - Influence of the Si substrate preparation on the magnetic anisotropy

In this section, the constraints to get a layer with a perpendicular magnetic anisotropy that can be integrated in a magnetic tunnel transistor are shown. In order to be flexible on the nature and the thickness of the precession layer, we have studied the growth of the PMA layer on top of the Schottky barrier. Once optimised, this layer will be common to all the samples grown and measured in this thesis.

Our starting point relays on a previous study made at the *Institut Jean Lamour* before the starting of my PhD [34, 46]. Lu *et al.* have optimised the growth of a Si[100]/Cu[100] Schottky diode to get a good energy filtering with a well defined energy threshold. Therefore, we have kept this structure for our study.

According to previous studies made since the nineties [42, 44, 45], a multilayer of cobalt and nickel with nanometer thicknesses can exhibit a PMA. The more common multilayer stack is made of repetitions of [Co(0.2)/Ni(0.6)] (thicknesses in nanometers). Therefore, as a starting point, we have grown $[\mathrm{Co}(0.2)/\mathrm{Ni}(0.6)]_5$ on Cu buffer layers. On the basis of our previous work, the Si/Cu Schottky barrier has adapted filtering properties when the Si substrate is cleaned from its oxide using deoxidization by hydrofluoric acid (HF, 3 minutes in a bath of HF 0.6%). The resulting multilayer consists then of a Si[100](HF)//Cu(10) Schottky on top of which a Pt(0.6) $[\mathrm{Co}(0.2)/\mathrm{Ni}(0.6)]_5$ Cu(3.5) Pt(5) is stacked (Sample 1). A Pt layer is inserted between Cu and the $[\mathrm{Co}(0.2)/\mathrm{Ni}(0.6)]_5$ since it is well known that Pt/Co interfaces promote perpendicular magnetisation.

In comparison, a Si[100](etch)//Cu(10) Pt(0.6) $[\mathrm{Co}(0.2)/\mathrm{Ni}(0.6)]_5$ Cu(3.5) Pt(5) stack has been grown after an Ar etch cleaning of the Si[100] substrate, the surface cleaning conventionally used for samples in our sputtering machine (Sample 2). The magnetic behaviours of these samples are shown in figure IV.1 by measuring "magnetisation versus field" loops $M(H)$ for a field applied parallel or perpendicular to the sample plane.

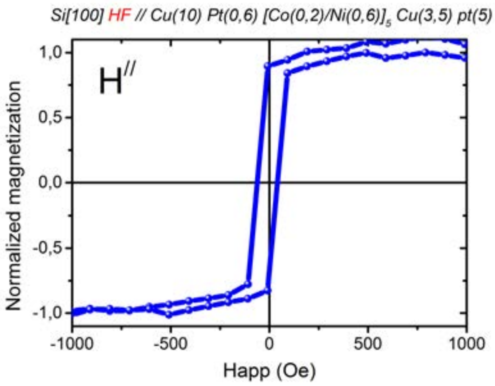

Fig. IV.1: *$M(H)$ loops of samples 1 (HF treated) with a field applied in the sample plane.*

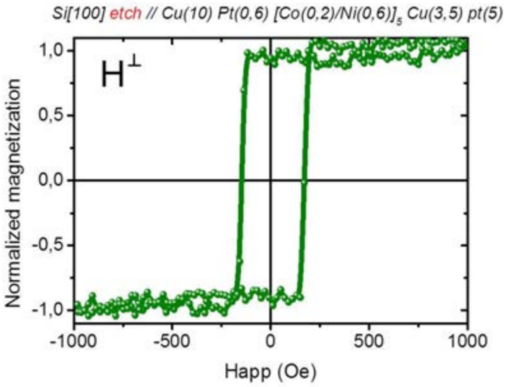

Fig. IV.2: *$M(H)$ loops of samples 2 (Ar-etched) with a field perpendicular to the sample plane.*

These curves show undoubtedly that the sample grown on HF-prepared Si surface has an in-plane easy axis of magnetisation (figure IV.1), whereas the Ar ions etching prepared surface leads to a PMA (figure IV.2). These behaviours do not help us in our study since PMA is needed on Cu grown on HF-prepared Si.

The magnetic properties of a [Co/Ni] multilayer depend on its crystalline quality, as shown in the bibliography study presented in the previous chapter. In order to understand these opposite behaviours, X-Rays diffraction (*XRD*) experiments have been performed on these two multilayer stacks but also on single Cu layers deposited on Si. The $\theta/2\theta$ spectra have been recorded using an anode in copper to emit the x-rays ($\lambda_{Cu} = 1.54056\text{Å}$). The XRD experiments have been associated with simulations on *Mathematica*. The theoretical expression used in the simulation takes into account the X-rays reflection on each interface. Thus, the structure factor of the total multilayer can be expressed as a function of $Q = 4\Pi Sin[\theta]/\lambda_{Cu}$. An example of the calculation can be found in the literature for a trilayer [47].

In a first step, the texture of the Cu layer grown on Si substrates has been studied. As shown in figure IV.3, the texture of the Cu layer is different for Si(etch)//Cu(10) and Si(HF)//Cu(10). As far as Si(etch)//Cu(10) is concerned, the Cu peak is located at a position $2\Theta \simeq 43^o$, close to the theoretical position of a Cu layer oriented along the [111] direction (43.32^o). On the other hand, for the sample Si(HF)//Cu(10), the Cu peak appears for the position $2\Theta \simeq 50^o$, close to the theoretical position of Cu oriented along the [200] direction (50.46^o). As a result, depending on the substrate preparation, the [Co/Ni] multilayer grows on a Cu buffer layer with different crystallographic orientations.

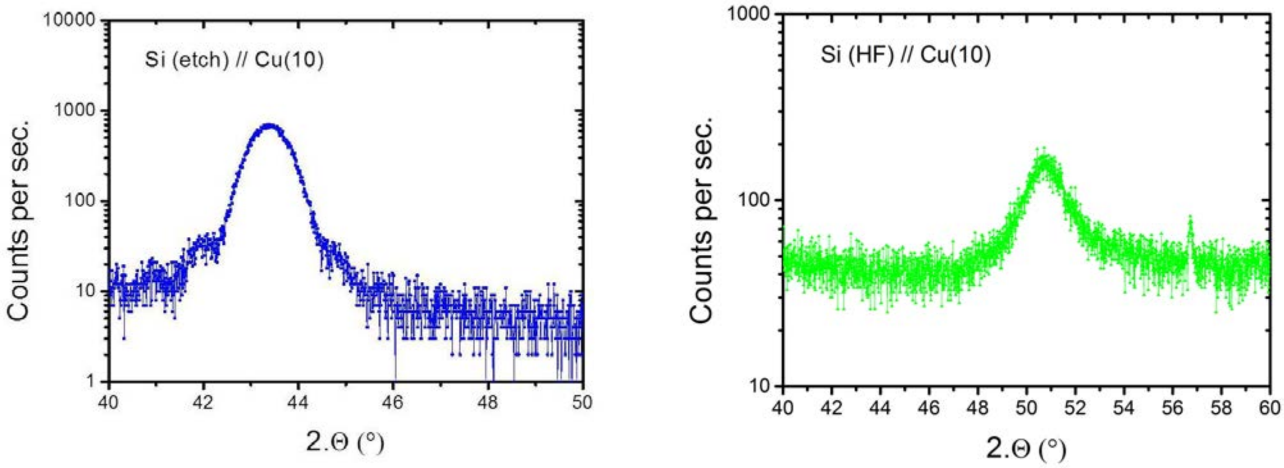

Fig. IV.3: *X-ray diffraction spectra measured in the $(\Theta - 2\Theta)$ geometry on Si/Cu(10nm) made on (a) Ar-etched Si or (b) HF-etched Si.*

On HF-prepared Si, the spectra of the Si[100](etch) // Cu(10) Pt(0.6) $[Co(0.2)/Ni(0.6)]_5$ Cu(3.5) Pt(5) sample is composed of large peaks of low intensity that can be attributed to Co[200], Ni[200], Pt[200] and Cu[200] (figure IV.4a). With the simulation of Small Angle X-ray Scattering (*SAXS*) experiments as shown in figure IV.5, the density and the effective thickness of each layer can be deduced. By combining these parameters with the crystallographic orientation expected via the lattice parameter of the layer, the XRD curve can be simulated on *Mathematica*. The $\theta/2\theta$ scan of sample 1 is theoretically computed considering that the entire multilayer is [200] textured, and acts as a coherent entity. The multiple reflection of the X-rays at each atomic plane in the multilayer are also computed. The theoretical curve is the red line in figure IV.4. The broad peak at $\sim 51^o$ is the superposition of the theoretically predicted Cu[100], Co[100] and Ni[100] peaks. While the texture is poor, it appears clearly that the multilayer stack follows the growth texture imposed by the Cu seed layer.

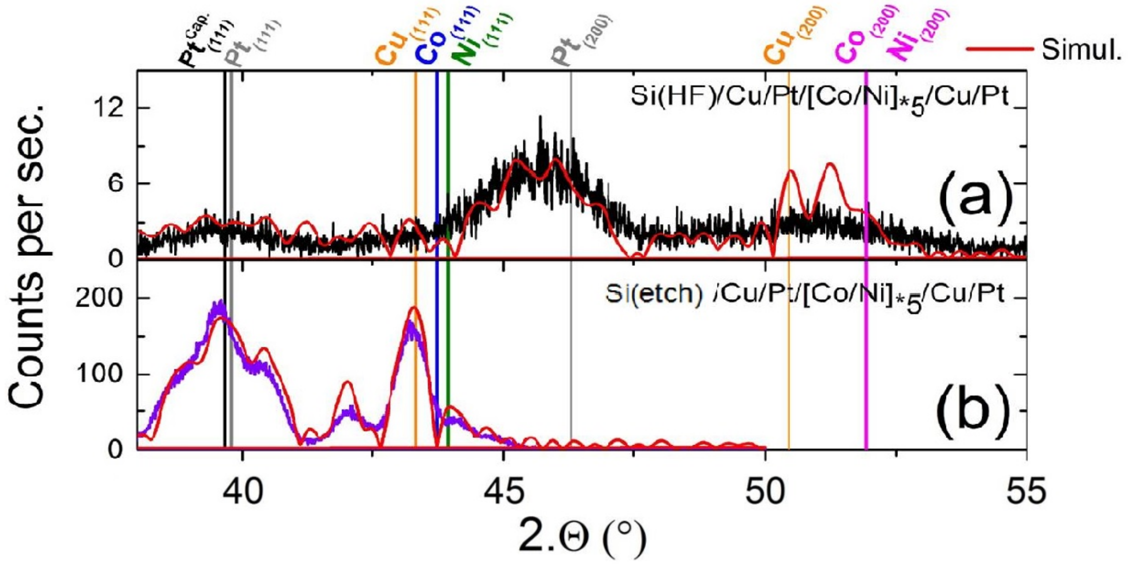

Fig. IV.4: *X-ray diffraction spectra measured in the* $(\Theta - 2\Theta)$ *geometry on* $Si//Cu(10nm)\ Pt(0.6nm)\ [Co(0.2nm)/Ni(0.6nm)]_5\ Cu(3.5nm)Pt(5nm)$ *made on HF-etched Si (a), Ar-etched Si (b). The theoretical spectra (continuous red lines) and especially the peak positions are in close agreement with the experiment.*

On the contrary, the spectra is composed of well defined peaks that can be attributed to Pt[111] and Cu[111] when the growth is done on Si[100](etch)//Cu(10). The peaks intensities are higher than for the same sample grown on Si[100](HF)//Cu(10), which indicates a better crystallographic quality. Here again the theoretical curve has been added in red in figure IV.4 by considering that the entire stack has a [111] texture. The Cu[111] and Pt[111] peaks and the occurrence of additional peaks (for example at 42^o) have been reproduced theoretically. These additional peaks are due to an interferential phenomenon: X-rays are reflected on each layer of the multilayer and interfere between them. This phenomenon is called Kiessing fringes. The regularity of the oscillations and their high intensities proves a great crystallographic quality of the multilayer.

The close agreement between simulations and experiments indicates that the stack is fully oriented [200] in the case of a HF cleaning of the Si substrate, whereas the crystallographic orientation is along the [111] direction when the Silicon is sputtered before the deposition. In fact, a cleaning by chemical attack with hydrofluoric acid (HF) removes the silicon oxide on the surface but without changing the crystallography of the surface, which is [200]. Thus, the multilayer grows with the same orientation as the Si substrate, along the [200] direction. On the contrary, by removing the oxide on the Si surface using Ar etch cleaning, a thin layer of amorphous Si is created on top of the surface. Then, as often observed in layers deposited by sputtering, Cu will grow by stacking close packed planes promoting the [111] texture. As a consequence, the entire stack, and especially the [Co/Ni] multilayer, is oriented [111]. In accordance with the properties of the [Co/Ni] multilayers, invoked in chapter IV, the Si[100](etch)//Cu(10) Pt(0.6) [Co(0.2)/Ni(0.6)]$_5$ Cu(3.5) Pt(5) with a (111) texture exhibits PMA [42, 45, 44].

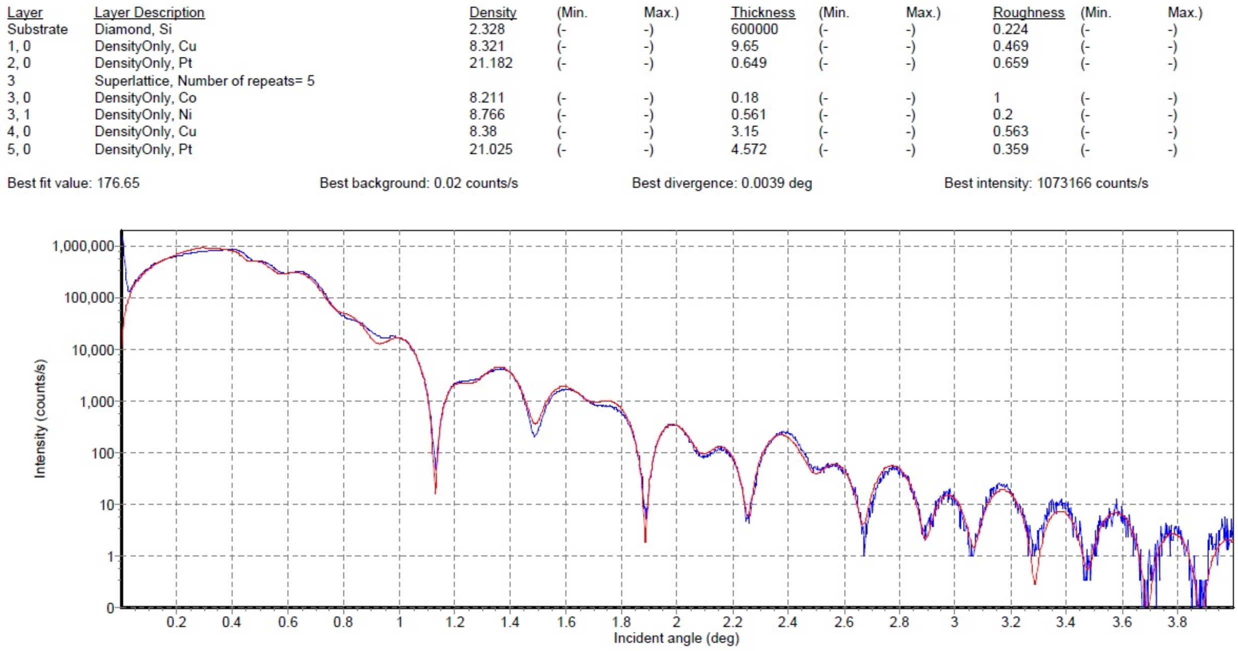

Layer	Layer Description	Density	(Min.	Max.)	Thickness	(Min.	Max.)	Roughness	(Min.	Max.)
Substrate	Diamond, Si	2.328	(-	-)	600000	(-	-)	0.224	(-	-)
1, 0	DensityOnly, Cu	8.321	(-	-)	9.65	(-	-)	0.469	(-	-)
2, 0	DensityOnly, Pt	21.182	(-	-)	0.649	(-	-)	0.659	(-	-)
3	Superlattice, Number of repeats= 5									
3, 0	DensityOnly, Co	8.211	(-	-)	0.18	(-	-)	1	(-	-)
3, 1	DensityOnly, Ni	8.766	(-	-)	0.561	(-	-)	0.2	(-	-)
4, 0	DensityOnly, Cu	8.38	(-	-)	3.15	(-	-)	0.563	(-	-)
5, 0	DensityOnly, Pt	21.025	(-	-)	4.572	(-	-)	0.359	(-	-)

Best fit value: 176.65 Best background: 0.02 counts/s Best divergence: 0.0039 deg Best intensity: 1073166 counts/s

Fig. IV.5: *SAXS experiment on Si[100](HF)//Cu(10nm) Pt(0.6nm) [Co(0.2nm)/Ni(0.6nm)]$_5$ Cu(3.5nm)Pt(5nm). Experimental parameters like the effective thicknesses or densities are extracted from the theoretical spectra (continuous red lines).*

In conclusion, at this stage, it does not seem possible to combine the optimised HF-prepared Cu[100]/Si[100] with a [Co/Ni] multilayer that exhibits a perpendicular magnetic anisotropy. Additional optimisation has to be done as discussed in the following.

II. Resolution of the dilemma

At this point, three strategies can be followed and will be tested. In the first one, the transport properties of the Si[100](etch)//Cu(10) Pt(0.6) [Co(0.2)/Ni(0.6)]$_5$ Cu(3.5) Pt(5) Schottky barrier are measured. The second one consists in testing the Schottky barrier quality and magnetic properties of a Si[111](HF)//Cu(10) Pt(0.6) [Co(0.2)/Ni(0.6)]$_5$ Cu(3.5) Pt(5) stack. The third one consists in finding a way to stack a [111] [Co/Ni] multilayer on top of a Si[100](HF)//Cu[100].

II.A. The Si[100](etch)//Cu(10) Schottky barrier

As explained in the introductory part of this thesis, our objective is to create a MTT with three ferromagnetic layers in order to study the electronic spin precession at low energy above the Fermi level. Several ingredients are absolutely needed in the functioning of the device. In particular, a good energy filter is necessary to collect only ballistic electrons. Therefore, the use of a Schottky barrier, which is created by the interface between a metal and a semiconductor, is expected. Thus, electrons must overcome the energy barrier of the Schottky diode to contribute to the collected current. This configuration is also convenient to measure the height of the Schottky barrier and it will be used here to get a characterisation of the Schottky barrier.

In a previous work, Lu *et al.* have optimised the Schottky barrier by growing a Cu layer on a Si substrate oriented [100] cleaned by 3 minutes in a bath of HF 0.6% [34, 46]. Nevertheless, this structure is not suitable to grow a multilayer that exhibits a PMA (see sample 1 of the previous section). On the contrary, a multilayer grown on Si[100](etch)//Cu(10) has a PMA (sample 2). To integrate the latter in a MTT, its Schottky barrier must be of good quality. We have measured and compared in figure IV.6 the characteristic of the Schottky diode for the samples with the two different substrate cleanings (HF or Ar etch cleaning). Therefore, non-polarised electrons are injected in the MTT (without the ferromagnetic layer before the tunnel barrier), and the current collected in the semiconductor is measured as a function of the applied voltage in the tunnel barrier (figure IV.7).

In figure IV.6, it is clear that the Schottky diode is efficient only in the case of the HF preparation of the Si substrate. If the applied voltage is smaller than 0.7V (which corresponds to an energy of 0.7eV above the Fermi level), no electron contributes to the collected current in the semiconductor: they cannot overcome the energy barrier of the Schottky diode. In the case of the sample 2 (Si[100](etch)//Cu(10) Pt(0.6) [Co(0.2)/Ni(0.6)]$_5$ Cu(3.5) Pt(5)), the collected current increases continuously with the voltage: there is no well defined energy threshold. As a consequence, this Schottky barrier is not energy selective and cannot be used in our MTT device. This strategy is not the good one.

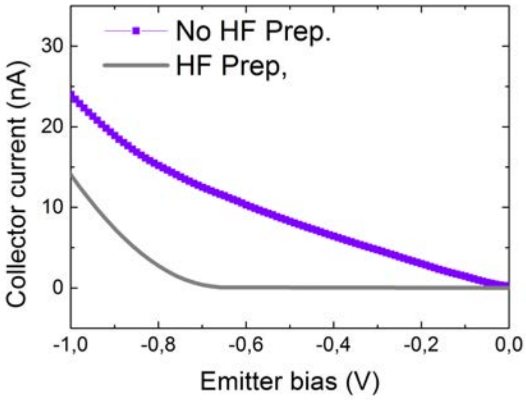

Fig. IV.6: *Schottky characteristic of the Si/Cu interface in the case of a HF cleaning of the Si substrate (grey curve) or with an Ar ions etching before deposition (blue curve) using a MTT structure.*

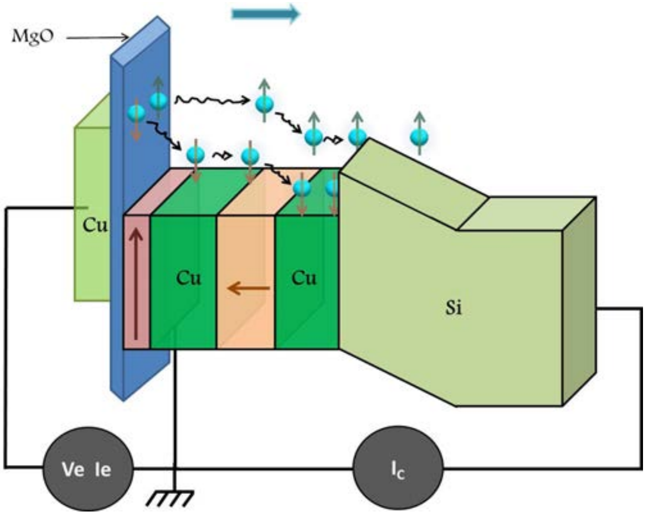

Fig. IV.7: *Scheme of the Schottky characteristic measurement. A non-polarised hot electrons current is injected in the base (in a crossed magnetic configuration here) by applying a voltage* V_e*. Only electrons with an energy larger than the Schottky barrier height contribute to the collected current* I_c*. This geometry enables the measurement of the top of the Schottky barrier.*

II.B. The Si[111](HF)//Cu(10) buffer

Since [111] texture is needed to get a PMA in a [Co/Ni] multilayer, the growth has been done on Si[111]. In a first step, the magnetic properties have been checked and reported in figure IV.8.

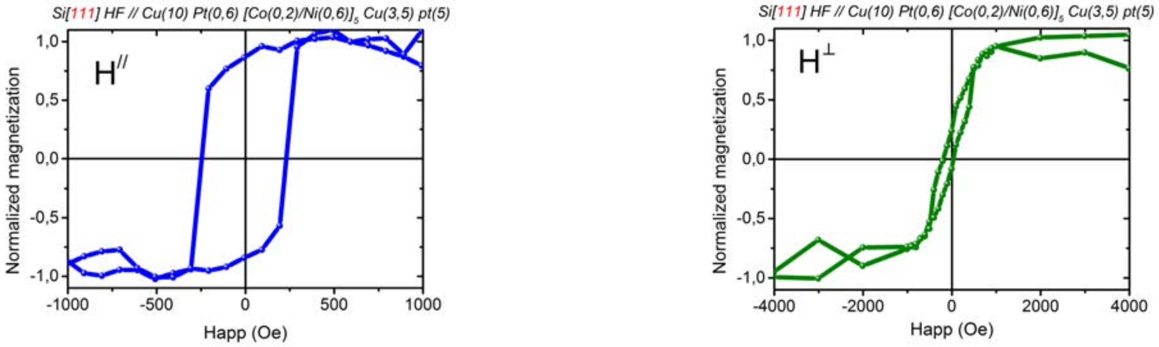

Fig. IV.8: *M(H) loops of Si[111](HF)//Cu(10) Pt(0.6) $[Co(0.2)/Ni(0.6)]_5$ Cu(3.5) Pt(5) stack with an applied field parallel (left-hand side) or perpendicular (right-hand side) to the sample plane.*

It appears clearly that the magnetic anisotropy lies in-plane with a saturation field perpendicular to the film plane around 1000 Oe. To understand the magnetic behaviour, XRD experiments have been performed to check the crystallographic orientation of the stack (see figure IV.9).

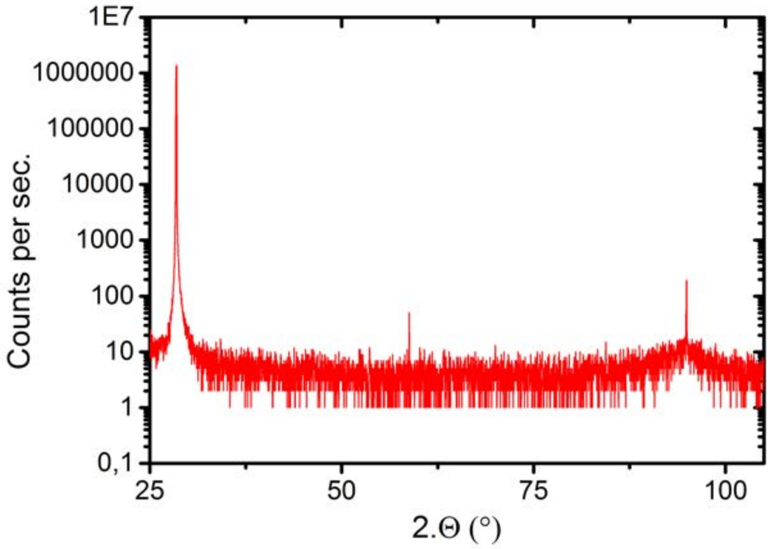

Fig. IV.9: *X-ray diffraction spectrum measured in the $(\Theta - 2\Theta)$ geometry on $Si//Cu(10nm)$ $Pt(0.6nm)$ $[Co(0.2nm)/Ni(0.6nm)]_5$ $Cu(3.5nm)Pt(5nm)$ made on HF-etched Si oriented [111].*

In this figure, only the peak for the Si[111] at a position $2\Theta = 28.5^o$ and the peak for the Si[222] at a position $2\Theta = 95^o$ appear. The other elements of the stack do not seem to be crystallised. This result is somehow surprising since in recent experiments the growth of well crystallized Cu layers has been done successfully on a Si substrate oriented along the [111] direction and cleaned with HF [48]. Moreover, other experiments claimed that the roughness of the surface is not more important in the case of the Si[111] compared to the Si[100] one. In both cases, the surfaces seem to be microscopically rough upon HF treatment [49]. Nevertheless, we know from our own experience, in particular thanks to the previous studies of Bernos [50], that our substrates of Si oriented [100] have a flatter surface than the Si substrate oriented along the [111] direction. That could explain the result of this experiment.

But since the magnetic properties are not the ones needed for our study, we have decided to stop our research in this direction.

II.C. The Si[100](HF)//Cu(10) Schottky barrier with Co/Ni[111]

Our third direction of work has consisted in finding a way to get a [111] texture for the [Co/Ni] multilayer grown on a Si[100](HF)//Cu Schottky diode. On the basis of the results obtained on the etched Si[100], we have tried to grow the [Co/Ni] multilayer on an amorphous layer. In sample 1, the Si(100)(HF)//Cu(10) has been sputtered using Ar plasma after Cu deposition to get an amorphous Cu top layer. For samples 2, 3 and 4, a Ta layer was inserted into the stack. Indeed, Ta layers with thicknesses smaller than 5nm are amorphous and have been used in the past in spintronics devices to promote [111] texture [51]. In samples 2 and 3, the Cu layer is capped with a Ta layer respectively 0.5nm and 1nm thick. For sample 4, a 1nm thick Ta layer is inserted in the middle of the Cu layer.

	Substrate and Buffer	**Stacking**	**Capping**
Sample 1	$Si[100]HF$ // $Cu(10)etch$	$Pt(0.6)$ $[Co(0.2)/Ni(0.6)]_5$	$Cu(3.5)$ $Pt(5)$
Sample 2	$Si[100]HF$ // $Cu(10)$ $Ta(0.5)$	$Pt(0.6)$ $[Co(0.2)/Ni(0.6)]_5$	$Cu(3.5)$ $Pt(5)$
Sample 3	$Si[100]HF$ // $Cu(10)$ $Ta(1)$	$Pt(0.6)$ $[Co(0.2)/Ni(0.6)]_5$	$Cu(3.5)$ $Pt(5)$
Sample 4	$Si[100]HF$ // $Cu(5)$ $Ta(1)$ $Cu(5)$	$Pt(0.6)$ $[Co(0.2)/Ni(0.6)]_5$	$Cu(3.5)$ $Pt(5)$

Table 4.1: **Description of the different [Co/Ni] multilayers investigated to obtain a perpendicular magnetic anisotropy on a Si[100](HF)//Cu Schottky barrier.**

II.C.1 Sample 1: etching of the Cu layer

In order to grow the [Co/Ni] multilayer according to the [111] direction, by keeping the HF treatment of the Si substrate, we have tried to etch the Cu layer with Ar ions before the deposition of Pt. Thus, if the surface of the Cu layer is amorphous, the Pt layer could grow according to its close packed planes [111]. At first, the magnetic properties of that sample have been measured (figure IV.10).

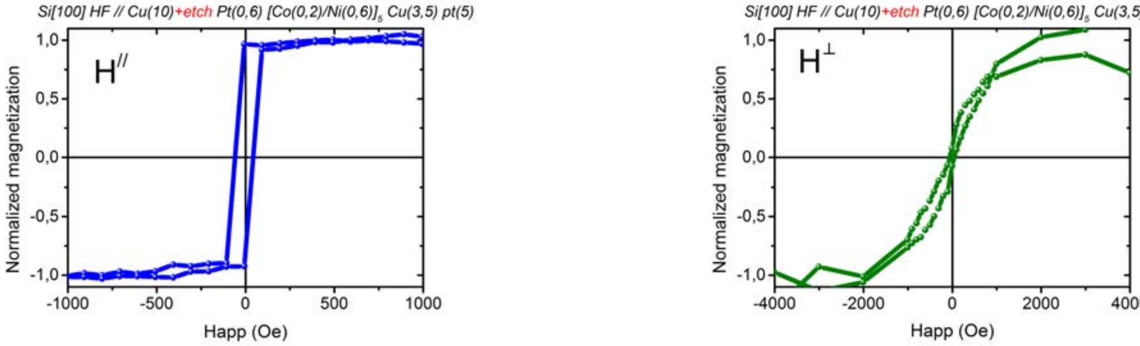

Fig. IV.10: *M(H) loops for* $Si[100]HF//Cu(10)etch\ \ Pt(0.6)[Co(0.2)/Ni(0.6)]_5\ Cu(3.5)Pt(5)$. *The magnetic field is applied parallel (left-hand side) or perpendicular (right-hand side) to the sample plane.*

Unfortunately, the magnetic anisotropy is in the sample plane. To understand the reasons, XRD diffraction experiments have been realised in that sample. The $\Theta/2\Theta$ spectrum is compared with the ones of the sample test of the first section (with the HF or the Ar ions treatment of the Si[100] substrate), as shown on the figure IV.11.

The figure shows a peak located at the position $2\Theta = 51^o$, close to the theoretical position of a Cu layer oriented along the [200] direction (50.46^o). This result is not surprising since the Cu has been grown on the Si oriented [100] and cleaned with HF. A peak located at the position $2\Theta = 46^o$ corresponds to the theoretical position of a Pt layer oriented along the [200] direction (46.2^o). So, the etching of the Cu layer did not induce the expected [111] orientation of the Pt layer and the [Co/Ni] multilayer, resulting in a magnetisation in the sample plane.

In fact, the energy of a covalent bond is around 1eV for Si. In the case of Cu, this energy is 0.1eV. As a consequence, when the Si is etched, the energy is too big to re-crystallise the surface, which is amorphous. Thanks to a smaller covalent bond energy, the Cu surface re-crystallize itself after an etching with Ar ions. That is what happened in our sample: the surface of the Cu layer stays well organised and induces the growth of the Pt layer and of the whole [Co/Ni] multilayer along the [200] direction.

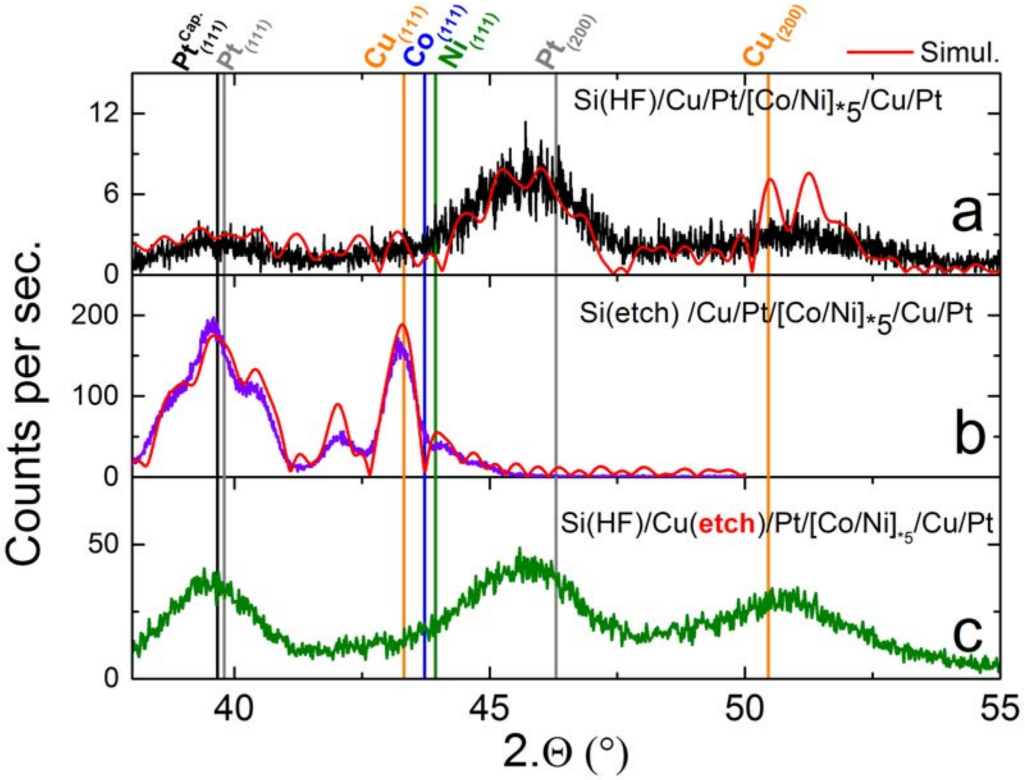

Fig. IV.11: *X-ray diffraction spectra measured in the* $(\Theta - 2\Theta)$ *geometry on* $Pt(0.6nm)\ [Co(0.2nm)/Ni(0.6nm)]_5\ Cu(3.5nm)Pt(5nm)$ *made on (a) HF-etched Si oriented [100], (b) sputtered Si oriented [100] and (c) HF-etched Si oriented [100] and after a etching of the Cu layer.*

Since the magnetic properties are not the ones needed for our study, we decided to stop our research in this direction.

II.C.2 Sample 2 and 3: addition of a Ta layer after the Cu one

In these two samples, a thin Ta layer 0.5nm or 1nm thick is added after the Cu one. The structure is: Si[100]HF//Cu(10) Ta(0.5 or 1) Pt(0.6) [Co(0.2)/Ni(0.6)]$_5$ Cu(3.5) Pt(5). Such a layer is amorphous and must allow the Pt layer to grow according to its close packed planes, that is to say along the [111] direction. At first, the magnetic properties have been measured (figure IV.12).

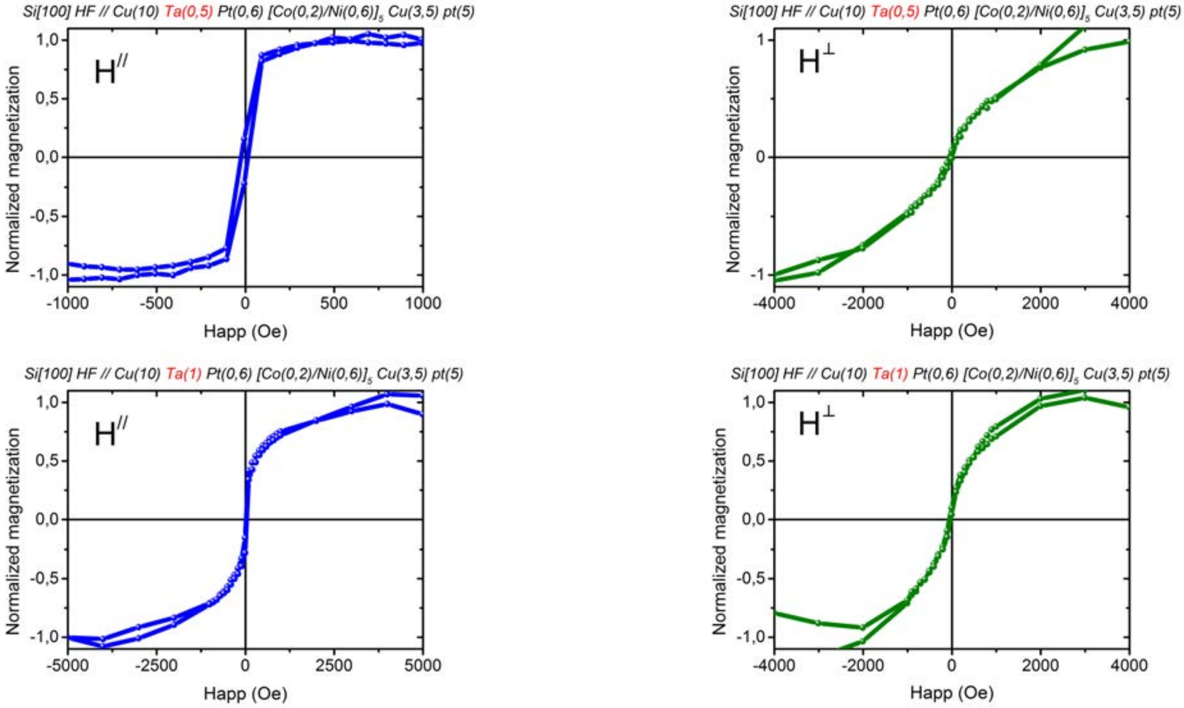

Fig. IV.12: *M(H) loops for $Si[100]HF//Cu(10)Ta(0.5or1)$ $Pt(0.6)[Co(0.2)/Ni(0.6)]_5$ $Cu(3.5)Pt(5)$. The magnetic field is applied parallel (left-hand side) or perpendicular (right-hand side) to the sample plane.*

Once again, PMA does not seem to be clear in those samples. But a clear evolution of the perpendicular anisotropy with the thickness is visible, with a decrease of the saturation field. The saturation field with a field applied perpendicular to the sample plane is equal to 1.5 kOe and 3 kOe with respectively 1nm and 0.5nm of Ta. Furthermore, the in-plane cycles are not square as usual, especially for the Ta(1) structure. With a saturation field in-plane of 5 kOe, it is clear that the magnetisation has an easy axis between the in-plane and the out-of-plane direction. This result shows that the insertion of Ta is a good strategy. XRD experiments have been realised on these two samples to correlate the magnetic behaviours with the crystallographic structures (figure IV.13).

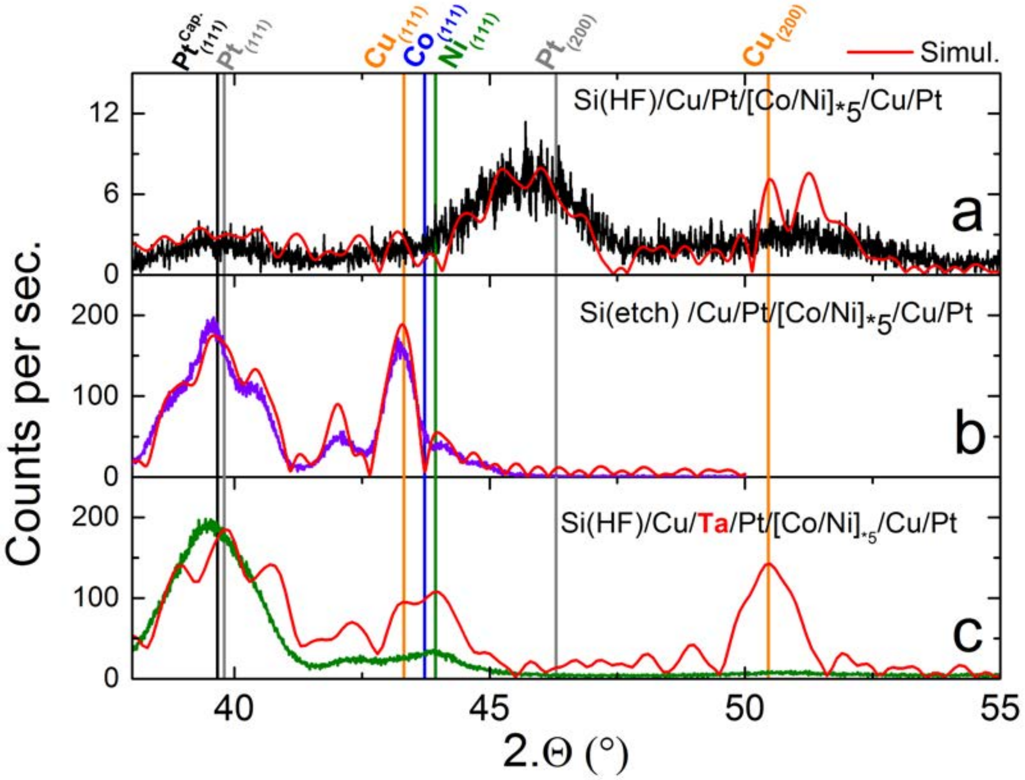

Fig. IV.13: *X-ray diffraction spectra measured in the* ($\Theta - 2\Theta$) *geometry on Si // Cu(10nm) Ta(1nm) Pt(0.6nm)* $[Co(0.2nm)/Ni(0.6nm)]_5$ *Cu(3.5nm)Pt(5nm) made on HF-etched Si oriented [111].*

A very small peak corresponding to the theoretical position of Cu oriented [200] is located close to the position $2\Theta = 51^o$: the Cu grown on the Si substrate is well oriented [200] when the Si surface is cleaned with HF. The peak intensity is in the same order than the Cu[200] one observed for the sample 1 of the first section (figure IV.3a). Thanks to the Ta layer, which is amorphous, the Pt layer grows according to its close packed planes, that is to say along the [111] direction, giving a strong peak at $2\Theta = 39^o$. As a consequence, the following elements of the stack grow in the same crystallographic orientation [111] (several peaks around the position $2\Theta = 43^o$). The simulation on *Mathematica* (red line on the figure) is made by considering that only the Cu layer before the Ta one is oriented [200]. The others layers are expected to be along the [111] direction in the simulation.

This result is in accordance with the magnetic behaviour of the sample, in which the magnetic anisotropy is between in-plane and out-of-plane. In fact, a [Co/Ni] multilayer oriented along the [111] direction must exhibit a PMA [42, 44, 45], but the intensity of the anisotropy strongly depends on the crystallography, on the interface roughness, ...

The intensity of the peaks corresponding to Cu, Co and Ni layers oriented along the [111] direction is smaller than for the sample with an etching of the Si surface (figure IV.15b), in which a PMA is obtained. The Kiessing fringes observed previously are also not visible in this last sample. Thus, the stack has a poorer crystallographic quality. The magnetic anisotropy depending strongly on the roughness and on the quality of the structures, this can explain why the sample does not exhibit an anisotropy constant sufficient to get a full PMA.

Since the magnetic properties are not the ones needed for our study, we decided to stop our research in this direction.

II.C.3 Sample 4: addition of a Ta layer in the middle of the Cu one

The last solution that has been tested is the insertion of the Ta layer in the middle of the Cu layer in contact with the Si substrate. Thus, the second part of the Cu layer could grow on the amorphous Ta layer along the [111] direction and initiate a [111] crystallographic orientation for the multilayer. In a first step, the magnetic behaviour of the Si[100]HF//Cu(5)Ta(1)Cu(5) Pt(0.6)[Co(0.2)/Ni(0.6)]$_5$ Cu(3.5) Pt(5) stack has been checked. The results are shown in the following figure IV.14.

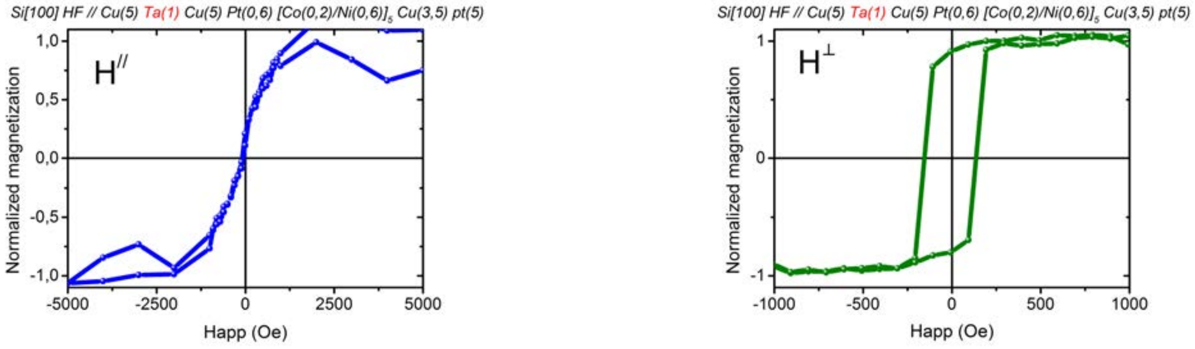

Fig. IV.14: *M(H) loops for* $Si[100]HF//Cu(5)Ta(1)Cu(5)$ $Pt(0.6)[Co(0.2)/Ni(0.6)]_5$ $Cu(3.5)Pt(5)$*. The magnetic field is applied parallel (left-hand side) or perpendicular (right-hand side) to the sample plane.*

In that case, the [Co/Ni] multilayer exhibits a PMA. To corroborate this result with the previous conclusions about the crystallographic structure, XRD experiments have been realised. The spectrum obtained in the Θ/2Θ geometry is shown in the figure IV.15.

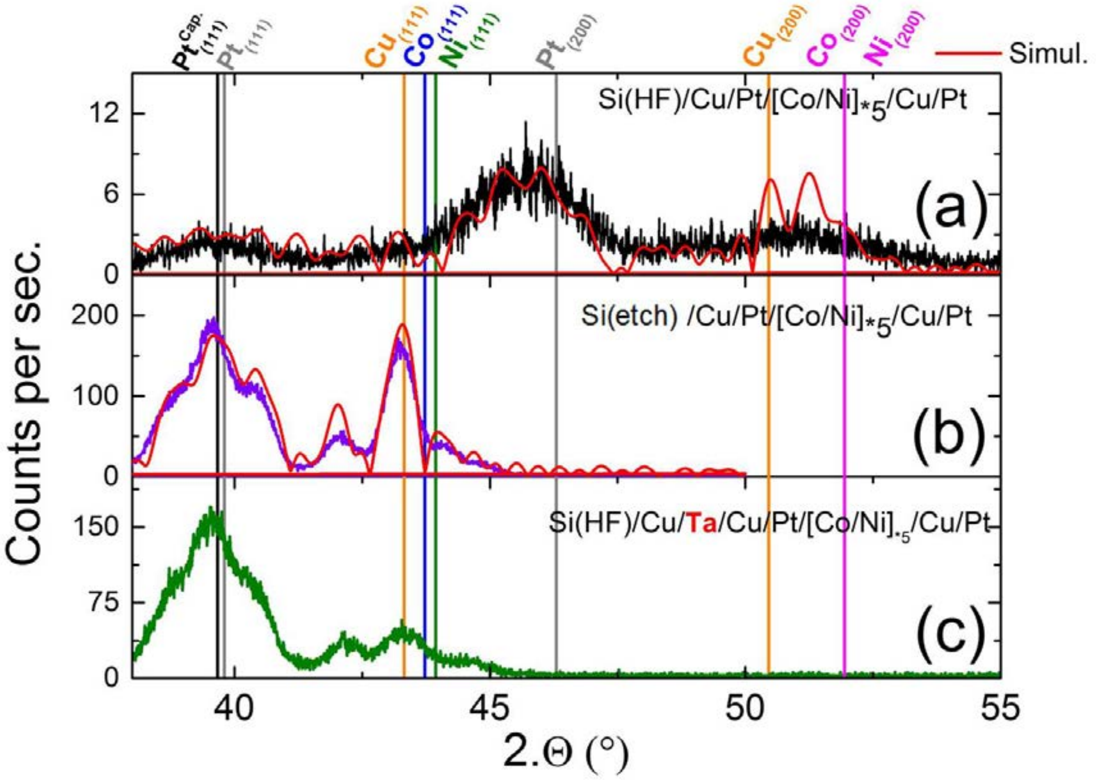

Fig. IV.15: *X-ray diffraction spectra measured in the* $(\Theta - 2\Theta)$ *geometry on (a)* $Si//Cu(10nm)$ $Pt(0.6nm)$ $[Co(0.2nm)/Ni(0.6nm)]_5$ $Cu(3.5nm)Pt(5nm)$ *made on HF-etched Si, (b)* $Si//Cu(10nm)$ $Pt(0.6nm)$ $[Co(0.2nm)/Ni(0.6nm)]_5$ $Cu(3.5nm)Pt(5nm)$ *made on Ar-etched Si, (c)* $Si//Cu(5nm)$ $Ta(1nm)$ $Cu(5nm)$ $Pt(0.6nm)$ $[Co(0.2nm)/Ni(0.6nm)]_5$ $Cu(3.5nm)Pt(5nm)$ *made on HF-etched Si. The theoretical spectra (continuous lines) and especially the peak positions are in close agreement with the experiment.*

In figure IV.15, the X-ray diffraction spectrum measured in the $(\Theta - 2\Theta)$ geometry on sample 4 has been added to figure IV.4. The spectrum is very close to the one measured on the sample Si[100](etch)//Cu(10) Pt(0.6) $[Co(0.2)/Ni(0.6)]_5$ Cu(3.5) Pt(5), composed of well defined peaks that can be attributed to Pt[111] and Cu[111] while the multilayer is grown on Si[100](HF)//Cu. The peak intensities are high, slightly smaller than for Si[100](etch)//Cu(10) Pt(0.6) $[Co(0.2)/Ni(0.6)]_5$ Cu(3.5) Pt(5) but really higher than for Si[100](HF)//Cu(10) Ta(1) Pt(0.6) $[Co(0.2)/Ni(0.6)]_5$ Cu(3.5) Pt(5) in figure IV.13, demonstrating a good enough crystallographic quality to have a PMA.

Once again, the XRD measurement (figure IV.15) corroborates the hypothesis about the link between PMA and a [111] texture of the multilayer as found in the literature [42, 44, 45]. The insertion of a thin layer of Ta ($\sim nm$) allows us to retrieve a PMA while keeping the structure of the Schottky diode optimised in the past. In fact, the thin amorphous layer of Ta allows the Cu layer to grow according to its close packed planes, that is to say along the [111] direction. In the XRD spectra, it is not clear if a part of the Cu layer is [200] oriented in this last sample. Therefore, a Transmission Electrons Microscopy (*TEM*) study has been done and a characteristic picture is reported in figure IV.16. It shows that the Cu layer is oriented along the [200] direction before the Ta layer and along the [111] direction after the amorphous Ta layer.

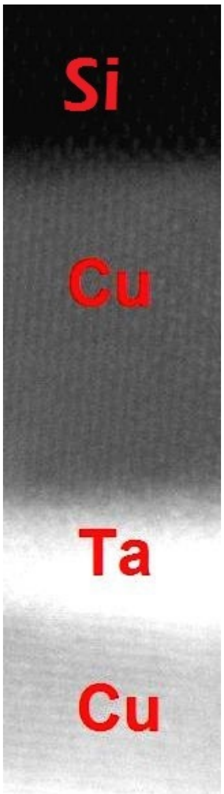

Fig. IV.16: *TEM picture of the sample* $Si[100](HF)//Cu(5nm)\ Ta(1nm)\ Cu(5nm)\ Pt(0.6nm)\ [Co(0.2nm)/Ni(0.6nm)]_5\ Cu(3.5nm)Pt(5nm)$. *Cu is oriented along the [200] direction before the Ta amorphous layer and along the [111] direction after.*

As a final test of our structure, the Schottky barrier is tested in the MTT geometry (figure IV.17). The threshold is well defined for that sample (with the Ta insertion and a HF treatment of the Si surface), as it can be in the sample without the Ta layer which does not exhibit a PMA. One can notice here that after the threshold, the collected current is smaller than for the sample without the Ta layer. In fact, it seems to be normal since an additional layer is added to the structure and contributes to the hot electron diffusion and so lowers the collected current. Thus, this Ta layer must be as small as possible in order to keep a current strong enough to be detected.

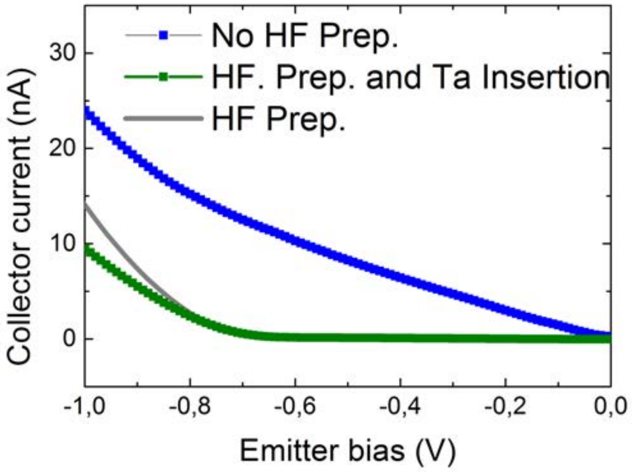

Fig. IV.17: *Schottky characteristic of the Si/Cu interface in the case of a HF cleaning of the Si substrate (grey curve) or with an Ar ions etching before deposition (blue curve). The Ta insertion allows us to keep the HF treatment (grey curve).*

In conclusion of this second section, the insertion of a thin Ta layer (1 nm) in the middle of the 10nm thick Cu layer ensures the [111] texture in order to get a PMA while keeping a good Schottky diode [52]. In the following, a study of the magnetic behaviour of such multilayers is made as a function of different parameters (number of repetitions of the multilayer or nature of the element at the interface with Cu).

III. Optimisation of the multilayer stack

As presented before, the [Co/Ni] multilayer is chosen as the layer that plays the role of the analyser in the MTT. Mandatory properties are a perpendicular magnetic anisotropy and a high spin polarisation. Moreover, the level of the collected current, in the nA or pA range, which depends strongly on the materials but also on the number of interfaces, is another important experimental parameter to be optimised for our experiment. As a first step, a study of the magnetic properties as a function of the number of repetitions is necessary. If the PMA is conserved over a large number of repetitions, a study of the magneto-current as a function of the number of repetitions will be interesting to measure the spin filtering efficiency of [Co/Ni]. Secondly, it has been shown in previous studies that the properties of [Co/Ni] [44] strongly depend on the temperature of annealing. For the technological process that enables the nanostructuration of the multilayer stack for transport measurements, a temperature of 140^oC is necessary to anneal the resin used for lithography. To pin the ferromagnetic layer that spin polarises the hot electron current, another annealing of 200^oC during 1 hour is also required. Thus, the thermal stability of the magnetic properties must be checked. Finally, the stability of PMA with respect to the ferromagnetic material in contact with the Cu layer will be also verified.

III.A. Magnetic properties versus number of repetitions

In this first part, we focus our study on the magnetic stability with the number of repetitions of the multilayer. In addition to the study as a function of the number of repetitions, two thicknesses of Ta have been tried ($0.5nm$ and $1nm$). If the thickness of Ta is too low, there is a risk of a non-continuous layer. If the thickness is too large, the hot electron current will be reduced as shown in figure IV.17

	Substrate and Buffer	**Stacking**	**Capping**
Sample 1	$Si[100]HF$ // $Cu(5)\ Ta(0.5)\ Cu(5)$	$[Co(0.2)/Ni(0.6)]_2$	$Cu(3.5)\ Pt(5)$
Sample 2	$Si[100]HF$ // $Cu(5)\ Ta(0.5)\ Cu(5)$	$[Co(0.2)/Ni(0.6)]_3$	$Cu(3.5)\ Pt(5)$
Sample 3	$Si[100]HF$ // $Cu(5)\ Ta(0.5)\ Cu(5)$	$[Co(0.2)/Ni(0.6)]_4$	$Cu(3.5)\ Pt(5)$
Sample 4	$Si[100]HF$ // $Cu(5)\ Ta(0.5)\ Cu(5)$	$[Co(0.2)/Ni(0.6)]_5$	$Cu(3.5)\ Pt(5)$
Sample 5	$Si[100]HF$ // $Cu(5)\ Ta(1)\ Cu(5)$	$[Co(0.2)/Ni(0.6)]_2$	$Cu(3.5)\ Pt(5)$
Sample 6	$Si[100]HF$ // $Cu(5)\ Ta(1)\ Cu(5)$	$[Co(0.2)/Ni(0.6)]_3$	$Cu(3.5)\ Pt(5)$
Sample 7	$Si[100]HF$ // $Cu(5)\ Ta(1)\ Cu(5)$	$[Co(0.2)/Ni(0.6)]_4$	$Cu(3.5)\ Pt(5)$

Table 4.2: **Description of the different [Co/Ni] multilayers investigated to decrease the number of repetitions while keeping PMA.**

As said before, the level of the collected current in our MTT determines the quality of the measurement, especially when the current is in the nA-pA range. Nevertheless, the MC in the magnetic tunnel transistor fixes the sensitivity of the measurement. If the MC is high, the direction of the electronic spin can be measured precisely. In the aim to maximise the MC, the thickness of the ferromagnetic layer can be simply increased, which leads to the multiplication of the number of repetitions in the case of [Co/Ni] multilayers. Unfortunately, each interface decreases strongly the current. A golden mean between a strong MC and a low collected current must be found. In order to study this specific point, multilayers have to keep the PMA regardless the number of repetitions. The influence of this parameter on the magnetic properties is shown in the figure IV.18.

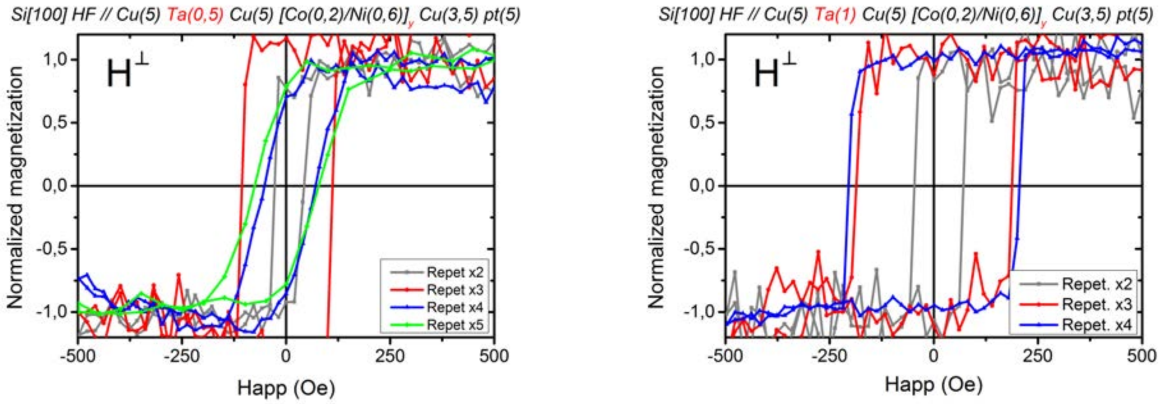

Fig. IV.18: *M(H) loops for different numbers of repetitions of the [Co/Ni] multilayer with an applied magnetic field perpendicular to the sample plane, measured with a Kerr microscope. The Ta thickness equals to* 0.5*nm on the left-hand side and* 1*nm on the right-hand side.*

With 0.5nm of Ta, the anisotropy begins to switch towards the sample plane from 4 repetitions of the [Co(0.2)/Ni(0.6)] multilayer. When the Ta thickness increases from 0.5nm to 1nm, the PMA is stabilised up to 4 repetitions of the multilayer. As said before, a 0.5nm thick Ta layer is a mono-layer, and there is a risk that the layer is not continuous. On the contrary, 1nm of Ta has more chance to be continuous and therefore to ensure the growth of continuous layers, that could explain the difference in the magnetic properties.

Another important point is the stability with the temperature. In fact, the technological process that shapes the sample for transport measurements in the clean room requires some annealing. The stability of the magnetic properties, in particular of the PMA, must be checked. The M(H) loops have been measured on the same series of samples (0.5 or 1nm of Ta and a number of repetitions between 1 and 5) which has suffered the same cycle of annealing than during the patterning process (several annealing steps at 115^oC or 140^oC during one or two minutes) and the annealing at 200^oC necessary to pin the top ferromagnetic layer of the MTT. The results for samples with 1 and 2 repetitions are shown in the figure IV.19.

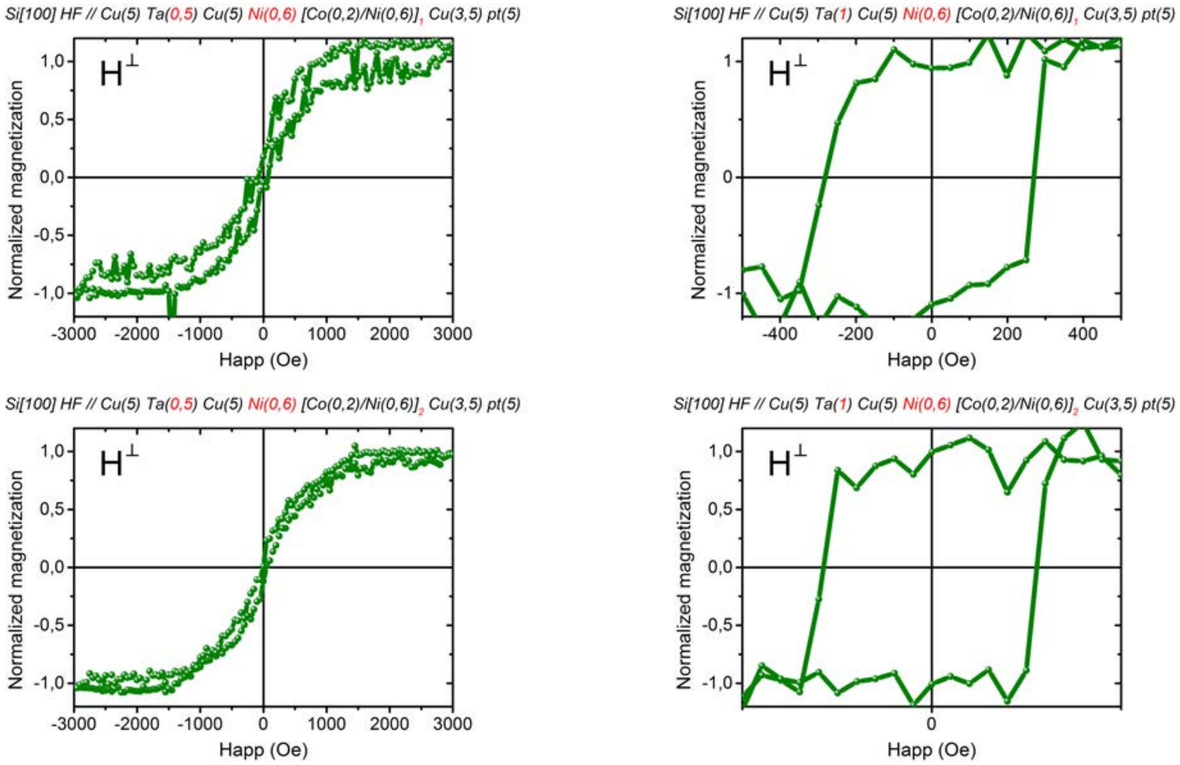

Fig. IV.19: M(H) loops for one (top) or two (bottom) number of repetitions of the [Co/Ni] multilayer after annealing, with a magnetic field applied perpendicular to the sample plane. The Ta thickness equals to 0.5nm on the left-hand side and 1nm on the right-hand side.

One can immediately notice here that when there is only 0.5nm of Ta, the sample becomes magnetised in-plane after the annealing cycle. As a consequence, these samples cannot be integrated in the MTT to measure the electronic spin precession. For a 1nm thick Ta, all samples with repetitions between 1 and 5 remains perpendicular. In the final structure, a 1nm thick Ta layer will be used.

III.B. Magnetic properties versus nature of the interfaces with Cu

As seen in the previous chapter, PMA appears mainly thanks to the surface or interface anisotropy in thin films. The nature of the magnetic layer starting or ending the [Co/Ni] multilayer may influence the magnetic anisotropy. Moreover, the spin polarisation depends also on the interfaces. Recent photo-emission experiments have shown that a [Co/Ni] [111] superlattice has a higher spin polarisation when the multilayer is finished with a Co layer [53]. Thus, samples with only Cu/Co interfaces have been grown (see table below).

	Substrate and Buffer	**Stacking**	**Capping**
`Sample 1`	$Si[100]HF$ // $Cu(5)$ $Ta(0.5)$ $Cu(5)$	$[Co(0.2)/Ni(0.6)]_3$ $Co(0.2)$	$Cu(3.5)$ $Pt(5)$
`Sample 2`	$Si[100]HF$ // $Cu(5)$ $Ta(0.5)$ $Cu(5)$	$[Co(0.2)/Ni(0.6)]_4$ $Co(0.2)$	$Cu(3.5)$ $Pt(5)$
`Sample 3`	$Si[100]HF$ // $Cu(5)$ $Ta(1)$ $Cu(5)$	$[Co(0.2)/Ni(0.6)]_3$ $Co(0.2)$	$Cu(3.5)$ $Pt(5)$
`Sample 4`	$Si[100]HF$ // $Cu(5)$ $Ta(1)$ $Cu(5)$	$[Co(0.2)/Ni(0.6)]_4$ $Co(0.2)$	$Cu(3.5)$ $Pt(5)$

Table 4.3: **Description of the different [Co/Ni] multilayers investigated with only Cu/Co interfaces.**

Measurements of the magnetic properties of theses samples are shown in figure IV.20.

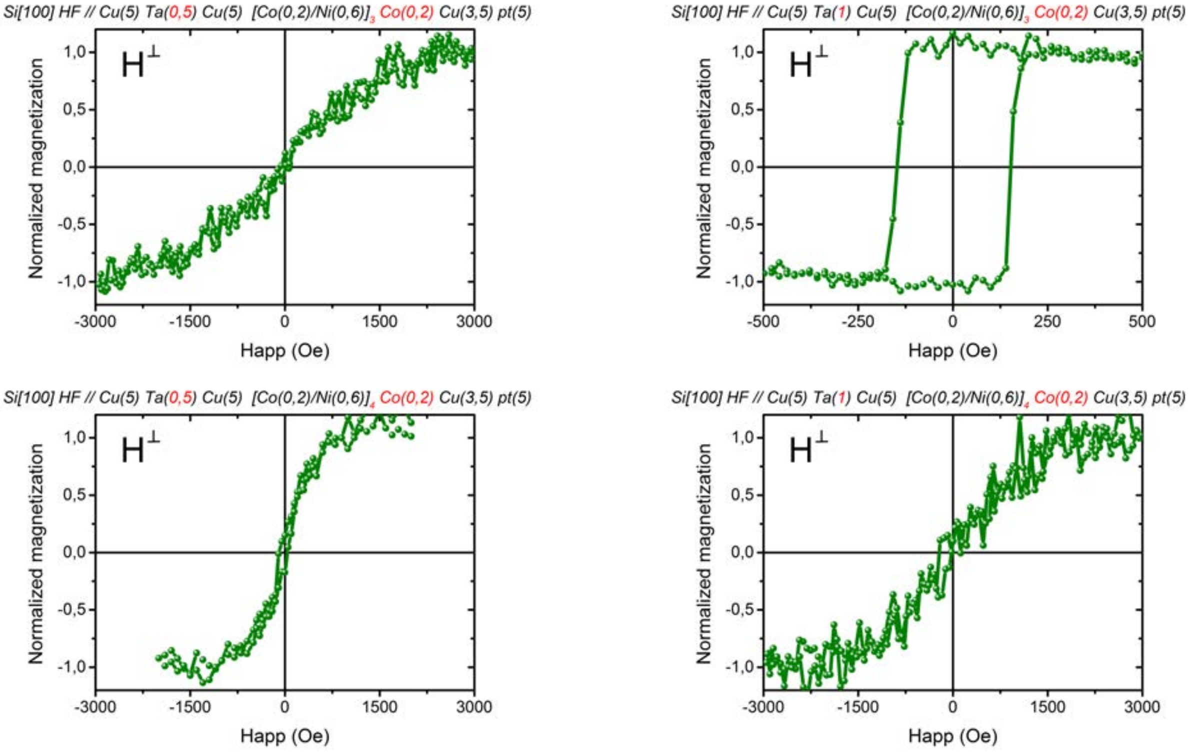

Fig. IV.20: *M(H) loops for samples with only Co/Cu interfaces. The Ta thickness is 0.5nm on the left-hand side and 1nm on the right-hand side.*

The addition of a Co layer after the multilayer seems to destabilise the PMA. With 0.5nm of Ta, the anisotropy lies in the sample plane regardless of the number of repetitions (3 or 4). With 1 nm of Ta, the PMA is maintained with 3 repetitions of the multilayers, but not with 4 repetitions. The influence of the Ta thickness is in accordance with the one observed in the previous section: the PMA is stronger with 1nm of Ta. Finally, these multilayers with a Co(0.2) end cannot be integrated in our MTT, having not a PMA for a large range of numbers of repetitions.

A Cu/Co interface destabilising the PMA in comparison with a Cu/Ni interface, samples with only Cu/Ni interfaces have then been made (see table below).

	Substrate and Buffer	**Stacking**	**Capping**
`Sample 1`	$Si[100]HF$ // $Cu(5)$ $Ta(0.5)$ $Cu(5)$	$Ni(0.6)$ $[Co(0.2)/Ni(0.6)]_1$	$Cu(3.5)$ $Pt(5)$
`Sample 2`	$Si[100]HF$ // $Cu(5)$ $Ta(0.5)$ $Cu(5)$	$Ni(0.6)$ $[Co(0.2)/Ni(0.6)]_2$	$Cu(3.5)$ $Pt(5)$
`Sample 3`	$Si[100]HF$ // $Cu(5)$ $Ta(0.5)$ $Cu(5)$	$Ni(0.6)$ $[Co(0.2)/Ni(0.6)]_3$	$Cu(3.5)$ $Pt(5)$
`Sample 4`	$Si[100]HF$ // $Cu(5)$ $Ta(1)$ $Cu(5)$	$Ni(0.6)$ $[Co(0.2)/Ni(0.6)]_1$	$Cu(3.5)$ $Pt(5)$
`Sample 5`	$Si[100]HF$ // $Cu(5)$ $Ta(1)$ $Cu(5)$	$Ni(0.6)$ $[Co(0.2)/Ni(0.6)]_2$	$Cu(3.5)$ $Pt(5)$
`Sample 6`	$Si[100]HF$ // $Cu(5)$ $Ta(1)$ $Cu(5)$	$Ni(0.6)$ $[Co(0.2)/Ni(0.6)]_3$	$Cu(3.5)$ $Pt(5)$
`Sample 7`	$Si[100]HF$ // $Cu(5)$ $Ta(1)$ $Cu(5)$	$Ni(0.6)$ $[Co(0.2)/Ni(0.6)]_4$	$Cu(3.5)$ $Pt(5)$
`Sample 8`	$Si[100]HF$ // $Cu(5)$ $Ta(1)$ $Cu(5)$	$Ni(0.6)$ $[Co(0.2)/Ni(0.6)]_5$	$Cu(3.5)$ $Pt(5)$

Table 4.4: **Description of the different [Co/Ni] multilayers investigated with only Cu/Ni interfaces.**

Measurements of the magnetic properties of theses samples are shown in figure IV.21.

The Ni/Cu interfaces clearly stabilise the anisotropy out of the plane. The sample has a PMA either with 0.5nm of Ta from 1 to 3 repetitions or with 1nm of Ta from 1 to 5 repetitions. Nevertheless, the magnetic anisotropy is in the sample plane when the number of repetitions exceeds 6 (figure IV.22).

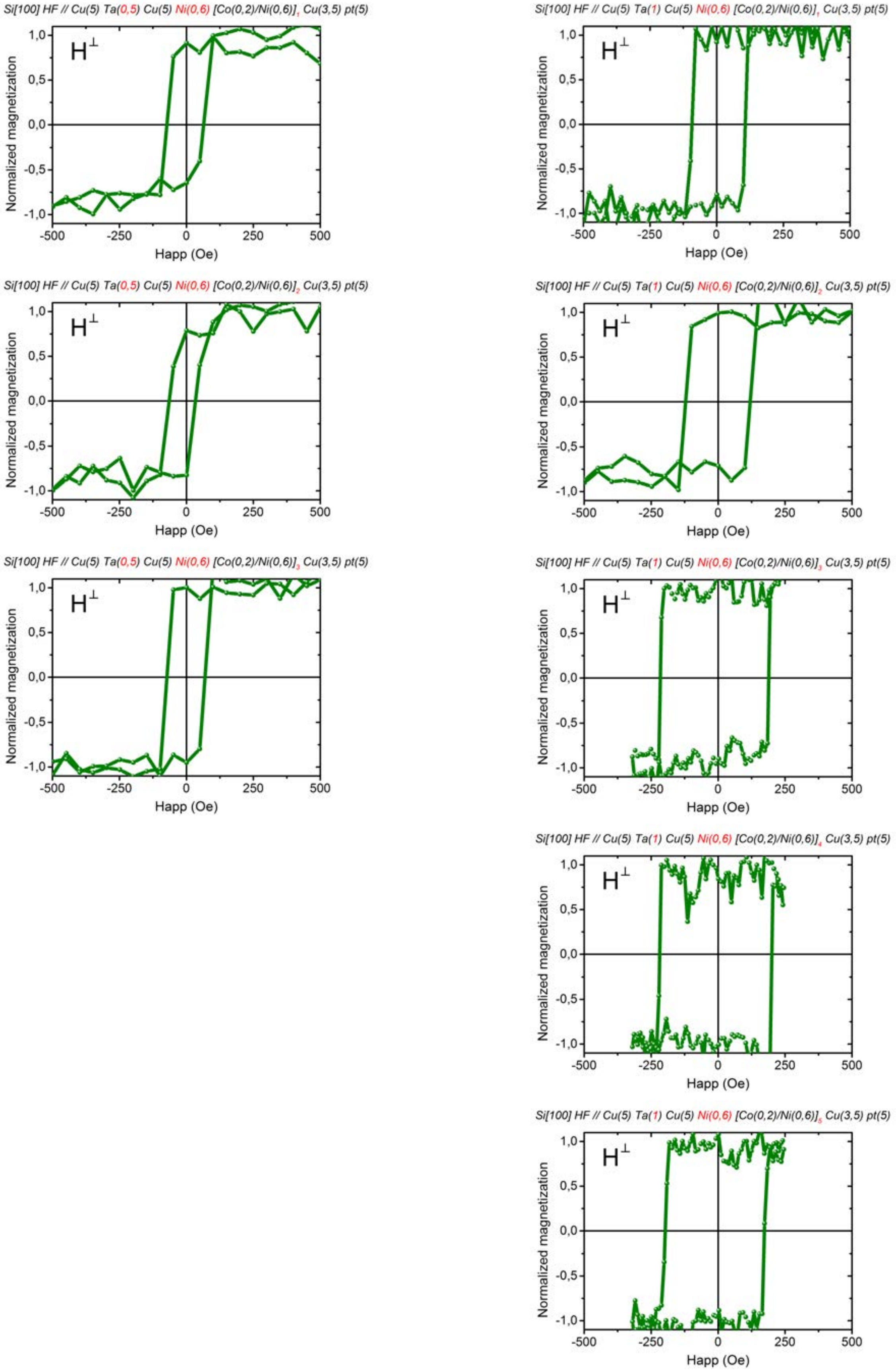

Fig. IV.21: *M(H) loops with a perpendicular field for samples with only Ni/Cu interfaces. Ta thickness is 0.5nm on the left-hand side and 1nm on the right-hand side.*

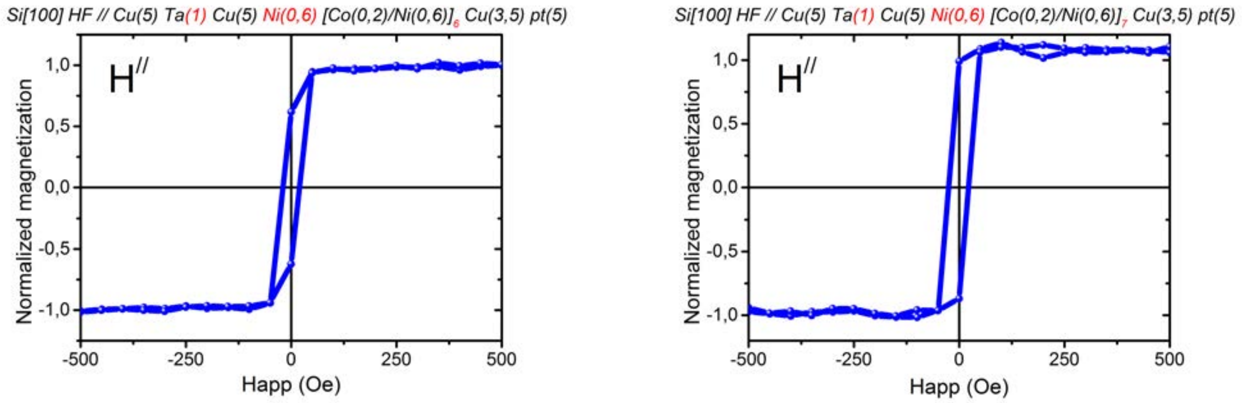

Fig. IV.22: M(H) loops of samples with only Ni/Cu interfaces. The magnetic field is applied in the sample plane and the Ta thickness equals to 1nm. The number of repetitions of the [Co/Ni] multilayer is 6 on the left-hand side and 7 on the right-hand side.

The values of the coercive field H_c and the magnetisation at saturation M_s are extracted from the in-plane M(H)loops. Thus, the effective anisotropy $Keff = \mu_0 M_s H_{Keff}/2$ can be calculated as a function of the number of repetitions (figure IV.23).

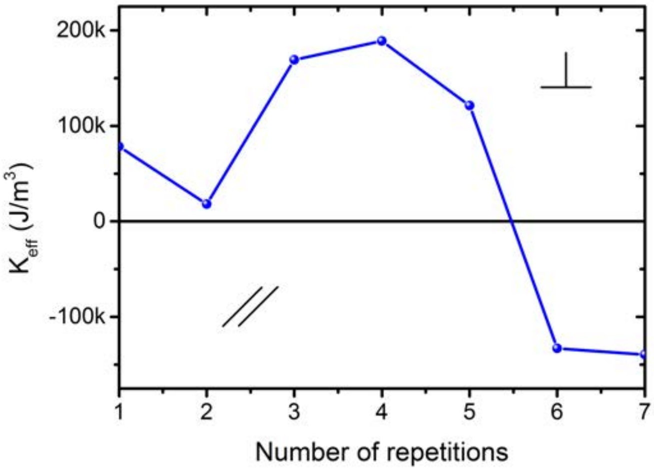

Fig. IV.23: Evolution of the effective magnetic anisotropy as a function of the number of repetitions of the Co/Ni multilayer.

Finally, with the addition of a Ni layer before the multilayer, a PMA is obtained for a number of repetitions going from 1 to 5. As seen before, it is preferable to have a layer of Ta 1nm thick in order to avoid that the magnetic anisotropy switches in the sample plane during the patterning process in the clean room or during the annealing process to set the exchange bias of the top layer. The final structure selected is:

Si[100](HF) // Cu(5)Ta(1)Cu(5) Ni(0.6) [Co(0.2)/Ni(0.6)]$_{1-5}$ Cu(3.5nm)...

IV. Conclusion

In this chapter, the addition of a thin Ta layer in Cu has been demonstrated to be a suitable solution to obtain a [Co/Ni] multilayer that exhibits a PMA while keeping a good Schottky characteristic. This result was obtained by combining VSM measurements and X-ray diffraction. The multilayer must be oriented along the [111] direction. Thus, the insertion of a Ta layer, which is amorphous, allows the Cu to grow according to its closed packed planes, that is to say [111]. As a consequence, the multilayer is also oriented along the [111] direction, which is a *sine qua non* condition to obtain a PMA.

We have demonstrated also that Ni/Cu interfaces favoured a PMA compared to Co/Cu ones. The Ta thickness plays also a role on the quality of the crystallographic orientation of the stack: 1 nm of Ta is more convenient to obtain a PMA, even after the annealing of the sample necessary to pin the top layer. Finally, the number of repetitions of the multilayer can increase up to 5 (with 1nm of Ta) in order to keep PMA. The final composition of the stack with a Schottky diode and a layer which exhibits PMA is the following:

$$Si[100]HF\ //\ Cu(5)\ Ta(1)\ Cu(5)\ Ni(0.6)\ [Co(0.2)/Ni(0.6)]_{1-5}\ Cu(3.5)\ Pt(5)$$

Résumé du chapitre :

Pour mesurer la précession du spin de l'électron dans un matériau ferromagnétique grâce à un transistor tunnel magnétique (TTM), il faut absolument qu'une couche de la vanne de spin possède une anisotropie magnétique perpendiculaire. Nous avons vu au chapitre précédant que plusieurs paramètres influencent l'anisotropie magnétique, telle la qualité structurale ou l'orientation cristallographique. Dans ce chapitre, nous nous concentrons sur une multicouche de cobalt et de nickel. En effet, il a été montré dans la littérature qu'une telle multicouche exhibe une anisotropie perpendiculaire sous certaines conditions. Il faut que le rapport des épaisseurs t_{Ni}/t_{Co} soit supérieur à 2 et que la multicouche soit orientée selon la direction cristallographique [111].

Dans un premier temps, nous avons montré en combinant des expériences de rayons X et des mesures de magnétométrie que la préparation du substrat, de première importance pour obtenir une diode Schottky de qualité, a un impact considérable sur l'anisotropie magnétique. En effet, la diode Schottky joue le rôle de filtre en énergie dans notre TTM. Pour avoir les caractéristiques électriques compatibles avec son rôle, il faut nécessairement que le substrat de Si[200] soit débarrassé de sa couche d'oxyde en surface par un nettoyage chimique à l'acide fluorhydrique. Cependant, cela ne permet pas la croissance d'une multicouche [Co/Ni] dans la direction [111]. D'un autre côté, en enlevant la couche d'oxyde par bombardement cathodique avant le dépôt, la multicouche est orientée dans la direction [111] et exhibe une anisotropie perpendiculaire.

Dans un deuxième temps, nous avons cherché une solution pour orienter la multicouche dans la direction [111] tout en gardant le nettoyage chimique à l'acide fluorhydrique de notre substrat de Si[200]. Diverses solutions ont été testées, avec notamment l'ajout d'une fine couche de Ta amorphe. La solution la plus efficace a été d'ajouter 1nm de Ta au milieu de la couche de Cu sur le Si. En effet, cette fine couche de Ta amorphe permet au cuivre supérieur de croître selon ses plans denses, qui sont dans la direction [111]. Ainsi, l'ensemble de l'échantillon, et en particulier la multicouche de [Co/Ni], croît dans la même direction.

Dans un troisième temps, l'influence du nombre de répétition sur l'anisotropie magnétique a été étudiée. Nous avons montré que l'anisotropie commence à basculer dans le plan pour 4 répétitions de la multicouche. Nous avons également vu que les échantillons ne comportant que 0.5nm de Ta voyaient leur anisotropie basculer dans le plan de l'échantillon lors de la nanostructuration en salle blanche nécessaire aux expériences de transport.

Enfin, l'influence de la nature de l'interface entre le Cu et la multicouche sur l'anisotropie a été démontrée. Alors que des interfaces Cu/Co sont prédites à donner une plus grande polarisation en spin, l'anisotropie magnétique est clairement stabilisée hors du plan pour des interfaces Cu/Ni. Ainsi, l'ajout d'une couche de Ni avant la multicouche [Co/Ni] permet d'avoir une anisotropie perpendiculaire pour un nombre de répétition allant de 1 à 5. La multicouche retenue finalement, et qui sera commune à tous nos échantillons à partir de maintenant, est :

$$Si[100]HF \; // \; Cu(5) \; Ta(1) \; Cu(5) \; Ni(0.6) \; [Co(0.2)/Ni(0.6)]_{1-5} \; Cu(3.5) \; Pt(5)$$

Chapter 5

Magnetic properties of a CoAl alloy

The goal of this chapter is to present a magnetic study made on alloys of cobalt and aluminium. In order to strengthen our results of spin precession in Co and CoFeB, we have decided to use a magnetic layer in which the molecular field varies with the temperature in our range of work (between 30K and 100K). We focus our attention on an alloy between a metal and a ferromagnetic layer. For the metal, our first choice was the use of Al. Indeed, alloys called transition metal aluminides (CoAl, NiAl, FeAl) are known to have a paramagnetic-ferromagnetic transition for compositions close to 50% of Al [54].

The first section of this chapter explains why we have used a CoAl alloy in our MTT, in particular by reviewing the existing experimental works on such an alloy. Because of the lack of complete experimental studies on CoAl alloys, especially for alloys that are paramagnetic at room temperature, the magnetic behaviours at room temperature for a composition above 60% of Co and at low temperature below 60% of Co have been studied in the second and third section.

I. Introduction

As seen in the first chapter, when a magnetic moment is in presence of a magnetic field, two phenomena happen: the spin filtering, which tends to align the magnetic moment with the direction of the field, and a precession motion. In both cases, the magnitude of the effect depends on the value of the magnetic field. One of our objectives is to study the electronic spin precession in a magnetic material which has a Curie temperature close to the working temperature of the MTT in order to see the variation of the precession angle with the internal field.

The choice of the alloy was first driven by the possibilities offered with our sputtering system. In particular, alloys between aluminium and a transition metal (TM), like Co and Ni, was possible. Such compounds are called transition metal aluminides, and have been studied at first by Butler *et al.* in 1669 [54]. In their experiments, they have measured the electrical resistivity, the thermoelectric power, and the magnetic susceptibility or magnetisation at room temperature, with a composition range of $49 - 51\%$ of Al for NiAl and $42 - 54\%$ of Al for CoAl. They have experimentally shown on the one hand that a CoAl alloy is ferromagnetic if the proportion of Al is smaller than 49% (left-hand side of figure V.1) and on the other hand that a NiAl alloy is paramagnetic regardless of the composition between 49% and 51% of Al. The saturation moment per excess cobalt atom is between 1.5 and $2.5\mu_B$ for the data between 42 and 49.0% of Al.

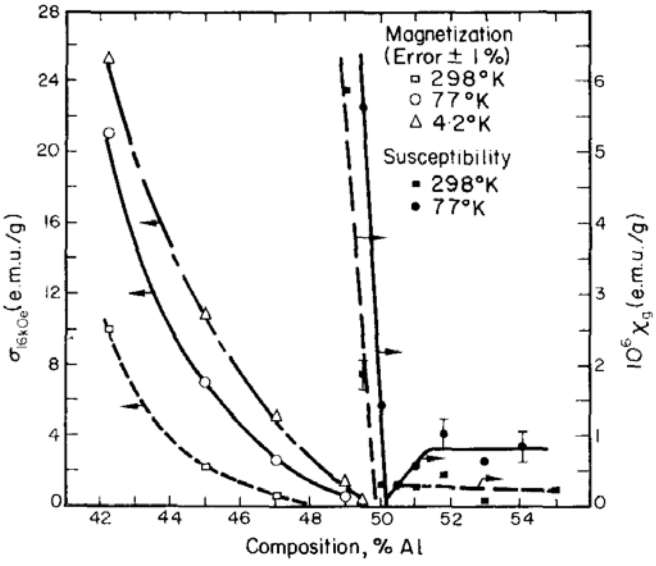

Fig. V.1: Magnetic susceptibility and saturation magnetisation of CoAl samples. The alloy is ferromagnetic only for composition with an excess of Co.

They have developed also a simplified electron energy band scheme to explain their results, with a broad hybrid s-p band and several narrow d-bands formed from transition metal atomic orbitals. All these binary compounds have a simple b.c.c. (body centered cubic) structure with Al at the body center of the cube formed by eight TM atoms (figure V.3). As a consequence, the nearest neighbour of a TM atom is an aluminium atom when the alloy is in a stoichiometric composition. The TM giving 2 electrons to the sp-band, the filling of the d-band is t^6e^1 for Co and t^6e^2 for Ni. In the case of a non-stoichiometric composition, with an excess of TM, Al atoms are replaced in the crystal by TM atoms. This re-positions the e-level of the wrong TM (those in the Al unit cell), giving a net magnetic moment of $2\mu_B$ per wrong Co atoms (t^6e^2 d-band), while no ferromagnetism is observed for NiAl (d-band t^6e^4 for the wrong Al atoms). Figure V.2 shows the filling of the sp-band and d-band in the case of a stoichiometric composition (A) and in the case of a non-stoichiometric composition (B).

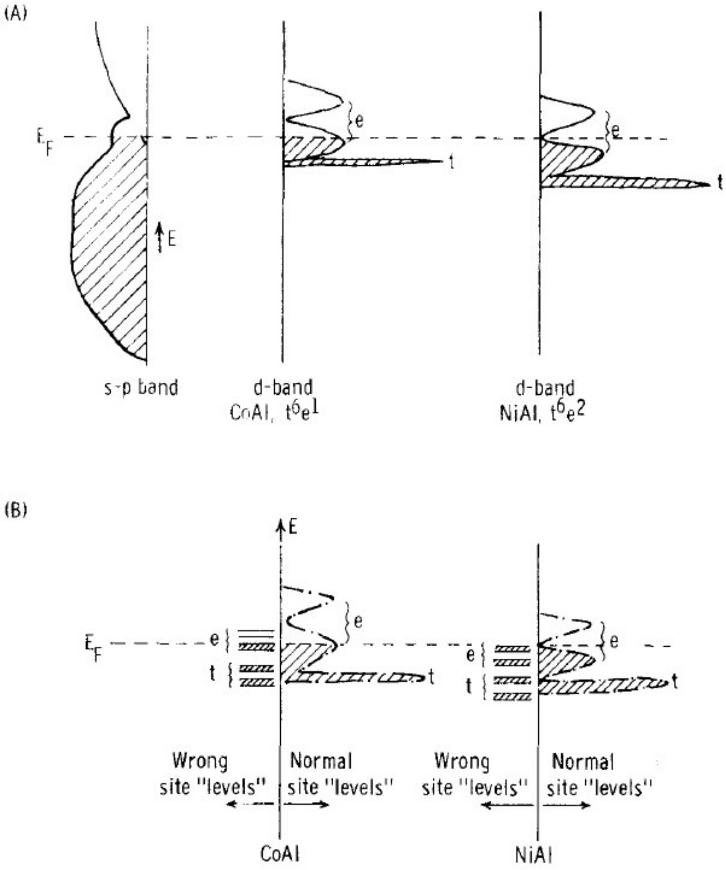

Fig. V.2: *Density of states for NiAl and CoAl. (A) In the case of a stoichiometric composition. (B) In non-stoichiometric compositions. The positions of the d-levels of wrong transition metal atoms (which occupy Al atom sites) are especially indicated.*

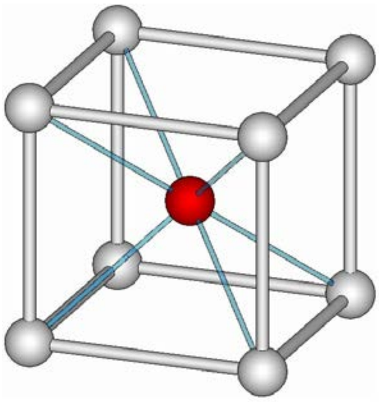

Fig. V.3: Scheme of a b.c.c. structure. The Al atom (in red) is surrounded by 8 TM atoms (in grey).

These results are in agreement with the electronic structure calculations of Sundararajan *et al.* made during the nineties [55]. In this study, they have worked only on an alloy which has a stoichiometric composition, and they have shown that only a FeAl alloy is ferromagnetic at the stoichiometric composition. In their calculation, the magnetism of pure elements Ni and Co is quenched in the alloy, whereas every Fe atoms retains a magnetic moment of $0.7\mu_B$. This explains why, in the study of Butler, they have found that the CoAl alloy is ferromagnetic only if the proportion of Al is smaller than 49%.

Finally, we have chosen to work on alloys between aluminium and cobalt. Indeed, even if Fe offers a larger range of composition in which the alloy is ferromagnetic, in particular in the stoichiometric composition, there is a lot of experimental difficulties linked to the deposition of Fe, like a rapid oxidation. The transition metal aluminide grown with Ni has not the magnetic properties wanted for our study, being paramagnetic. However, no complete experimental study can be found in the literature about CoAl alloys. We are especially interested in a composition with which the alloy has a paramagnetic-ferromagnetic transition for a temperature in the working range of our MTT (between 30 and 100K). Therefore, an experimental study is necessary. The next section shows our experimental work to determine the critical composition that gives a ferromagnetic behaviour to the alloy at room temperature.

II. Magnetic properties of CoAl alloys at room temperature

In this section, the magnetic behaviour of CoAl alloys at room temperature is studied. The composition of the alloys goes from 60% to 93% of Co, with a total thickness of 40nm. The alloy is grown on a Pt layer which is oriented along the [111] direction thanks to an amorphous Ta layer on top of the substrate. This allows the alloy to grow in the same condition that in the MTT, where the stack has to be oriented along the [111] direction because of the [Co/Ni] multilayer (see previous chapter). M(H) loops have been measured for each sample at room temperature, and the results are shown in the figure V.4.

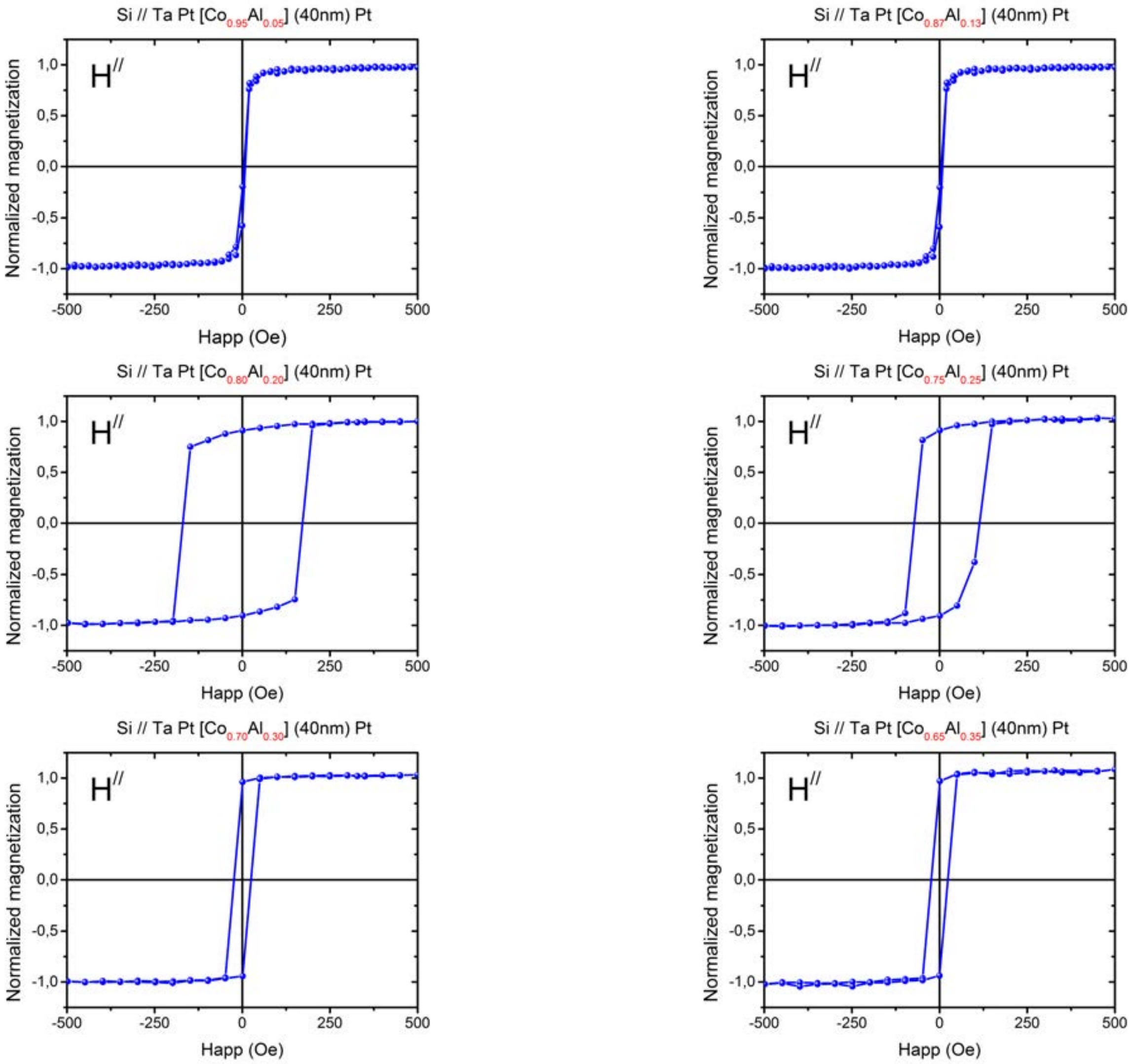

Fig. V.4: *M(H) loops measured at room temperature with an applied field in the sample plane. The percentage of Co varies between 95% (up left) and 65% (bottom right).*

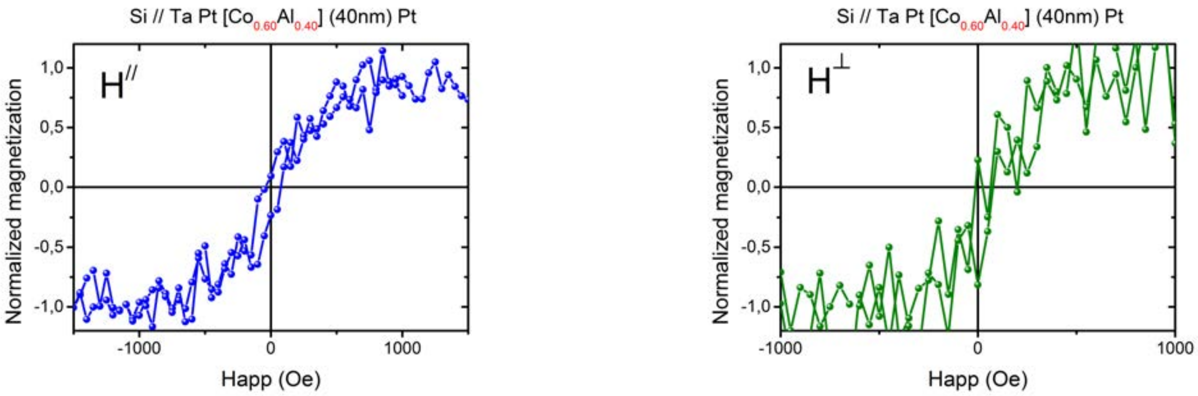

Fig. V.5: *M(H) loops at room temperature for an alloy with 60% of Co and 40% of Al. The magnetic field is applied in the sample plane on the left-hand side and perpendicular to the sample plane on the right-hand side.*

These figures show a ferromagnetic behaviour of the CoAl alloys for compositions with more than 65% of Co. The alloy is paramagnetic at room temperature with 60% of Co. These results are a little bit different from the ones obtained by Butler *et al.* [54], in which they have found that a CoAl alloy is ferromagnetic at room temperature as soon as there is more than 50% of Co. However, no information is given about their growth condition and about the crystallography of their samples, and as seen in the chapter III, these parameters have an influence on the magnetic anisotropy.

The magnetisation at saturation M_s is extracted from the previous M(H) cycles. The figure V.6 shows the variation of M_s with the percentage of Co in the alloy.

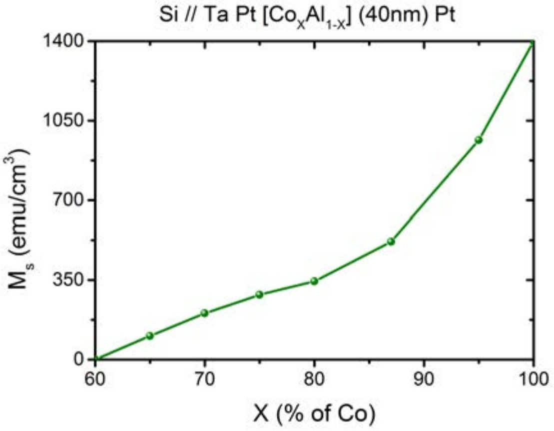

Fig. V.6: *Magnetisation at saturation as a function of the percentage of Co. Data taken at room temperature.*

As expected, the magnetisation at saturation increases with the percentage of Co. The magnetisation at saturation of a pure Co layer was added in the curve at the theoretical value of $1400 emu/cm^3$. This additional point is in great consistency with the tendency of the curve.

Since an alloy with a transition para-ferromagnetic between 30K and 100K is looked for, samples with Co concentration lower than 60% have been studied.

III. Magnetic properties of CoAl alloys as a function of the temperature

As seen in the previous section, CoAl alloys are paramagnetic at room temperature for a proportion of Co under 60%. For our study, an alloy with a paramagnetic-ferromagnetic transition that happens in the working range of temperature of our magnetic tunnel transistor, that is to say between 30K and 100K, is needed. Therefore, the magnetisation at saturation of CoAl alloys containing between 40 and 60% of Co has been measured as a function of temperature. The magnetic field is applied in the sample plane and is equal to 3 kOe (enough to saturate the sample).

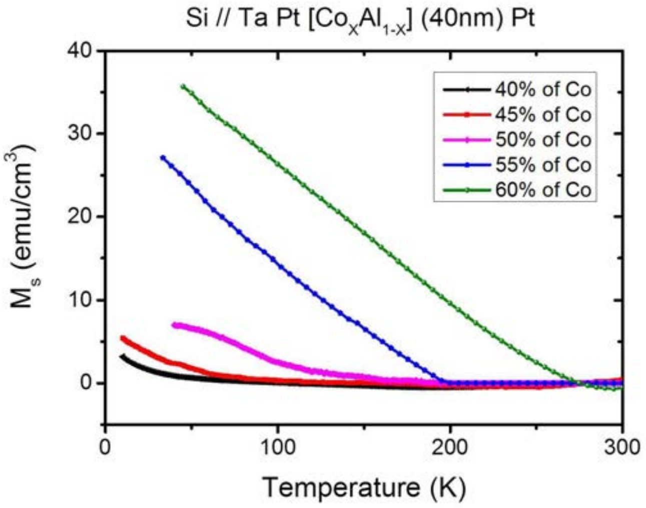

Fig. V.7: Magnetisation at saturation as a function of the temperature, for different compositions of the CoAl alloy (from 60% to 40% of Co). The applied field is equal to 3kOe.

When the percentage of Co in the alloy decreases, the transition between the paramagnetic and the ferromagnetic state happens at a temperature T_C which decreases. The left-hand side of figure V.8 shows the variation of this temperature with X, the percentage of Co. This temperature increases almost linearly with the percentage of Co.

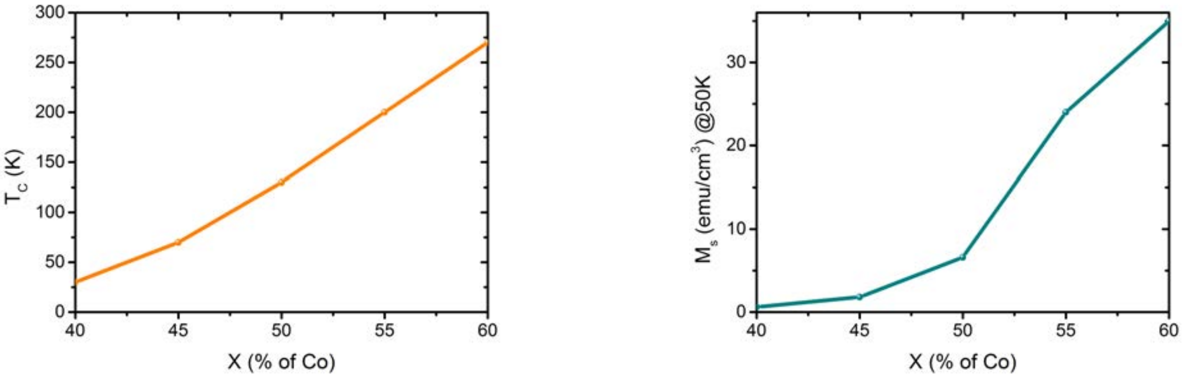

Fig. V.8: *Left: temperature of the paramagnetic ferromagnetic transition T_C as a function of X, the percentage of Co in the alloy. Right: magnetisation at saturation extracted from figure V.7 at 50K as a function of the percentage of Co.*

On the right-hand side of figure V.8, the magnetisation at saturation, extracted from the figure V.7 at 50K, is shown as a function of the alloy composition. This temperature is not chosen randomly: it is the temperature mostly used in the transport measurements made during this PhD. M_s is small for the alloy with 40% of Co (not even $1emu/cm^3$) but increases when the proportion of Co is higher. The magnetisation at saturation reaches a value of $35emu/cm^3$ at 50K when the alloy is composed by 60% of Co and 40% of Al.

IV. Conclusion

In this chapter, we have studied a transition metal aluminide made of cobalt and aluminium. In the literature, we can find some results on that kind of alloys (CoAl, NiAl or FeAl). It was shown in particular that a NiAl alloy is paramagnetic regardless of the composition, whereas a CoAl is ferromagnetic at room temperature if the proportion of Co is larger than the Al one. A FeAl alloy is ferromagnetic at the stoichiometric composition, but the experimental difficulties linked to the deposition of Fe, like a rapid oxidation, pushed us to use a CoAl alloy.

In the second part of the chapter, we studied CoAl alloy at room temperature for different percentages of Co. We have shown in particular that the alloy is ferromagnetic if there is more than 60% of Co. The third part shows the magnetisation at saturation as a function of the temperature for alloys with a concentration of Co below the critical value of 60%. The temperature of the paramagnetic-ferromagnetic transition varies linearly with the percentage of Co. The magnetisation at saturation is small (around $1emu/cm^3$) at 50K for alloys poor in Co (with 40 and 45%), but increases to $35emu/cm^3$ when the percentage of Co is equal to 60%.

Résumé du chapitre :

Afin de corroborer nos résultats sur la précession du spin de l'électron obtenus dans du Co ou du CoFeB, et ainsi prouver que ce qui est observé correspond bien à un phénomène de précession, nous avons décidé d'utiliser comme couche active un alliage composé de cobalt et d'aluminium. En effet, de tels alliages sont connus pour avoir une transition paramagnétique-ferromagnétique pour des compositions proches de la proportion stoechiométriques.

La première partie de ce chapitre est consacrée à l'étude bibliographique des alliages entre l'aluminium et un métal de transition (Co, Ni ou Fe). Butler [54] montre tout d'abord en 1969 qu'un alliage CoAl est ferromagnétique à température ambiante si la proportion d'aluminium est inférieure à 49%. Il a également montré dans cette étude qu'un alliage NiAl est super-paramagnétique entre 49 et 51% d'aluminium. Une deuxième étude théorique de Sundararajan [55] réalisée dans les années 90 corrobore ces résultats. Grâce à des calculs de structure de bandes pour des alliages à la composition stoechiométriques, il a montré que seul le FeAl est ferromagnétique. En effet, le magnétisme des atomes de Co et de Ni est écranté dans l'alliage. Seuls les atomes de Fe conservent chacun un moment équivalent à $0.7\mu_B$.

La deuxième partie de ce chapitre concerne l'étude expérimentale que nous avons réalisée sur des alliages CoAl à température ambiante. Nous avons montré que l'alliage est ferromagnétique dès lors que la proportion de Co est supérieure à 60%. A la suite de ces résultats, nous avons fait des échantillons avec une composition comprise entre 40% et 60% de Co, afin d'étudier leur comportement magnétique en fonction de la température. Nous avons notamment montré que la température de la transition paramagnétique-ferromagnétique décroit linéairement avec la température. Cependant, le moment à saturation est très faible dans la gamme de température où notre transistor tunnel magnétique fonctionne (entre 50K et 100K) si la proportion de Co est inférieure à 50%. Nous avons donc décidé d'étudier la précession du spin de l'électron dans des alliages de CoAl comprenant 50, 55 et 60% de Co.

PART III

TRANSPORT MEASUREMENTS

Chapter 6

Magneto-current optimisation of the spin valve

Once the growth of a magnetic layer that exhibits a perpendicular magnetic anisotropy (*PMA*) on top of a Schottky diode was optimised, the next step in the construction of the crossed Magnetic Tunnel Transistor (*MTT*) can be engaged. An important parameter of the MTT is the magneto-current (*MC*) of the spin valve. Indeed, the sensitivity of the precession measurement is directly related to the MC: if the MC is strong, the angle between the electronic spin and the magnetisation of the layer of analysis can be measured precisely. In the particular MTT geometry of this thesis, the crossed magneto-current ($MC^{\perp}$) of the spin valve is defined between the crossed and the parallel configurations of magnetisations.

In order to increase the $MC^{\perp}$, a simple way consists in increasing the spin polarisation of the current. Since we want to have flexibility on the active layer that hosts the precession, we have optimised the properties of the [Co/Ni] multilayer which is common to all the samples. To increase the spin polarisation of the current, we could either increase the thickness of each layer (Co and Ni) or increase the number of repetition of the multilayer. We have chosen the second solution, a Ni(0.6) $[\mathrm{Co}(0.2)/\mathrm{Ni}(0.6)]_x$ stack keeping a PMA from 1 to 5 repetitions (see Chapter IV). However, the current has to be checked because of the hot electron diffusion that occurs at each interface.

In the first part of this chapter, we will see how the collected current depends on the energy of the hot electrons injected, *i.e.* on the applied voltage on the tunnel barrier, and depends also on the magnetic configurations of the spin valve. This allows us to determine the crossed magneto-current ($MC^{\perp}$) of the spin valve as a function of the applied voltage. The variation of the $MC^{\perp}$ with the number of repetition of the [Co/Ni] multilayer is in particular studied. The third part will be dedicated to the variation of the collected current as a function of the direction of the applied magnetic field for different field intensities.

I. Collected current …

In a magnetic tunnel transistor, the current of hot electrons collected in the semiconductor (SC) depends on many different parameters. It depends on the energy of the hot electrons injected and so on the applied voltage on the tunnel barrier: this is the purpose of the first part of this section. It hinges also on the magnetic configuration of the spin valve, as it will be shown on the second part.

I.A. … as a function of the applied voltage

Hot electrons are injected in the spin valve thanks to a voltage V_e applied across a tunnel barrier. To contribute to the collected current I_c in the semiconductor, electrons must overcome the Schottky barrier. Thus, only electrons with enough energy, which is defined by the level of the applied voltage, can be collected. The figure VI.1 shows the energy landscape of the MTT used in this part of the thesis.

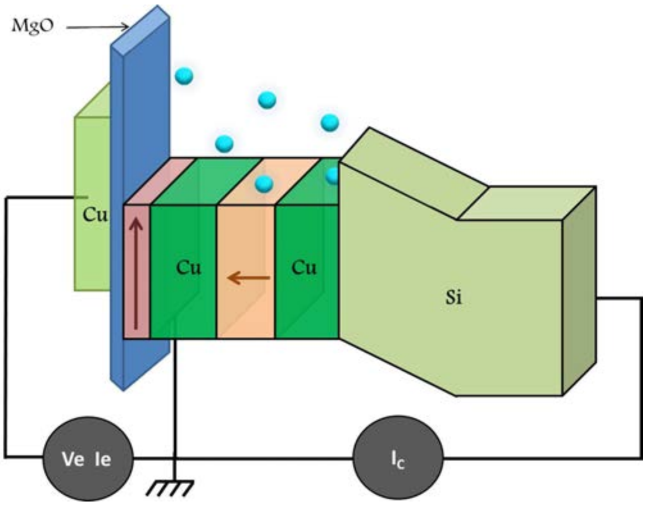

Fig. VI.1: Energy diagram of the MTT used in this part of the thesis. Hot electrons are injected thanks to a voltage V_e applied on a tunnel barrier. During the transport in the spin valve, electrons can lose a certain amount of energy. The level of the energy loss depends on the direction of the spin compared to the direction of the magnetisations. To contribute to the collected current I_c, electrons must overcome a Schottky barrier.

In our experiment, we had to define a common electrical ground between the source voltage which creates the hot electrons and the nano-amperemeter which measures the current in the semiconductor. Thus, we must apply a negative voltage on the tunnel barrier to inject hot electrons towards the spin valve, and the current collected in the semiconductor is measured negative. In the following, figure VI.2 shows on the left the result of a measurement of the current injected from the tunnel barrier and on the right the collected current in the semiconductor as a function of the applied voltage.

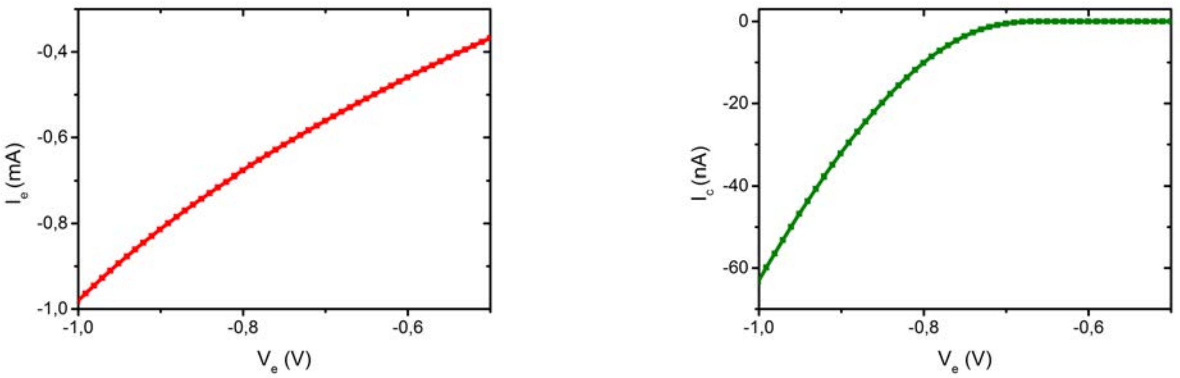

Fig. VI.2: *Left: current in the tunnel barrier I_e as a function of the voltage V_e. Right: current collected in the semiconductor I_c as a function of the voltage applied on the MgO tunnel barrier. The sample is $Si//Cu(5)Ta(1)Cu(5)$ $Ni(0.6)[Co(0.2/Ni(0.6)]_4$ $Cu(3.5)Co(3)MgO(2.8)Cu(20)Pt(5)$ (thickness in nanometer). The temperature is equal to 50K.*

The energy range available in our system for the incoming electrons goes up to 1.2eV, which corresponds to a maximum voltage of 1.2V before the tunnel barrier breakdown. The collected current is different from zero only when the injected electrons have an energy higher than the height of the Schottky barrier. The collected current is different from zero when the applied voltage is larger than -700mV: the Schottky barrier has an height of around 0.7eV. In this MTT, the transfer ratio, which is defined as the ratio between the collected current and the current in the tunnel barrier $TR = I_c/I_e$, is in the order of 10^{-5}. The figure VI.3 shows the transfer ratio as a function of the applied voltage.

The threshold at -700mV, due to the energy filtering of the Schottky diode, is also visible in the TR. For a voltage below the threshold, no electron can overcome the Schottky barrier and the transfer ratio is equal to zero. For a voltage just above the threshold, only electrons that do not lose energy in the spin valve can contribute to the collected current and the transfer ratio is small. If the voltage is further increased, even electrons that lose a little amount of energy but keep their wave-vector in the acceptance cone angle can be collected in the semiconductor: the transfer ratio increases.

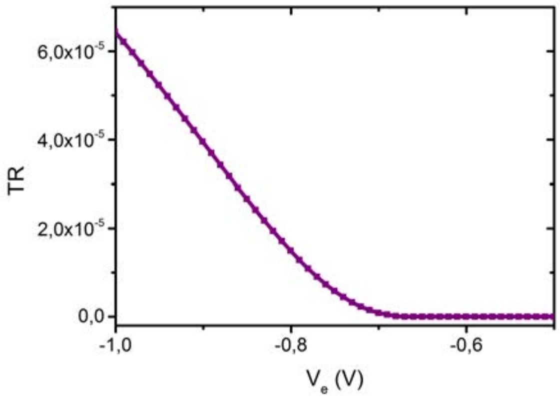

Fig. VI.3: *Transfer ratio (TR) as a function of the applied voltage at 50K.*

As introduced in the last paragraphs, even if the injected electrons have enough initial energy to overcome the Schottky barrier, they do not contribute necessarily to the collected current: they can lose energy during the transport in the spin valve. If the injected electrons are not spin-polarised (it is the case in this chapter), the amount of energy lost depends only on the magnetic configuration of the spin valve. The following paragraph shows the variation of the collected current with the magnitude of an external magnetic field applied either perpendicular or in the sample plane.

I.B. ... as a function of the magnetic field

The collected current strongly depends on the magnetic configuration of the spin valve. Indeed, as explained in the chapter II, the mean free path of an electron in a ferromagnetic layer is different if its spin is parallel or anti-parallel to the magnetisation. The energy loss is more important when the electronic spin is in the opposite direction of the magnetisation, leading to a smaller mean free path. As a consequence, the level of the collected current is a direct picture of the magnetisations configuration of the two ferromagnetic layers of the spin valve. In the following figure, the collected current is measured as a function of the applied magnetic field for an applied voltage of -750mV (which corresponds to an energy slightly higher than the Schottky threshold). The magnetic field is applied perpendicular to the sample plane in the figure VI.4 and in the sample plane in the figure VI.5. These measurements are confronted to the $M(H)$ loops that show the magnetic behaviour of the two ferromagnetic layers.

When the field is applied perpendicular to the sample plane, the hysteresis part of the $M(H)$ loop with a coercive field of 450 Oe corresponds to the magnetic response of the [Co/Ni] multilayer which has a perpendicular magnetic anisotropy. The Co layer has an in-plane anisotropy due to the shape anisotropy, with a saturation field of 17 kOe. The variation of the collected current with the applied field is consistent with the magnetic configuration of the spin valve. After a positive saturation (H_{app} >17kOe) of the magnetisations, the collected current decreases because of the progressive rotation of the Co layer magnetisation into the sample plane (represented by the blue arrow in figure VI.4) when the magnetic field decreases. The switching of the [Co/Ni] multilayer magnetisation (green arrow) at -450 Oe induces a jump in the collected current. The collected current increases again until both magnetisations are saturated with a negative field of -17 kOe. The curve is symmetric when the field is increased from a negative saturation value to a positive one (purple part of the curve in the figure VI.4).

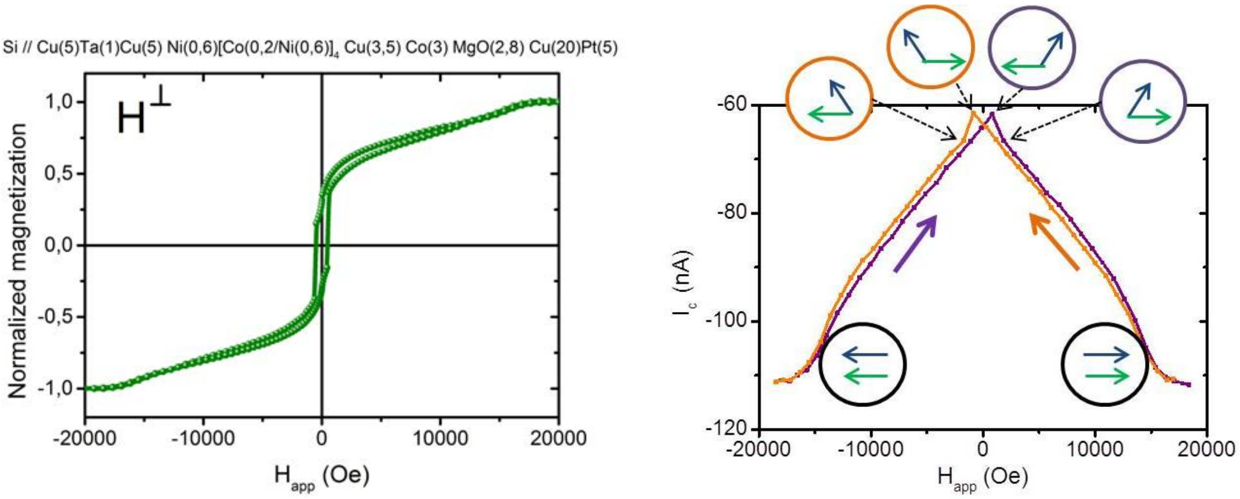

Fig. VI.4: *Left: M(H) loop of a* $Si//Cu(5)Ta(1)Cu(5)\ Ni(0.6)[Co(0.2/Ni(0.6)]_4\ Cu(3.5)Co(3)Mgo(2.8)Cu(20)Pt(5)$ *MTT for a field applied perpendicular to the sample plane. Right: Current of hot electrons collected in the semiconductor as a function of the magnetic field. The field decreases after a positive saturation in orange, and increases after a negative saturation in purple. In the inset, the magnetisation of the Co layer is represented with a blue arrow, and the one of the [Co/Ni] multilayer is in green. The applied voltage is equal to* $-750mV$ *and the temperature is 60K.*

The same measurements have been made with a field applied in the sample plane (figure VI.5). When the field is applied in the sample plane, the response of the Co layer is an hysteresis loop with a coercive field of 300 Oe. The field being applied along an hard axis of the [Co/Ni] multilayer, its magnetisation rotates progressively with a saturation field of 7500 Oe. Once again, the variation of the collected current with the applied field is in perfect agreement with the magnetic configuration of the spin valve.

However, one can notice that the responses are not equivalent for a field applied parallel or perpendicular to the sample plane, while in both cases the field is applied along a hard axis of one ferromagnetic layer. In section III, this difference will be studied in details.

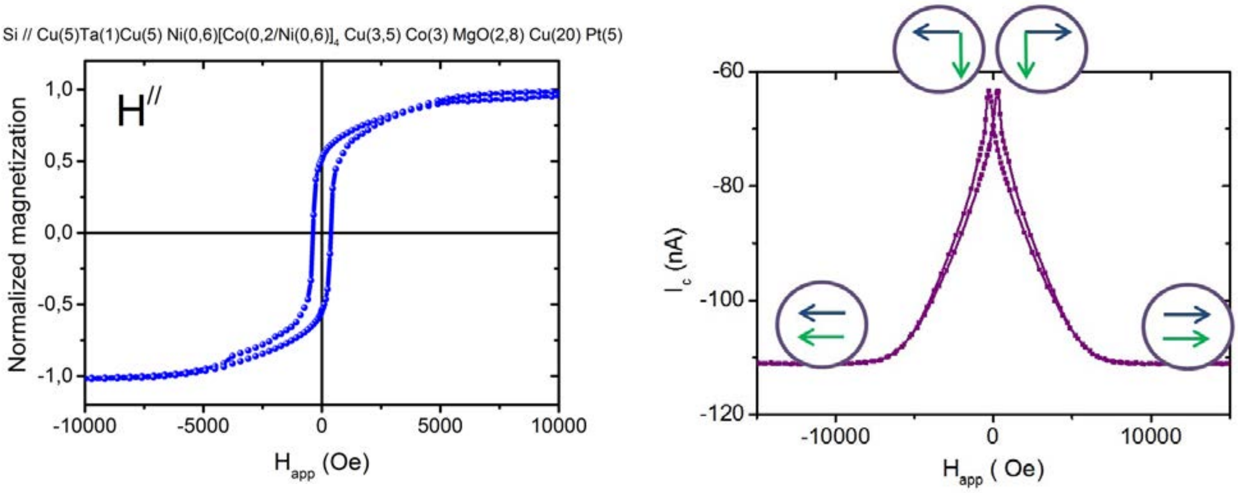

Fig. VI.5: *Magnetic behaviour of a* $Si//Cu(5)Ta(1)Cu(5)\ Ni(0.6)[Co(0.2/Ni(0.6)]_4$ $Cu(3.5)Co(3)MgO(2.8)Cu(20)Pt(5)$ *MTT for a field applied in the sample plane. Left: M(H) loop. Right: Current of hot electrons collected in the semiconductor as a function of the magnetic field. The applied voltage is equal to* $-750mV$ *and the temperature is 60K.*

In this first section, we have seen the dependence of the collected current with the applied voltage and with the magnetic configuration of the spin valve. When the electrons have enough energy to overcome the Schottky barrier, they can contribute to the collected current. The initial energy is defined by the applied voltage, but the energy of the electrons coming towards the Schottky barrier is also dependent on the magnetic configuration of the spin valve. As a consequence, we will define in the second section the crossed magneto-current ($MC^{\perp}$), which is the relative difference between the collected currents in the parallel and in the crossed magnetic configuration of the spin valve.

II. Magneto-current ...

With the crossed geometry that we have designed for our MTT, it is more relevant to define the magneto-current between the crossed and the parallel magnetic configurations:

$$MC^{\perp} = \frac{I_c^P - I_c^{\perp}}{I_c^{\perp}} \tag{6.1}$$

in which I_c^P and $I_c^{\perp}$ are respectively the collected current in a parallel and a crossed magnetic configuration of the spin valve. The parallel configuration can be obtained for a magnetic field larger than 10 kOe applied in the sample plane (see figure VI.5), or with a perpendicular magnetic field larger than 17 kOe (see figure VI.4). After a saturating field (positive or negative), the crossed configuration is obtained by decreasing the field to zero. In the following, we have chosen to apply systematically the magnetic field in the sample plane to obtain the different magnetic configurations.

II.A. ... as a function of the applied voltage

In the figure VI.6, the current collected in the semiconductor is measured as a function of the applied voltage for the spin valve in a parallel magnetic configuration (a magnetic field of 20 kOe is applied in the sample plane) or in a crossed magnetic configuration (after the decreasing of an in-plane magnetic field from 20 kOe to zero).

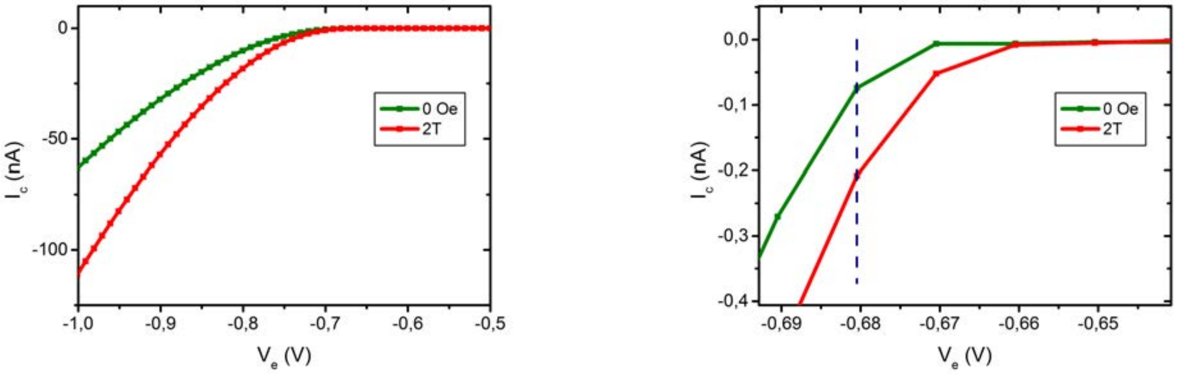

Fig. VI.6: Current collected in the semiconductor as a function of the voltage applied on the tunnel junction for a $Si//Cu(5)Ta(1)Cu(5)$ $Ni(0.6)[Co(0.2/Ni(0.6)]_4$ $Cu(3.5)Co(3)MgO(2.8)Cu(20)Pt(5)$ MTT. This measurement is made for the parallel magnetic configuration (red curve) and for the crossed magnetic configuration (green curve) of the spin valve. The temperature is 50K. The full curve is in the left, a zoom for voltages close to the Schottky threshold is in the right.

The current is higher in the case of the parallel magnetic configuration. In fact we have seen in the chapter II that an electron has a larger mean free path if its spin is parallel to the magnetisation of the ferromagnetic layer. An electron with a spin in the opposite direction suffers a lot of inelastic scattering events and loses a part of its energy. As a consequence, if the spin valve is in the parallel configuration, the electrons with the spin oriented parallel to the direction of both magnetisations can cross the spin valve with only a small energy loss. On the contrary, an electron with a spin in the opposite direction will lose too much energy to overcome the Schottky barrier. Thus, a current 100% polarised can be collected. If the spin valve is in a crossed configuration, an electron will lose a part of its energy regardless of the spin direction: the current collected is smaller. The sketches in the figure VI.7 represent the energy diagram of both cases.

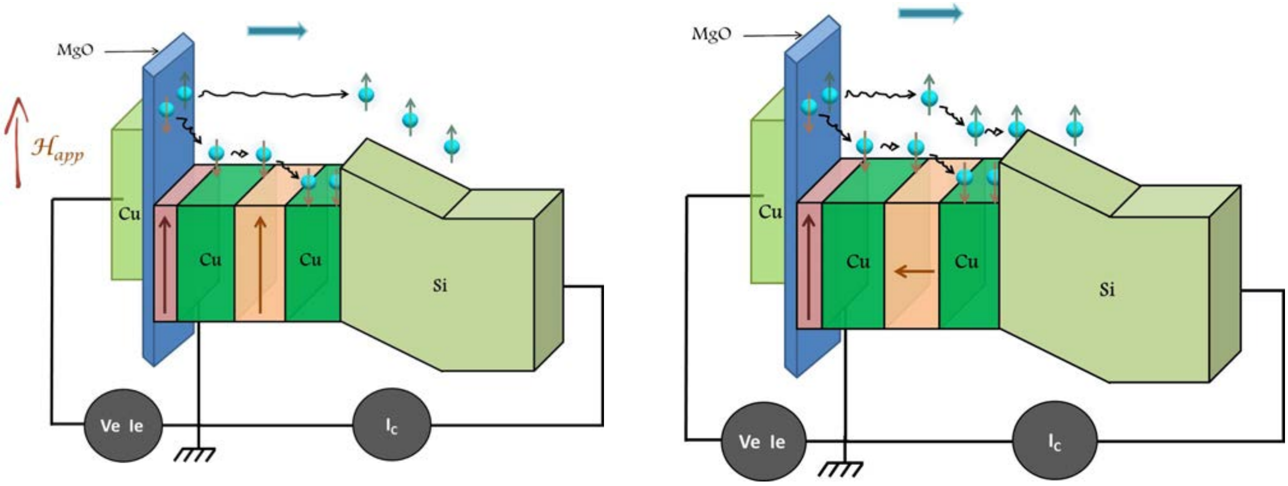

Fig. VI.7: *Energy diagram of the MTT in a parallel configuration on the left and in a crossed magnetic configuration on the right. In order to overcome the Schottky barrier, an injected electron must suffer only few scattering events: that happens when its spin is parallel to the magnetisation of the ferromagnetic layer. A pure spin current is collected in the parallel configuration.*

The $MC^{\perp}$ can be calculated from the measurements of the collected current in both magnetic configurations. The variation of the $MC^{\perp}$ with the applied voltage is shown in the figure VI.8.

A strong $MC^{\perp}$ is obtained just after the threshold of the Schottky barrier. Then, it decreases and reaches a value around 75% at higher voltages. As shown in the chapter III, our definition of the $MC^{\perp}$ involves a maximum value of 100%. Thus, one can wonder if the strong peak of the $MC^{\perp}$ just after the threshold of the Schottky diode is an electronic noise or a real physical effect not taken into account in the model used to express the current of the crossed configuration as the mean between the current of the parallel and the current of the anti-parallel configuration.

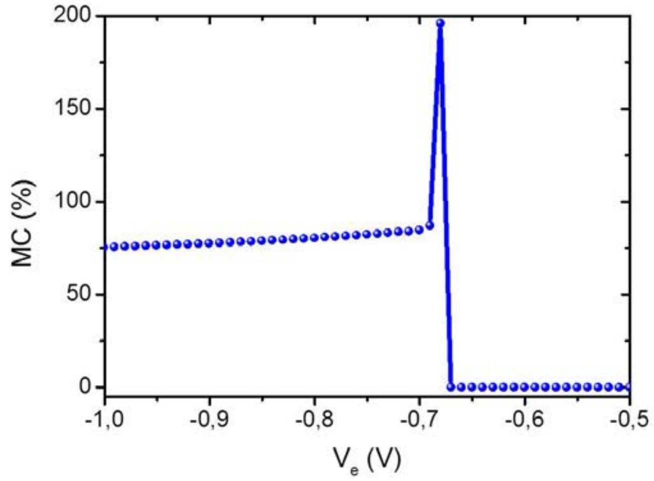

Fig. VI.8: *Crossed magneto-current as a function of the applied voltage for a* $Si//Cu(5)Ta(1)Cu(5)\ Ni(0.6)[Co(0.2/Ni(0.6)]_4\ Cu(3.5)Co(3)MgO(2.8)Cu(20)Pt(5)$ *MTT. The* $MC^{\perp}$ *is calculated via the curves of the hot electron current as a function of the applied voltage in the parallel and the crossed magnetic configurations of the spin valve. The temperature is 50K.*

To elucidate that question, we have measured the hot electron current collected in the semiconductor as a function of the applied field for different values of the applied voltage on the tunnel junction. The results are shown in the following figure VI.9.

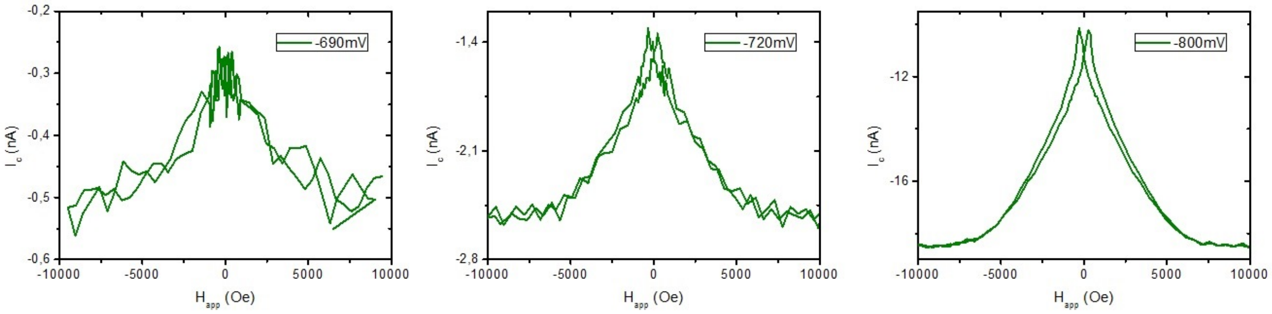

Fig. VI.9: *Current collected in the semiconductor as a function of the magnetic field for a* $Si//Cu(5)Ta(1)Cu(5)\ Ni(0.6)[Co(0.2/Ni(0.6)]_4\ Cu(3.5)Co(3)MgO(2.8)Cu(20)Pt(5)$ *MTT. The applied voltage on the tunnel junction equals* $-690mV$ *on the left (which corresponds to an energy for the electrons just higher than the Schottky barrier),* $-720mV$ *in the middle and* $-800mV$ *on the right. The temperature is 50K.*

A value of the $MC^{\perp}$ can be extracted from each curve by measuring the maximum and the minimum of the collected current. This kind of measurement has been made for several voltages between -650mV and -1V to reconstruct the curve of the $MC^{\perp}$ as a function of the applied voltage (figure VI.10).

When the applied voltage is slightly larger than the Schottky threshold, the collected current is really small ($\sim 10^{-10}A$ at $V_e = -690mV$). This is the limit of the current measurable because of the sensibility of our nano-amperemeter, and the noise is important. This must be taken into account in the curve of the $MC^{\perp}$. In the following figure VI.10, error bars have been added, by taking into account the maximum and the minimum contrast between the parallel and the crossed magnetic configurations.

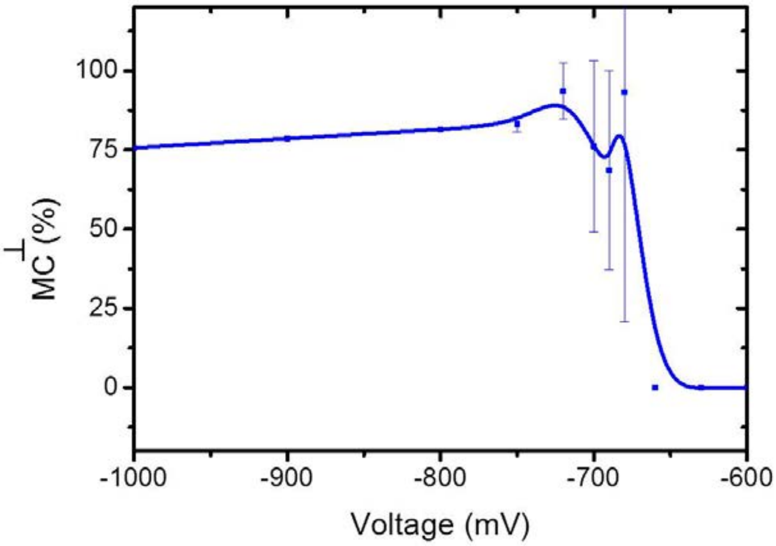

Fig. VI.10: *Crossed magneto-current as a function of the applied voltage for a* $Si//Cu(5)Ta(1)Cu(5)\ Ni(0.6)[Co(0.2/Ni(0.6)]_4\ Cu(3.5)Co(3)Mgo(2.8)Cu(20)Pt(5)$ *MTT. The* $MC^{\perp}$ *is calculated via the curves of the hot electron current as a function of the magnetic field for different values of the applied voltage. The temperature is 50K.*

This figure shows also a peak of $MC^{\perp}$ just after the Schottky threshold, but the amplitude is much smaller than the one observed in the figure VI.8. The $MC^{\perp}$ does not exceed 100% here but is close to 100%. The higher contrast between the parallel and the crossed magnetic configuration is obtained when the energy of the injected electrons is just higher than the top of the Schottky barrier. Indeed, the slightest event which decreases the energy of the electrons prevents them from contributing to the collected current if their initial energy was just sufficient to overcome the barrier. An electron with its spin parallel to the magnetisation has a chance to go through the ferromagnetic layer without losing energy. It is not the case if the spin is not parallel to the magnetisation, partially because of strong inelastic scattering events that can occur when the spin is not parallel to the magnetisation. As a consequence, the current of a non-parallel magnetic configuration is small just after the Schottky threshold. In theory, the MC between a parallel and an anti-parallel configuration can even be infinite just after the Schottky threshold, the collected current being zero in the anti-parallel configuration. If the energy given to the hot electrons is much bigger than the top of the Schottky barrier, even those that lose a small amount of energy can contribute to the collected current: the contrast between the magnetic configurations is decreased, and the $MC^{\perp}$ is smaller.

In the following, these measurements have been realised for different MTT with a number of repetition of the [Co/Ni] multilayer going from 1 to 5.

II.B. ... as a function of the number of repetition

In order to optimise the electronic spin precession measurement, the magneto-current must be as large as possible. The $MC^{\perp}$ can be amplified if the spin polarisation of the current is raised, by increasing the ferromagnetic layers thickness for instance. To have a flexibility on the choice of the precession layer, this work of optimisation has been done only on the $[\mathrm{Co}(0.2)/\mathrm{Ni}(0.6)]_n$ multilayer. The thicknesses of the Co and Ni layers have been kept constant: only the number of repetition of the multilayer will vary.

We have seen in the chapter V that a structure Ni(0.6) $[\mathrm{Co}(0.2)/\mathrm{Ni}(0.6)]_n$ grown on a Si[100](HF)//Cu Schottky diode exhibits a perpendicular magnetic anisotropy for a number of repetition n between 1 and 5. Thus, the $MC^{\perp}$ has been measured for five Si//Cu(5)Ta(1)Cu(5) Ni(0.6) $[\mathrm{Co}(0.2/\mathrm{Ni}(0.6)]_{1-5}$ Cu(3.5) Co(3) MgO(2.8) Cu(20) Pt(5) magnetic tunnel transistors. In the figure VI.11, the variation of the $MC^{\perp}$ as a function of the number of repetition is shown, for an applied voltage of -680mV.

As expected, the $MC^{\perp}$ increases with the number of repetition. The highest value of 85% is measured for the MTT with 5 repetitions of the multilayer. This value is close to the maximal value of 100% which can be obtained with our definition of the crossed magneto-current. This indicates a very large polarisation efficiency through the high quality spin valve structure.

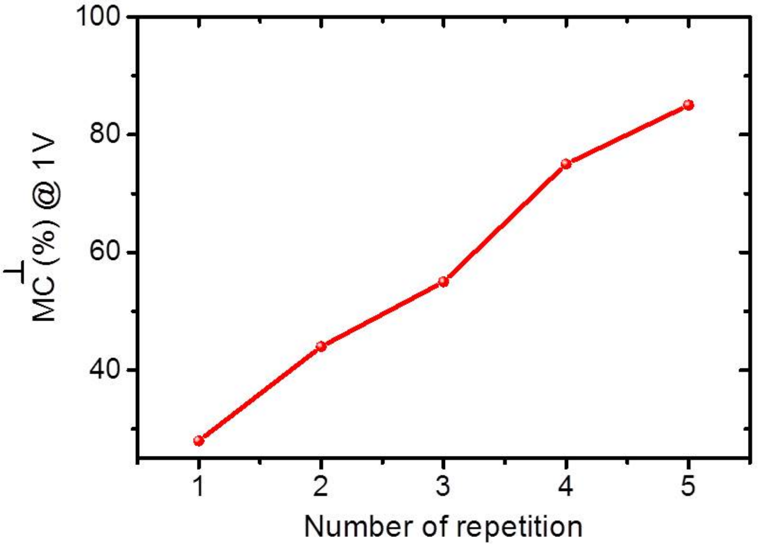

Fig. VI.11: *Crossed magneto-current* $MC^{\perp}$ *as a function of the number of repetition of the [Co/Ni] multilayer at an applied voltage of* $-1V$*, for a* $Si//Cu(5)Ta(1)Cu(5)$ $Ni(0.6)[Co(0.2/Ni(0.6)]_X$ $Cu(3.5)Co(3)Mgo(2.8)Cu(20)Pt(5)$ *MTT. The temperature is 50K.*

The last part of this section concerns the variation of the crossed magneto-current with the temperature.

II.C. ... as a function of the temperature

The temperature is an important parameter in our experiments. Indeed, the Schottky barrier has a strong leakage current when the temperature exceeds 100K: all our measurements must be done under this temperature to keep the energy filtering efficient. As a consequence, it is relevant to study the $MC^{\perp}$ as a function of the applied voltage for different temperatures. The results are shown in the figure VI.12.

A strong decrease of the crossed magneto-current happens for a temperature below 30K. The $MC^{\perp}$ even becomes negative at high voltages, which indicates that the current is larger for the crossed magnetic configuration than for the parallel one. This phenomenon was already observed in a MTT with in-plane magnetisations [34]. Y. Lu *et al.* have measured a strong decrease of the MC with the temperature on a Si//Cu(10) NiFe(4) Cu(3.5) Co(4) MgO(2.7) Cu(20) MTT. The MC goes from ∼ 2000% at 25K to ∼ 800% at 17K. This experiment has evidenced an interfacial trapping phenomenon for hot electrons injection in silicon. At low temperatures (T<25K), electrons are trapped at the Cu/Si interface and modify the interfacial electronic potential. Thus, the trapped electrons at the Cu/Si interface increase the backscattering of incoming hot electrons, which results in a decrease of the collected current. The amplitude of reduction being 2-3 times higher in the parallel magnetic configuration than in the anti-parallel one, a rapid reduction of the MC is observed. They have also shown that this interfacial trapping can be controlled by applying an electrical field across the Cu/Si interface [46].

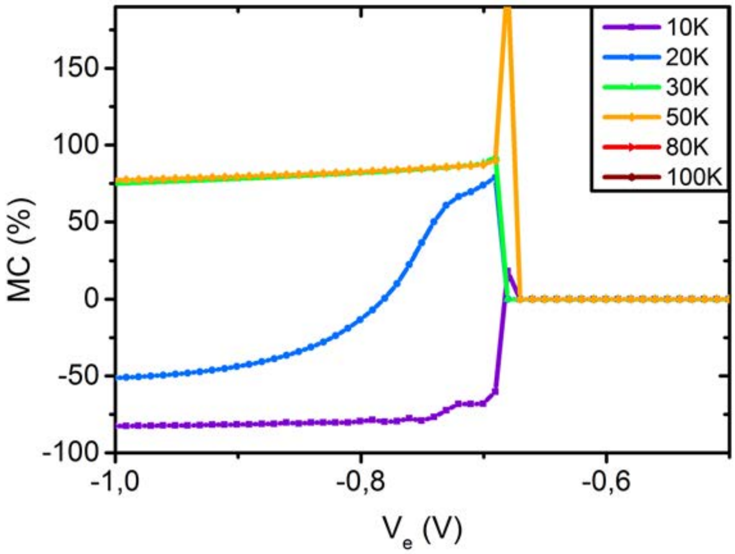

Fig. VI.12: *Crossed magneto-current as a function of the applied voltage for a* $Si//Cu(5)Ta(1)Cu(5)\ Ni(0.6)[Co(0.2/Ni(0.6)]_4\ Cu(3.5)Co(3)MgO(2.8)Cu(20)Pt(5)$ *MTT. The* $MC^{\perp}$ *is calculated via the curves of the hot electron current as a function of the applied voltage in the parallel and in the crossed magnetic configuration of the spin valve. These measurements have been done for several temperatures between 10K and 100K.*

This phenomenon of trapping reduces the range of temperatures in which our MTT is efficient. If the temperature is smaller than 30K, the interfacial trapping of hot electrons at the Cu/Si interface decreases the collected current and the MC. If the temperature is higher than 100K, the Schottky diode has leakage currents that decrease the energy filtering efficiency. In the following, our range of work is [30K-100K].

The second section of this chapter is dedicated to the variation of the collected current with the angle between the magnetisations of the ferromagnetic layers of the spin valve. Usually, only the collected currents in the parallel and in the anti-parallel magnetic configuration are measured to calculate the magneto-current. Nevertheless, to measure the electronic spin precession, it is necessary to know the variation law of the collected current with the angle between the magnetisations.

III. Magneto-current angular dependence

Up to now, all the solid state devices dealing with spin-polarised hot electrons transport were composed of ferromagnetic layers offering only a collinear alignment of their magnetisations. This magnetic configuration could provide only two well defined states of magnetisations, characterised by the relative angle between the ferromagnetic layers magnetisations: 0^o and 180^o. This is probably why the angular dependence of the magneto-current has never been studied in details.

Our device Si[100](HF)//Cu(5)Ta(1)Cu(5) Ni(0.6)[Co(0.2/Ni(0.6)]$_4$ Cu(3.5) Co(3) MgO(2.8) Cu(20) Pt(5) with crossed anisotropy presented in this chapter offers a unique opportunity to deepen our understanding of the magneto-current since the relative angle between the magnetisations can be controlled between 0^o and 90^o. Indeed, both magnetisations can be controlled independently, one magnetic layer exhibiting a perpendicular magnetic anisotropy (the [Co/Ni] multilayer).

Based on the GMR angular dependence [56, 57], we can infer that the collected current will be of the form:

$$I_c \;=\; I_c^{\perp}\;\left(1 + MC^{\perp}\;\overrightarrow{u_{Co}}\cdot\overrightarrow{u_{[Co/Ni]}}\right) \tag{6.2}$$

in which $I_c^{\perp}$ is the current collected in a crossed configuration of the spin valve and $MC^{\perp}$ the crossed magneto-current defined in equation 6.1. $\overrightarrow{u_{Co}}$ and $\overrightarrow{u_{[Co/Ni]}}$ are the unit vectors pointing in the directions of respectively the Co and [Co/Ni] magnetisation.

In figure VI.13, the collected current I_c has been measured as a function of φ_{Happ}, the angle between the sample plane and an applied field, for different magnitudes of the magnetic field (200, 1000, 3000, 5000 Oe). The goal of this section is to check the validity of equation 6.2 by using it to reproduce our experimental data.

For these experiments, φ_{Happ} is increased from -50^o to $+310^o$ and then decreased from $+310^o$ to -50^o. The collected current is measured at 60 K for an injection bias of -1V. At 200 Oe (blue curve), a reversible signal having mostly a cosine signature have been recorded. The increase of the applied magnetic field is accompanied by both the appearance of irreversible (hysteric) parts and the loss of the cosine shape.

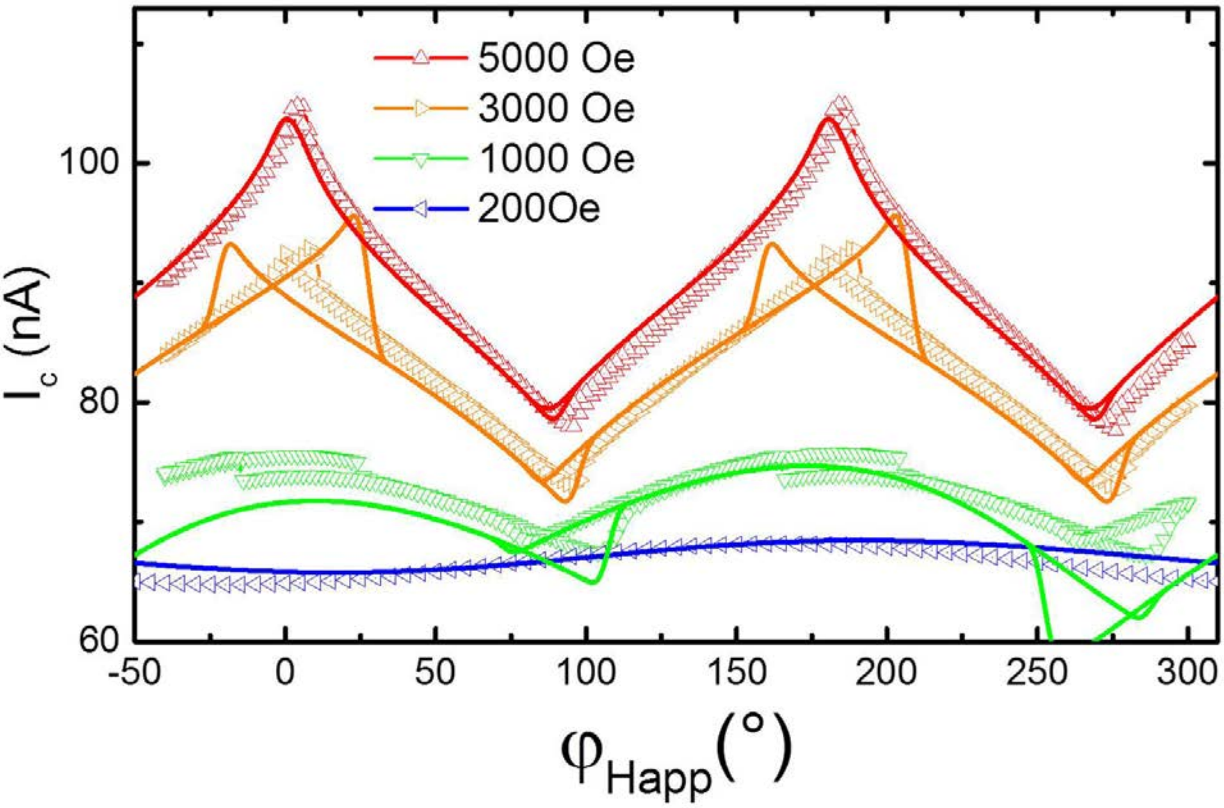

Fig. VI.13: *Collected current I_c as a function of the field angle φ_{Happ}, measured at 60 K and for an injected current $I_e = -1V$. The magnitude of the applied field is 200, 1000, 3000 or 5000 Oe. Continuous lines correspond to fits performed using the model under discussion.*

To achieve a robust testing procedure, the number of adjustable parameters must be reduced to its strict minimum. In a first step, the collected current I_c has been measured as a function of the applied field for an applied voltage I_e of 1V. In the first configuration, the magnetic field is applied out of the sample plane (OOP geometry): $\varphi_{Happ} = 90^o$. In the second configuration the field is applied in the sample plan (IP geometry): $\varphi_{Happ} = 0^o$. The figure VI.14 reports the obtained results in the two configurations. In both cases, the magnetisation of each layer is parallel and aligned along the magnetic field direction for a high field (2T). The same value of the collected current is obtained: $I^{//} = -110nA$. When the field is decreased to 0T, the magnetisations of both layers are orthogonal and the same value of the collected current is obtained again in both cases: $I^{\perp} = -65nA$. Thus, the $MC^{\perp}$ is determined to be equal to 70%.

We can reasonably state that the shapes of the curves are directly linked to the demagnetisation field of the Co layer with a perpendicular magnetic field, and to the perpendicular anisotropy of the Ni(0.6) [Co(0.2)/Ni(0.6)]$_4$ in the case of an in-plane applied field. To determine precisely these two values, it is required:

- to model the magnetic response of the system with respect to the magnetic field and thus to obtain values of $\overrightarrow{u_{Co}} \cdot \overrightarrow{u_{[Co/Ni]}}$ *vs.* H_{app}
- to use equation 6.2 to compute the collected current knowing the value of $\overrightarrow{u_{Co}} \cdot \overrightarrow{u_{[Co/Ni]}}$.

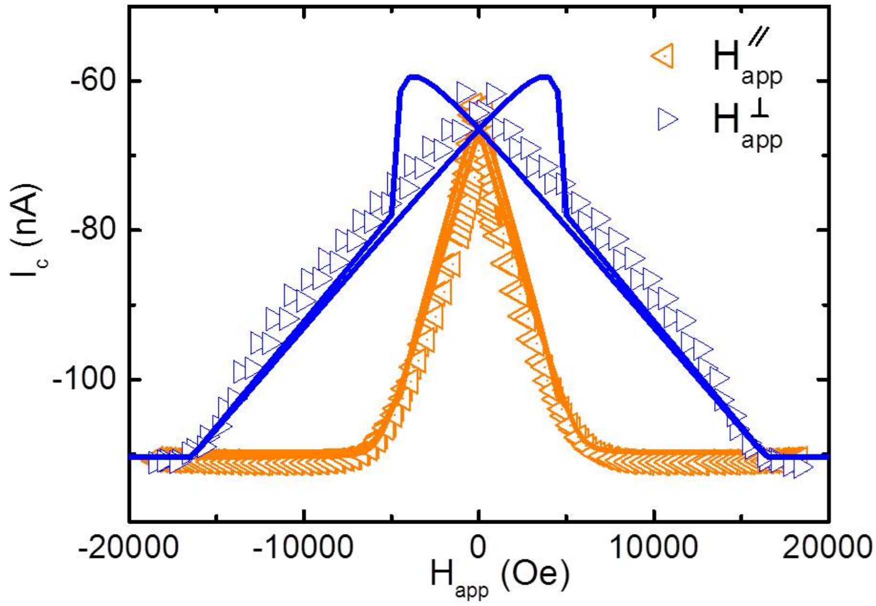

Fig. VI.14: *I_c vs H_{app} measured at 60K and at 1V of injection bias, with an in-plane field (orange curve) and an out-of-plan field (blue curve). Continuous lines correspond to fits performed using the model under discussion.*

The value of $\overrightarrow{u_{Co}} \cdot \overrightarrow{u_{[Co/Ni]}}$ *vs.* H_{app} in both geometry (IP and OOP) has been determined thanks to numerical computation supposing that: i) the magnetisations of both magnetic layers remain uniform regardless of the values and the directions of the applied field, ii) the magnetisations of each layer are independent from each other (uncoupled magnetic system), iii) only a first order uniaxial anisotropy is acting in each layer. In this framework we will divide our problem in two uncoupled systems having each an energy of the form:

$$E_Z + E_a + E_{dem}$$

where E_Z is the Zeeman energy equal to $-\overrightarrow{H_{app}} \cdot \overrightarrow{u}$. E_a corresponds to the first order uniaxial anisotropy expressed as $1/2H_{an}.sin^2(\overrightarrow{H_{an}} \cdot \overrightarrow{u}/H_{an})$, H_{an} being the anisotropy field. The last term taking into account the demagnetisation field is expressed as the following product:

$H_{dem}.sin^2(\varphi_u)$. H_{dem} is the demagnetisation field and φ_u is the angle between the magnetisation direction $\overrightarrow{u}$ and the sample plane, as defined in figureVI.15. Each layer magnetisation has only two degrees of freedom, denoted in the following $\theta_{[Co/Ni]}$ and $\varphi_{[Co/Ni]}$ in the case of the [Co/Ni] multilayer having an out-of-plan magnetisation and θ_{Co} and φ_{Co} in the case of the Co layer with a magnetisation lying on the sample plane. We have computed, in a recursive way, the stable state of magnetisation for each value of the field and in both geometries.

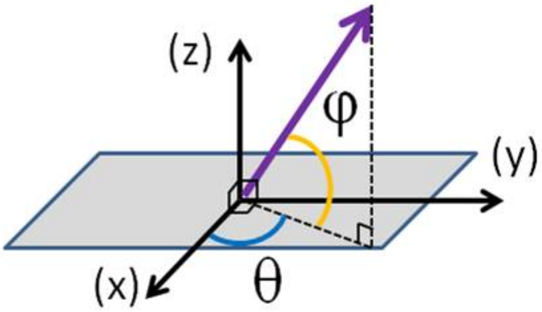

Fig. VI.15: *Angles definition with respect to the sample plan (in grey).*

Our best fits of the I_c *vs.* H_{app} curves are presented on figure VI.14 by the blue and orange continuous lines. This fitting procedure allows us to obtain a value of 0.55T for the perpendicular anisotropy field of the [Co/Ni] multilayer, and a value equal to 1.6T for the demagnetising field of the 3 nanometers thick Co layer sandwiched between the Cu layer and the MgO tunnel barrier. It is about 10% lower than 1.8T which is the expected value neglecting perpendicular anisotropy originating from the MgO/Co interface. The obtained fits are well reproducing the measured curves excepted for the hysteretic parts present at low fields. This is certainly a limitation of the used model that supposes that the magnetisation of every magnetic layer remains uniform during its reversal. This uniformity condition is probably not respected experimentally since the reversal of the Ni(0.6) $[Co(0.2)/Ni(0.6)]_4$ magnetisation in the OOP geometry is likely to take place by nucleation propagation. As aforementioned, the values of the collected current *vs.* the applied field are deduced from the simulated behaviour of $\overrightarrow{u_{Co}}$ and $\overrightarrow{u_{[Co/Ni]}}$ in the two experimental geometries. The figure VI.16 presents these behaviours in the two considered geometries. As expected, in the OOP geometry the collected current variation in field is mostly due to the progressive reversal of $\overrightarrow{u_{Co}}$ while the hysteretic parts can be attributed to the reversal of $\overrightarrow{u_{[Co/Ni]}}$. This is why we can easily extract the value of H_{dem}: the demagnetising field stabilising $\overrightarrow{u_{Co}}$ in the sample plan. From the IP geometry we can extract the value of the anisotropy field experienced by $\overrightarrow{u_{[Co/Ni]}}$ since in this geometry it has a progressive magnetic reversal, as it can be seen in the right part of figure VI.16.

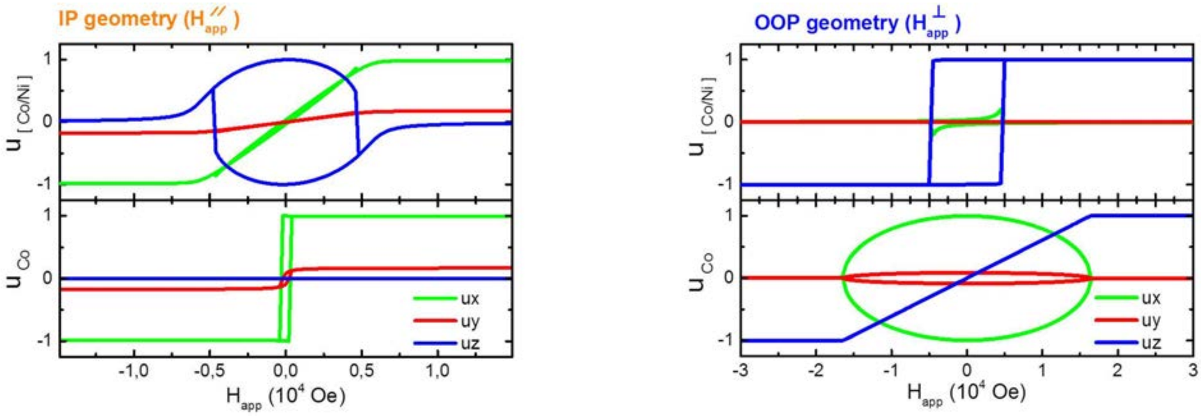

Fig. VI.16: *Projection of $u_{\vec{Co}}$ and $u_{[\vec{Co}/Ni]}$ in the three space directions x, y and z as a function of the applied field for both IP and OOP geometries. The sample plane is defined by the directions x and y.*

From this first step, the values of $I^{\perp}$, $MC^{\perp}$, H_{dem}, $H_{an}^{\perp}$ (the anisotropy of the Ni(0.6) [Co(0.2)/Ni(0.6)]$_4$ multilayer) have been obtained. In a second step, we have tried to reproduce our angular measurements (figureVI.13) using these parameters and the method aforementioned: for φ_{Happ} ranging from -50^o to 310^o the numerical values of $\theta_{[Co/Ni]}$, $\varphi_{[Co/Ni]}$, θ_{Co} and φ_{Co} are determined by minimising the energies of our two independent subsystems for each value of φ_{Happ}. This enables then the calculation of $I_c(\varphi_{Happ})$ thanks to equation 6.2. Our fits of the experimental data are presented by the continuous lines on figure VI.13. The table in figure VI.17 presents the parameters used to reproduce our measurements.

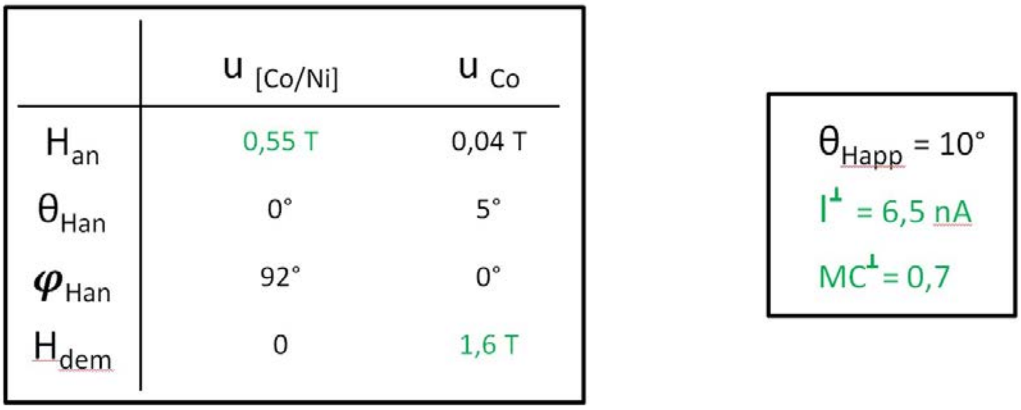

	$u_{[Co/Ni]}$	u_{Co}
H_{an}	0,55 T	0,04 T
θ_{Han}	0°	5°
φ_{Han}	92°	0°
H_{dem}	0	1,6 T

θ_{Happ} = 10°
$I^{\perp}$ = 6,5 nA
$MC^{\perp}$ = 0,7

Fig. VI.17: *Set of used parameters to reproduce our measurements. In green are presented the parameters extracted from the I_c vs. H_{app} fitting procedure. In black are presented the parameters used for the experimental angular dependence fitting.*

This set of parameters does not contain any surprising value. A slight misalignment between the samples anisotropies axes and the magnetic field direction has to be introduced in order to obtain a reasonable agreement between the computed signals and the measurements (see non-zero values of θ_{Han} , φ_{Han} and θ_{Happ}). Again, the magnetic part of the model failed to reproduce quantitatively the irreversible parts recorded in the I_c *vs.* φ_{Happ} curves. As previously done, we attribute this deviation to the non-uniform magnetic reversals occurring experimentally. However, it is remarkable that the model well captures the shape variation of our angular measurement when increasing the applied magnetic field. Furthermore, the variation of the base current with the field magnitude is also very well reproduced. The values of the collected current are deduced from the behaviour of the magnetisation of each layer *vs.* φ_{Happ}. Details of these behaviours are given in figure VI.18.

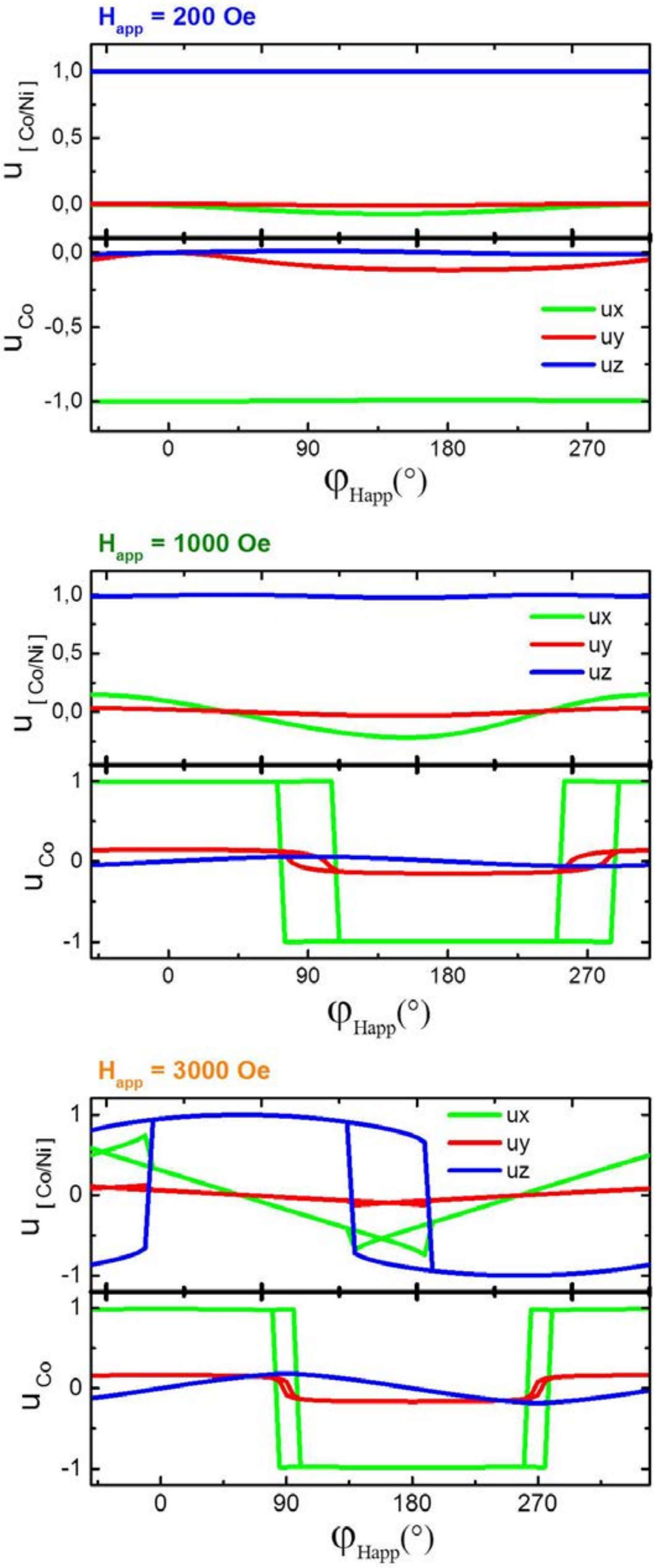

Fig. VI.18: *u_x, u_y, u_z vs. φ_{Happ} calculated for $u_{\vec{Co}}$ and $u_{[\vec{Co/Ni}]}$ and three values of the applied field.*

Résumé du chapitre :

Une fois la croissance d'une multicouche [Co/Ni], qui exhibe une anisotropie perpendiculaire, optimisée sur une jonction Schottky, nous avons pu passer à la deuxième phase de construction de notre système. Nous avons donc réalisé un transistor tunnel magnétique (TTM) comprenant deux couches ferromagnétiques, pour lequel l'injection est donc non polarisée en spin.

L'objectif de la première partie de ce chapitre était d'expliquer le principe des mesures de transport électroniques. Nous avons vu notamment que le courant collecté dans le silicium dépend de l'énergie des électrons injectés, qui doit être suffisante à l'arrivée pour permettre à l'électron de passer la barrière Schottky. Le courant collecté dépend aussi de la configuration magnétique des deux couches ferromagnétiques de la vanne de spin. En effet, nous avons vu que la différence de libre parcours moyen entre les électrons de spin majoritaire et ceux de spin minoritaire conduit à un courant plus important en configuration parallèle de la vanne de spin (I^P) comparé à la configuration où les aimantations sont perpendiculaires ($I^{\perp}$).

C'est ainsi que nous avons pu définir dans la deuxième partie ce que nous avons appelé le magnéto-courant croisé, qui s'exprime :

$$MC^{\perp} = (I^P - I^{\perp})/I^{\perp}$$

Nous avons alors étudié la dépendance du $MC^{\perp}$ avec la tension d'injection, avec le nombre de répétitions de la multicouche [Co/Ni], et avec la température. Nous avons en particulier observé l'augmentation du $MC^{\perp}$ avec le nombre de répétitions, pour aller jusqu'à 85% avec 5 répétitions, proche du maximum théorique de 100% atteignable avec une telle géométrie. En effet, l'augmentation du nombre de répétitions induit une augmentation de la polarisation en spin du courant d'électron et donc nécessairement une augmentation du $MC^{\perp}$.

Enfin, la dernière partie était consacrée à la vérification de la dépendance angulaire du MC prédite en cosinus de l'angle entre les aimantations de la vanne de spin. Pour cela, nous avons réalisé des mesures du courant collecté en fonction de l'angle du champ appliqué, pour différentes valeurs de champ. La simulation du comportement des aimantations avec l'angle, grâce à la minimisation de l'énergie totale (comprenant l'énergie Zeeman, l'énergie d'anisotropie et le champ démagnétisant), a permis de montrer que le courant collecté était bien proportionnel au produit scalaire des aimantations, et donc au cosinus de l'angle entre les deux couches magnétiques.

.

Chapter 7

Electronic spin precession - measurement principle

In this chapter, the third step of the magnetic tunnel transistor (MTT) construction is shown. Once the growth of a perpendicular magnetic layer on top of a Schottky diode is achieved, and after the necessary optimisation to obtain the maximum of magneto-current in the spin valve is done, the top layer growth can be realised.

In the first section, the growth of the top layer, which spin-polarises the injected electrons, is explained. The use of a CoFeB/MgO junction is demonstrated to be efficient in the injection of a current that is highly spin-polarised. The addition of an anti-ferromagnetic layer enables, via a strong exchange coupling, the pinning of the CoFeB layer. Thus, its magnetisation can be controlled independently of the one of the precession layer. The growth condition, in particular to obtain the desired textures, are shown.

In the second section, the theoretical expression of the transfer ratio of the MTT is demonstrated, especially as a function of the precession layer thickness. By combining the TR obtained in different magnetic configurations of the device, it is possible to reduce the number of unknown parameters and extract an expression that depends only on the precession angle and on the layer thickness.

I. Growth of the top layer

In order to study the electronic spin precession in a ferromagnetic layer, a MTT including three ferromagnetic layers with their magnetisations oriented in the three space directions is needed. In chapter IV of this thesis, we have seen the experimental work done to grow a $[\mathrm{Co}(0.2)/\mathrm{Ni}(0.6)]_n$ multilayer that exhibits a perpendicular magnetic anisotropy (PMA) on top of a Si//Cu Schottky diode. Then, the crossed magneto-current ($MC^{\perp}$) of the spin valve was optimised in chapter VI. It can reach more than 85% when the [Co/Ni] multilayer is repeated 5 times.

The last step of the MTT construction affects the hot electrons injection. A coherent electronic spin precession occurs in the second ferromagnetic layer of the MTT only if the hot electrons injected in the spin valve are spin-polarised. Therefore, a ferromagnetic layer must be grown on top of the tunnel barrier.

CoFeB(4)/MgO/CoFeB(4) magnetic tunnel junctions (MTJ) are known to present high tunnel magneto-resistance (TMR) ratios and will be used to inject hot electrons with high spin polarisation. Indeed, a TMR of 150% was already observed in the laboratory for a CoFeB/MgO/CoFeB tunnel junction. In the case of a symmetric junction in the Julliere model, the TMR can be expressed as a function of the polarisation power of the ferromagnetic layer:

$$TMR = \frac{2P^2}{1-P^2}$$

$$P = \sqrt{\frac{TMR}{2+TMR}}$$

With a TMR of 150%, a spin polarisation of 65% is found for the CoFeB layer. Here, we could measure a TMR of 50% in the MTT, giving a polarisation $P = 50\%$. That indicates that 75% of the injected electrons have a spin oriented in the direction of the CoFeB magnetisation, 25% have a spin in the other direction. The smaller value obtained here will be explained in the following by the [111] texture of the bottom layer.

Moreover, in order to get a crossed magnetisations configuration across the MTJ, which has two magnetic layers with an in-plane magnetic anisotropy, we used the pinning of one layer with an anti-ferromagnetic layer. We have chosen to fix the top layer to keep a flexibility on the precession layer. Thus, an IrMn anti-ferromagnetic layer is grown on top of the CoFeB ferromagnetic layer. Nevertheless, the highest exchange field is obtained if the IrMn layer is oriented along the [111] direction. In the same way as in the chapter IV, a thin amorphous Ta layer is deposited on top of the CoFeB layer. Then a Co layer can be grown according to its close packed planes, promoting the desired [111] texture for the IrMn layer. The final structure is:

$$...MgO(2.8)\ CoFeB(2)\ Ta(0.5)\ Co(2)\ IrMn(7.5)$$

After the sample growth, an annealing at 200^oC is realised during one hour. This temperature is larger than the Néel temperature of the anti-ferromagnetic layer but smaller than the Curie temperature of the ferromagnetic layer. Thus, the direction of the magnetic bias (also called exchange field) is fixed in the direction of a magnetic field that is applied during the annealing. The direction is set perpendicular to the easy axis of the precession layer.

Like the [Co/Ni] multilayer used as spin analysis layer, the top layer will be common for all the samples in the following. Figure VII.1 shows the energy landscape of the final MTT. Ferro 3 refers to the Ni(0.6) $[Co(0.2)/Ni(0.6)]_5$ multilayer which exhibits a perpendicular magnetic anisotropy. Ferro 1 is the CoFeB(2) Ta(0.5) Co(2) IrMn(7.5) top layer which spin-polarises the hot electrons injected in the spin valve. Finally, this system enables the study of the electronic spin precession in different active layers (Ferro2). In the next chapters, the spin precession will be measured in a Co layer (chapter VIII), in a CoFeB layer (chapter IX) and in a CoAl alloy (chapter X).

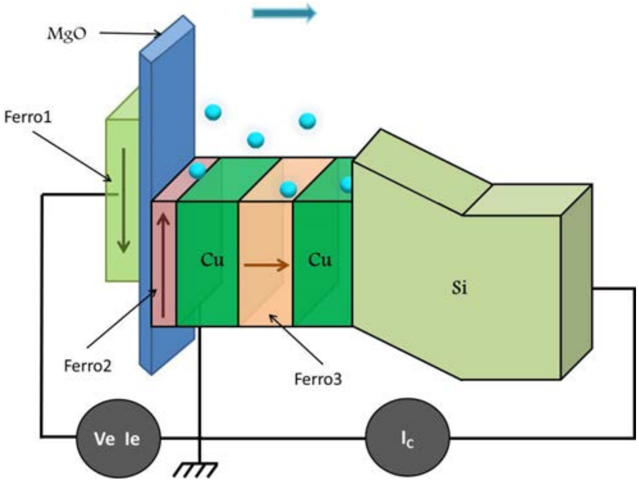

Fig. VII.1: *Energy landscape of a crossed MTT. The top layer $CoFeB(2)$ $Ta(0.5)$ $Co(2)$ $IrMn(7.5)$ (Ferro1) spin-polarises the hot electrons injected via the MgO tunnel barrier. The precession occurs in Ferro2. The $Ni(0.6)$ $[Co(0.2)/Ni(0.6)]_5$ multilayer (Ferro3), which exhibits a PMA, analyses the final spin direction. Electrons must have enough energy to overcome the Schottky barrier in order to contribute to the collected current I_c.*

II. Principle of the measurement

In the previous chapter, we have experimentally demonstrated the theoretical expression of the collected current I_c as a function of the magnetic configuration of the Co(3) Cu(3.5) Ni(0.6) [Co(0.2)/Ni(0.6)]$_4$ spin valve. In the case of an injected current that is not spin-polarised, the collected current is:

$$I_c \;=\; I_c^{\perp}\;(1 + MC^{\perp}\;\overrightarrow{u_{Co}} \cdot \overrightarrow{u_{[Co/Ni]}})$$

in which $I_c^{\perp}$ is the current collected in a crossed configuration of the spin valve, $\overrightarrow{u_{Co}}$ and $\overrightarrow{u_{[Co/Ni]}}$ are respectively the directions of the Co and [Co/Ni] magnetisations.

From now on, in this chapter and all the following, a top layer has been added to spin-polarise the current injected in the spin valve. As a consequence, the intensity of the injected current I_e depends on the magnetic configuration of the tunnel junction. Thus, the collected current must be replaced by the transfer ratio $TR = I_c/I_e$ in the expression above, which deals only with what happens in the spin valve. Moreover, the electronic spin is not parallel to the Co magnetisation when the electrons enter in the [Co/Ni] multilayer, because of the spin precession. As a consequence, the transfer ratio is proportional to the scalar product between the spin direction and the direction of the [Co/Ni] multilayer:

$$TR \;=\; TR^{\perp}\;\left(1 + MC^{\perp}\;\overrightarrow{P} \cdot \overrightarrow{u_{[Co/Ni]}}\right)$$

with $\overrightarrow{P}$ the spin polarisation of the electrons coming out of the precession layer.

In the following, the TR will be theoretically expressed for the different configurations of the MTT.

First configuration

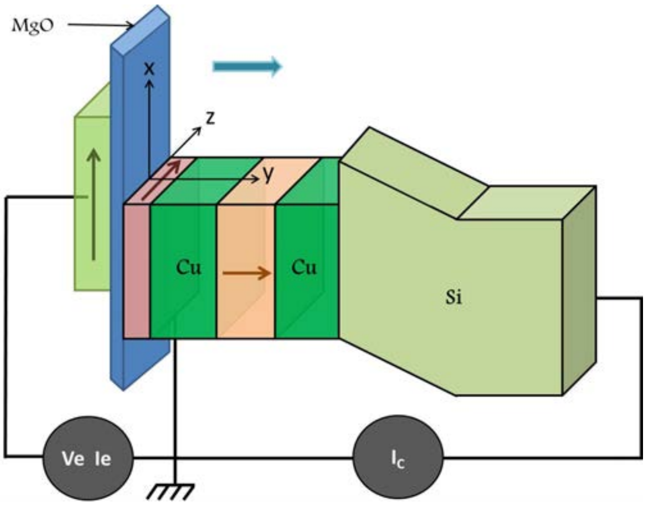

Fig. VII.2: Energy landscape of the MTT. The crossed configuration (crossed injection and crossed spin valve) enables the maximisation of the electronic spin precession.

In the case where the precession layer magnetisation is along the z axis and the initial polarisation $\overrightarrow{P_0}$ is parallel to the magnetisation of the top layer along the x axis, $\overrightarrow{P}$ can be expressed as:

$$\overrightarrow{P} = \begin{pmatrix} P_0 \sqrt{1-A^2}\ cos(\epsilon) \\ P_0 \sqrt{1-A^2}\ sin(\epsilon) \\ P_0\ A \end{pmatrix}$$

with $A = (I^{\uparrow} - I^{\downarrow})/(I^{\uparrow} + I^{\downarrow})$ the spin asymmetry in the precession layer, ϵ the precession angle and θ the spin filtering angle. Then, we assume the hypothesis of ballistic electrons, which means that both kind of electrons have travelled in the ferromagnetic a distance d which is the layer thickness. As a consequence, the current $I^{\uparrow(\downarrow)}$ in the precession layer is proportional to $exp\left(-d/\lambda^{\uparrow(\downarrow)}\right)$, d being the Co thickness and $\lambda^{\uparrow(\downarrow)}$ the mean free path of spin-up (spin-down) electrons. Thus, the spin asymmetry can be re-written as:

$$A \ = \ tanh\left(\frac{b.d}{2}\right) \qquad with \qquad b \ = \ \frac{1}{\lambda^{\downarrow}} - \frac{1}{\lambda^{\uparrow}}$$

Finally, the precession angle can be assumed to be proportional to the precession layer thickness: $\epsilon \ = \ a.d$. By projecting the polarisation along the y axis of the analyser ($\overrightarrow{u_{[Co/Ni]}} = \overrightarrow{u_y}$), the final expression of the transfer ratio is given by:

$$\begin{aligned} TR1 &= TR^{\perp}\left[1 + MC^{\perp}\ P_0\ \sqrt{1-A^2}\ sin(\epsilon)\right] \\ &= TR^{\perp}\left[1 + MC^{\perp}\ P_0\ \sqrt{1-tanh^2(b.d/2)}\ sin(a.d)\right] \end{aligned}$$

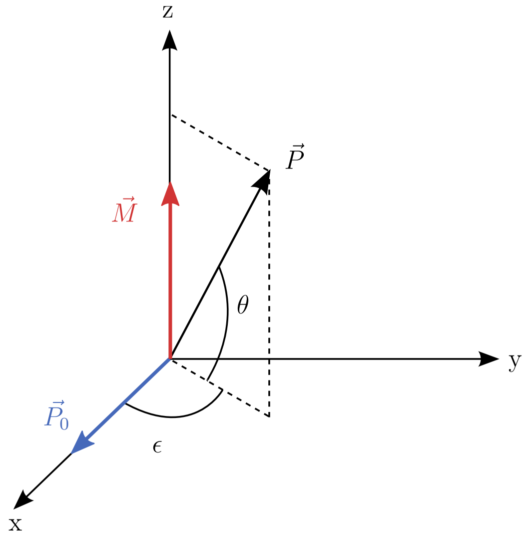

Fig. VII.3: *Schematic drawing of the precession angle (ϵ) and rotation angle linked to the spin filtering (θ) of the electronic spin polarisation vector $\vec{P}$ around the magnetisation $\vec{M}$ of a ferromagnetic layer oriented along the z-axis. The initial spin polarisation vector $\vec{P_0}$ is along the x-axis.*

This system with a crossed injection and a spin valve in a crossed configuration is the one that presents the best configuration to measure the electronic spin precession.

Second configuration

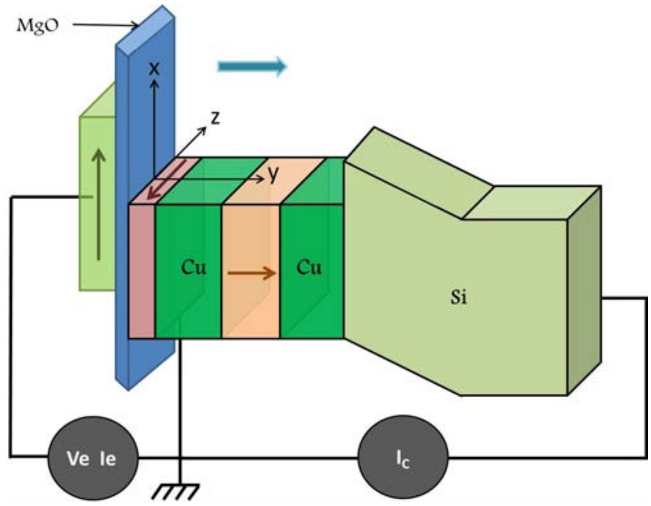

Fig. VII.4: Energy landscape of the MTT. The crossed configuration (crossed injection and crossed spin valve) enables the maximisation of the electronic spin precession. The magnetisation of the precession layer is in the opposite direction with respect to the first case.

This case is the same as before except the fact that the precession layer magnetisation is in the opposite direction. As a consequence, only the precession direction changes. The TR can be expressed by analogy with the previous calculations:

$$\begin{aligned} TR2 &= TR^{\perp}\left[1 + MC^{\perp}\ P_0\ sin(-a.d)\ \sqrt{1 - tanh^2(b.d/2)}\right] \\ &= TR^{\perp}\left[1 - MC^{\perp}\ P_0\ sin(a.d)\ \sqrt{1 - tanh^2(b.d/2)}\right] \end{aligned}$$

Third configuration

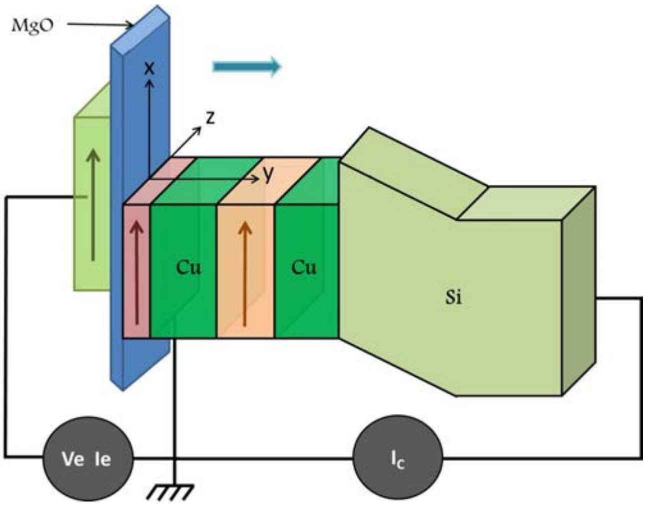

Fig. VII.5: Energy landscape of the MTT. A strong magnetic field saturates all the magnetisations in the same direction.

Here, there is no precession and no spin filtering that occurs in the active layer, the initial polarisation $\overrightarrow{P_0}$ being parallel to the precession layer magnetisation. Thus, the polarisation of the electrons coming out of the precession layer is the same as the polarisation of those coming in ($\overrightarrow{P} = \overrightarrow{P_0}$). The scalar product gives $\overrightarrow{P} \cdot \overrightarrow{u_{[Co/Ni]}} \; = \; P_0$ and the TR is expressed as:

$$TR3 \; = \; TR^{\perp} \left[1 + MC^{\perp} \, P_0 \right]$$

Expression of the electronic spin precession

The measurement in one magnetic configuration is not enough to extract a precession angle. Indeed, there is a lot of unknown quantities: $TR^{\perp}$, $MC^{\perp}$ and P_0. Nevertheless, by combining the expressions of TR obtained in the three magnetic configurations of the MTT, the unknown parameters can be suppressed:

$$\begin{aligned} \Delta_{rel} TR \; &= \; \frac{TR1 - TR2}{2TR3 - TR1 - TR2} \\ &= \; sin(a.d) \, \sqrt{1 - tanh^2(b.d/2)} \end{aligned}$$

Thus, by measuring the TR of the parallel and the two crossed configurations of the MTT, and that for different precession layer thicknesses, it is possible to determine the precession angle a (in $^o/nm$).

III. Conclusion

In this chapter, the growth of the top layer that spin-polarises the electrons injected in the spin valve is demonstrated. The CoFeB/MgO junction is chosen since the spin polarisation of the injected current is highly spin-polarised. In order to introduce a magnetic bias, a IrMn anti-ferromagnetic layer is grown. A Ta(0.5)Co(2) stack is inserted in order to promote a [111] texture on the IrMn layer. The final top layer, which will be common to all the following samples, is:

$$...MgO(2.8)\ CoFeB(2)\ Ta(0.5)\ Co(2)\ IrMn(7.5)$$

In the second section, the angular dependence of the magneto-current demonstrated in the previous chapter is used. Thus, the theoretical expression of the transfer ratio is demonstrated as a function of the scalar product between the spin polarisation of the electrons entering in the analysis layer and the [Co/Ni] magnetisation:

$$TR \ = \ TR^{\perp}\ \left(1 + MC^{\perp}\ \overrightarrow{P} \cdot \overrightarrow{u_{[Co/Ni]}}\right)$$

Then, the different magnetic configurations of the MTT are considered. In the case of a crossed configuration in which the magnetisations are oriented in the three space directions, the TR is expressed as a function of the precession velocity a and the active layer thickness d (TR1). Unknown parameters are eliminated by combining this TR with the one (TR2) obtained in a second crossed configuration (in which only the precession is in the opposite direction) and with the one obtained in the parallel configuration (TR3).

$$\begin{aligned}\Delta_{rel}TR \ &= \ \frac{TR1 - TR2}{2TR3 - TR1 - TR2}\\ &= \ sin(a.d)\ \sqrt{1 - tanh^2(b.d/2)}\end{aligned}$$

Thus, by measuring the different TR for several precession layer thicknesses, the fit of $\Delta_{rel}TR = f(d)$ with the expression above leads to the determination of a, the precession velocity, and b which is linked to the spin filtering.

Résumé du chapitre :

Dans ce chapitre, nous passons à la dernière étape dans la construction de notre transistor tunnel magnétique (TTM). Puisque la croissance d'une couche à anisotropie perpendiculaire et l'optimisation du magnéto-courant croisé ont été réalisées dans les chapitres précédents, nous pouvons désormais ajouter la troisième couche ferromagnétique (couche supérieure) qui sert à polariser en spin les électrons injectés.

Nous avons choisi d'utiliser une jonction CoFeB/MgO car celle-ci a prouvé dans d'autres expériences au laboratoire qu'elle permettait d'injecter un courant d'électrons polarisés à hauteur de 50%. Afin d'assurer la configuration croisée des aimantations de la couche d'injection et de la couche de precession, il est nécessaire d'introduire un biais magnétique pour l'une d'entre elles. Afin de garder une flexibilité dans le choix de la couche de précession, nous avons ajouté à la couche supérieure une couche antiferromagnétique (IrMn). Le fort couplage d'échange qui existe entre un ferromagnétique et un anti-ferromagnétique permet de décaler le cycle M(H) de la couche d'une quantité appelé le champ d'échange. Cependant, la couche d'IrMn doit être orientée selon la direction cristallographique [111] pour maximiser le champ d'échange. Une fine couche de Ta et une couche de Co sont donc insérées : le Co croit selon ses plans denses [111] sur le Ta amorphe et promeut la bonne texture à l'IrMn.

La deuxième partie de ce chapitre était consacrée au développement de l'expression théorique du taux de transfert (TR) mesuré en fonction des configurations magnétiques du TTM. A partir de la dépendance angulaire du magnéto-courant démontrée au chapitre précédent, nous avons déterminé le taux de transfert pour les deux configurations croisées (TR1 et TR2) et pour la configuration parallèle (TR3). Nous avons montré ainsi que :

$$\begin{aligned}\Delta_{rel}TR &= \frac{TR1 - TR2}{2TR3 - TR1 - TR2} \\ &= sin(a.d)\,\sqrt{1 - tanh^2(b.d/2)}\end{aligned}$$

Avec a la vitesse de précession (en $^o/nm$) et $b = \frac{1}{\lambda^{\downarrow}} - \frac{1}{\lambda^{\uparrow}}$ lié à l'asymétrie en spin qui existe dans un matériau ferromagnétique. Par conséquent, la mesure des taux de transfert pour différentes épaisseurs de la couche active devrait permettre de déterminer des vitesses de précession.

Chapter 8

Electronic spin precession in a Co layer

In this chapter, the electronic spin precession measurements are done in a Co layer. Indeed, all the elementary bricks of the all-solid-state device are now ready: i) the top layer which spin polarises the electrons injected in the spin valve is made of CoFeB(2) Ta(0.5) Co(2) IrMn(7,5). The strong exchange coupling between the ferromagnetic layer and the anti-ferromagnetic one enables the introduction of a magnetic bias in the magnetic response and orientates this layer at 90^o of the direction of the precession layer magnetisation, ii) the magneto-current of the spin valve is optimised in respect to the number of repetition of the [Co/Ni] multilayer, iii) the analysis layer exhibits a perpendicular magnetic anisotropy, iv) the Schottky diode is an efficient energy filter.

The first and second section are dedicated to the experimental studies of a MTT with a 3nm and 10nm thick Co precession layer. At first, the efficiency of the injection will be shown. The tunnel magneto-resistance (TMR) will be measured and the different magnetic configurations of the tunnel junction will be obtained. In particular, the crossed configuration between the top layer magnetisation and the Co magnetisation will be demonstrated. Then, the TR will be measured as a function of the applied voltage in the different MTT configurations available in our device.

In the last section, the precession and spin filtering angles will be extracted from the fit of the experimental data with the theoretical expression demonstrated in the previous chapter. The Co molecular field will be also extracted from the Bloch equations.

I. Study of a MTT with a Co(3) precession layer

I.A. Magnetic behaviour

First of all, the global magnetic response of the MTT is measured: the layer of analysis (Ferro3) is the [Co/Ni] multilayer, which must exhibit a perpendicular magnetic anisotropy; the precession layer (Ferro2) and the top layer (Ferro1), which are respectively a Co(3) layer and a CoFeB(2) Ta(0.5)Co(2)IrMn(7.5) stack, have an in-plane magnetic anisotropy.

In figure VIII.1, the M(H) loops obtained for the Si[100](HF)//Cu(5)Ta(1)Cu(5) Ni(0.6) [Co(0.2)/Ni(0.6)]$_5$ Cu(3.5)Co(3) MgO(2.8) CoFeB(2) Ta(0.5) Co(2) IrMn(7,5) Pt(5) MTT with a magnetic field applied in the sample plane are shown. The field is applied along the direction of the exchange field on the left-hand side of the figure, and perpendicular to it on the right-hand side.

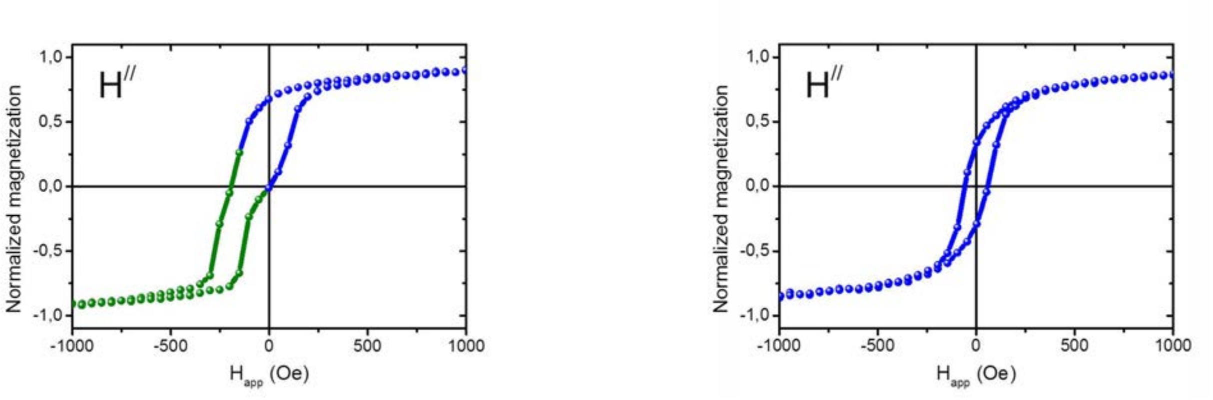

Fig. VIII.1: *M(H) loops of a* $Si[100](HF)//Cu(5)Ta(1)Cu(5)$ $Ni(0.6)[Co(0.2)/Ni(0.6)]_5$ $Cu(3.5)$ $Co(3)$ $MgO(2.8)$ $CoFeB(2)Ta(0.5)Co(2)IrMn(7,5)$ $Pt(5)$ *stack, with a field applied in the sample plane. The field is applied along the direction of the exchange field on the left-hand side and perpendicular to it on the right-hand side.*

When the field is applied along the direction of the exchange field, two hysteresis loops are observed. The first one, centered on zero field, has a coercive field of 200 Oe and corresponds to the magnetic response of the Co layer. Because of the small thickness of the Co layer, its magnetisation switches by creating ripple structures, *i.e.* domains in which the local magnetisation is distributed along the average magnetisation. As a consequence, the M(H) loop is rounded instead of straight. The second hysteresis, centered on H_{ex} = -200 Oe with a coercive field of

100 Oe, is due to the CoFeB(2)Ta(0.5)Co(2)IrMn(7.5) top layer.

When the field is applied perpendicular to the direction of the exchange field, the responses of both layers are superimposed. However, the little opening in the cycle can be attributed to the Co layer.

In figure VIII.2, the field is applied perpendicular to the sample plane.

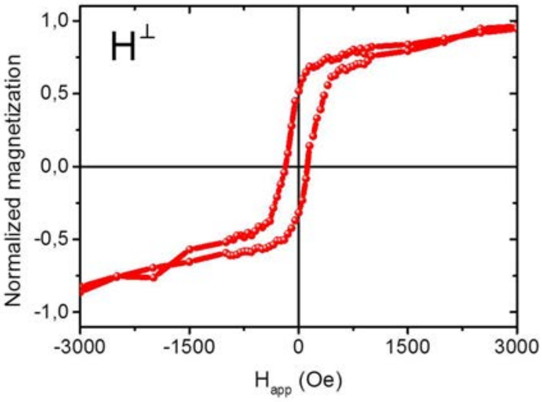

Fig. VIII.2: *M(H) loop of a* $Si[100](HF)//Cu(5)Ta(1)Cu(5)$ $Ni(0.6)[Co(0.2)/Ni(0.6)]_5$ $Cu(3.5)$ $Co(3)$ $MgO(2.8)$ $CoFeB(2)Ta(0.5)Co(2)IrMn(7,5)$ $Pt(5)$ *stack, with an applied field perpendicular to the sample plane*

With the field applied perpendicular to the sample plane, an hysteresis loop with a coercive field of 200 Oe is obtained. This corresponds to the magnetic response of the [Co/Ni] multilayer that exhibits a PMA.

Thus, our MTT is perfectly efficient from a magnetic point of view:

- It includes three ferromagnetic layers, in particular one with a PMA.
- From the in-plane M(H) curve, it is difficult here to show that a crossed configuration can be obtained. Furthermore, due to the technological process, the square shape given to the junction can change the in-plane response. This will be verified in the tunnel junction characterisation.

Other technical specifications are necessary to achieve the electronic spin precession measurements. We have already shown in Chapter IV that the Si//Cu Schottky diode is a good energy filter if the Si substrate is cleaned in a bath of hydrofluoric acid (HF 0.2%) for 3 minutes. The last characterisation needed is the one of the magnetic tunnel junction (MTJ), which is made in the next part.

I.B. Characterisation of the tunnel junction

I.B.1 Current in the tunnel junction as a function of the magnetic configuration between the ferromagnetic electrodes magnetisations

In this part, the current extracted from the MTJ (I_e) is measured as a function of the magnetic field, for an applied voltage V_e of -5mV. In figure VIII.3, the field is applied along the direction of the exchange field.

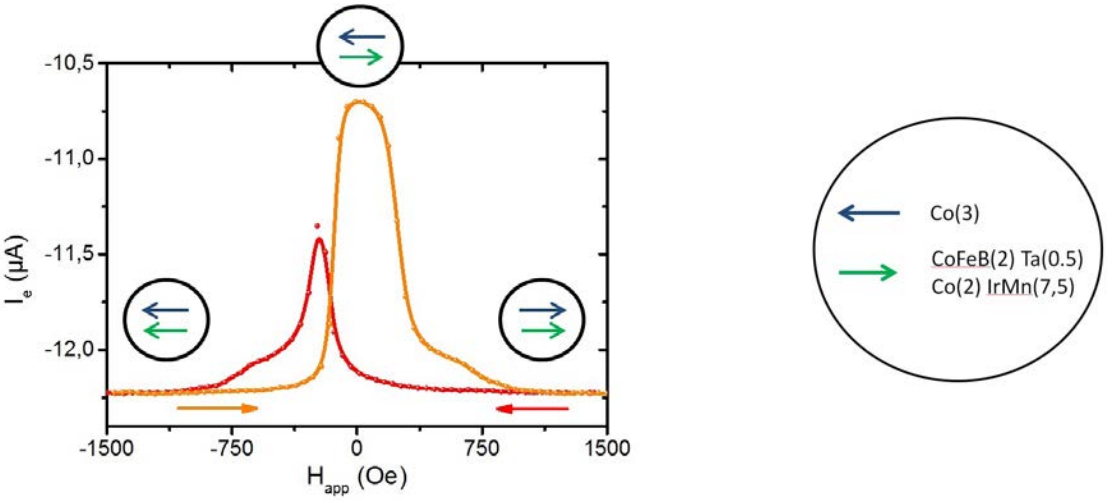

Fig. VIII.3: *Variation of the current extracted from the tunnel barrier (I_e) as a function of the in-plane magnetic field. The applied voltage is equal to $-5mV$ and the temperature is $60K$. In the insets, the magnetisation of Ferro1 (CoFeB(2)Ta(0.5)Co(2)IrMn(7.5)) is represented with a green arrow and the magnetisation of the Co(3) layer (Ferro2) with a blue arrow. In this case, the field is applied along the direction of the exchange field.*

At saturation, magnetisations of all the in-plane layers are parallel (current $I_e^P = -12.2\mu A$). When the field decreases (red curves), the magnetisation of the Co layer starts a rotation by creating ripple structures that reverse the Co magnetisation for an applied field of -200 Oe. At the same time, the top layer magnetisation switches. Both magnetisations are parallel again with a strong negative field of -1000 Oe . When the field is reversed and increases (orange curve), the top layer magnetisation switches at -100 Oe because of the magnetic bias, well before the ripple structures appear in the Co. Thus, the magnetisations are anti-parallel (current $I_e^{AP} = -10.75\mu A$), until the Co magnetisation switches at around 200 Oe.

This configuration does not allow us to obtain a crossed configuration of the tunnel junction, which is necessary for the measurement of the electronic spin precession, but it gives the full tunnel magneto-resistance (TMR) of the junction. Thus, I_e was measured also with an in-plane magnetic field applied perpendicular to the exchange field direction. The result is shown in figure VIII.4.

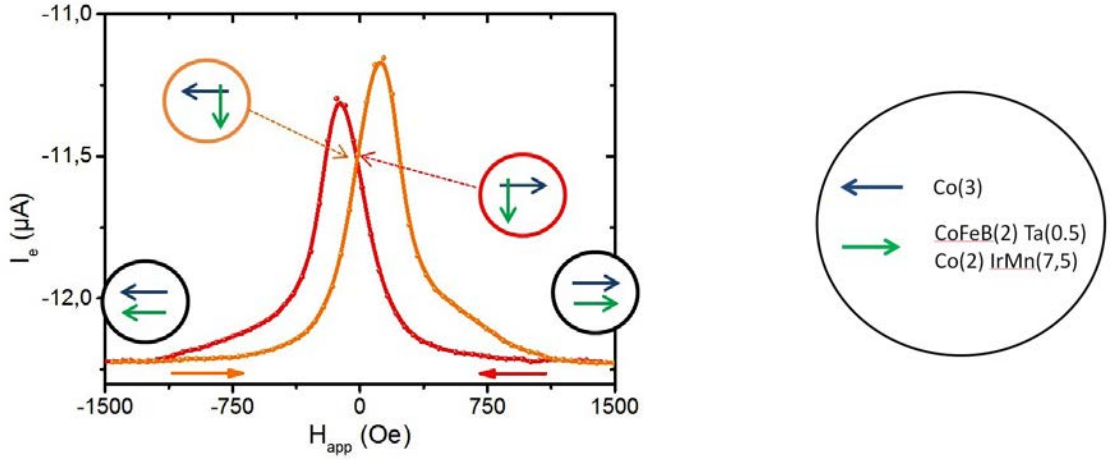

Fig. VIII.4: *Variation of the current extracted from the tunnel barrier (I_e) as a function of the in-plane magnetic field. The applied voltage is equal to $-5mV$ and the temperature is $60K$. In this case, the field is applied perpendicular to the exchange field.*

After a positive magnetic saturation, the CoFeB(2)Ta(0.5)Co(2)IrMn(7,5) magnetisation rotates progressively towards its easy direction when the field decreases, leading to a reduction of the current I_e. At zero field, the magnetisation of the Co layer and the magnetisation of the CoFeB(2)Ta(0.5)Co(2)IrMn(7,5) stack are crossed (current $I_e^{\perp} = -11.5\mu A$). In fact, we set the field angle in order to have the current at zero field that is the average of the current obtained in the parallel configuration and the one of the anti-parallel configuration ($I_e^{\perp} = 0.5\ (I_e^P + I_e^{AP})$). This technique ensures the obtention of the crossed configuration. If the field decreases again, the Co magnetisation switches at -150 Oe and the current increases until the saturation of both magnetisations at -2000 Oe. The curve is symmetric when the field increases after a negative saturation, but the crossed configuration obtained at zero field is different since the Co magnetisation is in the opposite direction (see insets in figure VIII.4).

I.B.2 Tunnel magneto-resistance

According to the previous part, it is possible to obtain the anti-parallel configuration of the tunnel junction with a magnetic field applied along the easy direction of the top layer (see figure VIII.3). After a negative saturation of the magnetisations (H_{app} = -3 kOe), the field is decreased until the magnetisation of the top layer switches, at around -100 Oe. The magnetisation of the Co layer has not switched yet, and the tunnel junction is in the anti-parallel configuration (current I_e^{AP}). The parallel configuration is obtained with a strong field (1 kOe), regardless of its direction in the sample plane (current I_e^P). The TMR can be deduced from this two measurements:

$$TMR = \frac{I_e^P - I_e^{AP}}{I_e^{AP}}$$

Its variation with the applied voltage V_e is shown in figure VIII.5:

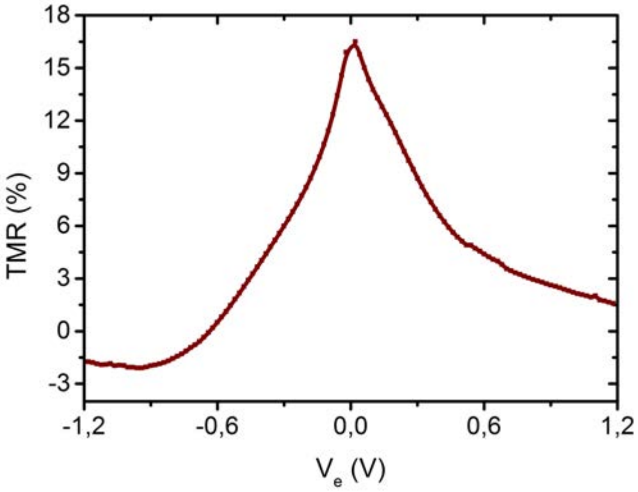

Fig. VIII.5: *TMR of the* $Co(3)$ $MgO(2.8)$ $CoFeB(2)Ta(0.5)Co(2)IrMn(7,5)$ *tunnel junction, as a function of the applied voltage* V_e*. The temperature is equal to* $60K$*.*

A maximum of 16.5% is obtained for the TMR at low voltages. This value is lower than the TMR of 150% obtained in the laboratory with a CoFeB/MgO/CoFeB tunnel junction. This is due to the use of Co instead of CoFeB. Indeed, a high TMR is a specificity of CoFeB/MgO/CoFeB junction with a [100] texture and is a consequence of symmetry filtering. Replacing CoFeB by Co, which in addition has certainly a [111] texture, decreases the symmetry filtering and the TMR is strongly reduced, down to $20 - 30\%$ like in a not-textured MTJ.

Nevertheless, the only important point is the fact that the top layer, which is always a CoFeB layer in this thesis, spin-polarises the injected electrons. Thus, even if the TMR measured in the case of a Co precession layer is small, the spin polarisation of the injected current is still high.

Under the applied voltage, the barrier is distorted because of the potential difference between the two ferromagnetic electrodes. This leads to a decrease of the TMR. First, the TMR decrease is monotonic. Then, the TMR even becomes negative for high voltages. In a free electron model, TMR is expected to decrease with voltage since electrons are injected in less polarised states at high energy. However, the polarisation of the injected electrons is not altered in first approximation.

The asymmetry of the curve is expected since both ferromagnetic electrodes of the tunnel junction are different: a Co layer on the one side, a CoFeB on the other side.

I.C. Transfer ratio as a function of the MTT configuration

I.C.1 Collected current I_c as a function of the applied field

Once the magnetic behaviour of the tunnel junction fully understood, the collected current in the semiconductor (I_c) can be measured as a function of the applied field. In figure VIII.6, a magnetic field is applied in the sample plane, perpendicular to the exchange field of the top layer.

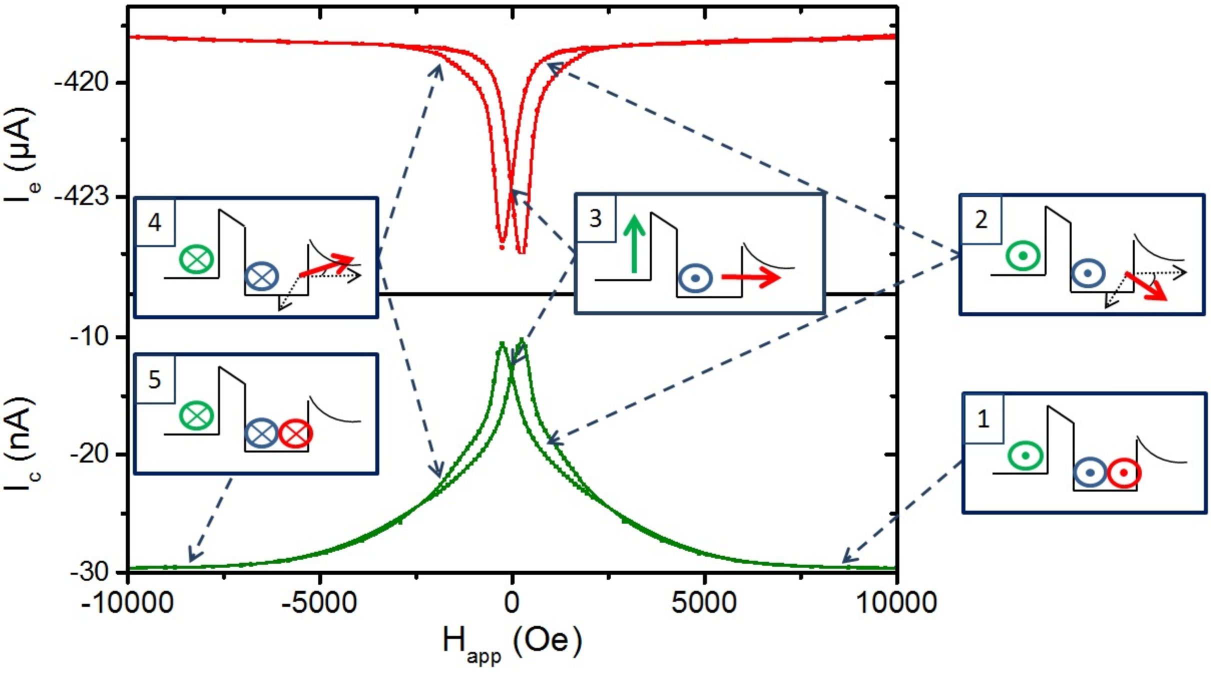

Fig. VIII.6: *Current extracted from the MTJ (I_e) and collected current I_c in the semiconductor as a function of the in-plane magnetic field, applied perpendicular to the exchange field of the top layer (Ferro1). The applied voltage is equal to $-900mV$. In the insets, the magnetisation of the [Co/Ni] multilayer (Ferro3) is represented with a red arrow, the magnetisation of the Co layer (Ferro2) with a blue arrow and the magnetisation of the $CoFeB(2)Ta(0.5)Co(2)IrMn(7,5)$ top layer (Ferro1) with a green arrow.*

To understand the variation of the collected current with the magnetic field, the current extracted from the tunnel barrier has been added in the figure. Different steps are identified in order to explain the curve:

1. When a strong in-plane field is applied (H_{app} = 10 kOe), all the magnetisations are saturated in the field direction, and the collected current is maximum (parallel injection; spin valve in a parallel configuration).

2. When the field intensity decreases, the magnetisation of the [Co/Ni] multilayer rotates progressively towards its easy direction, which is perpendicular to the sample plane (red arrow in the insets of figure VIII.6). The injection is still parallel, but the spin valve is between a parallel and a crossed configuration.

3. At around 1500 Oe, the magnetisation of the top layer (green arrow in figure VIII.7) begins to move towards its easy direction. At zero field, the crossed configuration expected to measure the electronic spin precession is obtained (crossed injection and crossed configuration of the spin valve).

4. At -150 Oe, the magnetisation of the Co layer switches (blue arrow in figure VIII.7), and the current increases again.

5. The parallel configuration is retrieved with a strong negative field of -10 kOe.

The behaviour is symmetric when the field is reversed and increases again.

The main conclusion of this curve is the fact that a configuration of the MTT where the three ferromagnetic layers have their magnetisations in the three space directions can be stabilised. This happens after a saturation of the magnetisations with a strong field (± 10 kOe), and a return at zero field. Moreover, it is possible to obtain two different crossed configurations of the tunnel junction, depending if the field increases after a negative saturation or decreases after a positive saturation. Indeed, the Co magnetisation is at zero field in the direction of the magnetic field, direction which depends on the sign of the saturation. The CoFeB(2)Ta(0.5)Co(2)IrMn(7,5) top layer has rotated towards its easy direction, which is always the same regardless of the sign of the saturation.

In this experiment, the field was applied along the hard direction of the top layer. This is of prime importance. Indeed, when the field decreases, the magnetisation of the CoFeB(2)Ta(0.5) Co(2)IrMn(7,5) layer rotates **uniformly** towards its easy axis: this is provided by the strong exchange coupling between the ferromagnetic and the anti-ferromagnetic layers. This should be not the case if the field was applied along the hard direction of the Co layer, which rotates by nucleation and propagation of domains. This point is very important in spin precession measurements, since the magnetisations must be uniform to not scramble the precession signal.

By injecting electrons with a spin perpendicular to the magnetisation of the active layer, a precession and a spin filtering will proceed. On the one hand, the amplitude of the spin filtering will be the same for the two crossed configurations of the tunnel junction evoked just before. On the other hand, the rotational direction of the spin precession will be different. By assuming that the spin filtering is not 100% in the precession layer, the direction of the electronic spin after the crossing of the precession layer will be different between the two crossed configurations of the tunnel junction, leading to a different collected current.

In the figure VIII.7, a summary of the MTT configurations as a function of the applied field is given.

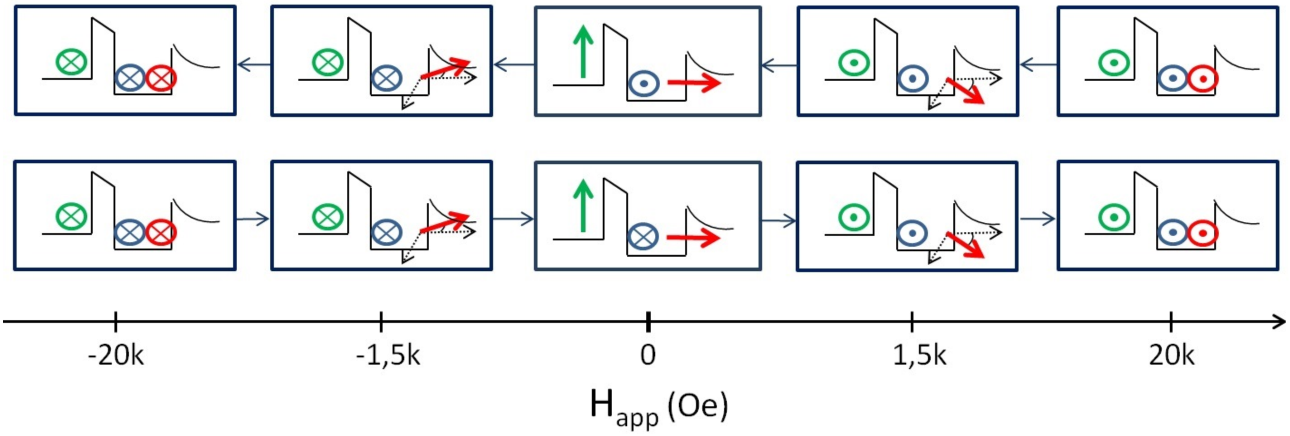

Fig. VIII.7: *Scheme of the MTT behaviour as a function of the in-plane magnetic field applied perpendicular to the exchange field of the top layer. The magnetisation of the* $[Co/Ni]$ *multilayer (Ferro3) is represented with a red arrow, the magnetisation of the Co layer (Ferro2) with a blue arrow and the magnetisation of the* $CoFeB(2)Ta(0.5)Co(2)IrMn(7,5)$ *top layer (Ferro1) with a green arrow. At zero field, two different crossed configurations can be stabilised.*

I.C.2 TR as a function of the applied voltage V_e

According to the previous results of this chapter, the transfer ratio $TR = I_c/I_e$ can be measured for different configurations of the MTT.

The parallel configuration is obtained with a strong magnetic field ($H_{app} = 10$ kOe), regardless of its direction. In this case, all the magnetisations are saturated in the field direction.

As seen before, it is possible to have a parallel or an anti-parallel configuration of the tunnel junction with an applied field along the exchange field.

When the field is applied in-plane, in a direction perpendicular to the exchange field, the two crossed configurations of the tunnel junction can be obtained at zero field, depending if the saturating field was positive or negative. In both cases, the magnetisation of the [Co/Ni] multilayer is perpendicular to the sample plane, and the spin valve is in a crossed configuration.

The results of these measurements are presented in figure VIII.8, where the $TR = I_c/I_e$ is shown as a function of the applied voltage V_e.

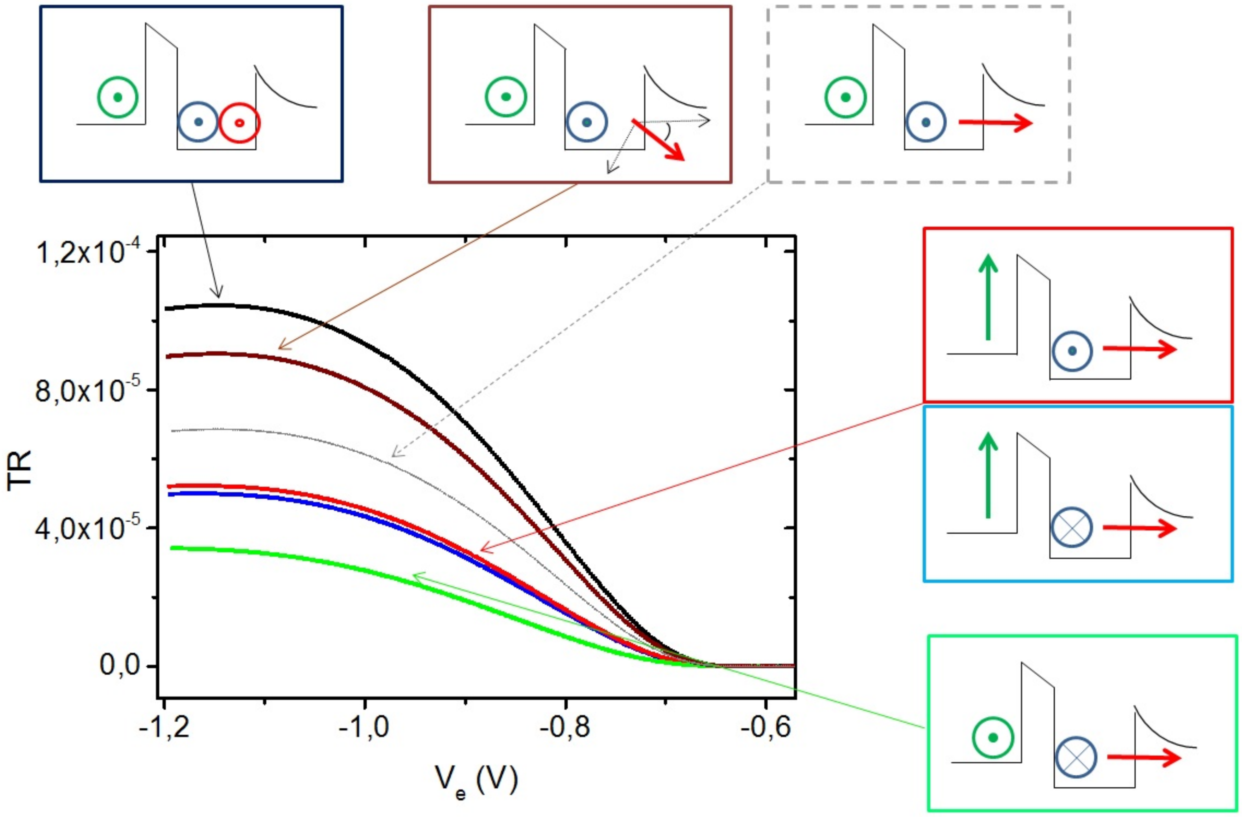

Fig. VIII.8: Transfer ratio of the $Si[100](HF)//Cu(5)Ta(1)Cu(5)$ $Ni(0.6)[Co(0.2)/Ni(0.6)]_5$ $Cu(3.5)$ $Co(3)$ $MgO(2.8)$ $CoFeB(2)Ta(0.5)Co(2)IrMn(7,5)$ $Pt(5)$ stack, for different magnetic configurations. In the insets, the magnetisation of the [Co/Ni] multilayer (Ferro3) is represented with a red arrow, the magnetisation of the Co layer (Ferro2) with a blue arrow and the magnetisation of the $CoFeB(2)Ta(0.5)Co(2)IrMn(7,5)$ top layer (Ferro1) with a green arrow.

The strongest TR is obtained for the parallel configuration (black curve), in which all the magnetisations are in the same direction. The lowest TR is measured for an anti-parallel injection and a crossed configuration of the spin valve (green curve).

A field of 3kOe is applied to obtain a parallel injection (brown curve). As a consequence, the magnetisation of the [Co/Ni] multilayer is between in-plane and out-of-plane. The angle α between the [Co/Ni] magnetisation and the direction perpendicular to the sample plane can be deduced from the measurement of the collected current as a function of the applied field (figure VIII.6). By assuming that the collected current varies like the cosine of the angle between the magnetisations of the Co layer and the [Co/Ni] multilayer, α has been determined equal to 40^o at 3kOe. Thus the TR can be corrected to correspond to the hypothetical configuration of the MTT with a parallel injection and a crossed spin valve (grey curve).

The main point here is that a different TR is measured between the two crossed configurations of the tunnel junction (red and blue curves). However, the current injected in the spin valve I_e is exactly the same in both cases, as shown in figure VIII.9, proving that the current injected is equivalent in both measurements.

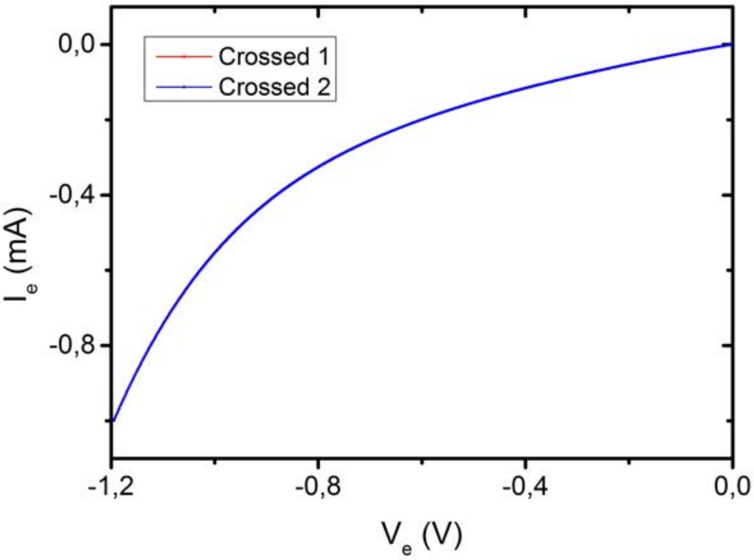

Fig. VIII.9: *Current extracted from the MTJ (I_e) as a function of the applied voltage V_e, for both crossed configurations of the tunnel junction.*

In the crossed configuration of the tunnel junction, the current I_e must be the average between the current in the parallel configuration and the anti-parallel configuration of the tunnel junction. Thus, the average TR between the parallel injection and the anti-parallel injection (grey and green curves) must be equal to the average TR of the two crossed injections (red and blue curve). This is demonstrated in figure VIII.10, where the orange curve is the average between green and grey curves. That point is a simple way to verify roughly if the tunnel junction is in a crossed configuration.

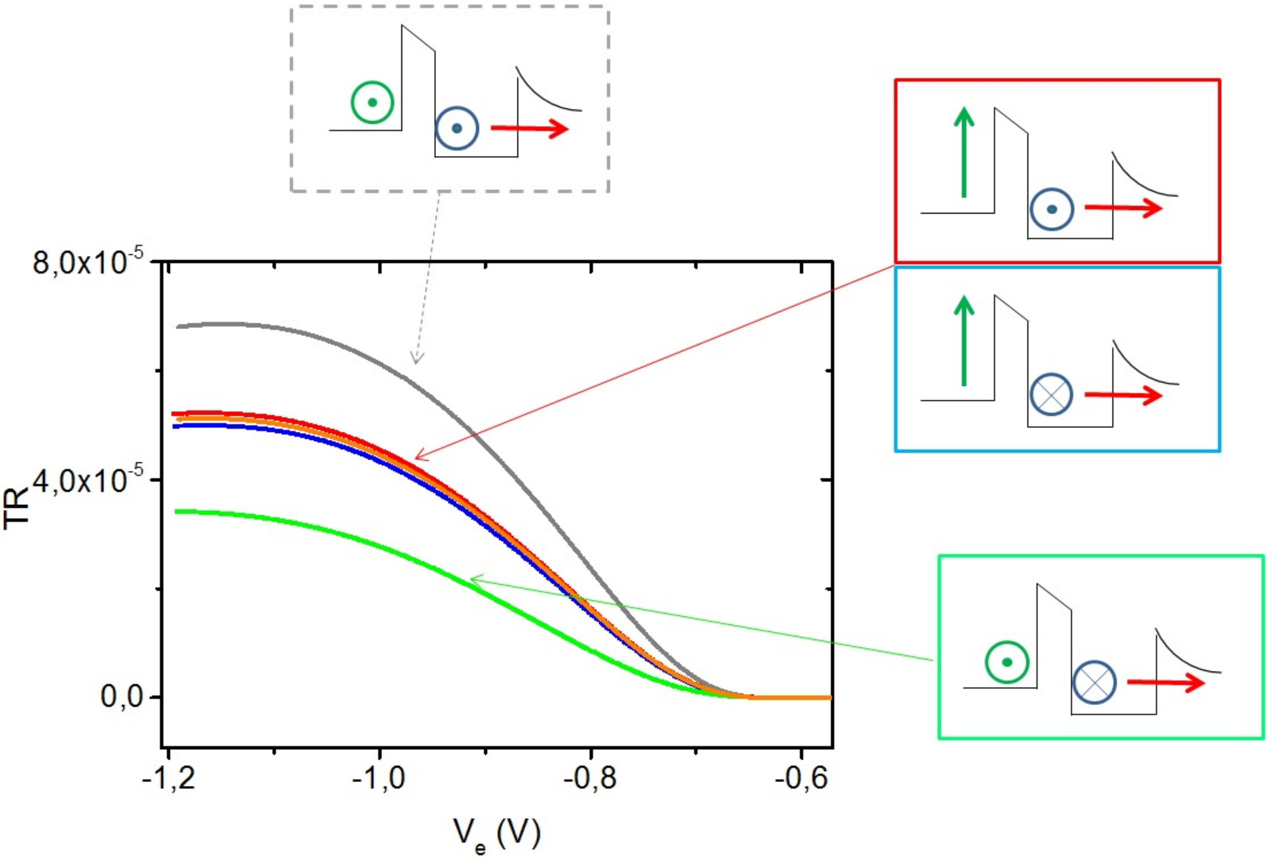

Fig. VIII.10: TR as a function of the applied voltage. The orange curve is the average between the grey curve (parallel injection) and the green curve (anti-parallel injection).

One would obtain the orange curve for the TR in the crossed configuration if the electronic spin were not precessing, or if the spin filtering were 100%. It is obvious in these experiments that 3nm of Co is not enough to rotate the spin in the magnetisation direction (spin filtering lower than 100%). Thus, the difference observed between the two crossed configurations (red and blue curves) is only an electronic spin precession effect.

As explained in the previous chapter, the important quantity to determine is:

$$\Delta_{rel}TR = \frac{TR1 - TR2}{2TR3 - TR1 - TR2}$$

in which $TR1$ and $TR2$ refer to the crossed configurations (red and blue curves in figure VIII.8), and $TR3$ is the TR of the parallel configuration (dark curve). The figure VIII.11 shows the variation of $\Delta_{rel}TR$ with the applied voltage.

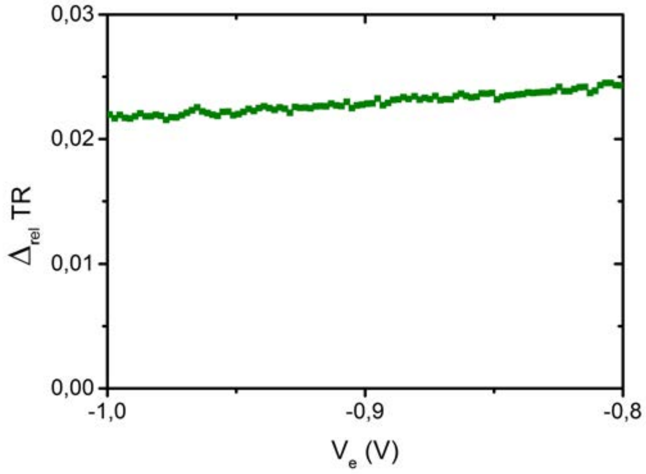

Fig. VIII.11: *Relative difference $\Delta_{rel}TR$ as a function of the applied voltage. The precession layer is a 3nm thick Co layer.*

$\Delta_{rel}TR$ does not change much within the small energy interval from 0.8 to 1eV above E_F, indicating an almost constant angle of precession. Only a slight decrease can be seen. Indeed, by assuming that the essential factor is the "time of journey" within the ferromagnet, then the precession angle is $\epsilon \propto 1/\sqrt{E_c}$, with E_c the kinetic energy of an electron within the sample. In the case of a Co layer, the inner potential is equal to 16eV. This is the energy gain if an electron from outside (in vacuum) enters the sample. As the hot electrons are directly created in the sample during these experiments (the electrons are injected via a tunnel barrier in our all-solid-state device), we have to subtract the work function of the metal (about 5eV) from the inner potential. Thus, an electron at the Fermi level has a kinetic energy of 11eV. As a consequence, the ratio between the precession angle at $E - E_F = 0.8eV$ and the precession angle at $E - E_F = 1eV$ is:

$$\frac{\epsilon(0.8eV)}{\epsilon(1eV)} = \sqrt{\frac{11+1}{11+0.8}} = 1.01$$

Thus, it is only a 1% effect which cannot be seen in the previous measurement.

In order to extract a precession angle, $\Delta_{rel}TR$ has to be measured for different Co thicknesses. In the next section, all the measurements presented above are repeated for a MTT with a Co(10) precession layer.

II. Study of a MTT with a Co(10) precession layer

II.A. Magnetic behaviour

In this section, the precession layer is a 10nm thick Co layer. The magnetic behaviour of the sample has been measured with an in-plane magnetic field, applied parallel or perpendicular to the exchange field. The results are shown in figure VIII.12.

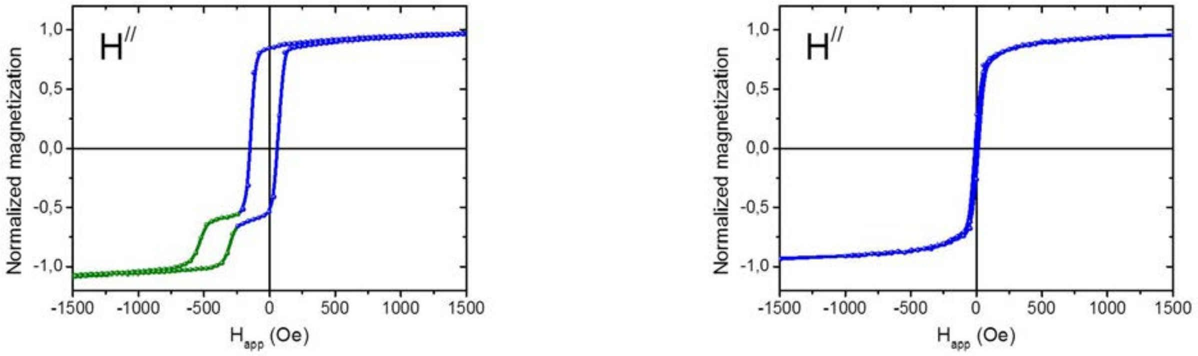

Fig. VIII.12: *M(H) loops of a* $Si[100](HF)//Cu(5)Ta(1)Cu(5)$ $Ni(0.6)[Co(0.2)/Ni(0.6)]_5$ $Cu(3.5)$ $Co(10)$ $MgO(2.8)$ $CoFeB(2)Ta(0.5)Co(2)IrMn(7,5)$ $Pt(5)$ *stack. The in-plane field is applied along the direction of the exchange field on the left-hand side and perpendicular to it on the right-hand side.*

When the field is applied along the direction of the exchange field, two hysteresis loops are observed: it is an easy direction for both layers. The first one, centered on zero field, has a coercive field of 100 Oe and corresponds to the magnetic response of the Co layer. With a Co thickness larger than in the previous section, the M(H) loop is straight and no ripple structures are created. The second hysteresis is due to the CoFeB(2)Ta(0.5)Co(2)IrMn(7,5) top layer. Centered on H_{ex} = -400 Oe, the coercive field is equal to 120 Oe. The main contribution to the in-plane magnetisation is due to the 10nm thick Co layer (blue part of the curve).

When the field is applied perpendicular to the direction of the exchange field, the responses of both layers are superimposed.

In figure VIII.13, the field is applied perpendicular to the sample plane.

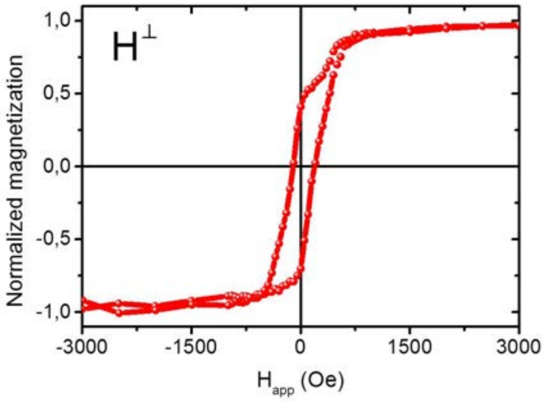

Fig. VIII.13: *M(H) loop of a* $Si[100](HF)//Cu(5)Ta(1)Cu(5)$ $Ni(0.6)[Co(0.2)/Ni(0.6)]_5$ $Cu(3.5)$ $Co(10)$ $MgO(2.8)$ $CoFeB(2)Ta(0.5)Co(2)IrMn(7,5)$ $Pt(5)$ *stack, with an applied field perpendicular to the sample plane*

With the field applied perpendicular to the sample plane, an hysteresis loop with a coercive field of 200 Oe is obtained. This corresponds to the magnetic response of the [Co/Ni] multilayer which exhibits a PMA.

II.B. Characterisation of the tunnel junction

II.B.1 Current in the tunnel junction as a function of the magnetic configuration between the ferromagnetic electrodes magnetisations

The magnetisation of the Co layer switches in this case without creation of ripple structures. As a consequence, the variation of the current in the tunnel junction with the applied voltage is slightly different from the one observed with a Co(3) precession layer when the field is applied along the direction of the exchange field (figure VIII.14).

At saturation, all the magnetisations are parallel (current $I_e^P = -513\mu A$). When the field decreases (red curve), the first magnetisation to switch at -100 Oe is the Co one. The configuration is anti-parallel until the CoFeB(2)Ta(0.5)Co(2)IrMn(7,5) magnetisation switches at -520 Oe (current $I_e^{AP} = -523\mu A$). When the field increases, the CoFeB(2)Ta(0.5)Co(2)IrMn(7,5) magnetisation switches first for an applied field equals to -280 Oe. The parallel configuration is obtained again when the Co layer switches at +100 Oe.

In this measurement, the current of the parallel configuration ($I_e^P = -513\mu A$) is smaller than the one of the anti-parallel configuration ($I_e^{AP} = -523\mu A$). Thus, the TMR is expected negative at this applied voltage ($V_e = -750mV$).

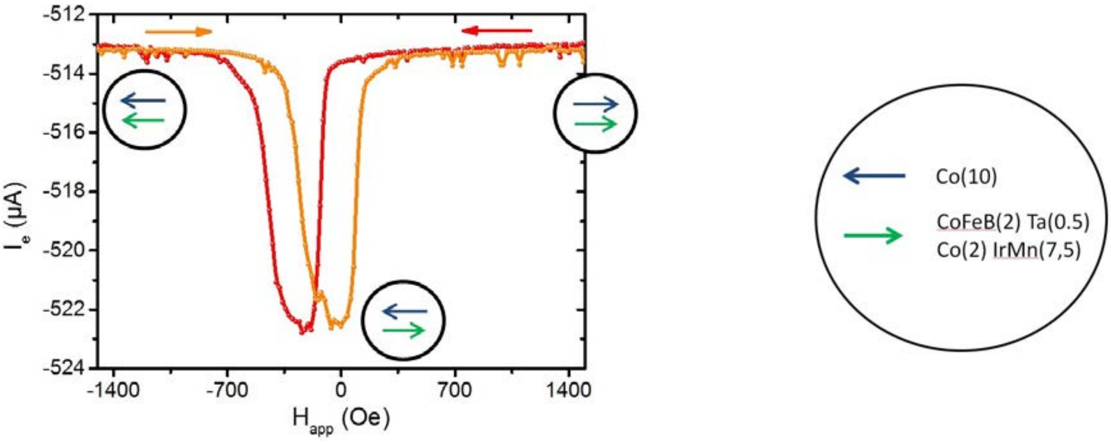

Fig. VIII.14: *Variation of the current in the tunnel barrier I_e as a function of the in-plane magnetic field. The applied voltage is equal to $-750mV$ and the temperature is $60K$. In the insets, the magnetisation of Ferro1 (CoFeB(2)Ta(0.5)Co(2)IrMn(7.5)) is represented with a green arrow and the magnetisation of the Co(10) layer (Ferro2) with a blue arrow. In this case, the field is applied along the direction of the exchange field.*

II.B.2 Tunnel magneto-resistance

The TMR of the tunnel junction has been measured between the parallel and the anti-parallel configurations of the tunnel junction, and its variation with the applied voltage V_e is shown in figure VIII.15.

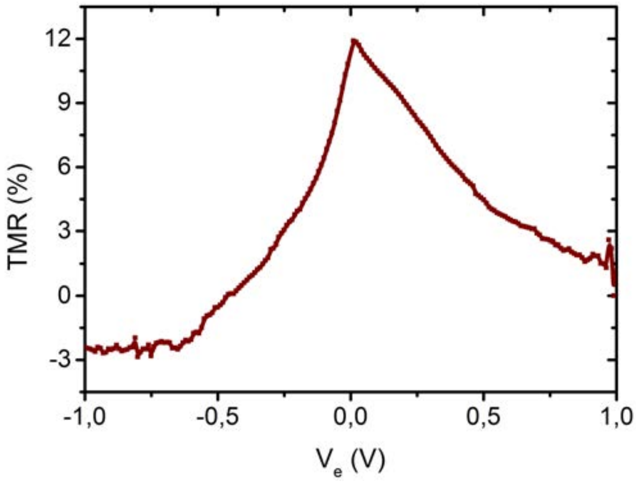

Fig. VIII.15: *TMR of the $Co(10)$ $MgO(2.8)$ $CoFeB(2)Ta(0.5)Co(2)IrMn(7,5)$ tunnel junction, as a function of the applied voltage V_e. The temperature is equal to $60K$.*

The maximum of TMR obtained at low voltages is equal to 12%, slightly lower than the TMR obtained with 3nm of Co. Once again, the curve is strongly asymmetric because of the different ferromagnetic materials used in the two sides of the tunnel junction. A negative TMR is observed for applied voltages smaller than $-500mV$.

II.C. Transfer ratio as a function of the MTT configuration

Once the magnetic behaviour of the tunnel junction is understood, the variation of the TR as a function of the applied voltage can be measured for different configurations of the MTT. The results are shown in figure VIII.16.

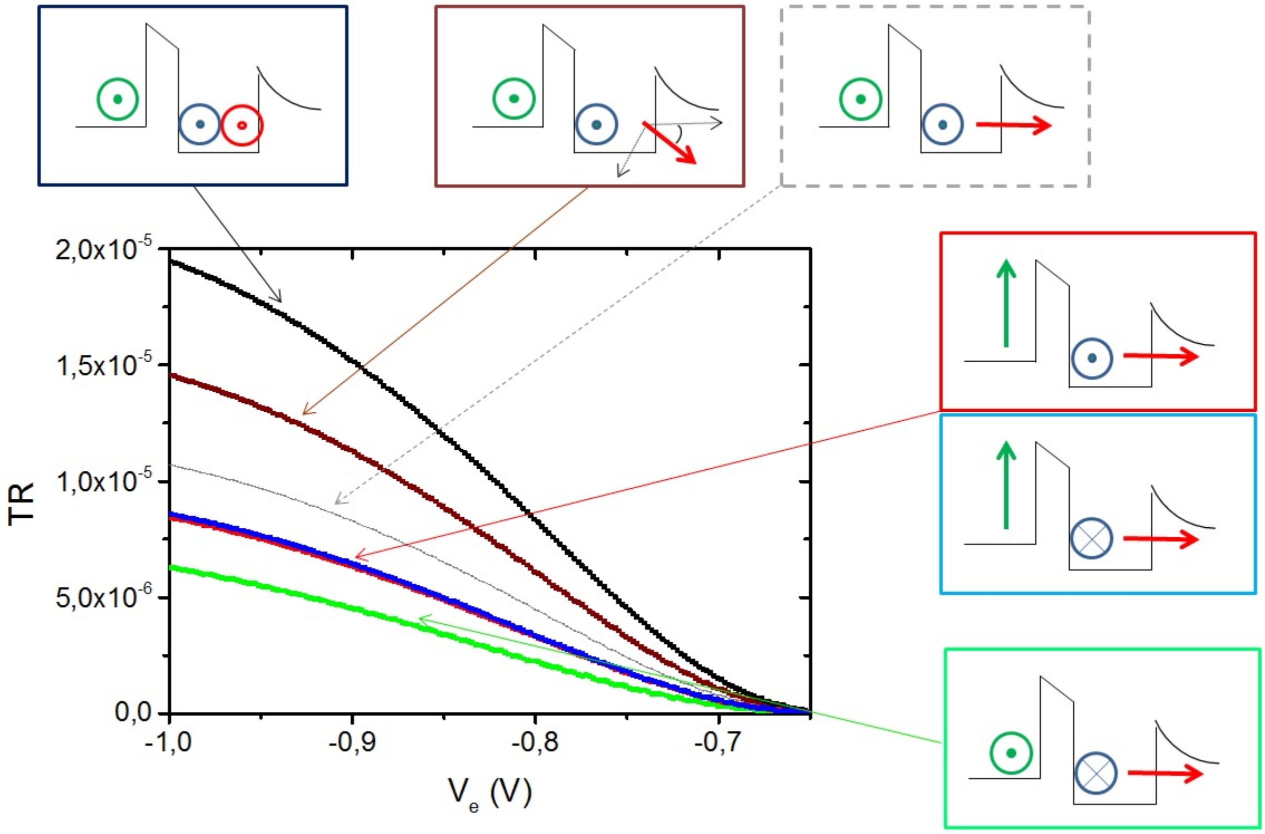

Fig. VIII.16: Transfer ratio of the $Si[100](HF)//Cu(5)Ta(1)Cu(5)$ $Ni(0.6)[Co(0.2)/Ni(0.6)]_5$ $Cu(3.5)$ $Co(10)$ $MgO(2.8)$ $CoFeB(2)Ta(0.5)Co(2)IrMn(7,5)$ $Pt(5)$ *stack, for different magnetic configurations. In the insets, the magnetisation of the* $[Co/Ni]$ *multilayer (Ferro3) is represented with a red arrow, the magnetisation of the Co layer (Ferro2) with a blue arrow and the magnetisation of the* $CoFeB(2)Ta(0.5)Co(2)IrMn(7,5)$ *top layer (Ferro1) with a green arrow.*

The TR are, in this case, almost ten times smaller than with 3nm of Co. The largest TR is obtained for the parallel configuration of the MTT (magnetisations of the three ferromagnetic layers oriented in the same direction, black curve), and the lowest TR for the anti-parallel configuration of the tunnel junction (green curve). The grey curve corresponds to the correction brought to the brown one (parallel injection), by taking into account that the [Co/Ni] magnetisation is not perfectly perpendicular to the sample plane.

The figure VIII.17 shows the injected current as a function of the applied voltage, for the two crossed configurations of injection. The current in both cases is exactly the same, showing that the difference observed in the TR is again caused by the spin precession.

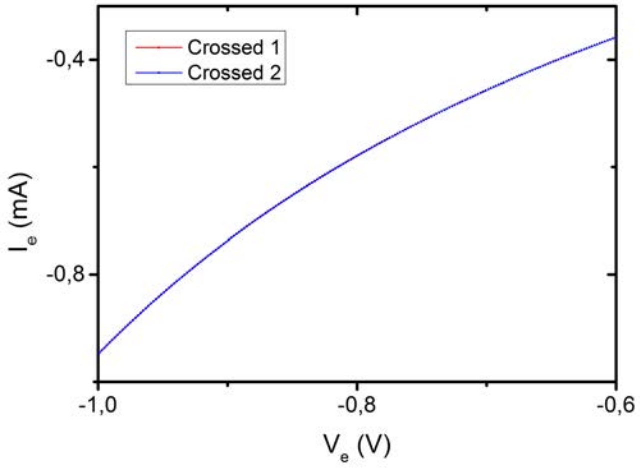

Fig. VIII.17: *Current extracted from the MTJ (I_e) as a function of the applied voltage V_e, for the two crossed configurations of the tunnel junction.*

The difference between the two crossed configurations is an effect of the electronic spin precession, and the important quantity $\Delta_{rel}TR$ is calculated as before. Its variation with the applied voltage is represented in the figure VIII.18.

It is clear that $\Delta_{rel}TR$ is smaller with 10nm of Co than with 3nm. Three hypotheses can explain that:

- First, $\Delta_{rel}TR$ can be equal to zero if the spin filtering is 100% efficient. In this case, the electronic spin is oriented along the direction of the Co magnetisation at the end of the layer. Thus, electrons arrive with their spins perpendicular to the magnetisation of the [Co/Ni] multilayer of analysis, regardless of the magnetic configuration of the tunnel junction.
- The second hypothesis is that the precession angle is a multiple of π. As a consequence,

the spin is oriented perpendicular to the [Co/Ni] multilayer at the end of the Co layer for both crossed configurations of the tunnel junction.

- The third hypothesis is that a strong decoherence of spins occurs for a large Co thickness, which induces a memory loss of the initial spin direction. Thus, the precession signal is scrambled by the random direction of spin. The diffusion of electrons can be a mechanism of spin decoherence. Indeed, if an electron, which was initially injected with a wave-vector perpendicular to the sample plane, is diffused and changes its trajectory, it will spend more time in the layer and the precession angle will be larger compared to a ballistic electron. Nevertheless, the Schottky diode has a small acceptance cone, that prevents electrons with a parallel wave-vector different from zero to enter the semiconductor (see chapter II).

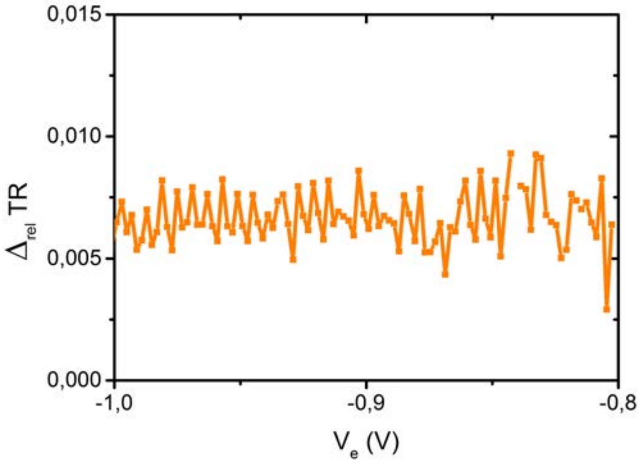

Fig. VIII.18: *$\Delta_{rel}TR$ as a function of the applied voltage. The precession layer of Co is 10nm thick.*

In the next section, the quantity $\Delta_{rel}TR$ obtained for two Co thicknesses will be fitted with the theoretical expression found in the previous chapter in order to extract the spin precession angle.

III. Electronic spin precession angle in Co

III.A. Determination of the spin filtering and precession angles

All the measurements shown above have for goal to extract $\Delta_{rel}TR = \frac{TR1-TR2}{2TR3-TR1-TR2}$ for different Co thicknesses. Only two samples could be grown with a Co precession layer in this thesis, with respectively 3nm and 10nm of Co. The figure VIII.19 shows the curve of $\Delta_{rel}TR$ as a function of the applied voltage in both cases.

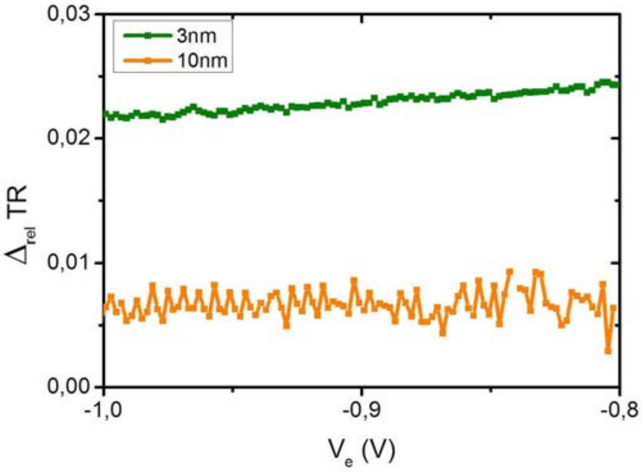

Fig. VIII.19: *Relative difference of the transfer ratios* $\Delta_{rel}TR = \frac{TR1-TR2}{2TR3-TR1-TR2}$ *as a function of the applied voltage. The green and orange curves correspond respectively to the cases of a Co layer 3nm and 10nm thick.*

Then, the experimental points are fitted with the theoretical variation of $\Delta_{rel}TR$ with the Co thickness (d):

$$\Delta_{rel}TR = \ sin(a.d)\ \sqrt{1 - tanh^2(b.d/2)}$$

An example is shown in figureVIII.20, in which the experimental points are extracted from the previous figure at $V_e = -965mV$.

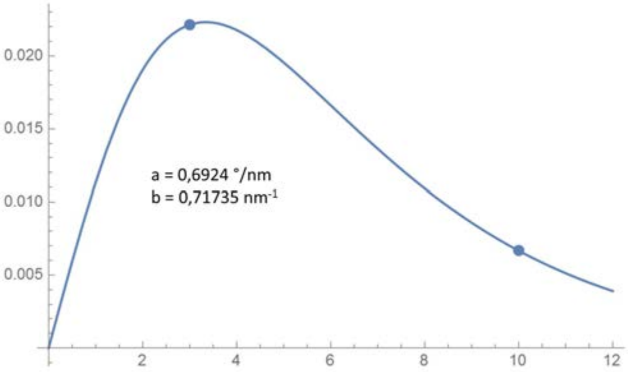

Fig. VIII.20: *Relative difference of the transfer ratios* $\Delta_{rel}TR = \frac{TR1-TR2}{2TR3-TR1-TR2}$ *as a function of the Co thickness. The continuous line is the fit, and the point corresponds to the experimental data taken at* $V_e = -965mV$.

The same procedure has been done for each value of the applied field, in order to obtain a, which corresponds to the precession angle per nanometer of the active layer, and $b = 1/\lambda^{\downarrow} - 1/\lambda^{\uparrow}$. The results are shown in figure VIII.21:

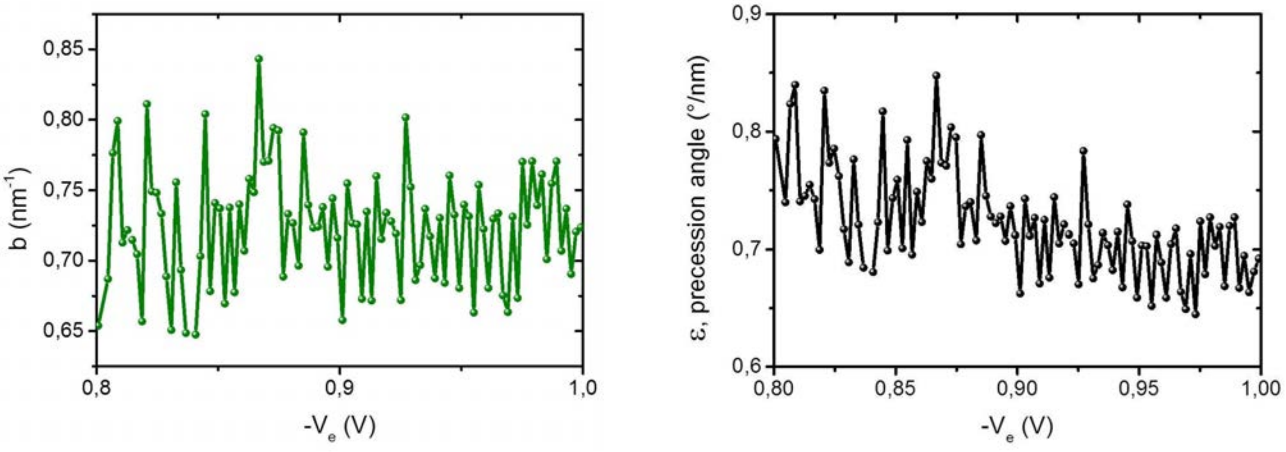

Fig. VIII.21: *Left: variation of $b = 1/\lambda^{\downarrow} - 1/\lambda^{\uparrow}$ with the applied voltage. Right: precession angle ϵ per nanometer of Co as a function of the applied voltage. Each point is obtained by fitting the curve of $\Delta_{rel}TR$ as a function of the Co thickness.*

No real trend can be deduced from the curve of the parameter b as a function of the applied voltage. Thus, b is assumed to be constant in our range of energy. An average value of $b = (0.72 \pm 0.04) nm^{-1}$ is calculated between 0.8 and $1eV$ above the Fermi level, close to the one that can be calculated with the mean free paths extracted from previous experiments for a Co layer at room temperature. With $\lambda^{\uparrow} = 5.5nm$ and $\lambda^{\downarrow} = 1nm$, $b = 1/\lambda^{\downarrow} - 1/\lambda^{\uparrow}$ is calculated equal to $0.82nm^{-1}$, only 13% higher than the value determined in this work. However, the value of the mean free paths tabulated was measured at room temperature, and they can be slightly different at our measurements temperature (50K): a decrease of b when the temperature decreases is expected since the mean free paths are larger at low temperature.

Then, the spin filtering angle θ can be extracted:

$$\theta = ArcTan\left[\frac{tanh(b.d/2)}{\sqrt{1 - tanh^2(b.d/2)}}\right]$$

Its variation with the Co thickness is shown in figure VIII.22.

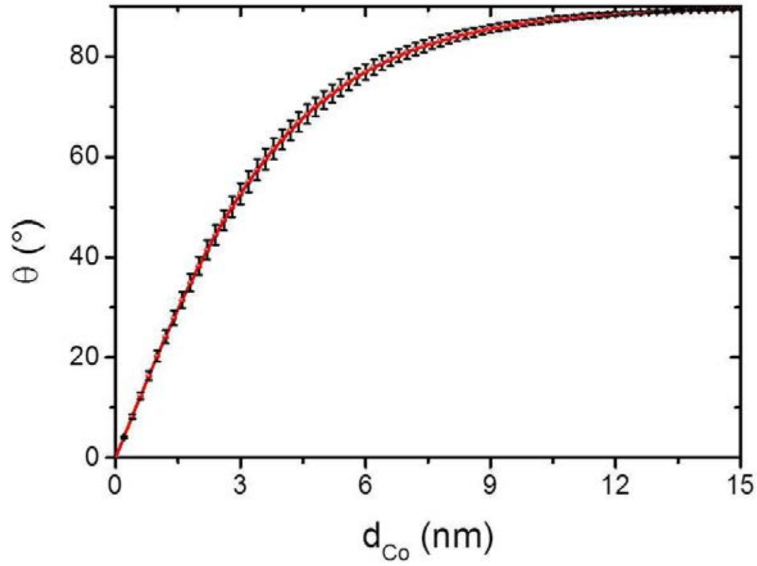

Fig. VIII.22: *Spin filtering angle as a function of the Co thickness, for an average energy of $0.9eV$ above the Fermi level.*

In contrast to b, the precession angle in figureVIII.21 seems to decrease with the energy: a precession velocity of $\epsilon = 0.7^o/nm$ is determined at $1eV$ and $\epsilon = 0.8^o/nm$ at $0.8eV$ above the Fermi level. In his work, Weber *et al.* had found a precession angle of $18^o/nm$ at $8eV$ above the Fermi level in a Co layer [37]. He had also shown that the precession angle is proportional to $1/\sqrt{E}$ in his energy range ($E - E_F > 4eV$). The values of precession determined in this thesis are not in agreement with the results of Weber *et al.* if the $1/\sqrt{E}$ law is maintained at low energy.

III.B. Determination of the molecular field

In our experiment, the spin relaxation in the direction of the precession layer magnetisation is fast. As a consequence, we have to consider the Bloch equations like in experiments of nuclear magnetic resonance. In these equations, the component of the spin parallel to the molecular field relaxes differently from the perpendicular components. In the following, we note $\overrightarrow{U}$ the average direction of the electronic spin.

When a static magnetic field is applied, the rotation of $\overrightarrow{U}$ towards $\overrightarrow{H} = H\overrightarrow{u_z}$ is done at a constant velocity proportional to $U_0 - U_z(t)$ ($U_0 =\mid \overrightarrow{U} \mid$):

$$\frac{dU_z}{dt} = \frac{1}{T_1}\left(U_0 - U_z(t)\right)$$

This simple equation can be solved as:

$$U_z(t) \;=\; U_0\,\left(1 - e^{-t/T_1}\right)$$

The characteristic time T_1 can be obtained by fitting the temporal variation of $U_z = sin(\theta)$ with a decaying exponential. The result is shown in figure VIII.23.

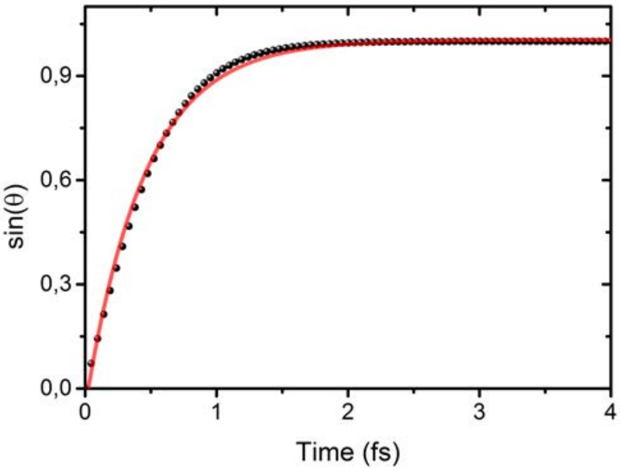

Fig. VIII.23: *Spin filtering angle as a function of the time spent in the Co layer at* $1eV$ *above the Fermi level. The continuous red line is the best fit obtained with a decaying exponential.*

Thus, a characteristic time $T_1 = 0.45fs$ is obtained.

For the temporal evolution of the perpendicular components $\overrightarrow{U_{xy}}$, an other effect has to be taken into account. Indeed, each electron feels a local magnetic field that fluctuates in time and in space. As a consequence, all the spins do not precess exactly at the same frequency but at a frequency distributed around the Larmor frequency ω_L. This leads to a decoherence between the spins, and a fast reduction of the in-plane average spin direction with a characteristic time T_2:

$$\frac{d\overrightarrow{U_{xy}}}{dt} \;=\; \gamma\,\overrightarrow{U_{xy}} \times \overrightarrow{H} \;-\; \frac{1}{T_2}\overrightarrow{U_{xy}}$$

The solution of these equations is:

$$U_x(t) \;=\; [\;U_x(0)cos(\omega_L t) - U_y(0)sin(\omega_L t)\;]\;\; e^{-t/T_2}$$

$$U_y(t) \;=\; [\;U_x(0)cos(\omega_L t) + U_y(0)sin(\omega_L t)\;]\;\; e^{-t/T_2}$$

The main conclusion is that the precession is made at the Larmor frequency $\omega_L = \gamma H$, with γ the gyromagnetic factor of an electron. In our case, we have found a precession angle of 0.7^o per nanometer of Co at $1eV$ above the Fermi level. To determine the equivalent frequency, we have to calculate the time that an electron spends to cross the precession layer. The velocity of an electron is $v = \sqrt{2E/m_e}$, in which $E = E_F + qV_e$ with $E_F = 11.7eV$ in the case of the Co precession layer. Thus, the time to go through 1nm of Co is $\tau = 0.473fs$ at $1eV$ above the Fermi level. This leads to a Larmor frequency $\omega_L = 2.58 \cdot 10^{13}\ rad.s^{-1}$, and a molecular field of $152T$.

Let us determine an approximate value of the molecular field in a simple way. The exchange energy between two spins can be written via the Heisenberg Hamiltonian as:

$$\begin{aligned} E_{exch} &= \sum_{<i,j>} J_{ij}\ \overrightarrow{\mu_i}\ \overrightarrow{\mu_j} \\ &= \frac{1}{2}\ \sum_i \overrightarrow{\mu_i} \sum_{j \neq i} J_{ij}\ \overrightarrow{\mu_j} \end{aligned}$$

where the $\frac{1}{2}$ factor is introduced to avoid that the same contribution is counted two times. In the Weiss theory, the molecular field $\overrightarrow{H_{int}}$ is defined as the mean field that an individual spin probes, created by its nearest neighbours:

$$E_{exch} = \mu_0 \sum_i \overrightarrow{\mu_i}\ \overrightarrow{H_{int}}$$

By combining the two last equations, the molecular field is:

$$\mu_0 \overrightarrow{H_{int}} = \frac{1}{2} \sum_{j \neq i} J_{ij}\ \overrightarrow{\mu_j}$$

If all the spins are oriented in the same direction, we obtain:

$$\mu_0 \overrightarrow{H_{int}} = \frac{1}{2} \overrightarrow{\mu} J\ C$$

with C the occupancy. In the Weiss theory, the magnetisation can be also expressed as:

$$\overrightarrow{M} = \overrightarrow{\mu} \frac{N_{cell}}{V_{cell}}$$

with N_{cell} the number of atoms per unit cell, and V_{cell} its volume. Finally, the exchange parameter J being not tabulated, it is bound to the exchange stiffness A by:

$$J = \frac{aA}{C\mu}$$

in which a is the lattice parameter and C the occupancy. By combining all these equations, the molecular field is expressed as:

$$H_{int} = \frac{A\ N_{cell}}{2\mu_0\ M\ a^2}$$

By considering a b.c.c. Co layer, $N_{cell} = 2$, $a = 0.25nm$, and $\mu_0 M = 1.8T$. The exchange stiffness can be found equal to $15.10^{-12} Jm^{-1}$ in the literature [58]. Thus a molecular field of $167T$ is found, close to the value that we have determined ($152T$).

IV. Conclusion

In this chapter, the experimental study of a MTT including three ferromagnetic layers have been shown. The precession layer is made of Co for this chapter.

The first step has consisted in the characterisation of the tunnel junction as a function of the applied field. We have shown that a parallel, an anti-parallel and two different crossed configurations of magnetisations can be stabilised. This allows us to calculate in particular the TMR, which can reach at low voltages 16% and 12% when the precession layer is respectively 3nm and 10nm thick.

Then, the $TR = I_c/I_e$ is measured in different cases. We have shown in particular all the experimental cautions that had been taken so as to prove undoubtedly that the crossed configurations, which maximises the precession phenomenon (the three magnetisations are in the three space directions), are well obtained. In addition to the TR in the two crossed configurations (TR1 and TR2), the TR in the case where all the magnetisations are in the same direction under the influence of a strong magnetic field is also measured (TR3).

When these measurements have been made for different MTT (with a Co precession layer of 3nm and 10nm), $\Delta_{rel}TR$ can be fitted with its theoretical expression for each applied voltage:

$$\begin{aligned} \Delta_{rel}TR &= \frac{TR1 - TR2}{2TR3 - TR1 - TR2} \\ &= sin(a.d)\ \sqrt{1 - tanh^2(b.d/2)} \end{aligned}$$

with a the precession velocity (in $^o/nm$), d the Co thickness and $b = 1/\lambda^{\downarrow} - 1/\lambda^{\uparrow}$. b being almost constant in our energy range, an average value of $0.72nm^{-1}$ is calculated, enabling the determination of the spin filtering angle θ as a function of the Co thickness:

$$\theta \ = \ ArcTan\left[\frac{tanh(b.d/2)}{\sqrt{1 - tanh^2(b.d/2)}}\right]$$

The precession angle decreases with the energy: it is equal to $0.8^o/nm$ at $0.8eV$ and $0.7^o/nm$ at $1eV$ above the Fermi level.

By using the Bloch equations, we have determined that such precession can be obtained with a molecular field of $152T$. A simple model based on the molecular field theory leads to an estimated Co molecular field of $167T$, close to our experimental value.

Résumé du chapitre :

Dans ce chapitre, nous avons réalisé la première étude expérimentale d'un transistor tunnel magnétique (TTM) constitué de trois couches ferromagnétiques dont l'une possède une anisotropie perpendiculaire. Ce chapitre est consacré uniquement au cas d'une couche active de Co.

La première étape expérimentale a consisté en la caractérisation de la jonction tunnel pour différentes configurations magnétiques. Avec un champ magnétique appliqué dans la direction du champ d'échange de la couche supérieure, les configurations où les aimantations sont parallèles ou antiparallèles peuvent être obtenues. Cela permet de calculer la magnétorésistance tunnel (MRT) :

$$MRT = \frac{I^{P} - I^{AP}}{I^{AP}}$$

Une MRT de 16% est mesurée pour l'échantillon contenant 3nm de Co et 12% pour celui avec 10nm de Co. Les configurations d'aimantations croisées sont obtenues avec un champ appliqué perpendiculairement au champ d'échange.

Le taux de transfert est ensuite mesuré pour chaque échantillon dans trois configurations magnétiques choisies. Nous avons montré notamment toutes les précautions expérimentales qui ont été prises afin de s'assurer de la bonne obtention des configurations triplement croisées (les trois couches ferromagnétiques ont leurs aimantations qui pointent dans les trois directions de l'espace). Nous avons ainsi déterminé $\Delta_{rel}TR$ pour deux épaisseurs de Co (3nm et 10nm).

L'utilisation de l'expression théorique démontrée au chapitre précédent nous a alors permis de déterminer une vitesse de précession dans le Co, qui varie entre $0.8^{o}/nm$ à 0.8eV au-dessus du niveau de Fermi et $0.7^{o}/nm$ à 1eV au-dessus du niveau de Fermi. Ainsi, le champ moléculaire permettant une telle précession est déterminée égale à 152T grâce à la simulation de la précession avec les équations de Bloch.

Chapter 9

Electronic spin precession in a CoFeB layer

In this chapter, the electronic spin precession measurements are done in a CoFeB layer. The same procedure as the one used for the spin precession measurements in a Co layer is applied here. Three magnetic tunnel transistors (MTT) have been grown with different CoFeB thicknesses, equal to 1nm, 3nm or 4nm.

In the first section, the tunnel junction of these three MTT will be characterised. In order to understand the behaviour of the current extracted from the magnetic tunnel junction (MTJ) with an applied field, the magnetic response of the samples will be shown at first. Then, the variation of the current extracted from the MTJ (I_e) with the field will be studied for an in-plane magnetic field applied parallel or perpendicular to the exchange field of the top layer.

Then, the transfer ratio (TR) will be measured for different magnetic configurations of the MTT as a function of the applied voltage. The important parameter $\Delta_{rel}TR$ is extracted for the three CoFeB thicknesses.

In the last section, the precession and spin filtering angles are extracted from the fit of the experimental data with the theoretical expression demonstrated in chapter VII. The CoFeB molecular field is then determined thanks to the Larmor frequency.

I. Characterisation of the tunnel junction

I.A. Case of a 1nm thick CoFeB layer

I.A.1 Magnetic properties

First of all, the global magnetic response of the magnetic tunnel transistor (*MTT)* is measured: the layer of analysis (Ferro3) is the [Co/Ni] multilayer that must exhibit a perpendicular magnetic anisotropy; the precession layer (Ferro2) and the top layer (Ferro1), which are respectively a CoFeB(1) layer and a CoFeB(2)Ta(0.5)Co(2)IrMn(7,5) stack, have an in-plane magnetic anisotropy.

In figure IX.1, the M(H) loops obtained for the Si[100](HF) // Cu(5)Ta(1)Cu(5) Ni(0.6) $[Co(0.2)/Ni(0.6)]_5$ Cu(3.5) CoFeB(1) MgO(2.8) CoFeB(2) Ta(0.5) Co(2) IrMn(7,5) Pt(5) MTT with a magnetic field applied in the sample plane are shown. The field is applied along the direction of the exchange field on the left-hand side of the figure, and perpendicular to it on the right-hand side.

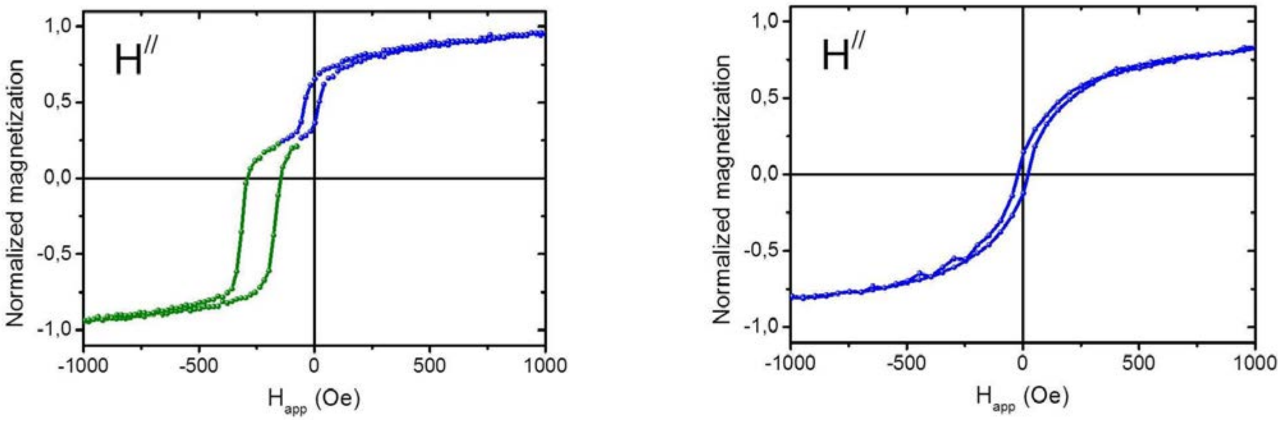

Fig. IX.1: *M(H) loops of a* $Si[100](HF)//Cu(5)Ta(1)Cu(5)$ $Ni(0.6)[Co(0.2)/Ni(0.6)]_5$ $Cu(3.5)$ $CoFeB(1)$ $MgO(2.8)$ $CoFeB(2)Ta(0.5)Co(2)IrMn(7,5)$ $Pt(5)$ *stack, with an applied field in the sample plane. On the left-hand side, the field is applied along the direction of the exchange field. On the right-hand side, the field is applied perpendicular to the direction of the exchange field.*

When the field is applied along the direction of the exchange field, two hysteresis loops are observed. The first one, centered on zero field, has a coercive field of 50 Oe and corresponds to the magnetic response of the CoFeB. The second hysteresis centered on H_{ex} = -250 Oe with a coercive field of 70 Oe is due to the CoFeB(2)Ta(0.5)Co(2)IrMn(7,5) top layer.

When the field is applied perpendicular to the direction of the exchange field, the responses of both layers are superimposed. However, the slight opening of the M(H) cycle around zero field can be attributed to the CoFeB precession layer.

In figure IX.2, the field is applied perpendicular to the sample plane.

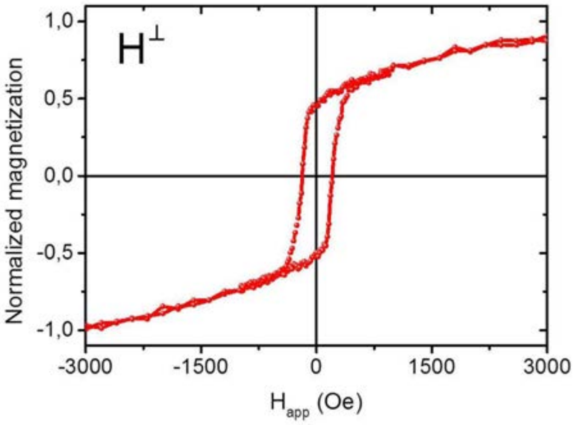

Fig. IX.2: *M(H) loop of a* $Si[100](HF)//Cu(5)Ta(1)Cu(5)$ $Ni(0.6)[Co(0.2)/Ni(0.6)]_5$ $Cu(3.5)$ $CoFeB(1)$ $MgO(2.8)$ $CoFeB(2)Ta(0.5)Co(2)IrMn(7,5)$ $Pt(5)$ *stack, with a field applied perpendicular to the sample plane.*

When the field is applied perpendicular to the sample plane, an hysteresis loop with a coercive field of 200 Oe is obtained, which corresponds to the magnetic response of the [Co/Ni] multilayer exhibiting a perpendicular magnetic anisotropy (PMA).

I.A.2 Magnetic configuration of the tunnel junction

In this part, the current extracted from the MTJ (I_e) is measured as a function of the magnetic field, for an applied voltage V_e of -750mV. In figure IX.3, the field is applied along the direction of the exchange field.

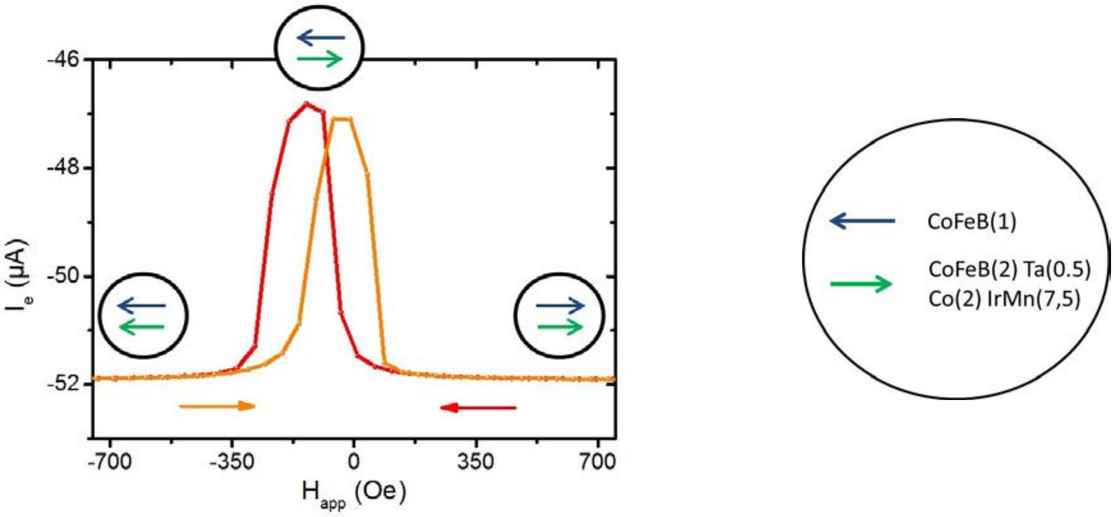

Fig. IX.3: *Variation of the current extracted from the MTJ (I_e) as a function of the in-plane magnetic field. The applied voltage is equal to $-750mV$ and the temperature is $60K$. In the insets, the magnetisation of Ferro1 (CoFeB(2)Ta(0.5)Co(2)IrMn(7.5)) is represented with a green arrow and the magnetisation of the CoFeB(1) layer (Ferro2) with a blue arrow. In this case, the field is applied along the direction of the exchange field.*

At saturation, the magnetisations of all the in-plane layers are parallel (current $I_e^P = -52\mu A$). When the field decreases (red curve), the CoFeB magnetisation switches first for an applied field of -50 Oe. Thus, the tunnel junction is in the anti-parallel configuration (current $I_e^{AP} = -47\mu A$), until the top layer magnetisation is reversed at -320 Oe, leading to a parallel configuration of magnetisations. When the field increases from a negative saturation (orange curve), the top layer magnetisation has already switched at -180 Oe because of the magnetic bias, and the anti-parallel configuration is stabilised until the Co magnetisation switches again at around 50 Oe.

In this case, the parallel and the anti-parallel configurations of the tunnel junction can be stabilised. Thus, the tunnel magneto-resistance (TMR) can be extracted as a function of the applied voltage:

$$TMR = \frac{I_e^P - I_e^{AP}}{I_e^{AP}}$$

Its variation with the applied voltage is shown on figure IX.4:

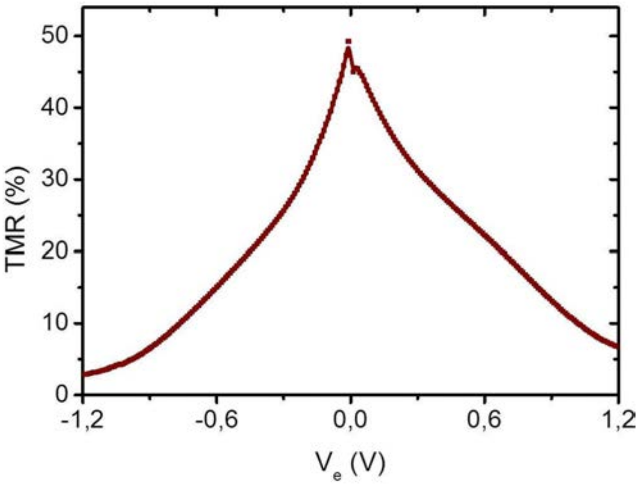

Fig. IX.4: *TMR of the $CoFeB(1)\ MgO(2.8)\ CoFeB(2)Ta(0.5)Co(2)IrMn(7,5)$ tunnel junction, as a function of the applied voltage V_e. The temperature is equal to $60K$.*

A maximum of 50% is obtained for the TMR at low voltages. This value is lower than the TMR of 150% previously obtained in the laboratory with a CoFeB/MgO/CoFeB tunnel junction. Nevertheless, the high TMR observed before was due to symmetry filtering that occurs with a MTJ textured [100]. In our case, the CoFeB precession layer is textured [111]. Even if the top layer is oriented along the [100] direction thanks to the MgO barrier, the symmetry filtering must be different and the TMR is decreased.

Considering the tunnel junction is symmetric (the ferromagnetic electrode is the same at each side of the tunnel barrier), the TMR can be expressed as a function of the polarisation P of the CoFeB electrodes:

$$TMR = \frac{2P^2}{1-P^2}$$

$$P = \sqrt{\frac{TMR}{2+TMR}}$$

With a TMR of 50% obtained at low voltages, the polarisation of the CoFeB electrodes is equal to $P = 45\%$. That means that for 100 electrons injected in the spin valve, 72.5 have their spin oriented along the top layer magnetisation, 27.5 have their spin in the opposite direction.

With the field applied in the direction of the exchange field, the crossed configuration of the tunnel junction, which is optimum for the measurement of the electronic spin precession, is not obtained. Therefore, the current extracted from the MTJ (I_e) was also measured with a magnetic field applied perpendicular to the exchange field direction. The result is shown in figure IX.5.

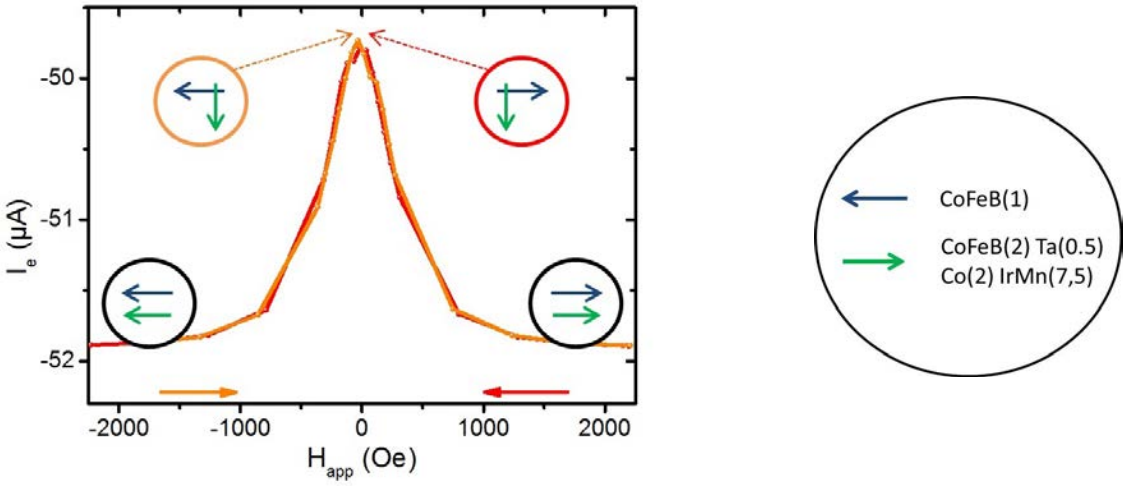

Fig. IX.5: *I_e as a function of the in-plane magnetic field. The applied voltage is equal to $-750mV$ and the temperature is $60K$. In this case, the field is applied perpendicular to the direction of the exchange field.*

After a positive magnetic saturation, the CoFeB(2)Ta(0.5)Co(2)IrMn(7,5) magnetisation rotates progressively towards its easy direction when the field decreases, leading to a reduction of the current I_e. At zero field, the magnetisation of the CoFeB precession layer and the one of the CoFeB(2)Ta(0.5)Co(2)IrMn(7,5) stack are crossed. To ensure the obtention of a crossed configuration of the MTJ, the current in the crossed configuration must be the average of the current obtained in the parallel configuration and the one of the anti-parallel configuration:

$$I_e^{\perp} = -49.5\mu A \simeq \frac{1}{2}(I_e^P + I_e^{AP})$$

If the field decreases again, the CoFeB magnetisation switches at -50 Oe and the current increases until the saturation of both magnetisations is reached at -2000 Oe. The curve is symmetric when the field increases after a negative saturation, but the crossed configuration obtained at zero field is different, the CoFeB magnetisation being in the opposite direction (see insets in figure IX.5).

Apply the field perpendicular to the exchange field ensures also a perfect single domain state. Indeed, along this axis, only rotation of magnetisation occurs since reversal does not occur through nucleation and propagation of domain walls. The current $I_e^{\perp}$ is only due to a crossed configuration and not due to parts of the MTJ parallel and parts of the MTJ anti-parallel.

In the following, tunnel junctions with CoFeB electrodes 3nm and 4nm thick are also characterised.

I.B. Case of a 3nm thick CoFeB layer

I.B.1 Magnetic properties

The same measurements as the ones shown above have been realised for a MTT in which the CoFeB precession layer is 3nm thick. In figure IX.6, the M(H) loops obtained for the Si[100](HF)// Cu(5)Ta(1)Cu(5) Ni(0.6) [Co(0.2)/Ni(0.6)]$_5$ Cu(3.5) CoFeB(3) MgO(2.8) CoFeB(2) Ta(0.75) Co(2) IrMn(7,5) Pt(5) MTT with a magnetic field applied in the sample plane are shown. The field is applied along the direction of the exchange field on the left-hand side of the figure, and perpendicular to it on the right-hand side.

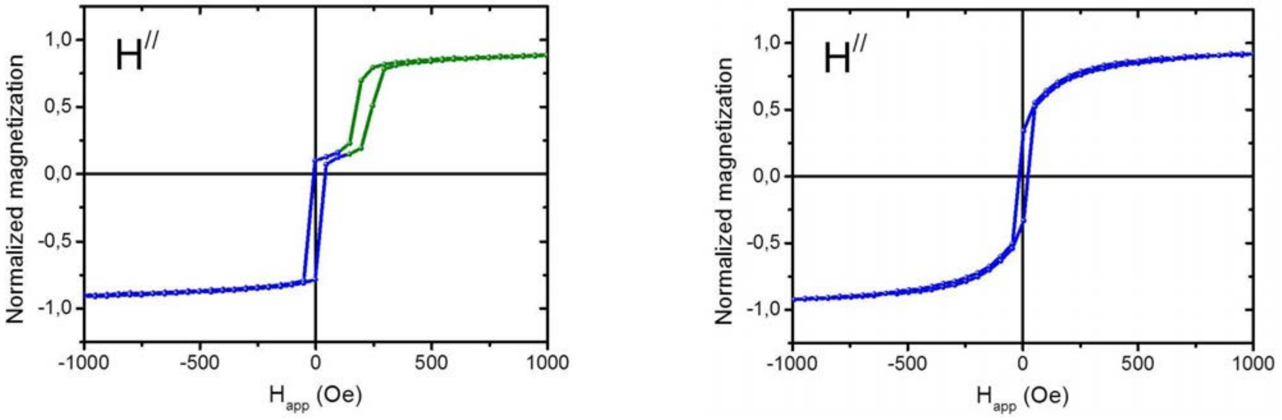

Fig. IX.6: *M(H) loops of a $Si[100](HF)//Cu(5)Ta(1)Cu(5)$ $Ni(0.6)[Co(0.2)/Ni(0.6)]_5$ $Cu(3.5)$ $CoFeB(3)$ $MgO(2.8)$ $CoFeB(2)Ta(0.75)Co(2)IrMn(7,5)$ $Pt(5)$ stack, with a field applied in the sample plane. The field is applied along the direction of the exchange field on the left-hand side and perpendicular to it on the right-hand side.*

When the field is applied along the direction of the exchange field, two hysteresis loops are observed. The first one, centered on zero field, has a coercive field of 50 Oe and corresponds to the magnetic response of the CoFeB(3) layer. The second hysteresis is due to the CoFeB(2)Ta(0.75)Co(2)IrMn(7,5) top layer. Centered on H_{ex} = +250 Oe, the coercive field is equal to 50 Oe.

When the field is applied perpendicular to the direction of the exchange field, the responses of both layers are superimposed. However, the slight opening of the M(H) cycle around zero field can be attributed to the CoFeB precession layer.

In figure IX.7, the field is applied perpendicular to the sample plane.

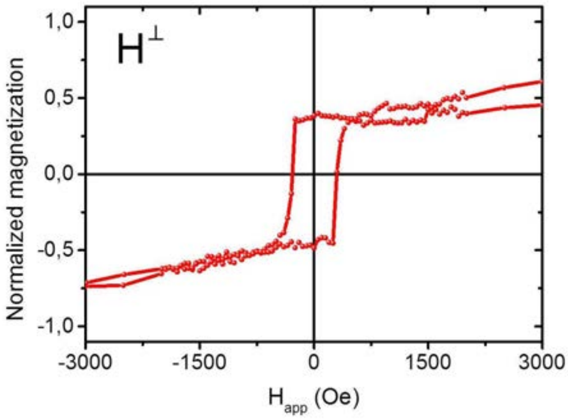

Fig. IX.7: *M(H) loop of a* $Si[100](HF)//Cu(5)Ta(1)Cu(5)$ $Ni(0.6)[Co(0.2)/Ni(0.6)]_5$ $Cu(3.5)$ $CoFeB(3)$ $MgO(2.8)$ $CoFeB(2)Ta(0.5)Co(2)IrMn(7,5)$ $Pt(5)$ *stack, with an applied field perpendicular to the sample plane.*

When the field is applied perpendicular to the sample plane, an hysteresis loop with a coercive field of 200 Oe is obtained, which corresponds to the magnetic response of the [Co/Ni] multilayer exhibiting a perpendicular magnetic anisotropy (PMA).

I.B.2 Magnetic configuration of the tunnel junction

In this part, the current I_e is measured as a function of the magnetic field, for an applied voltage V_e of -100mV. In figure IX.8, the field is applied along the direction of the exchange field.

At saturation, the magnetisations of all the in-plane layers are parallel (current $I_e^P = -11.4\mu A$). When the field decreases (red curve), the top layer magnetisation switches first for an applied field of 200 Oe because of the exchange field of 250 Oe. Thus, the tunnel junction is in the anti-parallel configuration (current $I_e^{AP} = -8.2\mu A$), until the CoFeB(3) magnetisation is reversed at -50 Oe: the two magnetisations are again parallel. When the field increases (orange curve), the CoFeB(3) layer magnetisation switches at 50 Oe , and the anti-parallel configuration is stabilised until the top layer magnetisation switches again at around 300 Oe.

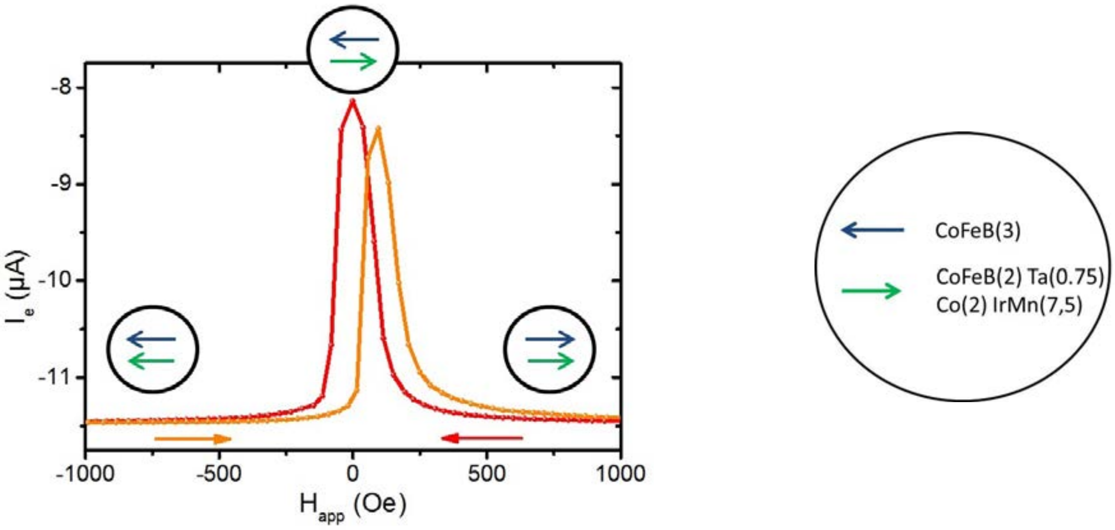

Fig. IX.8: *Variation of the current extracted from the MTJ (I_e) as a function of the in-plane magnetic field. The applied voltage is equal to $-100mV$ and the temperature is $60K$. In the insets, the magnetisation of Ferro1 (CoFeB(2)Ta(0.5)Co(2)IrMn(7.5)) is represented with a green arrow and the magnetisation of the CoFeB(3) layer (Ferro2) with a blue arrow. In this case, the field is applied along the direction of the exchange field.*

In this case, the parallel and the anti-parallel configurations of the tunnel junction can be stabilised. Thus, the tunnel magneto-resistance (TMR) can be extracted as a function of the applied voltage (figure IX.9):

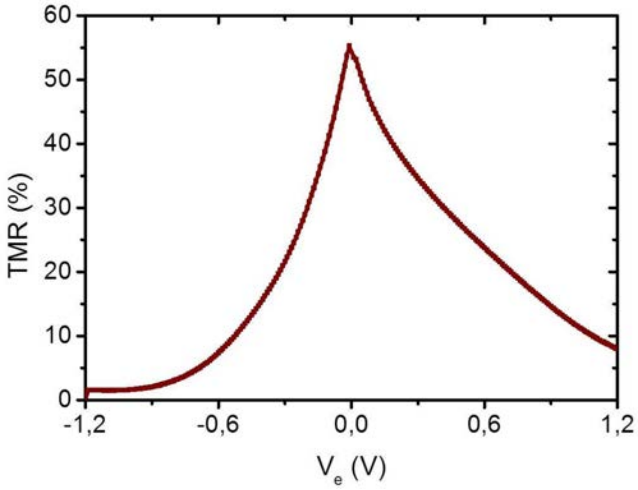

Fig. IX.9: *TMR of the $CoFeB(3)$ $MgO(2.8)$ $CoFeB(2)Ta(0.75)Co(2)IrMn(7,5)$ tunnel junction, as a function of the applied voltage V_e. The temperature is equal to $60K$.*

A maximum of 55% is obtained for the TMR at low voltages, slightly larger than with the CoFeB(1) electrode.

Since the magnetic configuration is not fully known during reversal because nucleation and propagation occurs along the easy axis, the current extracted from the tunnel barrier (I_e) was measured also with a magnetic field applied perpendicular to the exchange field direction. The result is shown in figure IX.10.

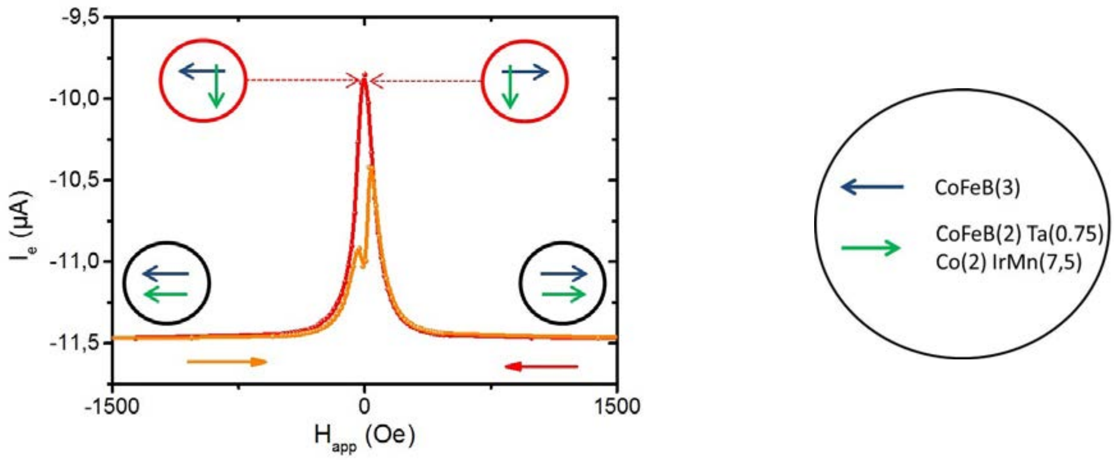

Fig. IX.10: *Variation of the current extracted from the MTJ (I_e) with the in-plane magnetic field. The applied voltage is equal to $-100mV$ and the temperature is $60K$. In this case, the field is applied perpendicular to the direction of the exchange field.*

After a positive magnetic saturation, the CoFeB(2)Ta(0.75)Co(2)IrMn(7,5) magnetisation rotates progressively towards its easy direction when the field decreases, leading to a reduction of I_e. At zero field, the magnetisations of the CoFeB layer and the CoFeB(2)Ta(0.75)Co(2)IrMn(7,5) stack are crossed. The current is the average of the current obtained in the parallel configuration and the one of the anti-parallel configuration, that ensures the obtention of a crossed configuration:

$$I_e^{\perp} = -9.8\mu A \simeq \frac{1}{2}(I_e^P + I_e^{AP})$$

If the field decreases again, the CoFeB magnetisation switches at -50 Oe and the current increases until the saturation of both magnetisations is reached at -2000 Oe. The curve is symmetric when the field increases after a negative saturation, but the crossed configuration obtained at zero field is different because the CoFeB magnetisation is in the opposite direction (see insets in figure IX.10).

I.C. Case of a 4nm thick CoFeB layer

I.C.1 Magnetic properties

The same measurements as the ones shown above have been realised for a MTT in which the CoFeB precession layer is 4nm thick. In figure IX.11, the M(H) loops obtained for the Si[100](HF)//Cu(5)Ta(1)Cu(5) Ni(0.6) [Co(0.2)/Ni(0.6)]$_5$ Cu(3.5) CoFeB(4) MgO(2.8) CoFeB(2) Ta(0.5) Co(2) IrMn(7,5) Pt(5) MTT with a magnetic field applied in the sample plane are shown. The field is applied along the direction of the exchange field on the left-hand side of the figure, and perpendicular to it on the right-hand side.

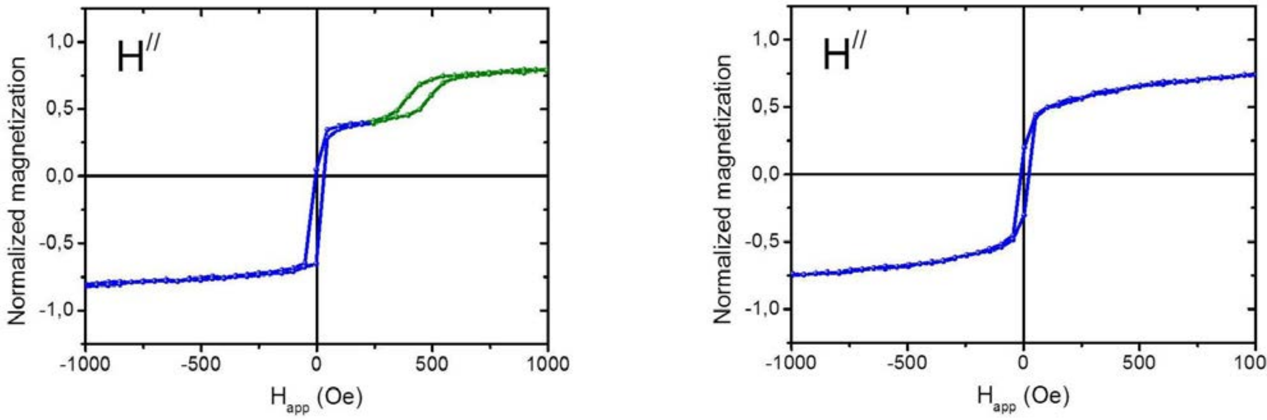

Fig. IX.11: *M(H) loops of a* $Si[100](HF)//Cu(5)Ta(1)Cu(5)$ $Ni(0.6)[Co(0.2)/Ni(0.6)]_5$ $Cu(3.5)$ $CoFeB(4)$ $MgO(2.8)$ $CoFeB(2)Ta(0.5)Co(2)IrMn(7,5)$ $Pt(5)$ *stack, with an applied field in the sample plane. The field is applied along the direction of the exchange field on the left-hand side and perpendicular to it on the right-hand side.*

When the field is applied along the direction of the exchange field, two hysteresis loops are observed. The first one, centered on the zero field, has a coercive field of 50 Oe and corresponds to the magnetic response of the CoFeB(4) layer. The second hysteresis, due to the CoFeB(2)Ta(0.5)Co(2)IrMn(7,5) top layer, is centered on H_{ex} = +400 Oe and has a coercive field of 50 Oe.

When the field is applied perpendicular to the direction of the exchange field, the responses of both layers are superimposed. However, the slight opening of the M(H) cycle around zero field can be attributed to the CoFeB precession layer.

In figure IX.12, the field is applied perpendicular to the sample plane.

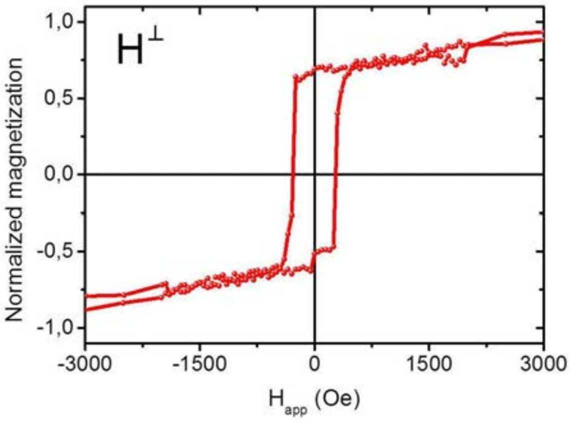

Fig. IX.12: *M(H) loop of a* $Si[100](HF)//Cu(5)Ta(1)Cu(5)$ $Ni(0.6)[Co(0.2)/Ni(0.6)]_5$ $Cu(3.5)$ $CoFeB(4)$ $MgO(2.8)$ $CoFeB(2)Ta(0.5)Co(2)IrMn(7,5)$ $Pt(5)$ *stack, with an applied field perpendicular to the sample plane.*

When the field is applied perpendicular to the sample plane, an hysteresis loop with a coercive field of 200 Oe is obtained, which corresponds to the magnetic response of the [Co/Ni] multilayer exhibiting a perpendicular magnetic anisotropy (*PMA*).

I.C.2 Magnetic configuration of the tunnel junction

In this part, the current extracted from the MTJ (I_e) is measured as a function of the magnetic field, for an applied voltage V_e of -100mV. In figure IX.13, the field is applied along the direction of the exchange field.

At saturation, the magnetisations of all the in-plane layers are parallel (current $I_e^P = -4.25\mu A$). When the field decreases (red curve), the top layer magnetisation switches first for an applied field of 300 Oe because of the exchange field of 400 Oe. Thus, the tunnel junction is in the anti-parallel configuration (current $I_e^{AP} = -2.75\mu A$), until the CoFeB(4) magnetisation is reversed at -50 Oe and the two magnetisations are back being parallel. When the field increases (orange curve), the CoFeB(4) layer magnetisation switches at 50 Oe, and the anti-parallel configuration is obtained until the top layer magnetisation switches again at around 50 Oe.

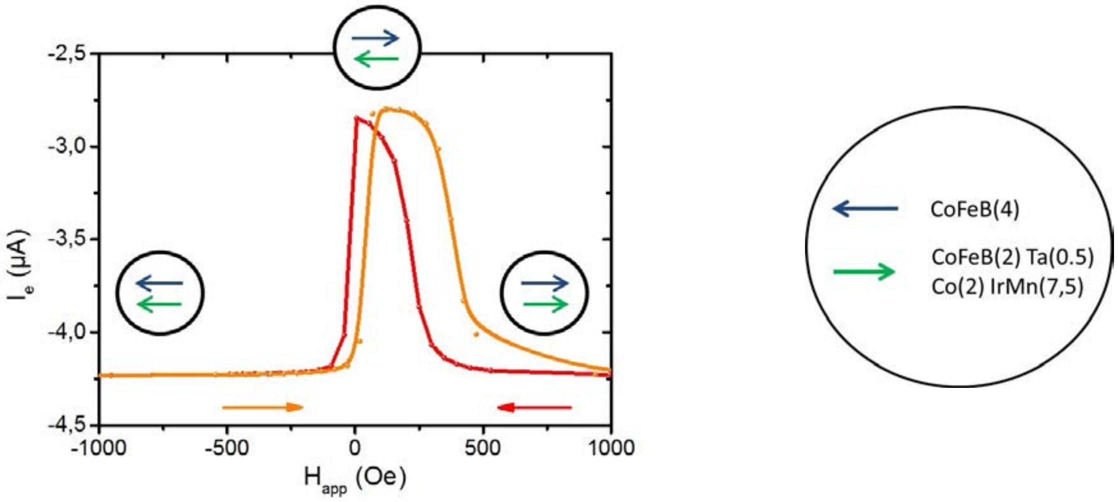

Fig. IX.13: *I_e as a function of the in-plane magnetic field. The applied voltage is equal to $-100mV$ and the temperature is $60K$. In the insets, the magnetisation of Ferro1 (CoFeB(2)Ta(0.5)Co(2)IrMn(7.5)) is represented with a green arrow and the magnetisation of the CoFeB(4) layer (Ferro2) with a blue arrow. In this case, the field is applied along the direction of the exchange field.*

In this case, the parallel and the anti-parallel configurations of the tunnel junction can be obtained. Thus, the tunnel magneto-resistance (TMR) can be extracted as a function of the applied voltage (figure IX.14).

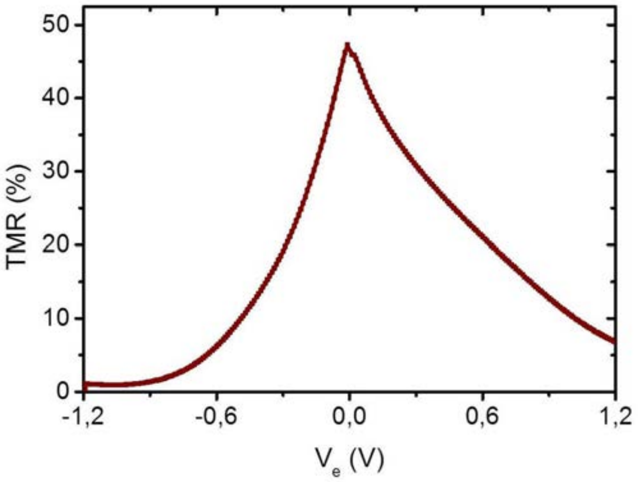

Fig. IX.14: *TMR of the $CoFeB(4)$ $MgO(2.8)$ $CoFeB(2)Ta(0.5)Co(2)IrMn(7,5)$ tunnel junction, as a function of the applied voltage V_e. The temperature is equal to $60K$.*

A maximum of 50% is obtained for the TMR at low voltages as before with the CoFeB(1) or CoFeB(3) electrodes.

With the field applied in the direction of the exchange field, the crossed configuration of the tunnel junction, which is necessary for the measurement of the electronic spin precession, is not obtained. Therefore, I_e was also measured with a magnetic field applied perpendicular to the exchange field direction. The result is shown in figure IX.15.

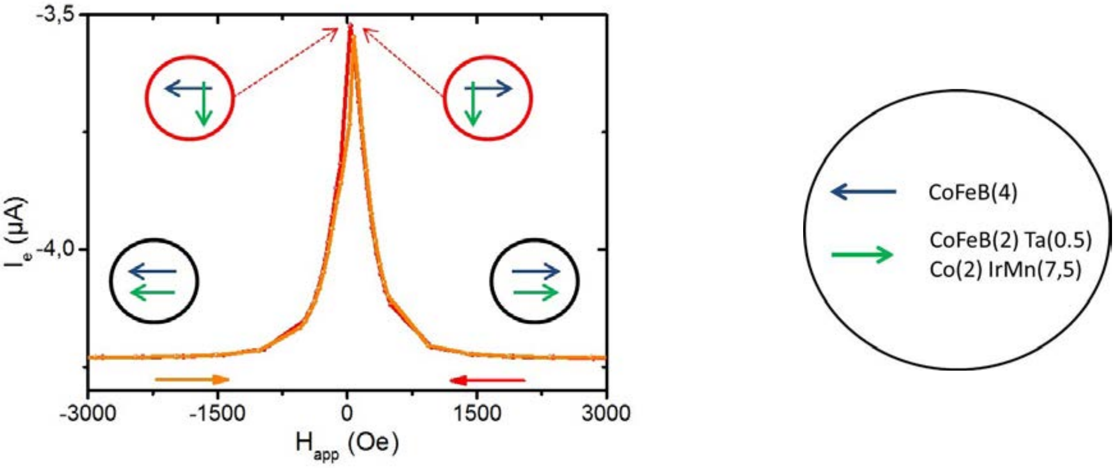

Fig. IX.15: *Variation of the current extracted from the MTJ (I_e) with the in-plane magnetic field. The applied voltage is equal to $-100mV$ and the temperature is $60K$. In the insets, the magnetisation of Ferro1 (CoFeB(2)Ta(0.5)Co(2)IrMn(7.5)) is represented with a green arrow and the magnetisation of the CoFeB(4) layer (Ferro2) with a blue arrow. In this case, the field is applied perpendicular to the direction of the exchange field.*

After a positive magnetic saturation, the CoFeB(2)Ta(0.5)Co(2)IrMn(7,5) magnetisation rotates progressively towards its easy direction when the field decreases, leading to a reduction of the current I_e. At zero field, the magnetisation of the CoFeB layer and the magnetisation of the CoFeB(2)Ta(0.5)Co(2)IrMn(7,5) stack are crossed. The current in the crossed configuration is again the average of the current obtained in the parallel configuration and the one of the anti-parallel configuration:

$$I_e^{\perp} = -3.5\mu A \simeq \frac{1}{2}(I_e^P + I_e^{AP})$$

If the field decreases again, the CoFeB magnetisation switches at -50 Oe and the current increases until the saturation of both magnetisations is reached at -2000 Oe. The curve is symmetric when the field increases after a negative saturation, but the crossed configuration obtained at zero field is different because the CoFeB magnetisation is in the opposite direction (see insets in figure IX.15).

Finally, all the magnetic configurations can be obtained for the tunnel junction regardless of the CoFeB thickness. In particular, the two crossed configurations expected to measure the electronic spin precession are easily obtained with a magnetic field applied perpendicular to the exchange field. Thus, the magnetisation of the top layer progressively rotates towards its easy direction when the magnetic field decreases. This ensures uniform magnetisations (the exchange field of the top layer induces an uniform rotation of its magnetisation) in the crossed configuration, which is a very important point for the electronic spin precession measurements.

In the following, the TR of the three MTT are measured as a function of the applied voltage, for different magnetic configurations. The first part deals with the MTT containing a CoFeB(1) precession layer. Then, the MTT with a CoFeB(3) precession layer and the one with a CoFeB(4) precession layer are treated in the same way.

II. Transfer ratio for different magnetic configurations

II.A. Case of a 1nm thick CoFeB layer

In this part, the measurements are made on the MTT that has a 1nm thick CoFeB precession layer.

Once the magnetic behaviour of the tunnel junction is fully understood, the transfer ratio ($TR = I_c/I_e$) can be measured as a function of the applied voltage V_e for different magnetic configurations:

- The parallel configuration is obtained with a strong magnetic field (H_{app} = 20kOe), regardless of its direction. In this case, all the magnetisations are saturated in the field direction.

- As seen before, it is possible to have a parallel or an anti-parallel configuration of the tunnel junction with an applied field along the exchange field. To obtain the parallel configuration, an in-plane field of 1500 Oe is applied. Thus, the [Co/Ni] multilayer magnetisation rotates of 40^o from its easy direction (which is perpendicular to the sample plane). To determine the angle of rotation, the curve of the collected current as a function of the applied field is used, in the same way as for the Co precession layer (see previous chapter).

- When the field is applied in a direction orthogonal to the exchange field, the two crossed configurations of the tunnel junction can be obtained at zero field, depending if the saturating field was positive or negative. In both cases, the magnetisation of the [Co/Ni] multilayer is perpendicular to the sample plane, and the spin valve is in a crossed configuration.

The results of these measurements are presented in figure IX.16, where the $TR = I_c/I_e$ is shown as a function of the applied voltage V_e.

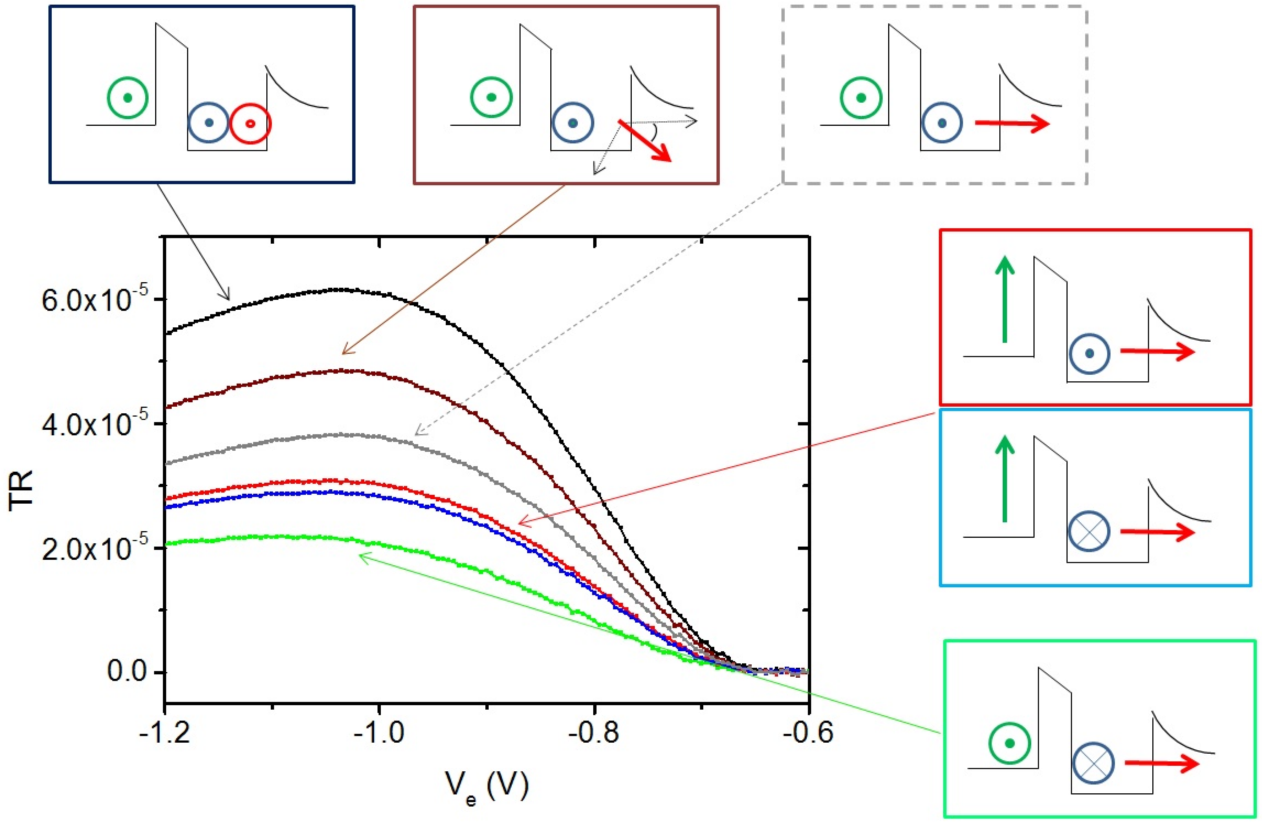

Fig. IX.16: *Transfer ratio of the* $Si[100](HF)//Cu(5)Ta(1)Cu(5)\ Ni(0.6)[Co(0.2)/Ni(0.6)]_5\ Cu(3.5)\ CoFeB(1)\ MgO(2.8)\ CoFeB(2)Ta(0.5)Co(2)IrMn(7,5)\ Pt(5)$ *stack, for different magnetic configurations. In the insets, the magnetisation of the [Co/Ni] multilayer (Ferro3) is represented with a red arrow, the magnetisation of the CoFeB layer (Ferro2) with a blue arrow and the magnetisation of the* $CoFeB(2)Ta(0.5)Co(2)IrMn(7,5)$ *top layer (Ferro1) with a green arrow.*

The strongest TR is obtained for the parallel configuration (black curve), in which all the magnetisations are in the same direction. The lowest TR is measured for an anti-parallel injection and a crossed configuration of the spin valve (green curve). The grey curve corresponds to the hypothetical case in which the spin valve is in a crossed configuration with a parallel injection, calculated by correcting in the brown curve the angle between the [CO/Ni]magnetisation and its easy axis (parallel injection but the [Co/Ni] magnetisation is not perpendicular to the sample plane).

The main point here is that a different TR is measured between the two crossed configurations of the tunnel junction (red and blue curves). However, the current injected in the spin valve I_e is exactly the same in both cases, as shown in figure IX.17, proving that the injection is equivalent in the two measurements. For the green, grey, red and blue curves, the spin valve is in the same crossed configuration. Thus, the fact that the average TR between the blue and red curves (which would be the TR obtained with the crossed injection if there were not any spin precession) is equal to the average TR between grey and green curves proves that the magnetisations of the tunnel junction electrodes are well crossed for the red and blue curves (the tunnel current is, in this case, the average between the one obtained with a parallel injection and the one of the anti-parallel injection).

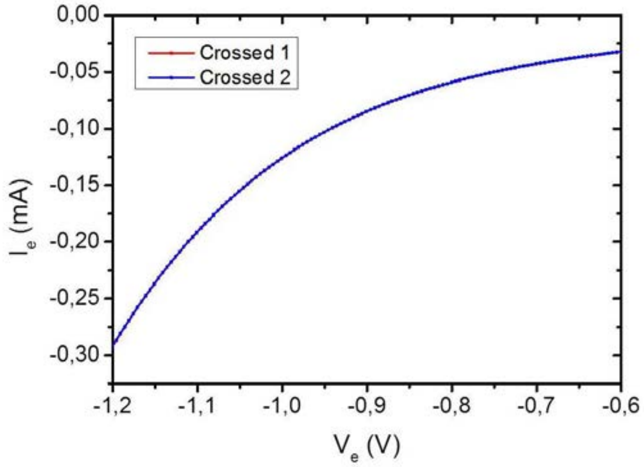

Fig. IX.17: *Current extracted from the tunnel junction (I_e) as a function of the applied voltage V_e, for both crossed configurations of the tunnel junction.*

As explained in the chapter VII, the important quantity to determine is:

$$\Delta_{rel}TR = \frac{TR1 - TR2}{2TR3 - TR1 - TR2}$$

in which $TR1$ and $TR2$ refer to the crossed configurations (red and blue curves in figure IX.16), and $TR3$ is the TR of the parallel configuration (dark curve). The figure IX.18 shows the variation of $\Delta_{rel}TR$ with the applied voltage.

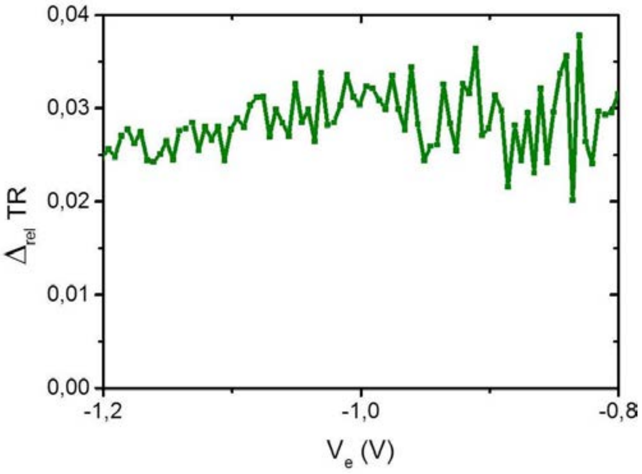

Fig. IX.18: *Relative difference of the transfer ratio $\Delta_{rel}TR$ between the two crossed configurations of the tunnel junction as a function of the applied voltage. The precession layer is a 1nm thick CoFeB layer.*

In order to extract a precession angle in CoFeB from those data, all these measurements have to be done again for MTT with different thicknesses of the precession layer.

II.B. Case of a 3nm thick CoFeB layer

In this part, the measurements are made on the MTT that has a 3nm thick CoFeB precession layer.

Once the magnetic behaviour of the tunnel junction is fully understood, the transfer ratio ($TR = I_c/I_e$) can be measured as a function of the applied voltage V_e for different magnetic configurations:

- The parallel configuration is obtained with a strong magnetic field ($H_{app} =$ 20kOe), regardless of its direction. In this case, all the magnetisations are saturated in the field direction.

- As seen before, it is possible to have a parallel or an anti-parallel configuration of the tunnel junction with a field applied along the exchange field. To obtain the parallel configuration, an in-plane field of 1000 Oe is applied. Thus, the [Co/Ni] multilayer magnetisation rotates of 30^o from its easy direction (which is perpendicular to the sample plane).

- When the field is applied in a direction orthogonal to the exchange field, the two crossed configurations of the tunnel junction can be obtained at zero field, depending if the saturating field was positive or negative. In both cases, the magnetisation of the [Co/Ni] multilayer is perpendicular to the sample plane, and the spin valve is in a crossed configuration.

The results of these measurements are presented in figure IX.19, where the $TR = I_c/I_e$ is shown as a function of the applied voltage V_e.

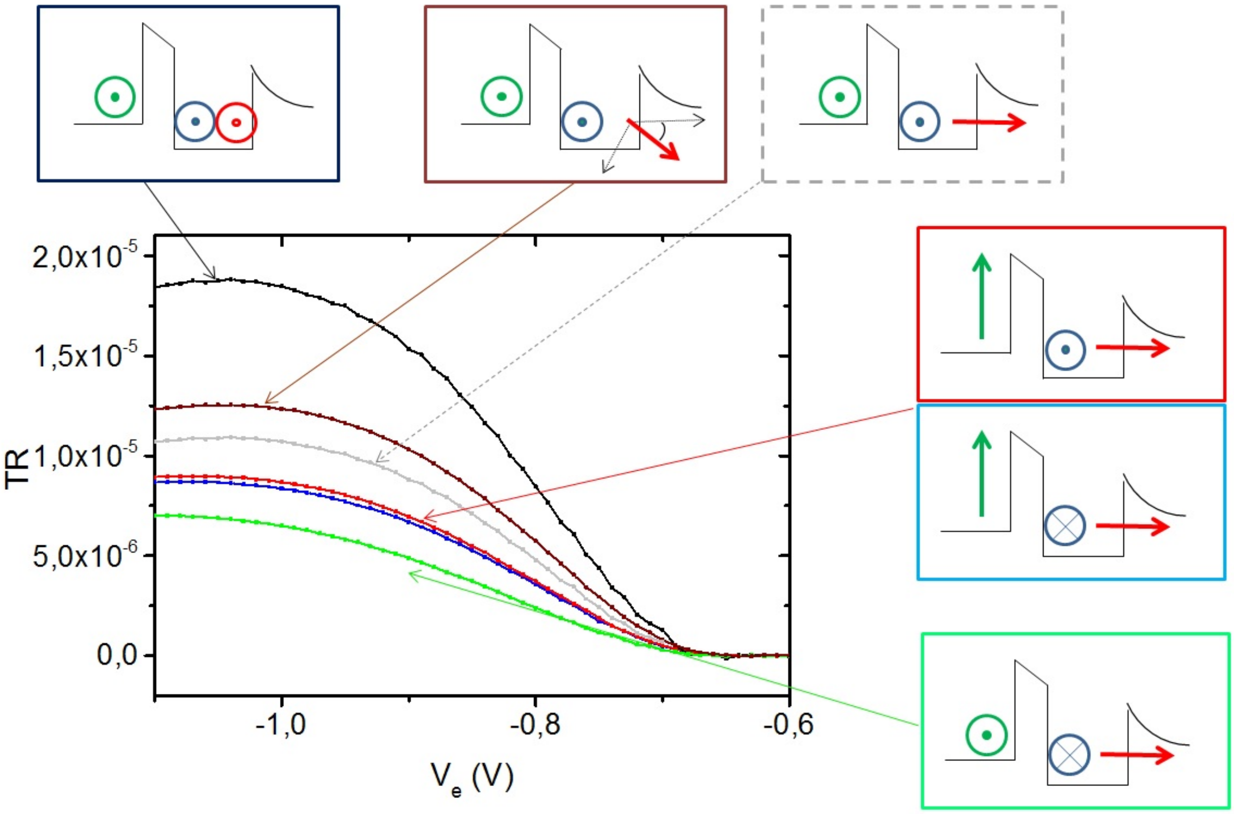

Fig. IX.19: *Transfer ratio of the* $Si[100](HF)//Cu(5)Ta(1)Cu(5)\ Ni(0.6)[Co(0.2)/Ni(0.6)]_5$ $Cu(3.5)$ $CoFeB(3)$ $MgO(2.8)$ $CoFeB(2)Ta(0.5)Co(2)IrMn(7,5)$ $Pt(5)$ *stack, for different magnetic configurations. In the insets, the magnetisation of the [Co/Ni] multilayer (Ferro3) is represented with a red arrow, the magnetisation of the CoFeB layer (Ferro2) with a blue arrow and the magnetisation of the* $CoFeB(2)Ta(0.5)Co(2)IrMn(7,5)$ *top layer (Ferro1) with a green arrow.*

The strongest TR is obtained for the parallel configuration (black curve), in which all the magnetisations are in the same direction. Its magnitude is three times smaller than the TR obtained in the previous case (CoFeB(1)), because of the larger thickness of CoFeB. The lowest TR is measured for an anti-parallel injection and a crossed configuration of the spin valve (green curve). The brown curve corresponds to the hypothetical case in which the spin valve is in a crossed configuration with a parallel injection, calculated by correcting the brown curve (parallel injection but [Co/Ni] magnetisation not perpendicular to the sample plane).

The main point here is that a different TR is measured between the two crossed configurations of the tunnel junction (red and blue curves). However, the current I_e injected in the spin valve is exactly the same in both cases, as shown in figure IX.20, proving that the injection is equivalent in both measurements. Once again, the average between the TR obtained with a parallel injection and with an anti-parallel injection (green and grey curves) is in the middle of the red and blue curves of the TR obtained with crossed injections.

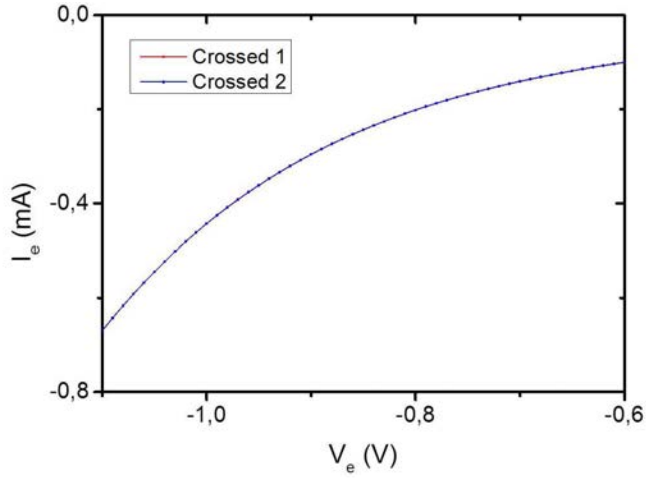

Fig. IX.20: *Current in the tunnel barrier (I_e) as a function of the applied voltage V_e, for both crossed configurations of the tunnel junction.*

The value of $\Delta_{rel}TR = \frac{TR1-TR2}{2TR3-TR1-TR2}$, in which $TR1$ and $TR2$ refer to the crossed configurations (red and blue curves in figure IX.19), and $TR3$ is the TR of the parallel configuration (dark curve) is extracted from the previous measurements. The figure IX.21 shows the variation of $\Delta_{rel}TR$ with the applied voltage.

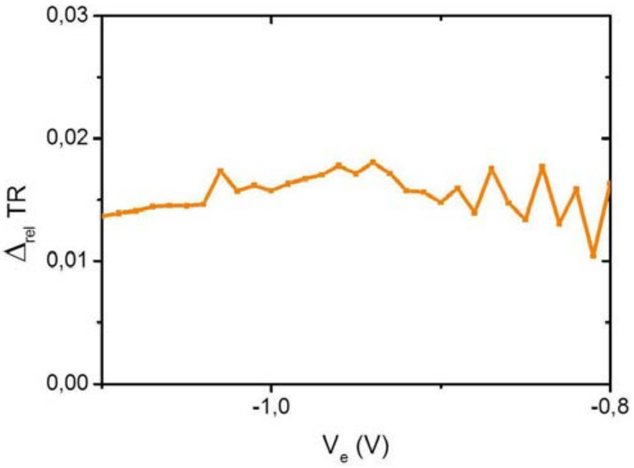

Fig. IX.21: *Relative difference of the transfer ratio $\Delta_{rel}TR$ between the two crossed configurations of the tunnel junction as a function of the applied voltage. The precession layer here is a 3nm thick CoFeB layer.*

The same measurements are repeated again for a MTT with a CoFeB(4) precession layer

II.C. Case of a 4nm thick CoFeB layer

In this part, the measurements are made on the MTT that has a 4nm thick CoFeB precession layer.

Once the magnetic behaviour of the tunnel junction is fully understood, the transfer ratio ($TR = I_c/I_e$) can be measured as a function of the applied voltage V_e for different magnetic configurations:

- The parallel configuration is obtained with a strong magnetic field (H_{app} = 20kOe), regardless of its direction. In this case, all the magnetisations are saturated in the field direction.
- As seen before, it is possible to have a parallel or an anti-parallel configuration of the tunnel junction with a field applied along the exchange field. To obtain the parallel configuration, an in-plane field of 500 Oe is applied. Thus, the [Co/Ni] multilayer magnetisation rotates of 11^o from its easy direction (which is perpendicular to the sample plane).
- When the field is applied in a direction orthogonal to the exchange field, the two crossed configurations of the tunnel junction can be obtained at zero field, depending if the saturating field was positive or negative. In both cases, the magnetisation of the [Co/Ni]

multilayer is perpendicular to the sample plane, and the spin valve is in a crossed configuration.

The results of these measurements are presented in figure IX.22, where the $TR = I_c/I_e$ is shown as a function of the applied voltage V_e.

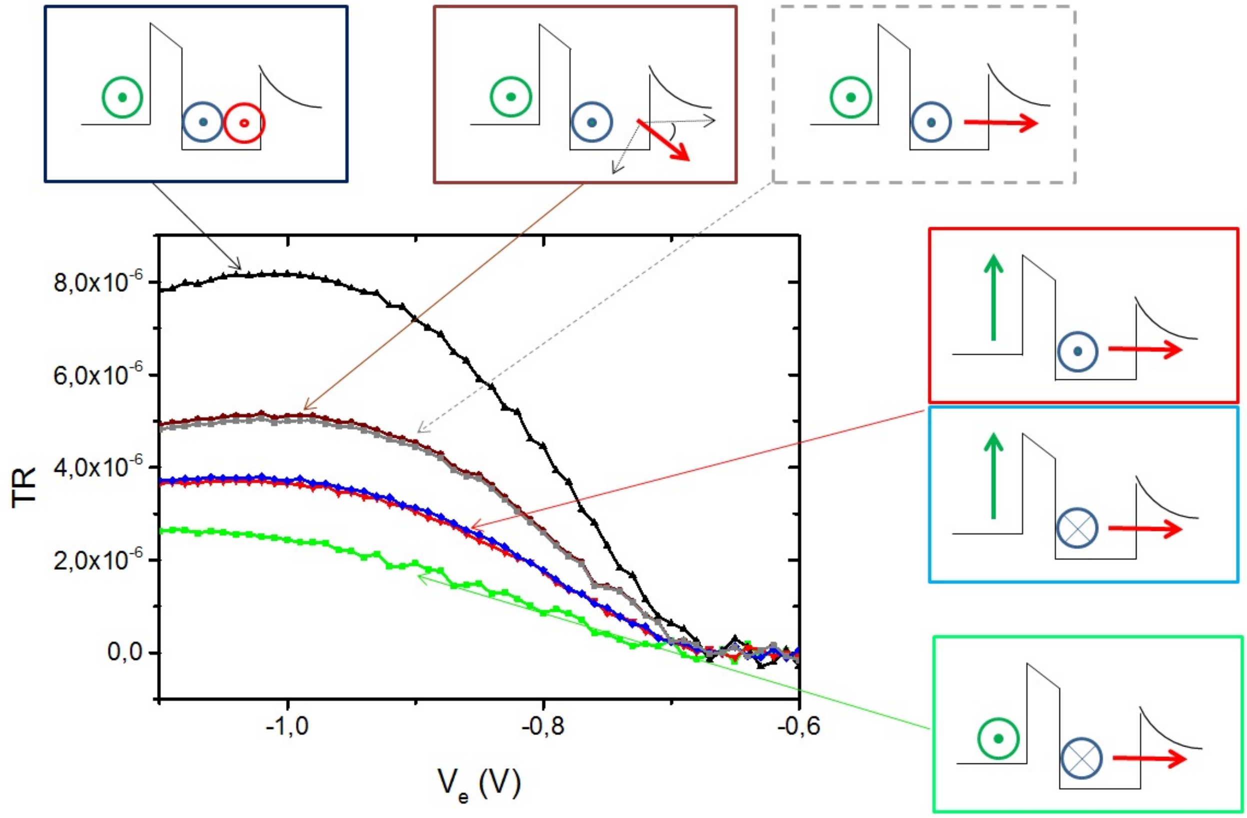

Fig. IX.22: *Transfer ratio of the* $Si[100](HF)//Cu(5)Ta(1)Cu(5)\ Ni(0.6)[Co(0.2)/Ni(0.6)]_5\ Cu(3.5)\ CoFeB(4)\ MgO(2.8)\ CoFeB(2)Ta(0.5)Co(2)IrMn(7,5)\ Pt(5)$ *stack, for different magnetic configurations. In the insets, the magnetisation of the* $[Co/Ni]$ *multilayer (Ferro3) is represented with a red arrow, the magnetisation of the CoFeB layer (Ferro2) with a blue arrow and the magnetisation of the* $CoFeB(2)Ta(0.5)Co(2)IrMn(7,5)$ *top layer (Ferro1) with a green arrow.*

The strongest TR is obtained for the parallel configuration (black curve), in which all the magnetisations are in the same direction. The measurements show a noise because of the strong decrease of the collected current (and so of the TR) compared to the two previous cases. The lowest TR is measured for an anti-parallel injection and a crossed configuration of the spin valve (green curve). The brown curve corresponds to the hypothetical case in which the spin valve is in a crossed configuration with a parallel injection, calculated by correcting the brown curve (parallel injection but [Co/Ni] magnetisation not perpendicular to the sample plane).

The main point here is that a different TR is measured between the two crossed configurations of the tunnel junction (red and blue curves). However, the current injected in the spin valve I_e is exactly the same in both cases, as shown in figure IX.23, proving that the injection is equivalent in both measurements.

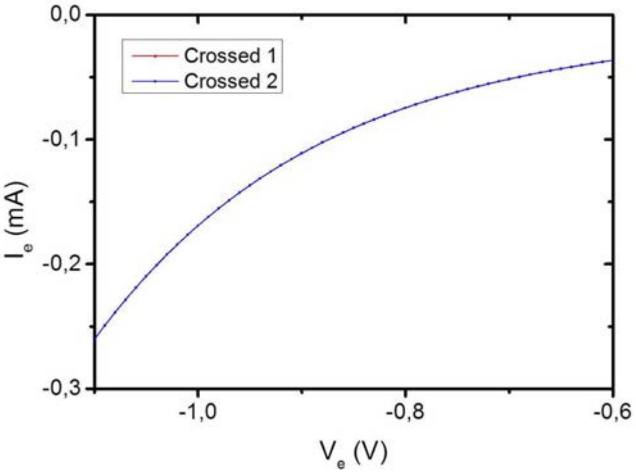

Fig. IX.23: Current in the tunnel barrier (I_e) as a function of the applied voltage V_e, for both crossed configurations of the tunnel junction.

The value of $\Delta_{rel}TR = \frac{TR1-TR2}{2TR3-TR1-TR2}$, in which $TR1$ and $TR2$ refer to the crossed configurations (red and blue curves in figure IX.22), and $TR3$ is the TR of the parallel configuration (dark curve) is extracted from the previous measurements. The figure IX.24 shows the variation of $\Delta_{rel}TR$ with the applied voltage.

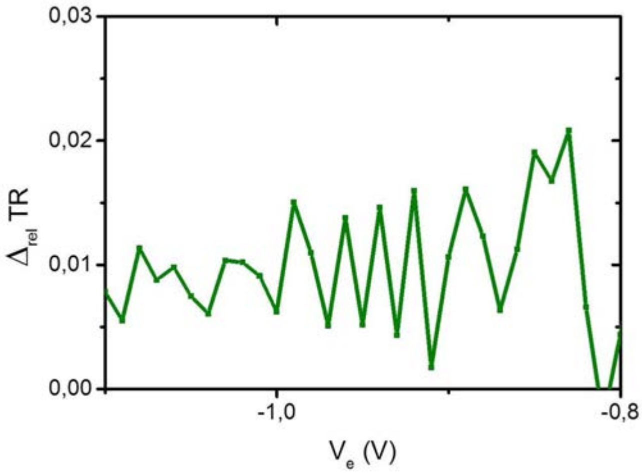

Fig. IX.24: *Relative difference of the transfer ratio $\Delta_{rel}TR$ between the two crossed configurations of the tunnel junction as a function of the applied voltage. The precession layer here is a 4nm thick CoFeB layer.*

Once $\Delta_{rel}TR$ obtained for three CoFeB thicknesses (1nm, 3nm and 4nm), we will use the theoretical model developed in the chapter VII to extract a precession angle.

III. Electronic spin precession in CoFeB

III.A. Determination of the spin filtering angle

In chapter VII, we have demonstrated the theoretical expression of $\Delta_{rel}TR$:

$$\Delta_{rel}TR = \ sin(a.d)\ \sqrt{1 - tanh^2(b.d/2)}$$

in which a is the precession velocity (in $^o/nm$), $b \ = \ \left(1/\lambda^{\downarrow} - 1/\lambda^{\uparrow}\right)$ is linked to the spin asymmetry and d is the precession layer thickness.

In the previous sections, $\Delta_{rel}TR$ has been measured as a function of the applied voltage in the case of a CoFeB layer with a thickness equal to 1nm, 3nm or 4nm. The figure IX.25 shows the results obtained.

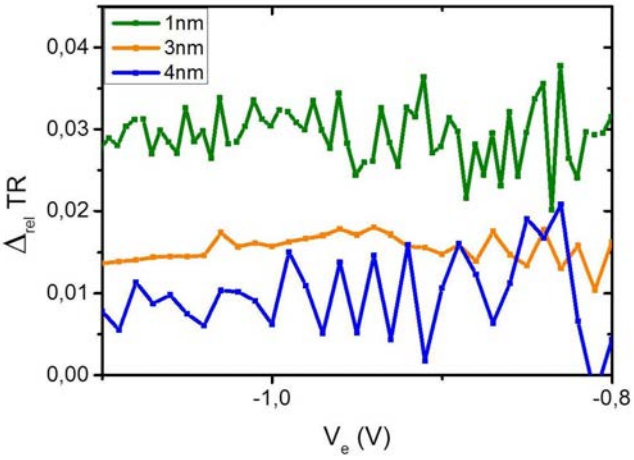

Fig. IX.25: *Relative difference of the transfer ratio $\Delta_{rel}TR$ between the two crossed configurations of the tunnel junction as a function of the applied voltage. The CoFeB thickness is 1nm for the green curve, 3nm for the orange one and 4nm for the blue one.*

As shown in the previous chapter, there is no effect of the energy increase between $E - E_F = 0.8eV$ and $E - E_F = 1.1eV$ on the value of b. Thus, we extract from the previous curves an average value of $\Delta_{rel}TR$ in our energy range in order to determine the mean value of b. The following figure IX.26 shows the best fit of the experimental points with the theoretical expression.

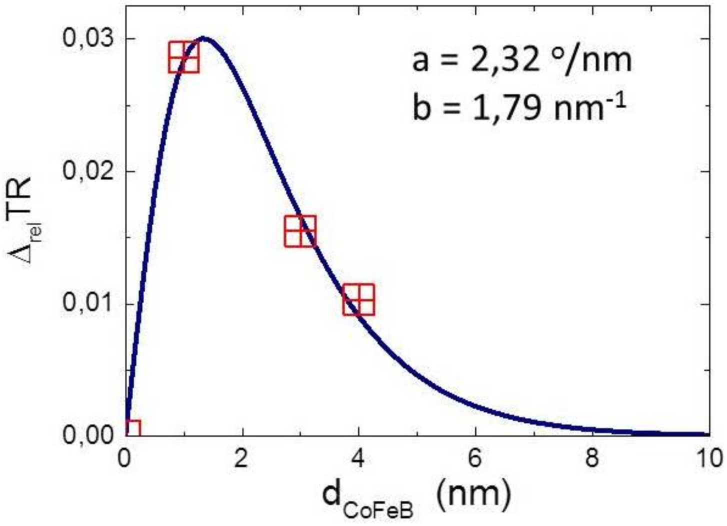

Fig. IX.26: *Mean $\Delta_{rel}TR = \frac{TR1-TR2}{2TR3-TR1-TR2}$ in our energy range ($E_F + 0.8eV < E < E_F + 1.1eV$) as a function of the CoFeB thickness. The continuous line is the fit, and the point corresponds to the experimental data.*

The best fit gives $b = (1.79 \pm 0.06)nm^{-1}$. Thus, the spin filtering angle θ can be extracted from the value of b:

$$\theta \;=\; ArcTan\left[\frac{tanh(b.d/2)}{\sqrt{1-tanh^2(b.d/2)}}\right]$$

Its variation with the CoFeB thickness is shown in the figure IX.27:

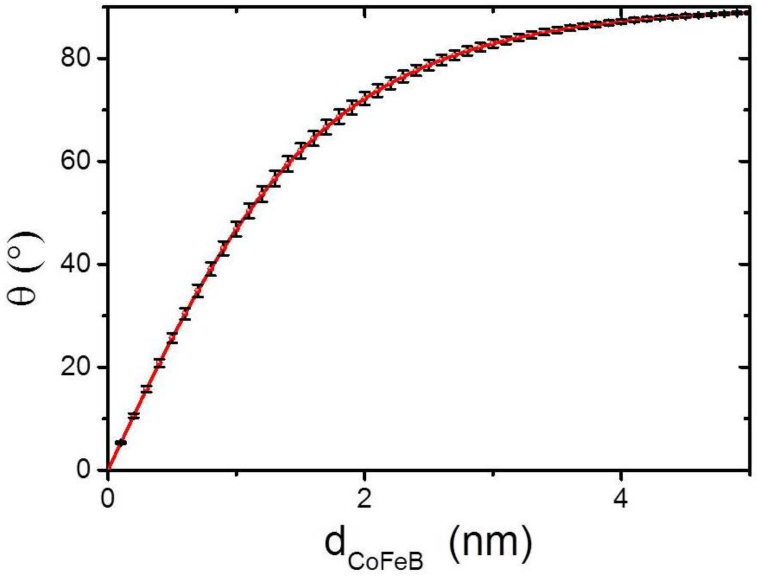

Fig. IX.27: *Spin filtering angle θ as a function of the CoFeB thickness for an average energy of $0.95eV$ above the Fermi level.*

This value of b is high compared to the one found for a Co precession layer. Nevertheless, the spin filtering seems to be more important in the case of a CoFeB layer, since the spins are almost filtered in the direction of the magnetisation after 3nm of CoFeB. No value of the mean free paths can be found in the literature for a CoFeB layer at 60K in order to confront with our results.

III.B. Determination of the precession angle

Once the spin filtering angle is determined for each CoFeB thickness, the precession angle can be calculated:

$$sin(\epsilon) \;=\; \frac{\Delta_{rel}TR}{cos(\theta)}$$

By assuming that θ is constant in our energy range, the variation of the precession angle with the applied voltage can be calculated for 1nm, 3nm and 4nm of CoFeB (figure IX.28).

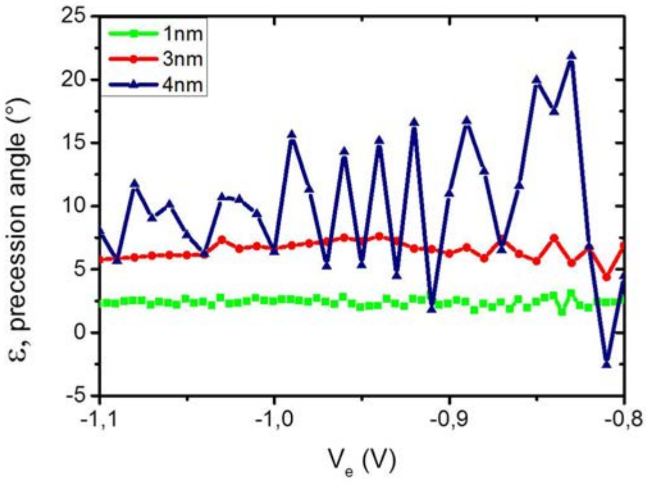

Fig. IX.28: *Precession angle in a CoFeB layer as a function of the applied voltage V_e. The blue line corresponds to a 4nm thick precession layer, the red line to a 3nm thick layer and the green line to a 1nm thick layer.*

In this figure, the precession angle seems to be constant in the energy range measured. As a consequence, an average value of the precession angle is extracted for each CoFeB thickness. Then, the precession velocity a (in $^o/nm$) can be obtained by fitting the variation of the precession angle with the thickness of the CoFeB precession layer (figure IX.29):

$$\epsilon = a.d$$

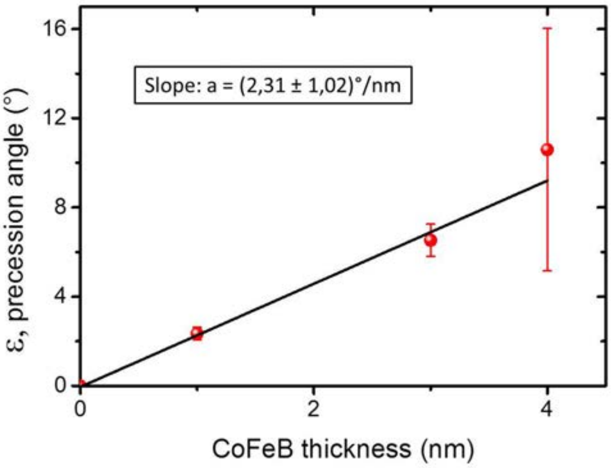

Fig. IX.29: *Precession angle as a function of the CoFeB thickness. The dark line is the best linear fit.*

A precession angle of $\epsilon = (2.31 \pm 1.02)^o$ per nanometer of CoFeB is determined

at an average energy of $0.95eV$ above the Fermi level. In his work [37], Weber *et al.* had found a precession angle of $19^o/nm$ in Co, and $33^o/nm$ in Fe at $7eV$ above the Fermi level. The values of precession angles found here are much smaller than the ones of Weber *et al.* in all the material studied.

The precession angle in CoFeB ($2.31 \pm 1.02^o/nm$) at around 1eV above the Fermi level is larger than the one found for a Co precession layer determined in the previous chapter ($0.7^o/nm$): the addition of Fe has increased the precession velocity. This seems to follow the trend of Weber, who had found the largest precession angle in the case of a Fe active layer.

III.C. Determination of the molecular field

Finally, the Bloch equations equation can be used to determine the molecular field in which the electronic spins have such a precession angle.

The velocity of an electron is $v = \sqrt{2E/m_e}$, in which $E = E_F + qV$ with $E_F = 11.4eV$ in the case of a CoFeB precession layer. Thus, the time to go through 1nm of CoFeB is $\tau = 0.479fs$ at $1eV$ above the Fermi level. This leads to a Larmor frequency $\omega_L = 8.41 \cdot 10^{13}\ rad.s^{-1}$, and a molecular field of $495T$.

The characteristic time T_1 is also obtained by fitting the temporal variation of $sin(\theta)$ with a decaying exponential. The result is shown in figure IX.30.

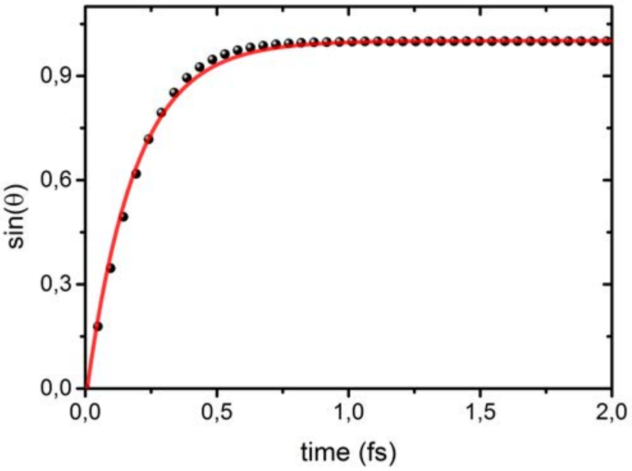

Fig. IX.30: *Spin filtering angle as a function of the time spent in the Co layer at 1eV above the Fermi level. The continuous line is the best fit obtained with a decaying exponential.*

Thus, a characteristic time $T_1 = 0.184 fs$ is obtained.

By considering a f.c.c. CoFeB layer, we have $N_{cell} = 4$ and $a = 0.29nm$. The magnetisation of a CoFeB layer is $\mu_0 M = 1.2T$ [59, 60]. In the literature, the exchange stiffness of $20.10^{-12} Jm^{-1}$ can be found [61]. With all these parameters, a molecular field of $498T$ is determined, close to the value that we have obtained by assuming a precession at the Larmor frequency ($495T$).

IV. Conclusion

In this chapter, the experimental study of MTT including three ferromagnetic layers have been shown. This chapter is focused on the study of a CoFeB precession layer.

The first step has consisted in the characterisation of the tunnel junction as a function of the applied field. We have shown that a parallel, an anti-parallel and two different crossed configurations of magnetisations can be obtained. This enables the calculation of the TMR, which can reach 50% at low voltages. The tunnel junction being symmetric, the polarisation of the CoFeB can be calculated:

$$P = \sqrt{\frac{TMR}{2 + TMR}}$$

A polarisation of 45% is found, indicating that 72.5% of the injected electrons have their spin oriented in the direction of the top layer magnetisation.

Then, the $TR = I_c/I_e$ is measured in different cases. We have shown in particular all the experimental cautions that have been taken so as to prove undoubtedly that the crossed configurations which highlighted the precession phenomenon (the three magnetisations are in the three space directions) are well obtained. In addition to the TR in the two crossed configurations (TR1 and TR2), the TR in a case where all the magnetisations are in the same direction under the influence of a strong magnetic field is also measured (TR3).

When these measurements have been made for different MTT (with a CoFeB precession layer of 1nm, 3nm and 4nm), $\Delta_{rel}TR$ can be fitted with its theoretical expression for applied voltages between 0.8 and 1.1V:

$$\begin{aligned}\Delta_{rel}TR &= \frac{TR1 - TR2}{2TR3 - TR1 - TR2} \\ &= sin(a.d)\,\sqrt{1 - tanh^2(b.d/2)}\end{aligned}$$

with a the precession velocity (in $^o/nm$), d the CoFeB thickness and $b = 1/\lambda^{\downarrow} - 1/\lambda^{\uparrow}$. By noticing that $\Delta_{rel}TR$ is almost constant in the energy range of the experiment, an average value of $\Delta_{rel}TR$ is calculated for each CoFeB thickness.

Thus, a precession angle of $(2.35 \pm 0.11)^o/nm$ in CoFeB is found at an average energy of $0.95eV$ above the Fermi level.

By using the Larmor frequency, we have determined that such a precession angle can be obtained with a molecular field of $495T$. A simple model based on the molecular field theory leads to an estimated Co molecular field of $498T$.

Résumé du chapitre :

Dans ce chapitre, nous avons étudié des transistors tunnels magnétiques (TTM) constitués de trois couches ferromagnétiques dont une possède une anisotropie perpendiculaire, et dont la couche active est composée de CoFeB. Les échantillons étudiés possèdent une épaisseur de 1nm, 3nm ou 4nm de CoFeB.

La première étape expérimentale a consisté en la caractérisation de la jonction tunnel pour différentes configurations magnétiques. Avec un champ magnétique appliqué dans la direction du champ d'échange de la couche supérieure, les configurations où les aimantations sont parallèles ou antiparallèles peuvent être obtenues. Cela permet de calculer la magnétorésistance tunnel :

$$MRT \ = \ \frac{I_e^P - I_e^{AP}}{I_e^{AP}}$$

Une MRT de 50% est mesurée pour les trois échantillons. Les configurations d'aimantations croisées sont obtenues quant à elles avec un champ appliqué perpendiculairement au champ d'échange.

Le taux de transfert est ensuite mesuré pour chaque échantillon dans toutes les configurations magnétiques possibles. Nous avons montré notamment toutes les précautions expérimentales qui ont été prises afin de s'assurer de la bonne obtention des configurations triplement croisées (les trois couches ferromagnétiques ont leurs aimantations qui pointent dans les trois directions de l'espace). Nous avons ainsi déterminé $\Delta_{rel}TR$ pour trois épaisseurs de CoFeB (1nm, 3nm et 4nm).

L'utilisation de l'expression théorique démontrée au chapitre précédent nous a alors permis de déterminer une vitesse de précession dans le CoFeB, qui est de $2.35^o/nm$ à 1eV au-dessus du niveau de Fermi. Ainsi, le champ moléculaire permettant une telle précession à la fréquence de Larmor est déterminé égale à 495T.

Chapter 10

Electronic spin precession in a CoAl alloy

In the previous chapters, the precession angle has been calculated for a Co or a CoFeB precession layer via the difference of the transfer ratio (TR) measured in the two crossed magnetic configurations. In this chapter, measurements are made for a magnetic tunnel transistor (MTT) including a CoAl precession layer. Indeed, we have seen in chapter V that such alloys have a Curie temperature (T_c) that can be adjusted around 100K, the optimum working temperature of the MTT. Thus, an extinction of the difference of TR between the two crossed configurations is expected above T_c, and so an additional proof of precession could be given.

In the first section, the magnetic tunnel junction (MTJ) is characterised, for a precession layer with 60% and 50% of Co. In particular, the tunnel magneto-resistance is measured as a function of the applied voltage for different temperatures. Its variation with the temperature appears to be correlated to the variation of the saturation magnetisation.

In the second section, the TR is measured as a function of the applied voltage for the different MTT magnetic configurations.

I. Characterisation of the tunnel junction

I.A. Case of a $Co_{0.6}Al_{0.4}$ alloy

I.B. Magnetic configuration of the tunnel junction

In the simple picture of the Weiss theory, the molecular field is proportional to the magnetisation of the sample. Thus, it is very interesting to study the electronic spin precession in a magnetic layer for which the magnetisation varies in the range of temperature (30K-100K) in which the MTT is working properly. In chapter V, we have studied CoAl alloys for different compositions. The alloys that contain more than 35% of Al are particularly interesting since they have a Curie temperature below the room temperature. Thus, the precession layer is a $Co_{0.6}\ Al_{0.4}$ alloy in this chapter.

In this section, a MTT including a $Co_{0.6}\ Al_{0.4}$ $(5nm)$ precession layer is studied. In this first part, the current extracted from the MTJ (I_e) is measured as a function of the applied field, for a voltage $V_e = -100mV$. In figure X.1, the field is applied along the exchange field of the CoFeB(2)Ta(0.5)Co(2)IrMn(7.5) top layer.

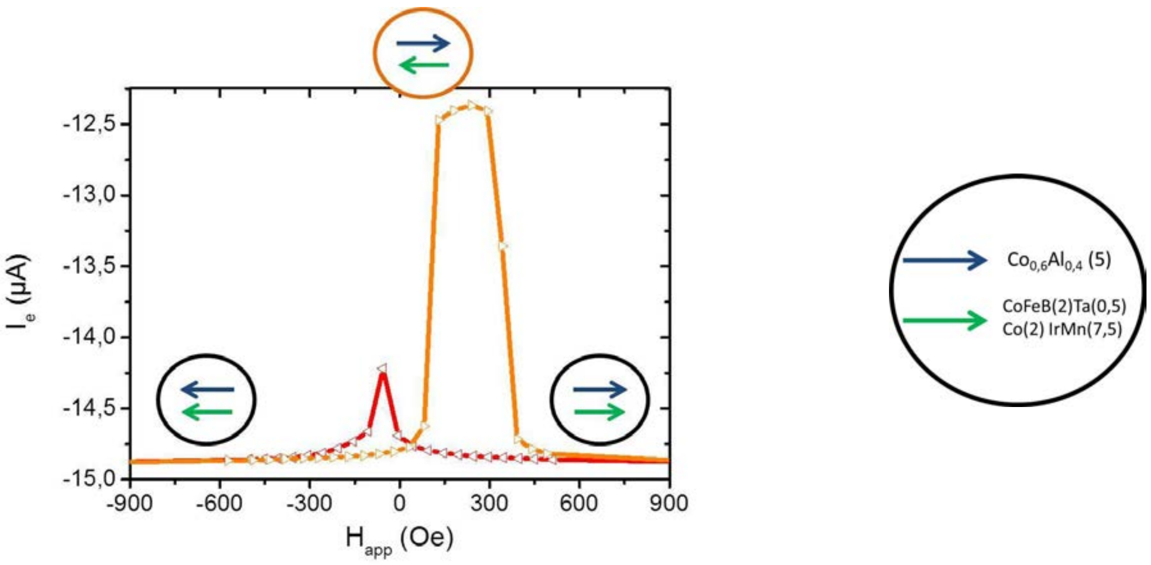

Fig. X.1: *Variation of the current extracted from the MTJ (I_e) as a function of the in-plane magnetic field. The applied voltage is $V_e = -100mV$ and the temperature is $20K$. In the insets, the $Co_{0.6}Al_{0.4}$ magnetisation is represented by a blue arrow and the magnetisation of the CoFeB(2)Ta(0.5)Co(2)IrMn(7.5) top layer by a green arrow. In this case, the field is applied along the direction of the exchange field.*

At saturation, the magnetisations of the CoAl layer and top layer are parallel (current $I_e^P = -14.8\mu A$). When the field decreases, (red curves), the CoAl and CoFeB(2)Ta(0.5)Co(2)IrMn(7.5) magnetisations switch almost at the same field around -100 Oe. When the field is reversed and increases from a negative saturation, the CoAl magnetisation switches at first at 100 Oe. Thus, the tunnel junction is in the anti-parallel configuration (current $I_e^{AP} = -12.4\mu A$), until the top layer magnetisation switches at 400 Oe (the magnetic bias of the top layer is equal to 150 Oe).

This configuration gives the full TMR of the junction but does not allow to get a crossed configuration of magnetisation of the tunnel junction, which is necessary for the measurement of the electronic spin precession. As a consequence, I_e has been also measured with an in-plane field applied perpendicular to the exchange field of the top layer (figure X.2).

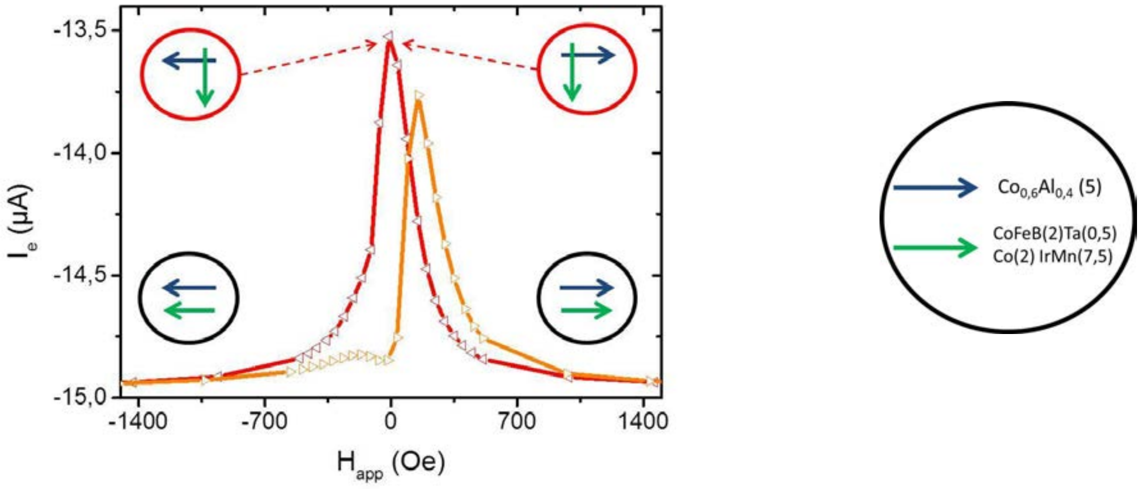

Fig. X.2: *Variation of the current extracted from the MTJ (I_e) as a function of the in-plane magnetic field. The applied voltage is $V_e = -100mV$ and the temperature is $20K$. In the insets, the $Co_{0.6}Al_{0.4}$ magnetisation is represented by a blue arrow and the magnetisation of the CoFeB(2)Ta(0.5)Co(2)IrMn(7.5) top layer by a green arrow. In this case, the field is applied perpendicular to the direction of the exchange field.*

After a positive magnetic saturation, the CoFeB(2)Ta(0.5)Co(2)IrMn(7.5) magnetisation rotates progressively towards its easy direction when the field decreases, leading to a reduction of the current I_e. At zero field, the magnetisation of the CoAl layer and the magnetisation of the top layer are crossed. Thus, the current in the crossed configuration is:

$$I_e^{\perp} = -13.6\mu A \simeq \frac{1}{2} \left(I_e^P + I_e^{AP} \right)$$

If the field decreases again, the CoAl magnetisation switches at -50 Oe and the second crossed configuration needed is obtained. Then, the current increases until the saturation of both magnetisations in the same direction is reached, at -1000 Oe.

I.B.1 Tunnel magneto-resistance as a function of the temperature

According to the previous part, it is possible to stabilise an anti-parallel configuration of the tunnel junction. This happens when the magnetic field is applied along the exchange field of the top layer. After a negative saturation (H_{app}=-3000 Oe), the field is increased until the magnetisation of the CoAl alloy switches at 50 Oe (current I_e^{AP}). Because of its magnetic bias, the top layer has not switched yet and the tunnel junction is in the anti-parallel configuration. Thus, the tunnel magneto-resistance (TMR) can be calculated:

$$TMR = \frac{I_e^P - I_e^{AP}}{I_e^{AP}}$$

Its variation with the applied voltage for different temperatures is shown in figure X.3:

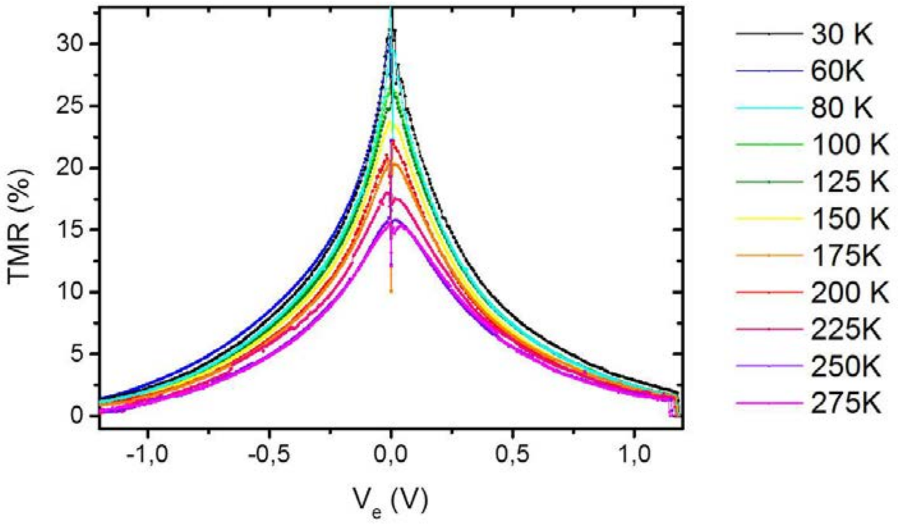

Fig. X.3: TMR of the $Co_{0.6}\ Al_{0.4}$ (5) $MgO(2.8)\ CoFeB(2)Ta(0.5)Co(2)IrMn(7.5)$ *tunnel junction as a function of the applied voltage* V_e*. Measurements were made for different temperatures between 30K and 275K.*

The main point here is that the TMR decreases when the temperature increases. A maximum of 30% is obtained at 30K for the low voltages, whereas the TMR only reaches 15% at 275K.

In the following figure X.4, the variation of the magnetisation at saturation with the temperature (measured in chapter V) is superimposed with the variation of the TMR taken at -100mV with the temperature.

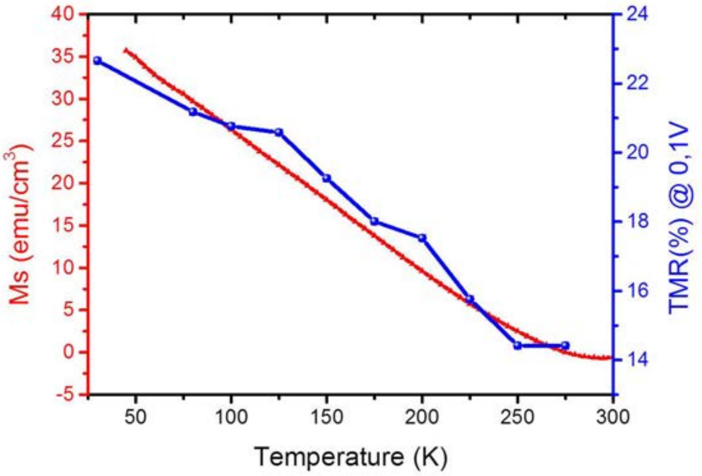

Fig. X.4: *Left scale: magnetisation at saturation of* $Co_{0.6}$ $Al_{0.4}$ (40) *as a function of the temperature. Right scale: TMR of the* $Co_{0.6}$ $Al_{0.4}$ (5) $MgO(2.8)$ $CoFeB(2)Ta(0.5)Co(2)IrMn(7.5)$ *tunnel junction at* $V_e = -100mV$ *as a function of the temperature.*

Results are surprising since a TMR different from zero is found for temperatures larger than T_c (and so M must be equal to zero). M(H) curves have been measured on 40nm thick layers: one could explain the results by the fact that magnetism of the 5nm and 40nm thick CoAl are different.

One could also argue that the properties of the interfaces are not those of the volume, and oxidation or segregation could occur at the interface (diffusion of Al towards MgO by the attraction of oxygen for instance). This could change the concentration of Al at the interface and on the volume, leading to reacher Co alloys, and leading to keep magnetism at higher temperature than expected.

I.C. Case of a $Co_{0.5}Al_{0.5}$ alloy

I.D. Magnetic configuration of the tunnel junction

In this section, a MTT including a $Co_{0.5}$ $Al_{0.5}$ (5) precession layer is studied. In this first part, the current extracted from the MTJ (I_e) is measured as a function of the applied field, for a voltage $V_e = -100mV$. In figure X.5, the field is applied along the exchange field of the

CoFeB(2)Ta(0.5)Co(2)IrMn(7.5) top layer.

At saturation, the magnetisations of the CoAl layer and top layer are parallel (current $I_e^P = -22.3\mu A$). When the field decreases (red curves), the CoAl and CoFeB(2)Ta(0.5)Co(2)IrMn(7.5) magnetisations switches almost at the same time, at around -20 Oe. When the field is reversed and increases, the CoAl magnetisation switches at first at 20 Oe. Thus, the tunnel junction is in the anti-parallel configuration (current $I_e^{AP} = -20.2\mu A$), until the top layer magnetisation switches at 250 Oe (the magnetic bias of the top layer is equal to 115 Oe).

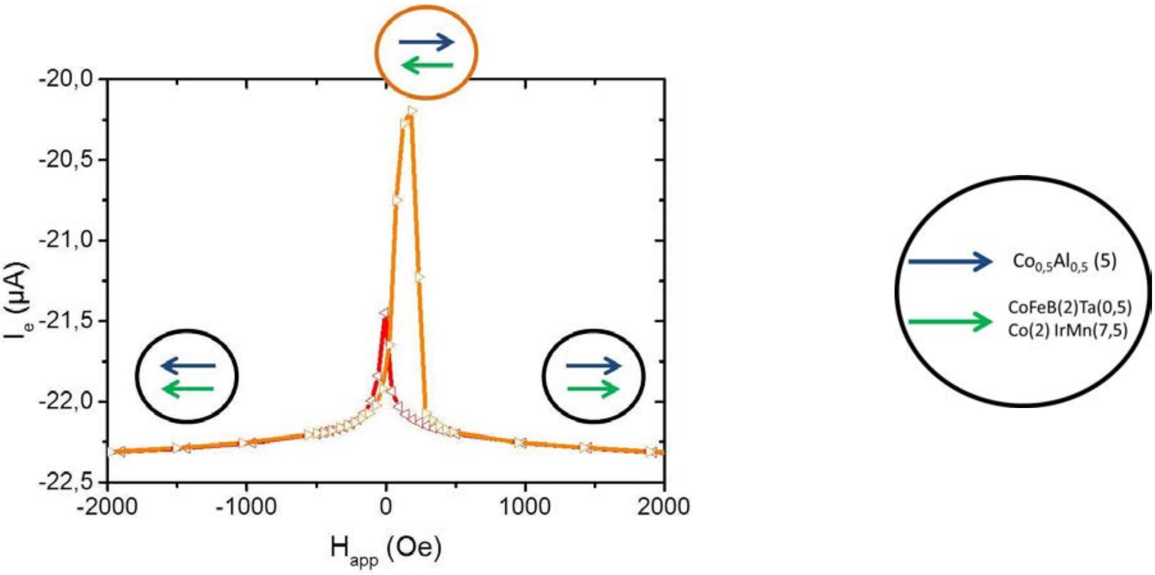

Fig. X.5: *Variation of the current extracted from the MTJ (I_e) as a function of the in-plane magnetic field. The applied voltage is $V_e = -100mV$ and the temperature is $20K$. In the insets, the $Co_{0.5}Al_{0.5}$ magnetisation is represented by a blue arrow and the magnetisation of the CoFeB(2)Ta(0.5)Co(2)IrMn(7.5) top layer by a green arrow. In this case, the field is applied along the direction of the exchange field.*

This configuration gives the full TMR of the junction but does not enable the obtention of a crossed configuration of the tunnel junction, which is necessary for the measurement of the electronic spin precession. As a consequence, I_e has been also measured with an in-plane field applied perpendicular to the exchange field of the top layer (figure X.6).

After a positive magnetic saturation, the CoFeB(2)Ta(0.5)Co(2)IrMn(7.5) magnetisation rotates progressively towards its easy direction when the field decreases, leading to a reduction of the current I_e. At zero field, the magnetisation of the CoAl layer and the magnetisation of the top layer are crossed. Thus, the current is the average of the currents of the parallel and anti-parallel configurations, ensuring the obtention of the crossed configuration:

$$I_e^{\perp} \; = \; -21.25\mu A \; \simeq \; \frac{1}{2} \left(\; I_e^{P} \; + \; I_e^{AP} \; \right)$$

If the field decreases again, the CoAl magnetisation switches at -50 Oe and the current increases until the saturation of both magnetisations in the same direction is reached, at -1000 Oe. The curve is symmetric when the field increases after a negative saturation, but the crossed configuration obtained at zero field is not the same. Indeed, the top layer magnetisation has rotated towards its easy direction regardless of the sign of the saturation. Nevertheless, the CoAl magnetisation is still in the direction of the saturating field at zero field, which depends obviously on the sign of the saturation (see insets in figure X.6).

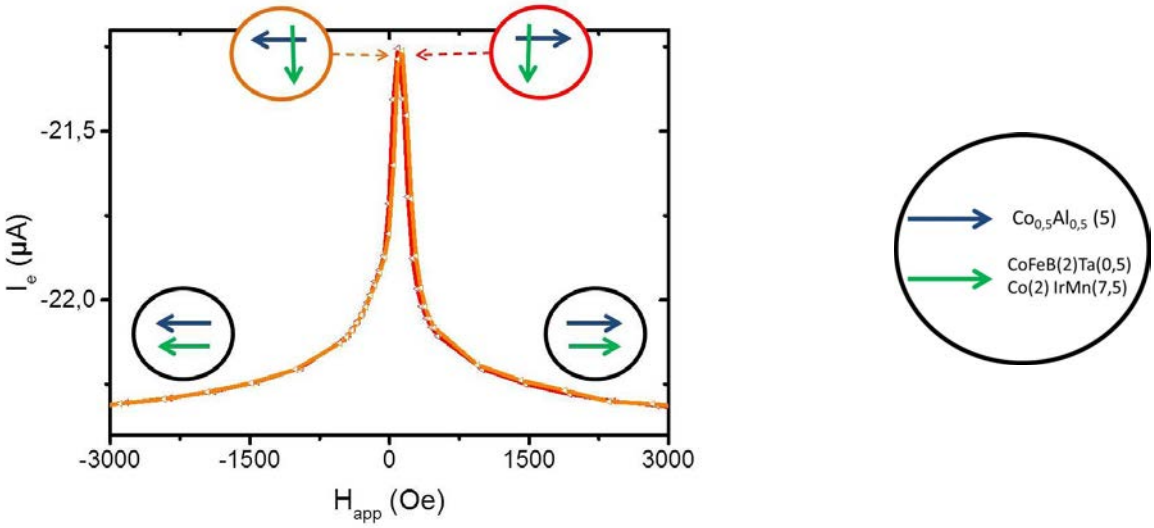

Fig. X.6: *Variation of the current extracted from the MTJ (I_e) as a function of the in-plane magnetic field. The applied voltage is $V_e = -100mV$ and the temperature is $20K$. In the insets, the $Co_{0.5}Al_{0.5}$ magnetisation is represented by a blue arrow and the magnetisation of the CoFeB(2)Ta(0.5)Co(2)IrMn(7.5) top layer by a green arrow. In this case, the field is applied perpendicular to the direction of the exchange field.*

I.D.1 Tunnel magneto-resistance as a function of the temperature

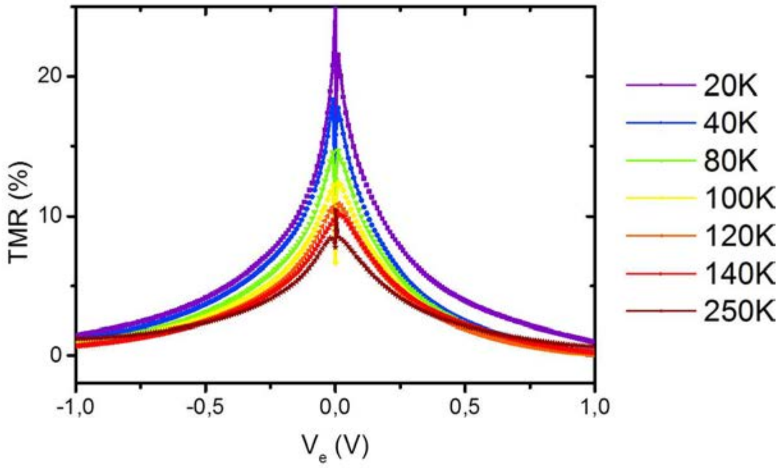

Fig. X.7: *TMR of the $Co_{0.5}$ $Al_{0.5}$ (5) $MgO(2.8)$ $CoFeB(2)Ta(0.5)Co(2)IrMn(7.5)$ tunnel junction as a function of the applied voltage V_e. Measurements were made for different temperatures between 30K and 275K.*

According to the previous part, it is possible to stabilise an anti-parallel configuration of the tunnel junction. This happens when the magnetic field is applied along the exchange field of the top layer. After a negative saturation (H_{app}=-3000 Oe), the field is increased until the magnetisation of the CoAl alloy switches at 50 Oe (current I_e^{AP}). Because of its magnetic bias, the top layer has not switched yet and the tunnel junction is in the anti-parallel configuration. Thus, the tunnel magneto-resistance (TMR) can be calculated. Its variation with the applied voltage for different temperatures is shown in figure X.3.

The main point here is that the TMR decreases when the temperature increases. A maximum of 25% is obtained at 30K for the low voltages, whereas the TMR only reaches 8% at 250K.

In the following figure X.8, the variation of the magnetisation at saturation with the temperature (measured in chapter V) is superimposed with the variation of the TMR taken at $-100mV$ with the temperature.

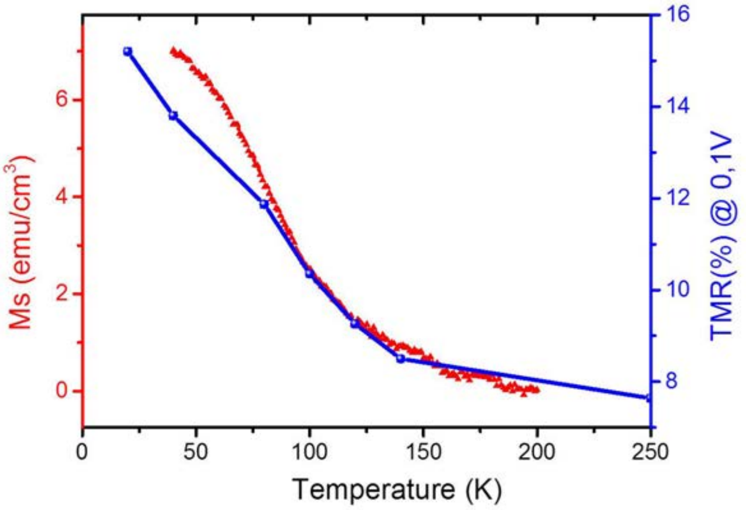

Fig. X.8: *Left scale: magnetisation at saturation of* $Co_{0.5}$ $Al_{0.5}$ (40) *as a function of the temperature. Right scale: TMR of the* $Co_{0.5}$ $Al_{0.5}$ (5) $MgO(2.8)$ $CoFeB(2)Ta(0.5)Co(2)IrMn(7.5)$ *tunnel junction at* $V_e = -100mV$ *as a function of the temperature.*

Here again, the same trend can be extracted. First, the TMR decreases when the saturation magnetisation decreases, but a TMR different from zero is obtained with $M_s = 0$.

This observation, made on two alloy concentrations, could not be explained up to know. Further investigations are needed.

II. Transfer ratio as a function of the MTT configuration

Once the magnetic behaviour of the magnetic tunnel junction is understood, the variation of the TR as a function of the applied voltage can be measured for different configurations of the MTT:

- The parallel configuration is obtained by saturating all the magnetisations in the direction of a large magnetic field.
- The crossed configurations can be obtained at zero field with a saturating field applied perpendicular to the direction of the exchange field of the top layer.
- A configuration with an anti-parallel injection and a crossed spin valve is stabilised with a field of 200 Oe applied in the direction of the exchange field, after a negative magnetic

saturation.

- A configuration with a parallel injection and a crossed spin valve is stabilised with a field of -500 Oe applied in the direction of the exchange field.

The figure X.9 shows the measurements realised at 20K on the MTT with a $Co_{0.6}$ $Al_{0.4}$ (5) precession layer.

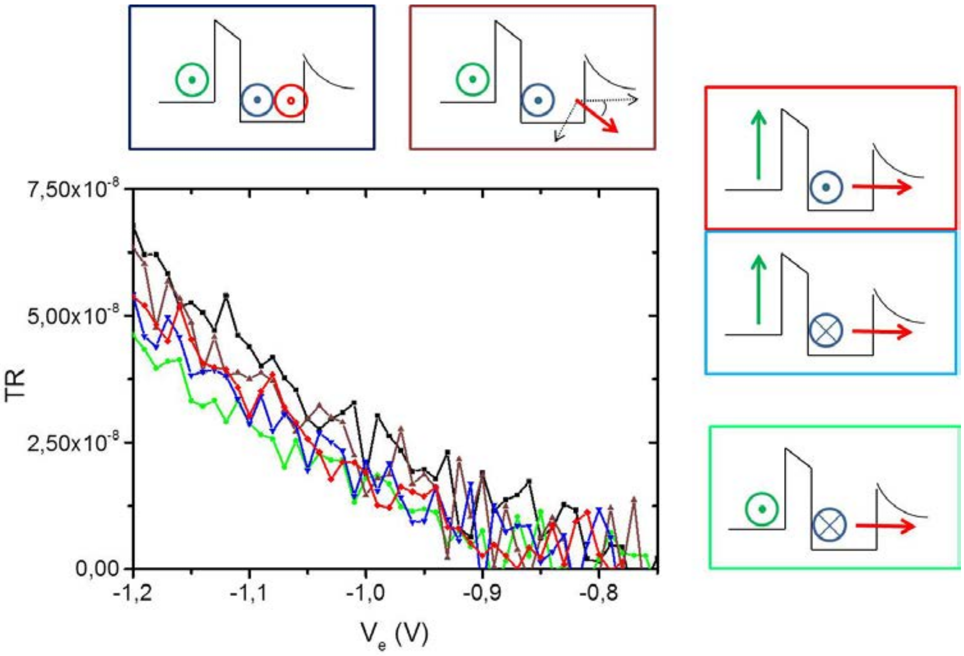

Fig. X.9: *Transfer ratio of the Si[100](HF) // Cu(5)Ta(1)Cu(5) Ni(0.6) [Co(0.2)/Ni(0.6)]*$_5$ *Cu(3.5)* $Co_{0.6}$ $Al_{0.4}$*(5) MgO(2.8) CoFeB(2)Ta(0.5)Co(2)IrMn(7, 5)Pt(5) stack, for different magnetic configurations. In the insets, the magnetisation of the [Co/Ni] multilayer is represented with a red arrow, the magnetisation of the CoAl alloy with a blue arrow and the magnetisation of the CoFeB(2)Ta(0.5)Co(2)IrMn(7, 5) top layer with a green arrow.*

In these experiments, the collected current in the semiconductor was really small. The measurements presented above were averaged 130 times in order to decrease the noise. Unfortunately, this was not enough to smooth the curve and extract any information. The same problem was encountered with the MTT with a $Co_{0.5}$ $Al_{0.5}$ (5) precession layer.

In a last experiment, the collected current has been measured for a fixed applied voltage for the different magnetic configurations of the MTT during several hours. The results are shown in figure X.10

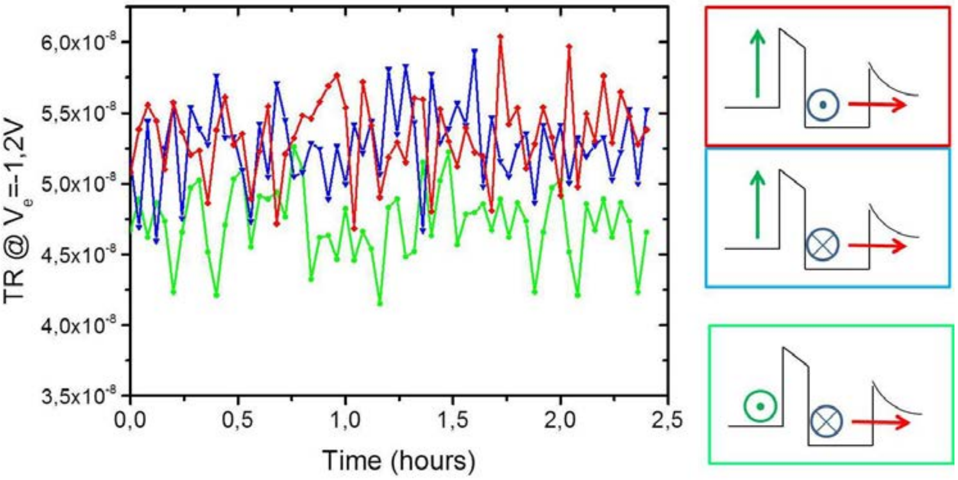

Fig. X.10: *Transfer ratio of the Si[100](HF) // Cu(5)Ta(1)Cu(5) Ni(0.6) [Co(0.2)/Ni(0.6)]$_5$ Cu(3.5) $Co_{0.6}$ $Al_{0.4}$(5) MgO(2.8) CoFeB(2)Ta(0.5)Co(2)IrMn(7, 5)Pt(5) stack, for different magnetic configurations. In the insets, the magnetisation of the [Co/Ni] multilayer is represented with a red arrow, the magnetisation of the CoAl alloy with a blue arrow and the magnetisation of the CoFeB(2)Ta(0.5)Co(2)IrMn(7, 5) top layer with a green arrow.*

Even now, no difference that can enable the determination of a precession angle is measured between the two crossed configurations. Up to know, we do not know if the small measured current is due to a real physical effect (for instance because of a strong scattering in the CoAl alloy, or because the mean free paths are reduced in the alloy compared to a Co layer), or due to experimental issues. Indeed, we have been experiencing some issues in the nanostructuration of our sample(s) for almost a year.

III. Conclusion

In this chapter, MTT including a CoAl precession layer are studied. In the first section, the current extracted from the tunnel junction has been measured as a function of the magnetic field. When the field is applied in the direction of the top layer exchange field, an anti-parallel configuration of magnetisations is stabilised at 200 Oe after a negative saturation. When the field is applied perpendicular to the exchange field, the crossed configuration of magnetisations is obtained. Once again, it is the top layer magnetisation that has rotated, ensuring uniform magnetisations. Then, the TMR has been measured as a function of the applied voltage, for different temperatures. A maximum of 30% is obtained at 30K for a $Co_{0.6}$ $Al_{0.4}$(5) precession layer and 25% for a $Co_{0.5}$ $Al_{0.5}$(5) alloy.

While a clear correlation of TMR and M_s could be observed, the persistence of TMR even with $M_s = 0$ is a mystery! The properties of 40nm and 5nm thock CoAl alloys are certainly not equivalent. Additional work has to be done to shed light on this inconstancy.

The TR has been measured in the case of a $Co_{0.6}$ $Al_{0.4}(5)$ precession layer in the second section. Unfortunately, the current measured is too small to enable the determination of a precession angle.

Résumé du chapitre :

Dans ce chapitre, nous avons étudié des transistors tunnels magnétiques (TTM) constitués de trois couches ferromagnétiques dont l'une possède une anisotropie perpendiculaire. La couche active est quant à elle composée d'un alliage de cobalt et d'aluminium. Les échantillons étudiés possèdent une proportion de Co valant 40% ou 60%.

La première étape expérimentale a consisté en la caractérisation de la jonction tunnel pour différentes configurations magnétiques. Avec un champ magnétique appliqué dans la direction du champ d'échange de la couche supérieure, les configurations où les aimantations sont parallèles ou antiparallèles peuvent être obtenues. Cela permet de calculer la magnétorésistance tunnel (*MRT*) :

$$MRT \;=\; \frac{I_e^P - I_e^{AP}}{I_e^{AP}}$$

Une MRT de 30% est mesurée lorsque l'alliage possède 60% de Co. Ces mesures ont été réalisées à différentes températures. Nous avons alors montré que la MRT décroit avec la température à cause de la diminution de l'aimantation à saturation.
Les configurations d'aimantations croisées sont quant à elles obtenues avec un champ appliqué perpendiculairement au champ d'échange.

Le taux de transfert est ensuite mesuré pour chaque échantillon dans toutes les configurations magnétiques possibles. Malheureusement, le courant collecté est très petit dans les deux TTM (60 ou 50% de Co) et ne permet pas de déterminer un angle de précession.

GENERAL CONCLUSION

In this thesis, we have built up from scratch an all-solid-state device enabling the measurement of the electronic spin precession in the molecular field of a magnetic layer. The novelty of this work is the fact that the measurement is performed at low energy just above the Fermi level. Therefore, our device is a magnetic tunnel transistor (MTT) including three ferromagnetic layers. The working principle of a MTT is the following:

- The electrons are injected via a tunnel barrier. As a consequence, they possess a low energy above the Fermi level, which is fixed by the voltage applied to the barrier. The injected electrons can be spin-polarised if a ferromagnetic layer is grown on top of the tunnel barrier.

- Then, electrons flow across a spin valve, which is composed by two ferromagnetic layers spaced by a non-magnetic metal. The mean free path of an electron in a ferromagnet depends on the orientation of its spin compared to the magnetisation: if the spin is in the same direction, the electron experiences few scattering events and the energy losses are small; if the spin is in the opposite direction, more scattering events occur, which leads to a stronger decrease of the energy.

- To contribute to the collected current in the final semiconductor, electrons must overcome an energy barrier, which is created by the interface between a metal and the semiconductor (named a Schottky barrier). Thus, the magnetic configuration of the spin valve has a strong impact on the energy of the spin-up and spin-down electrons, and the collected current depends on the relative orientation of the spin valve magnetisations.

Many MTT structures have already been studied by various team, but none of them enables the measurement of the electronic spin precession. Indeed, a non-collinear configuration of the three magnetisations is required. This means that one magnetic layer must have a perpendicular magnetic anisotropy (PMA). The first ferromagnetic layer on top of the tunnel barrier spin-polarises the injected electrons. The precession phenomenon occurs in the second ferromagnetic layer. The third ferromagnetic layer enables the spin direction analysis via a GMR effect. The energy landscape of the MTT expected to measure the electronic spin precession is presented in the following figure:

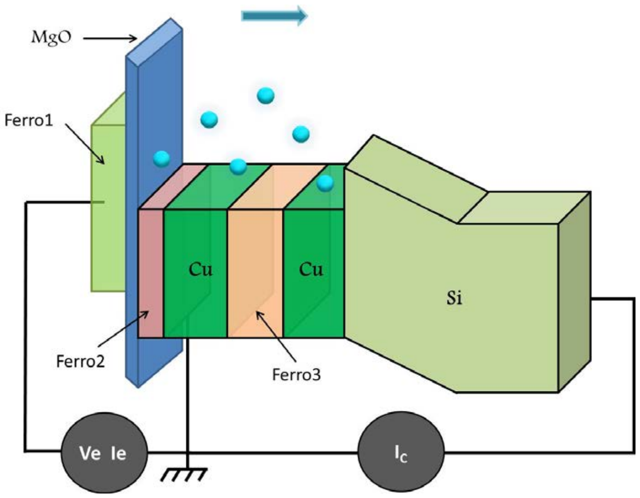

Fig. X.11: *Energy landscape of the MTT built in this thesis.*

During the three years of my PhD as well as on this thesis, we have performed a step-by-step approach to develop and optimise successively the different elementary bricks of the device.

In the first step, the growth of a magnetic layer that exhibits a PMA on top of a Schottky diode has been optimised. On the one hand, previous studies in the laboratory had demonstrated that a Si[100] substrate cleaned in a bath of hydrofluoric acid (HF 0.6%) associated with a Cu layer defines a good Schottky diode. On the other hand, literature reported that a multilayer of Co and Ni exhibits a PMA, if the ratio of thickness t_{Ni}/t_{Co} is larger than 2 and if the multilayer has a [111] texture. Nevertheless, the growth of a $[\mathrm{Co}(0.2)/\mathrm{Ni}(0.6)]_5$ multilayer on top of a Si[100]/Cu Schottky diode does not enable the obtention of a PMA. By associating magnetometry measurements with X-ray diffraction experiments, we could determine that the HF cleaning of the substrate induces a [100] texture of the entire sample, while the [111] texture is needed for the [Co/Ni] multilayer to get perpendicular. The HF cleaning being absolutely necessary to remove the Si oxide on the surface and ensure the quality of the energy filtering, a solution was found to orientate the multilayer along the [111] direction anyway: a thin amorphous Ta layer is inserted in the middle of the Cu. Thus, the Cu layer on top of the Ta layer can grow according to its close packed planes, along the [111] direction, and promotes this texture for the Co/Ni multilayer.

Then, the optimisation of the [Co/Ni] multilayer was achieved. An optimum Ta layer of 1nm was found to preserve the PMA of the multilayer during the annealing necessary to pin the top layer. Then, we showed that Cu/Ni interfaces stabilise the PMA compared to the Cu/Co interfaces. Finally, we have shown that the Co/Ni multilayer exhibits a PMA from 1 to 5 repetitions of the multilayer. As a result, the first brick “analysis layer + energy filter” is the following (thickness in nanometers):

$$Si[100]\ (HF)\ //\ Cu(5)Ta(1)Cu(5)\ Ni(0.6)\ [Co(0.2)/Ni(0.6)]_5 \ldots$$

The second step of the MTT construction consisted in the optimisation of the spin valve. In order to keep flexibility on the precession layer, this work was done only on the [Co/Ni] analysis layer. As explained before, the current measured in the semiconductor depends on the magnetic configuration of the spin valve: if the magnetisations are parallel, a strong current is measured; if the magnetisations are crossed, only a small current is observed. This enables the definition of the crossed magneto-current:

$$MC^{\perp} = \frac{I^P - I^{\perp}}{I^{\perp}}$$

The sensitivity of the electronic spin precession will be determined partly by the value of the crossed magneto-current: the higher $MC^{\perp}$, the smaller the measurable precession angle. In order to increase the $MC^{\perp}$, one could simply enhance the spin polarisation of the current, by increasing the ferromagnetic layer thickness for instance. In our case, that means multiply the number of repetition of the Co/Ni multilayer. Thus, the $MC^{\perp}$ has been measured as a function of the number of repetitions. It reaches 85% for 5 repetitions, close to the theoretical maximum of 100% that can be obtained with this geometry. The variation of the $MC^{\perp}$ with the applied voltage was also measured for different temperatures. We have shown in particular that a phenomenon decreases the $MC^{\perp}$ if the temperature is lower than 30K: a phenomenon close to the previous electrons trapping process at the Cu/Si interface is certainly at the origin of this decrease.

In a last experiment, we have measured the variation of the collected current with a rotating field. The experiments have been theoretically reproduced by assuming that the $MC^{\perp}$ is proportional to $cos(\phi)$, with ϕ the angle between the spin valve magnetisations. Finally, the structure of the MTT at this point is:

$$Si[100](HF)//\ Cu(5)Ta(1)Cu(5)\ Ni(0.6)\ [Co(0.2)/Ni(0.6)]_5\ Cu(3.5)\ [Precession\ layer]\ MgO(2.8) \ldots$$

On the last step of the MTT construction, the top layer that spin-polarises the injected electrons can be added. A CoFeB on top of the MgO is needed since a highly spin-polarised current had been already measured in the laboratory with a CoFeB(4)/MgO(2.8)/CoFeB(4) magnetic tunnel junction. In order to pin the top layer, an antiferromagnetic layer (IrMn) is added. However, the highest exchange field is obtained in the case of a layer oriented along the [111] direction, while the top CoFeB layer is oriented along the [200] direction because of the

MgO layer. Thus, a thin amorphous Ta layer and a Co layer are inserted between CoFeB and IrMn. The Ta layer being amorphous, the Co layer grows according to its close packed planes and promotes the [111] texture for the IrMn layer. The final MTT structure is:

$$Si[100]\ (HF)\ //\ Cu(5)Ta(1)Cu(5)\ Ni(0.6)\ [Co(0.2)/Ni(0.6)]_5\ Cu(3.5)$$

$$[Precession\ layer]\ MgO(2.8)\ CoFeB(2)Ta(0.5)Co(2)IrMn(7.5)\ Pt(5)$$

At this point, the device is ready to measure the electronic spin precession in different kinds of active layers. Firstly, the measurements were performed in a Co layer. Then, a CoFeB precession layer was used. In both cases, the same procedure has been followed.

At first, the magnetic tunnel junction was characterised. In all the MTT studied, a parallel and an anti-parallel configuration of the MTJ can be obtained with a field applied along the exchange field of the top layer, and the tunnel magneto-resistance (TMR) can be calculated. TMR values of 50% are obtained with a CoFeB precession layer, which means that the CoFeB polarisation is equal to 45%. Thus, 72.5% of the injected electrons have a spin in the direction of the top layer, 27.5% have it in the other direction. In the case of a Co precession layer, a TMR of 15% is obtained. Anyway, the top layer is still a CoFeB layer and the injected current is still spin-polarised at 45%.

The crossed configurations are obtained at zero field with an applied field perpendicular to the exchange field. In this case, the magnetisation of the top layer has rotated towards its easy direction. This point is important because all the magnetisations must be uniform to perform spin precession measurements, uniformity ensured in the top layer during the rotation by the strong exchange coupling with the anti-ferromagnetic layer.

Then, the transfer ratio of the MTT is measured for different magnetic configurations, in particular for the two different crossed configurations of the MTT (TR1 and TR2) and for the parallel configuration with a strong magnetic field (TR3). By measuring these quantities for different thicknesses d of the precession layer, it is possible to obtain the precession angle a (in $^o/nm$);

$$\Delta_{rel}TR \ = \ \frac{TR1 - TR2}{2TR3 - TR1 - TR2}$$

In the case of a Co precession layer, we could determine the precession angle and b as a function of the electrons energies. b being almost constant in our energy range, a mean value of

$b = 0.7nm^{-1}$ was determined in our energy range. Thus, the spin filtering angle was determined as a function of the Co thickness:

$$\theta \ = \ ArcTan\left[\frac{tanh(b.d/2)}{\sqrt{1 - tanh^2(b.d/2)}}\right]$$

A spin filtering almost equal to 100% is found for a 10nm thick Co layer. The precession angle decreases with the energy, from $0.8^o/nm$ at $0.8eV$ to $0.7^o/nm$ at $1eV$ above the Fermi level. These values are really different from the one obtained by W. Weber *et al.*, who had measured a precession of $18^o/nm$ at $E + E_F = 8eV$. Finally, a molecular field of $152T$ is required to obtain such a precession angle in the Bloch equations. A quick calculation using the Heisenberg Hamiltonian in the Weiss theory gives a molecular field of around $167T$ in the case of a Co layer.

With a CoFeB precession layer, the experimental data presented too much noised to calculate a precession angle and spin filtering angle at each energy. Thus, only mean values on our energy range were determined. A precession angle of $2.31 \pm 1.02^o/nm$ is obtained, and the value $b = 1.79nm^{-1}$ enables the calculation of θ as a function of the CoFeB thickness. An almost 100% efficient spin filtering is found for a 4nm thick CoFeB layer. The molecular field required to obtain such a precession angle is $495T$, almost equal to the field estimated with the Weiss theory ($498T$).

In the last chapter of this thesis, a MTT including a CoAl alloy is presented. It was demonstrated in a previous chapter that a CoAl alloy has a Curie temperature below the room temperature if the proportion of Co is smaller than 65%. The interest in using such a precession layer is the fact that there is no precession and $\Delta_{rel}TR$ is cancelled when the temperature increases up to the ferromagnetic-paramagnetic transition. Two MTT were realised with respectively a $Co_{0.6}Al_{0.4}$ and $Co_{0.5}Al_{0.5}$ as precession layers. The MTJ were characterised and all the magnetic configurations required were obtained. A TMR of 30% was measured at low temperature, and a TMR decrease with the temperature was observed. Nevertheless, the collected current in the semiconductor was too small to enable precise measurements of the electronic spin precession. We do not know today if the collected current is reduced by a real physical effect, or if some issues occur during the sample growth or during the nanostructuration.

Finally, this thesis is the result of almost 15 years of successful studies of my supervisors. The device built in this work was based on the knowledge accumulated over time on sample growth, on nanostructuration, on electronics ...

PERSPECTIVES

In this thesis, we have built a device, based on an MTT structure, in order to measure the electronic spin precession in Co and CoFeB. The device was developed and optimised in a way that gives a large flexibility in the choice of the precession layer. Thus, it can be used to measure the electronic spin precession in a large range of active layers. We have already tried with a CoAl layers, but additional works are needed in order to perform the measurement in such alloys.

Moreover, the different bricks that have been optimised in our device can be used for other kinds of experiments. We have recently made preliminary experiments in which the hot electron current is created by a laser excitation. Then, the current flows across a spin valve grown on our Schottky diode. This could allow us to determine the quantity of hot electrons generated by the laser excitation by tuning their energies around the barrier height with the wavelength of the laser. This point should be interesting for those who study the ultrafast demagnetisation by laser excitation for instance.

Bibliography

[1] *Magnetism: From Fundamentals to Nanoscale Dynamics.* Berlin: Springer-Verlag, 2006.

[2] Jedema F.J. *Electrical Spin Injection in metallic Mesoscopic Spin Valves.* PhD thesis, University of Groningen, 2002.

[3] Appelbaum I., Huang B., and Monsma D.J. Electronic measurement and control of spin transport in silicon. *Nature 447, 295-298*, 2007.

[4] Weber W., Riesen S., and Siegmann H.C. The dynamic response of magnetization to hot spins. *SLAC-PUB-10018*, 2002.

[5] Weber W., Riesen S., Back C.H., Shorikov A., Anisimov V., and Siegmann H.C. Spin motion of electrons during reflection from a ferromagnetic surface. *Phys. Rev. B 66, 100405(R)*, 2002.

[6] Weber W., Oberli D., Riesen S., and Siegmann H.C. The electron analogue to the faraday rotation. *New Journal of Physics 1: 9.1–9.6*, 1999.

[7] Jedema F.J., Costache M.V., Heersche H.B., Baselmans J.J.A., and van Wees B.J. Electrical detection of spin accumulation and spin precession at room temperature in metallic spin valves. *Appl. Phys. Letter 81, 5162*, 2002.

[8] Julliere M. Tunneling between ferromagnetic films. *Phys. Lett. A 54, 225*, 1975.

[9] Moodera J.S. and al. Large magneto-resistance at room temperature in ferromagnetic thin film tunnel junction. *Phys. Rev. Letter 74, 3273*, 1995.

[10] Harrison W.A. Tunneling from an independent-particle point of view. *Phys. Rev. B 123, 85*, 1961.

[11] Brinkman W. and al. Tunneling conductance of asymmetrical barriers. *Journal of Applied Physics, vol. 41, p. 1915*, 1970.

[12] Straton R. and al. Volt-current characteristics for tunneling through insulating films. *Journal of Physic and Chemistry of Solids, vol. 23, p. 1177*, 1962.

[13] Akerman J.J. and al. Criteria for ferromagnetic–insulator–ferromagnetic tunneling. *Mag. Mag. Mat. 240, 86*, 2002.

[14] Tedrow P.M. and Meservey R. Spin-dependent tunneling into ferromagnetic nickel. *Phys. Rev. Letter 26, 192*, 1971.

[15] Meservey R. Tunnelling in a magnetic field with spin-polarized electrons. *Physica Scripta. Vol. 38, 272-276*, 1988.

[16] Slonczewski J.C. Conductance and exchange coupling of two ferromagnets sperated by a tunneling barrier. *Phys. Rev. B 39, 6995*, 1989.

[17] De Teresa J.M., Barthélémy A., Fert A., J.P.Contour, Lyonnet R., F.Montaigne, P.Seneor, and Vaurès A. Inverse tunnel magnetoresistance in co/srtio3/la0.7sr0.3/mno3: New ideas on spin-polarized tunneling. *Phys. Rev. Letter 82, p. 4288*, 1999.

[18] Chulkov E.V. and al. Electronic excitations in metals and at metal surfaces. *Chem. Rev. 106, 4160*, 2006.

[19] Knorren R., Bennemann K.H., Burgermeister R., and Aeschlimann. M. Dynamics of excited electrons in copper and ferromagnetic transition metals: Theory and experiment. *Phys. Rev. B 61 (14), 9427*, 2000.

[20] Burgi L., Jeandupeux O., Brune H., and K. Kern. Probing hot-electron dynamics at surfaces with a cold scanning tunneling microscope. *Phys. Rev. Letter 82 (22), 4516*, 1999.

[21] Zarate E., Apell P., and P.M. Echenique. Calculation of low-energy-electron lifetimes. *Phys. Rev. B. 60, 2326*, 1999.

[22] Aeschlimann M., Bauer M., Pawlik S., Weber W., Burgermeister R., Oberli D., and Siegmann H.C. Ultrafast spin-dependent electron dynamics in fcc co. *Phys. Rev. Letter 79, 5158*, 1997.

[23] Carpene E. and al. Dynamics of electron-magnon interaction and ultrafast demagnetization in thin iron films. *Phys. Bev. B 78, 174422*, 2008.

[24] Knorren R., Bouzerar G., and Bennemann. K.H. Theory for the dynamics of excited electrons in noble and transition metals. *J. Phys.: Condens. Matter 14, R739*, 2002.

[25] McDougall B.A., Balasubramanian T., and Jensen. E. Phonon contribution to quasiparticle lifetimes in cu measured by angle-resolved photoemission. *Phys. Rev. B. 51 (19), 13891*, 1995.

[26] Eiguren A. and al. Role of bulk and surface phonons in the decay of metal surface states. *Phys. Rev. Letter 88 (6), 066805*, 2002.

[27] Plihal M., Mills D.L., and Kirschner J. Spin wave signature in the spin polarized electron energy loss spectrum of ultrathin fe films: Theory and experiment. *Phys. Rev. Letter 82, 2579*, 1999.

[28] *Introduction to solid state physics.* Wiley and Sons, inc., 1966.

[29] Brown R.H., Nicholson D.M.C., Wang X., and Schulthess T.C. First principles theory of spin waves in fe, co, and ni. *J. Appl. Phys. 85, 4830*, 1999.

[30] Kim S. Micromagnetic computer simulations of spin waves in nanometre-scale patterned magnetic elements. *J. Phys. D: Appl. Phys. 43, 264004*, 2010.

[31] Hong J. and Mills D.L. Theory of the spin dependence of the inelastic mean free path of electrons in ferromagnetic metals: A model study. *Phys. Rev. B. 59, 13840*, 1999.

[32] Hong J. and Mills D.L. Spin dependence of the inelastic electron mean free path in fe and ni: Explicit calculations and implications. *Phys. Rev. B. 62, 5589*, 2000.

[33] *Physics of semiconductor devices.* Inc 2nd edition, 1981.

[34] Lu Y., Lacour D., Lengaigne G., Le Gall S., Suire S., Montaigne F., and Hehn M. Interfacial trapping for hot electron injection in silicon. *Appl. Phys. Letter 103, 022407*, 2013.

[35] van Dijken S., Jiang X., and Parkin S.S.P. Giant magnetocurrent exceeding 3400with spin-valve base layers. *Appl. Phys. Letter 83, 951*, 2003.

[36] Hehn M. and al. A high magnetic field sensor based on magnetic tunnel junctions. *European Physical Journal : Applied Physics 28, 79*, 2004.

[37] Weber W. and al. Magnetization precession by hot spin injection. *Science 291, 1015*, 2001.

[38] Valet T. and Fert A. Theory of the perpendicular magnetoresistance in magnetic multilayers. *Phys. Rev. B. 48, 7099*, 1993.

[39] Jansen R. The spin-valve transistor: a review and outlook. *J. Phys. D: Appl. Phys. 36, R289*, 2003.

[40] Néel L. Anisotropie magnétique superficielle et surstructures d'orientation. *J. Phys. Radium, 15:225–239*, 1954.

[41] Carcia et al. P.F. Perpendicular magnetic anisotropy in pd/co and pt/co thin film layered structures. *J. Appl. Phys. 63, 5066*, 1988.

[42] Daalderop G.H.O., Kelly P.J., and den Broeder F.J.A. Prediction and confirmation of perpendicular magnetic anisotropy in co/ni multilayers. *Phys. Rev. Letter, 68, 682*, 1992.

[43] *Magnetism and magnetic materials.* 2009.

[44] den Broeder F.J.A., anssen E., Hoving W., and Zeper W.B. Perpendicular magnetic anisotropy and coercivity of co/ni multilayers. *IEEE TRANSACTIONS ON MAGNETICS, VOL. 28, NO. 5*, 1992.

[45] Johnson M.T., de Vries J.J., McGee N.W.E., aan de Stegge J., and den Broeder F.J.A. Orientational dependence of the interface magnetic anisotropy in epitaxial ni/co/ni sandwiches. *Phys. Rev. Letter 69, 3575*, 1992.

[46] Lu Y., Lacour D., Lengaigne G., Le Gall S., Suire S., Montaigne F., Hehn M., and Wu M.W. Electrical control of interfacial trapping for magnetic tunnel transistor on silicon. *Appl. Phys. Letter 104, 042408*, 2014.

[47] Malinowski G. *Transport dépendent du spin et couplage d'échange : de la jonction tunnel au capteur magnétique intégré.* PhD thesis, Université Henri Poincaré - Nancy I, 2004.

[48] Chang C. Formation of copper silicides from cu(100)/si(100) and cu(111)/si(111) structures. *Journal of Applied Physics 67, 566*, 1990.

[49] Chabal Y.J., G.S.Higashi, and Raghavachari K. Infrared spectroscopy of si(111) and si(100) surfaces after hf treatment: Hydrogen termination and surface morphology. *Journal of Vacuum Science and Technology A: Vacuum, Surfaces, and Films 7, 2104*, 1989.

[50] Bernos J. *Elaboration de jonctions tunnel magnétiques et de jonctions métal/oxyde/semiconducteur pour l'étude du transport et de la précession du spin d'électrons chauds.* PhD thesis, Université Henri Poincaré - Nancy 1, 2010.

[51] *Magnetic Multilayers and Giant Magnetoresistance.* Springer ISBN 978-3-642-08487-4, 2000.

[52] Vautrin C., Lu Y., Robert S., Sala G., Lenoble O., Petit-Watelot S., Devaux X., Montaigne F., Lacour D., and Hehn M. Magnetic tunnel transistor with a perpendicular co/ni

multilayer sputtered on a si/cu[100] schottky diode. *J. Phys. D: Appl. Phys. 49, 355003 (4pp)*, 2016.

[53] Gottwald M. *Nouveaux systèmes modèles à aimantation perpendiculaire pour l'étude des effets de transfert de spin.* PhD thesis, Université Henri Poincaré, 2011.

[54] Butler S.R., Hanlon J.E., and Wasilewski R.J. Electric and magnetic properties of b2 sturcture componds: Nial, coal. *J. Phys. Chem. Solids Pergamon Press 1969. Vol. 30, pp. 1929-1934*, 1969.

[55] Sundararajant V., Sahut B.R., .Kanherel D, G, Panatt P.V., and Das G.P. Cohesive, electronic and magnetic properties of the transition metal aluminides feal coal and nial. *J. Phys.: Condens. Matter 7, pp. 6019-6034*, 1995.

[56] Vedyayev A., Dieny B., Ryzhanova N., Genin B., and Cowache C. Angular dependence of giant magnetoresistance in magnetic multilayered structures. *Europhys. Lett., 25 (6), pp. 465-470*, 1994.

[57] Steren L.B., Barthelemy A., Duvail J.L., Fert A., Morel R., and Petroff F. Angular dependence of the giant magnetoresistance effect. *Phys. Rev. B 51, 1*, 1995.

[58] Eyrich C., Huttema W., Arora M., Montoya E., Rashidi F., Burrowes C., Kardasz B., Girt E., Heinrich B., Mryasov O.N., From M., and O.Karis. Exchange stiffness in thin film co alloys. *J. Appl. Phys. 111, 07C919*, 2012.

[59] Qiu X., Narayanapillai K., Wu Y., Deorani P., Yang D., Noh W., Park J., Lee K., Lee H., and Yang H. Spin–orbit-torque engineering via oxygen manipulation. *Nature nanotechnology, vol. 10, p333*, 2015.

[60] Chen Y. and Xie S.M. Magnetic and electric properties of amorphous $co_{40}fe_{40}b_{20}$ thin films. *Journal of Nanomaterials Volume 2012*, 2012.

[61] Devolder T., Kim J.V., Nistor L., Sousa R., B.Rodmacq, and Diény B. Exchange stiffness in ultrathin perpendicularly magnetized cofeb layers determined using the spectroscopy of electrically excited spin waves. *Journal of Applied Physics 120, 183902*, 2016.

ANNEX A

In order to realise transport measurements in which the electric flux is perpendicular to the sample plane, it is necessary to structure the sample. The goal of the nanostructuration is to define the size of junctions, to take electrical contacts and to isolate electrodes between them. We have used for that a process based on UV lithography associated with ion beam etching and cathodic pulverisation. All the samples were processed in the cleaning room of the C.C. (*centre de compétence*) "Minalor" of the Jean Lamour Institute.

The different steps of the process used to take electrical contacts at three different points of a multilayer are described here. This one was developed by François Montaigne and Gwladys Lengaigne of C.C. Minalor.

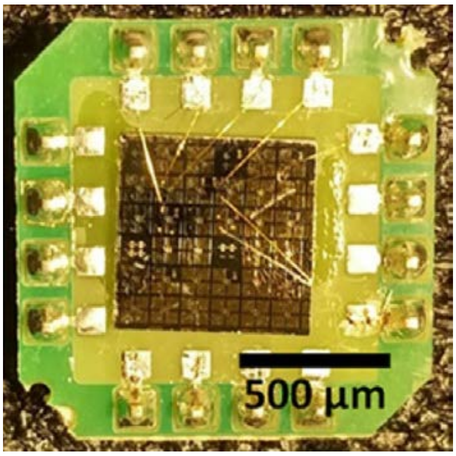

I. Top electrode

In order to define the top electrode, a double step "lithography + ion beam etching" is used.

I.A. Sample preparation

At first, the sample is cleaned in a bath of acetone for 5 minutes with an ultra-sonic bath. Then, the sample is rinsed for 20 seconds with isopropanol and dried with a flux of nitrogen. Then, the sample is coated with the resin Shipley S1813 by using a spinner that enables the homogenisation of the resin thickness. The spinner goes at 10000 rounds per minutes (rpm) for 60 seconds. After the spin-coating, the sample is heated at 115^oC for 60 seconds in order to evaporate the solvent contained in the resin.

I.B. Photolithography

The photo-lithography is a well-known technique in micro-electronics: in every technological process, it defines patterns in resin at the sample surface. These patterns protect the parts of the sample they recover. Thus, when the sample deals with a treatment, like an etching, only the area without resin is modified.

The insulation of the resin is made with a mask and a light which wavelength is 365 nm for 20s. This mask in quartz contains patterns in chromium which define the square shape of the top electrode by preventing areas to be insulated. In our case, the resin used is said positive and only the area exposed to the light will be dissolved during the development in a bath of MF319. The duration of the development is 40s. Then, the sample is immersed in deionised water for 20 seconds and dried with nitrogen. At the end, the patterns on the mask are reproduced on the surface of the sample (see figure A1). The thickness of the resin is about 1.3 μm.

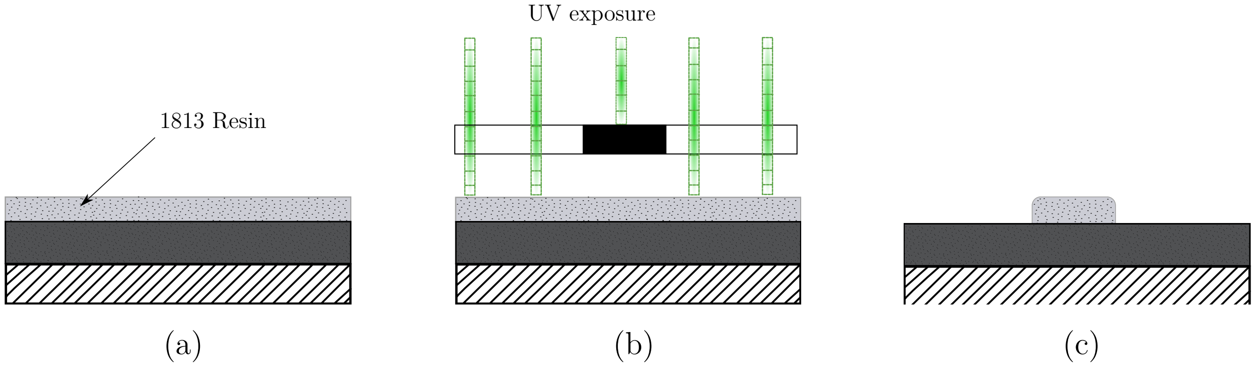

Fig. A1: *The substrate is represented in hatched, the layer that will be etched is coloured in grey and the resin is in stippling. The sample is covered with the most homogeneous possible layer of resin (a). The resin is then insulated across a mask that defines the shape of the electrode (b) and developed (c).*

I.C. Dry etching

In our measurements, we need to take an electrical contact at the bottom of the tunnel junction. The etching of the sample is made with a beam of argon ions (figure A2a). The working pressure is around 1.5 10^{-4} $mbar$ and the ions energies for the etching is equal to 200 eV. We control the depth of the etching with a SIMS (*secondary ion mass spectrometer*). This chemical characterisation consists in analysing the composition of the surface exposed to know the nature of the element etched (figure A2b). Only the area that is not protected by the resin is etched. Then, the resin is dissolved in acetone for at least two hours (figure A2c), and the top electrode appears.

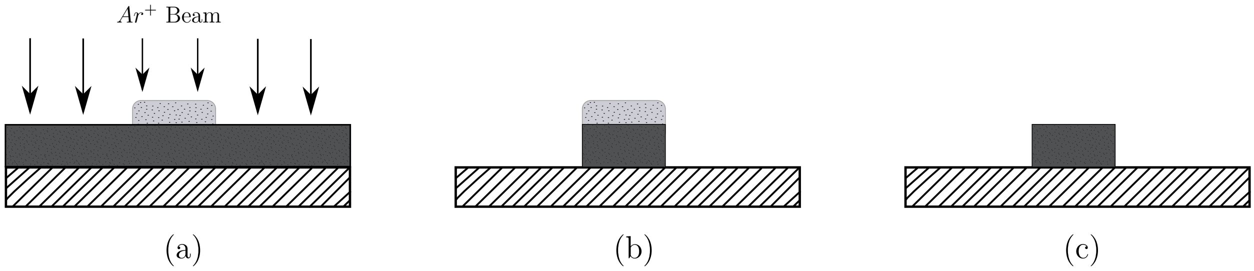

Fig. A2: *After an etching with an argon ion beam (a), only the area protected with resin stays unmodified (b). The resin remaining is dissolved with acetone (c).*

A drawing of the topology of the sample after that double-step "lithography + dry etching" and a top view picture are shown in the figure A3.

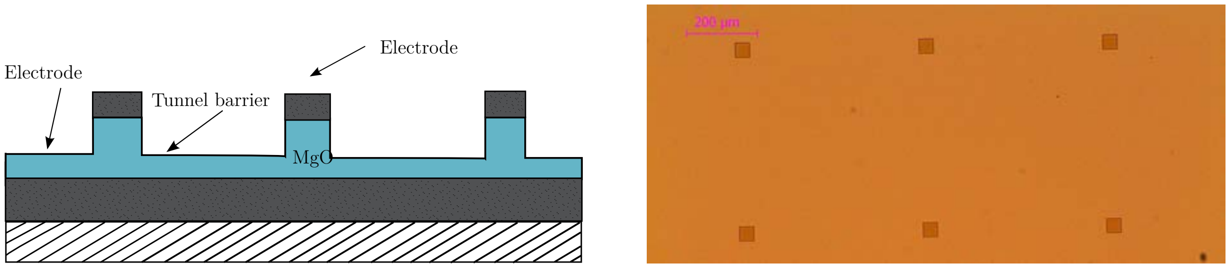

(a) (b)

Fig. A3: *Drawing (a) and top view picture (b) of the sample after the first step of lithography and dry etching.*

II. Bottom electrodes

A second step of lithography associated again with a dry etching defines the electrodes at the bottom of the tunnel junction and on the substrate.

The sample preparation is the same as the previous step (cleaning with acetone and coating with $1.3\mu m$ of S1813 resin). The photolithography defines a rectangular shape around the previous patterns (see picture (b) of figure A4). Then, the sample is etched until the silicon substrate on which the bottom electrode will sit. The sample profile at the end of this step is represented on the drawing (a) of figure A4.

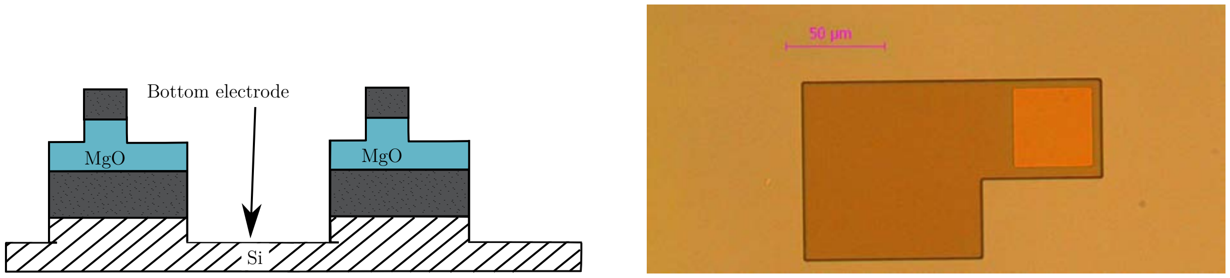

(a) (b)

Fig. A4: *Drawing (a) and top view picture (b) of the sample after the second step of lithography and dry etching.*

III. Insulation of the electrodes

The third step consists in insulating the three electrodes (top, at the end of the tunnel junction, and bottom electrodes) in order to prevent short circuits. Therefore, a 150nm thick layer of SiO_2 is grown by cathodic pulverisation (AC450 Alliance Concept of CC Minalor). In order to drill the insulator layer and take electrical contacts on the electrodes, a photolithography has defined before an area on each electrodes. Unfortunately, the lift-off of the resin after the deposition is hard due to the insulating layer. That is why a "cap shape" is defined on the resin by coating the sample with LOR3A before the S1813 resin, which is a resin that develops faster than the S1813 in MF319 (see figure A5a). A primer is used to stick well the LOR3A resin on the sample. The primer is spin-coated for 30 seconds at 7000 rpm, and heated at 115^oC for 30 secondes. LOR3A is spin-coated for 30 seconds also and heated at 140^oC for 120 seconds.

Finally, to realise electrical contacts, a fourth lithography step is made. The patterns left after the resin development constitute big squared electrodes. They are filled with a deposition of tantalum and aluminum (see figure A5c).

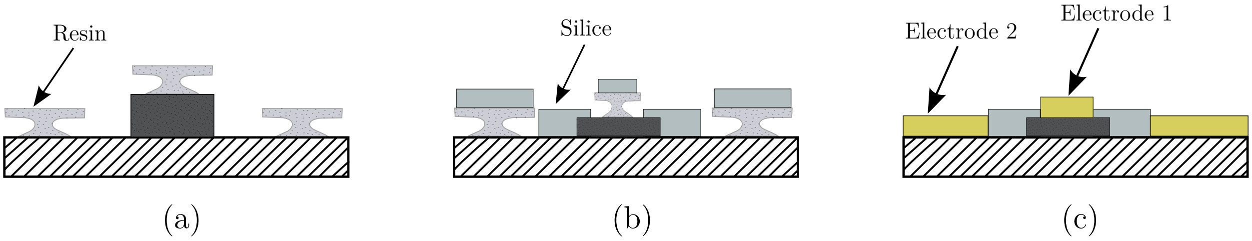

(a) (b) (c)

Fig. A5: *Opening of the insulating layer and deposition of the metal. The substrate is represented hatched, the insulator is in yellow-green and the metallic layer in yellow. After the development, the resin has disappeared in the area which will be filled with the insulator, that is to say on horseback under the different places of electrical contact. The resin take a shape of a cap (a), that will facilitate the lift-off. The silica is then deposited by cathodic pulverisation (b). After the resin lift-off and a fourth lithography, the metal is deposited on the electrodes (c).*

Stages	Conditions	
Cleaning	Acetone	5 min
	Isopropanol	20 s
Litho 1	Insulation S1813	20 s
	Development MF 319	40 s
Dry etching	Stop at the end of tunnel junction	
Resin remove	Acetone	2 h + 5 min US
	Isopropanol	20 s
Litho 2	Insulation S1813	20 s
	Development MF 319	40 s
Dry etching	Stop in the substrate	
Resin remove	Acetone	2 h + 5 min US
	Isopropanol	20 s
Litho 3	Insulation S1813 + LOR3A + primer	20 s
	Development MF 319	60 s
Deposition of insulator	SiO_2	150 nm
Lift off	Acetone	12 h + 5 min US
	MF 319	5 min
Litho 4	Insulation S1813	20 s
	Development MF 319	40 s
Deposition of metal	Pt	10 nm
Resin remove	Acetone	12 h + 5 min US
	Isopropanol	20 s

Fig. A6: **Table summarising the different steps of the nano-structuration**

Stages	Conditions	
Lithography 1, 2, 4		
`Deposition of 1813 resin`	10000 rpm	60 s
`Heat`	115^oC	1 min
`Insulation`	$\lambda = 365\ nm$	35 $mJ.cm^{-2}$
`Development`	MF319	40 s
`Rinsing`	Deionised water	20 s
`Drying`	Nitrogen	
Lithography 3		
`Drying`	115^oC	2 min
`Deposition of primer`	7000 rpm	30 s
`Heat`	115^oC	30 s
`Deposition of LOR3A`	7000 rpm	30 s
`Heat`	140^oC	2 min
`Deposition of 1813 resin`	10000 rpm	60 s
`Heat`	115^oC	1 min
`Insulation`	$\lambda = 365\ nm$	35 $mJ.cm^{-2}$
`Development`	MF319	60 s
`Rinsing`	Deionised water	20 s
`Drying`	Nitrogen	

Fig. A7: **Table summarising the conditions for lithography**

Remerciement :

Avant toutes choses, je tiens à remercier Claire Baraduc et Wolfgang Weber qui ont accepté de rapporter cette thèse. Je remercie également Coriolan Tiusan d'être rapporteur, ainsi que Bertrand Kierren qui a assuré la présidence de ce jury.

Après quatre années passées à Paris pour mes études, je n'avais qu'une idée en tête : revenir dans ma campagne natale, à Nancy. C'est dans cet état d'esprit que j'ai contacté au cours du printemps 2014 Daniel Lacour et Michel Hehn, que je connaissais d'un stage d'initiation à la recherche réalisé en 2012, pour leur demander s'il voulait bien de moi en thèse. C'est ainsi que j'ai débarqué en Septembre 2014 au sein de l'équipe 101 de l'Institut Jean Lamour (IJL). Je remercie au passage Stéphane Mangin de m'avoir si bien accueilli dans l'équipe.

Je tiens en premier lieu à remercier très chaleureusement Dan et Michel, mes deux mentors. Vous m'avez appris énormément durant ces trois années, tant d'un point de vue scientifique que d'un point de vue humain. Ça aura été un plaisir continue de bosser avec vous, de boire des bières avec vous, de parler de tout et de rien avec vous. Gardez aussi toujours cette bonne humeur qui fait de votre bureau un lieu toujours animé. Je tiens également à vous dire qu'un doctorant ne pourrait pas espérer de meilleurs encadrants, et même si je ne continue pas dans la recherche, vous aurez réussi à me faire aimer ces 3 années. Je remercie Sébastien Petit Watelot et Grégory Malinowski de m'avoir aidé pour différentes manips. Je pense notamment aux expériences réalisées sur le Laser, qui ont donné des résultats préliminaires encourageants. J'espère que la poursuite de ces expériences donnera des résultats fabuleux. J'ai une pensée également pour tous ceux avec qui j'ai pu échanger sur mes travaux. Je remercie Yuan Lu, Stéphane Andrieu, Carlos Sanchez, Noël Montblanc et tous les autres pour avoir pris de leur temps pour m'éclairer.

Je remercie également tous ceux qui m'ont aidé à un moment ou un autre. Je pense à Sylvie Robert et Vincent Polewczyk pour les expériences de rayons X, Xavier Devaux pour les images TEM, Ludovic Pasquier et Guillaume Sala du C.C. Daum ainsi qu'Alexandre Boucher pour les différents petits coups de mains. Merci à Isabelle Fournelle pour son efficacité au secrétariat et sa gentillesse. Merci également aux membres du C.C. Minalor, François Montaigne, Stephane McMurtry, Gwladys Langaigne et Laurent Badie pour avoir toujours été là pour me former, réparer mes bêtises et me conseiller pour la nano-structuration de mes échantillons. Enfin je n'oublie pas ceux du C.C. magnétisme qui m'ont beaucoup aidé, Thomas Hauet, Stéphane Suire et Crosby Chang.

Ce qui fût incroyable durant ces trois dernières années est que l'ambiance au sein du labo a toujours été fabuleuse. J'ai eu la chance de faire partie d'un groupe de thésards extraordinaire, qui a su dynamiser la vie du labo. Je remercie donc le gang des thésards composé de Damien, Florent, Mohamed, Marion, les Hugos, Vincent, Sarah, Sébastien, Abdelak, Pierre, Alex, Thibaud, Kathleen, Julien et Charles avec qui j'ai partagé des repas souvent animés, des soirées endiablés, et des moments toujours délicieux. J'ai eu l'occasion de passer des soirées inoubliables à Nancy ces dernières années. Je remercie donc tous ceux avec qui j'ai pu partager une (plutôt plusieurs) bières. Je pense en particulier à Olivier, Ludo et Guigui. J'ai trouvé en vous de véritables amis et j'espère que nous resterons longtemps en contact. Je remercie également Arnaud et les autres Post Doc, ainsi que Diego, Philippe et Gauthier pour les différents moments que nous avons partagés. Enfin, les remerciements seraient incomplets sans évoquer mes co-bureaux. Vincent tout d'abord, Sarah ensuite. Merci à vous deux d'avoir partagé ma vie de tous les jours, vous êtes de fabuleuses personnes. Un grand merci à ceux qui m'ont filé un coup de main dans le rush du manuscrit, à savoir Sarah aux Fit, Vincent aux X, Alex et Pierre au VSM, Kathleen pour ne pas m'avoir laissé mourir de faim, et surtout Thibaud et Alex sans qui le niveau grammaticale de ce manuscrit serait tout autre.

Tous ceux qui me connaissent savent bien que le rugby tient une place importante dans ma vie. Je remercie ainsi tout ceux du Cos Villers pour les supers saisons que nous avons réalisées, pour les superbes soirées que nous avons passées. Qui dit rugby dit aussi petits bobos. Je remercie donc mon médecin, mon radiologue, le chirurgien qui m'a réparé la main et ma kiné pour leurs compétences et leur sympathie.

J'ai également une pensée pour ceux qui sont là pour moi depuis longtemps : mes potes de l'ENS Carmelo, Laurie, Cécile, Aurélien, Romain, Clément, Mathieu, Thibaud ; mes vieux potes de collège Charles et Florent ; et enfin ma vieille branche Charly, qui me supporte depuis plus de 25 ans. Un grand merci à tous. Pour finir, un énorme merci à mes parents qui ont toujours tout fait pour moi et qui ont fait de moi ce que je suis aujourd'hui, à mes frères et à ma sœur ainsi que leur conjoint, à mon papy, mes tantes, oncles, cousines et cousins. Un énorme bisous enfin à mes neveux et nièces : Nolann, Lola, Camille, Zoé et Elise la dernière venue. Je vous aime fort.

J'espère n'avoir oublié personne. Dans le doute, simplement un grand merci à tous ceux qui ont partagé de près ou de loin ma vie durant ces trois années.